Exploring Neuroinflammatory Processes in a Mouse Model of Amyotrophic Lateral Sclerosis

Matthew Evans

Magdalen College, University of Oxford



A thesis submitted for the degree of Doctor of Philosophy
Nuffield Department of Clinical Neurosciences
University of Oxford

Michaelmas Term 2012

Abstract

Amyotrophic lateral sclerosis (ALS) is a devastating degenerative disease, affecting both upper and lower motor neurons in the CNS. Around 10% of ALS cases are classed as familial, and around 20% of these are due to a mutation in the gene *superoxide dismutase-1 (SOD1)*. The *SOD1*^{G93A} mouse is one of the transgenic rodent models of this disease. Both in humans and animal models of ALS, neuroinflammation is an important theme that has attracted much research attention over the past few decades. An area that has attracted much less attention, though, is the neurovascular aspect of pathology. In both these fields, the literature is biased towards the spinal cord, with little information available about *SOD1* pathology in other CNS regions. In this context, we sought to investigate pathological components of ALS pathology throughout the CNS, using a multi-disciplinary approach. First, I explore the use of MRI as in *in vivo* biomarker of brainstem pathology, showing that ALS pathology can be tracked using short sequences, paving the way for MRI as a high-throughput biomarker for clinical trials. Secondly, I use *in* vivo MRI and immunohistochemistry to investigate vascular and inflammatory components of the pathology. I show that there is very little cellular adhesion molecule expression in the CNS of *SOD1*^{G93A} mice, despite post-symptomatic expression of cytokines and chemokines, and no disruption to the BBB at any point in the disease. Finally, I investigate whether steroids have therapeutic value in *SOD1*^{G93A} mice, when delivered specifically into the CNS using targeted liposomes, and show that centrally-targeted methylprednisolone has a significant impact of brainstem pathology, but no effect on spinal pathology in this model.

In summary, inflammation is a key aspect of *SOD1*^{G93A} pathology, although changes in the permeability of the BBB may be more contentious than the previous literature would suggest. Targeting inflammatory processes using more targeted approaches may offer hope for development of therapies for ALS in the future.

Acknowledgements

I would like to start by thanking my many supervisors and advisors, in their many official and unofficial forms. To Drs Martin Turner and Nicola Sibson – thank you for the help and support throughout the DPhil, but in particular, thank you for allowing me the freedom to develop my own interests, and sense of ownership of my work. Martin -Thank you also for making me always think about the clinical relevance of research; this is one of the many reasons for my decision to move into medicine, as well as your enviable dedication to neurology. Niki - thank you so much for the constant help with the many MRI woes I have managed to stumble upon! Without the help from you and your lab, I would have been completely lost.

I of course also have to thank various members of Niki's lab for the help, support and guidance during the DPhil. Sasha – thank you for being a general MR wizard and helping make things work. Sebastien – you are comedy gold, and thanks for all the day-to-day help with MR work. Alastair – thank you for the help with VCAM analysis; I'm very glad it was you and not me that had to do battle with Matlab. And finally, James – you are a genius, thanks for responding to the torrent of emails and phone calls that come your way, and thank you for helping with my many computer-related nightmares.

And so onto the unofficial supervisors! I must give a massive thank you to Dr Daniel Anthony for offering his help and advice, and lab facilities, at a crucial time in my DPhil. Without your input, I don't know how the DPhil would have come together. Thank you also for being an excellent supervisor to work for day-to-day. You are the most emotionally demanding person I think I've ever met, but also one of the funniest and most generous, so these things balance out! Helen – I'm not even sure what to say. You have been the single most helpful, and inspiring person to work with, and I have been grateful to have the input of such a great scientist, and friend. You have given me so

much help and support over the last 2 and a half years, I am actually lost for words when it comes to thanking you. So I guess I'll stick with "thank you, you have been great" and go with that. I know you have cultural issues with emotional displays anyway, so that's probably for the best! Finally on the "unofficial supervisor" front, thank you very much to Dr Kevin Talbot – thank you for including me in your group discussions, and giving valuable informal advice with the progression of my work, and thank you (I think) for introducing me to the wonder of the SOD1 mouse.

There are a large number of people, more than can fit on these pages sadly, who's invaluable friendship over the past three years has helped me get through some of the more stressful times. Yvonne, again, I'm not really sure quite how to sum up how helpful (intentionally or not) you have been in my time in the lab. Your knowledge and expertise has helped me out scientifically more times than I can remember, but more importantly you are a brilliant friend, and your help and support in the more wafty sense has been a huge help, and gotten me through some really tricky moments. Emma – thank you for always brightening up my day with your cheeriness. You make doing long days on the scanner more bearable than they would otherwise be! Lizzy, Kath, Paul and Taya – you have all been superb in cheering me up when I'm down, distracting me with South-East Asian endocrinological male sopranos and pub-quiz, and of course, allowing me to have a roof over my head for the past few months. Andre and Ruxi – you were brilliant housemates, and I had such a great time with you for the 2 years we lived together. And many, many others, who I'm afraid I don't have time to mention, if I want to submit any time this term.

Which just leaves three very important people to thank before I stop rambling on, with this Oscar-moment-inspired diatribe. To my wonderful partner, Peter, thank you so much for being there, day-to-day, dealing with all the many, many stresses that were associated with this DPhil, and making me very happy over the past few years. I love you very much, and am grateful for your support every day. And finally, to my parents,

thank you for all of your help and support, financially, emotionally, and otherwise over the past 26 years. None of this would ever have been possible without your endless love and attention, and you will be glad to know that I am at least now on my way to a “real job”.

Publications

Publications relevant to this work

Evans MC, Modo M, Talbot K, Sibson N, Turner, MR (2012). “Magnetic resonance imaging of pathological processes in rodent models of amyotrophic lateral sclerosis”. *Amyotrophic lateral sclerosis*, 13(3), 288-301

Evans MC, Couch, Y, Sibson N, Turner, MR (In Press). “Inflammation and neurocascular changes in amyotrophic lateral sclerosis”. *Molecular and Cellular Neuroscience*.

Evans MC, Gaillard P, de Boer M, Appeldoorn C, Dorland R, Sibson N, Turner MR, Anthony DC, Stolp HB (in preparation). “CNS-targeted anti-inflammatory agent reduces pathology in mouse model of ALS”.

Evans MC, Serres S, Khraptichev A, Stolp HB, Anthony DC, Talbot K, Turner MR, Sibson N (in preparation). “The nature and timing of brainstem MRI changes in the *SOD1* mouse model of amyotrophic lateral sclerosis”.

Selected poster presentations / abstracts

Evans MC, Stolp HB, Talbot K, Anthony D, Sibson N, Turner MR (2012). “Pre-symptomatic neuroinflammatory insights from multimodal MRI in the *SOD1* mouse model of ALS”. Poster and abstract presented at *FENS*, Barcelona, Spain.

***Evans MC**, Stolp HB, Talbot K, Anthony D, Sibson N, Turner MR (2012). “Pre-symptomatic neuroinflammatory insights from multimodal MRI in the *SOD1* murine model of ALS”. Abstract and poster presented at *ENCALS* meeting, Dublin, Ireland.

Stolp HB, **Evans MC**, Molnar Z, Anthony D (2012). “Vascular effects of developmental inflammation”. Abstract and oral presentation (HS) at BBB meting, Potsdam, Germany.

Stolp HB, **Evans MC**, Molnar Z, Anthony D (2012). “Vascular response to perinatal inflammation: variation with age and site of insult”. Abstract and oral presentation (HS) given at *Society for Neuroscience,* New Orleans, US.

Evans MC, Stolp HB, Talbot K, Anthony D, Sibson N, Turner MR (2011). “Investigating vascular changes in the SOD1 mouse model of ALS”. Abstract and poster presented at *International symposium on ALS/MND*, Sydney, Australia.

Evans MC, Stolp HB, Talbot K, Anthony D, Sibson N, Turner MR (2011). “A novel method for endothelial cell isolation to investigate neuroinflammatory changes in SOD1 ALS”. Abstract and poster presented at *ENCALS* meeting, Dublin, Ireland.

* This poster also presented at Departmental research day, and was awarded third year poster prize

Other publications during period 2009-2012

Anthony D, Couch Y, Losey P, **Evans MC** (2012). “The systemic response to brain injury and disease”. *Brain, behaviour and immunity*, 26(4), 534-540.

Evans MC, Barnes J, Nielson C, Kim LG, Blair M, Leung KK, Douiri A, Boyes RG, Ourselin S, Fox NC, Alzheimer’s disease neuroimaging initiative (2010). “ Volume changes in Alzheimer’s disease and mild cognitive impairment: cognitive associations. *European Radiology*, 20(3), 674-682.

Table of contents

Chapter 1 : Introduction **1**

1.1 Background to disorders of the motor system **1**

1.1.1 The motor neuron diseases 1

1.1.2 Other disorders of the motor neuron system 2

1.2 Amyotrophic lateral sclerosis **3**

1.2.1 Symptoms and diagnosis 3

1.2.2 Genetics of ALS 5

1.2.3 Disease mechanisms 11

1.2.4 Therapeutic interventions in ALS 14

1.3 Preclinical models of ALS **18**

1.3.1 *SOD1* transgenic models 20

1.3.2 Models created by mutagenesis 23

1.3.3 *TDP-43* models 24

1.3.4 *FUS* models 25

1.3.5 Non-murine models 25

1.4 Inflammation and neuro-vasculature **26**

1.4.1 The blood-brain barrier 27

1.4.2 Inflammatory cellular interactions in the CNS 29

1.4.3 Role of astrocytes in ALS 31

1.4.4 Role of microglia in ALS 34

1.4.5 Role of lymphocytes in ALS 36

1.4.6 Neurovascular changes in ALS 38

1.5 Magnetic resonance imaging (MRI) in ALS **40**

1.5.1 T_1 and T_2(*)-weighted MRI 41

1.5.2 MRI relaxometry 42

1.5.3 Diffusion-weighted and tensor imaging 45

1.5.4 MR Spectroscopy 45

1.6 Aims of this thesis 48

1.6.1 Aims and hypotheses 50

Chapter 2 : Materials and methods 51

2.1 Animals 51

2.2 Reagents and kits 51

2.3 Genotyping 51

2.3.1 Protein confirmation of genotyping 53

2.4 *In vivo* procedures 55

2.4.1 Anaesthesia 55

2.4.2 MRI protocols 55

2.4.3 Behavioural testing 55

2.4.4 Intracerebral injections 56

2.4.5 Intravenous injections 56

2.5 Histology 57

2.5.1 Gelatinising slides 57

2.5.2 Fixative preparation for histology 57

2.5.3 Tissue preparation 57

2.5.4 Tissue sectioning 58

2.5.5 Immunohistochemistry 58

2.5.6 Haematoxylin and Eosin (H&E) 60

2.5.7 CNS regions analysed 60

2.5.8 Analysis of immunohistochemistry/histology 65

2.6 Quantitative polymerase chain reaction (qRT-PCR) 65

2.6.1 Tissue preparation 65

2.6.2 RNA isolation and cDNA conversion 66

2.6.3 Setup and reagents 66

2.6.4 PCR analysis 68

Chapter 3 : MRI investigation of vascular changes in relation to neurodegeneration in *SOD1*^{G93A} mice 70

3.1 Aims of this chapter 70

3.2 Introduction 70

3.3 Materials and Methods 75

3.3.1 Experimental groups 75

3.3.2 Behavioural testing 75

3.3.3 VCAM-MPIO 75

3.3.4 MRI 75

3.3.5 Immunohistochemistry 79

3.3.6 Intracerebral injections 80

3.3.7 Immunohistochemistry analysis 81

3.3.8 Statistical analysis 83

3.4 Results 85

3.4.1 Behaviour / weights 85

3.4.2 Investigating signal change with *in vivo* MRI 87

3.4.3 Exploration of pathological changes using histology and immunohistochemistry 96

3.4.4 Correlation between T_2 hyperintensity and histological markers 109

3.4.5 BBB permeability 110

3.4.6 *In vivo* MRI with VCAM-MPIO contrast agent to detect endothelial activation 110

3.5 Discussion 116

Chapter 4 : Exploring the inflammatory environment in the *SOD1*^{G93A} mouse at multiple levels of the neuraxis 125

4.1 Aims of this chapter 125

4.2 Introduction 126

4.3 Methods 134

4.3.1 Experimental groups 134

4.3.2 Behavioural testing 134

4.3.3 Quantitative real-time PCR (qRT-PCR) 134
4.3.4 Immunohistochemistry 135
4.3.5 Positive control tissue 135
4.3.6 Statistical analysis 135
4.4 Results 136
4.4.1 qRT-PCR for IL-1β 136
4.4.2 qRT-PCR of TNF-α 138
4.4.3 qRT-PCR for IFN-γ 140
4.4.4 qRT-PCRT for CXCL-10 141
4.4.5 ICAM-1 immunohistochemistry 143
4.4.6 E-selectin immunohistochemistry 147
4.4.7 VAP-1 immunohistochemistry 147
4.5 Discussion 150
Chapter 5 : Liposomally-packaged steroids as a treatment of neuroinflammation associated with *SOD1* ALS 155
5.1 Aims of this chapter 155
5.2 Introduction 155
5.3 Materials and Methods 161
5.3.1 Drug administration 161
5.3.2 Behavioural testing 161
5.3.3 MRI experimental protocol 161
5.3.4 Histology and immunohistochemistry 161
5.3.5 Positive control tissue 163
5.3.6 Statistical analysis 163
5.4 Results 165
5.4.1 Behaviour and weights 165
5.4.2 T_2 MRI 167
5.4.3 Histological confirmation of vacuolation 168

5.4.4 Motor neuron counts 172

5.4.5 GFAP staining 179

5.4.6 Iba1 staining 183

5.5 Discussion 187

Chapter 6 : General discussion 193

6.1 Principal findings 193

6.2 T_2 MRI as a cost-effective biomarker in pre-clinical trials 193

6.3 No change in BBB permeability 195

6.4 Activation of the endothelium 199

6.5 Integration of inflammatory changes in *SOD1*^{G93A} 201

6.6 Perspectives on therapeutic interventions 204

6.7 Future directions 207

6.8 Conclusion 209

References 210

Appendix 251

Principles of MRI 251

List of Figures and Tables

Figure 1.1 – Relative prevalence of genetic causes of sporadic and familial ALS in Caucasian populations. 6

Figure 1.2 – Pie chart illustrating the popularity of different *SOD1* rodent models, as defined by PubMed search hits 21

Figure 1.3 – Inflammatory cellular interactions in the CNS 26

Figure 1.4 - T_2-weighted MRI of a transgenic *SOD1*^{G93A} mouse 44

Figure 2.1 - Gel picture from genotyping of SOD1-11-1 to SOD1-11-11 53

Figure 2.2 - Immunofluorescent images for DAPI (blue) and human SOD1 protein (red). 54

Figure 2.3 - Diagram illustrating the position of the motor cortex 61

Figure 2.4 – Diagram illustrating the position of the trigeminal nucleus (MN V) .. 62

Figure 2.5 - Diagram illustrating the position of the facial nucleus (MN VII) 63

Figure 2.6 - Diagram illustrating the position of the hypoglossal nucleus (MN XII) 64

Figure 2.7 - Diagram illustrating the position of the ventral horn of the spinal cord (lumbar) 65

Figure 2.8 – Example standard curve (GAPDH) with line of best fit and linear equation 68

Figure 3.1 – Representative image illustrating the principle of slice selection 77

Figure 3.2 – Illustration of ROI placement for wild type and *SOD1*^{G93A} T_2 images 79

Figure 3.3 – Demonstration of the analysis method for immunohistochemistry . 82

Figure 3.4 – Demonstration of the analysis method for vacuole quantification ... 83

Figure 3.5 - Rotarod scores and weights across lifespan for *SOD1*^{G93A} and wild type littermates used in the MRI study. 86

Figure 3.6 Comparison of *T2* signal intensity in the trigeminal nucleus (V) in *SOD1*^{G93A} and wild type mice 88

Figure 3.7 Comparison of T_2 signal intensity in the facial nucleus (VII) in *SOD1*^{G93A} and wild type mice 89

Figure 3.8 Comparison of T_2 signal intensity in the hypoglossal nucleus (XII) in *SOD1*^{G93A} and wild type mice 90

Figure 3.9 Comparison of T_1 signal intensity in the three motor nuclei in *SOD1*^{G93A} and wild type mice 92

Figure 3.10 – Comparison of T_2 signal intensity, MTR and ADC in *SOD1*^{G93A} and control mice at 120 days. 95

Figure 3.11 – Representative H&E images, showing the development of vacuolation in the trigeminal, facial and hypoglossal nuclei 97

Figure 3.12 – Quantification of vacuolation in the trigeminal, facial and hypoglossal nuclei using ImageJ 98

Figure 3.13 – Representative images of GFAP immunohistochemistry in the trigeminal, facial and hypoglossal nucleus 101

Figure 3.14 - Representative images of GFAP immunohistochemistry in the spinal cord and sensorimotor cortex 102

Figure 3.15 – Quantification of optical density of DAB product from GFAP staining, in the spinal cord, cranial nuclei and sensorimotor cortex 103

Figure 3.16 - Representative images of Iba1 immunohistochemistry in the trigeminal, facial and hypoglossal nucleus 106

Figure 3.17 - Representative images of Iba1 immunohistochemistry in the spinal cord and sensorimotor cortex 107

Figure 3.18 - Quantification of optical density of DAB product from Iba1 staining, in the spinal cord, cranial nuclei and sensorimotor cortex 108

Figure 3.19 - Time course of T_2 signal change plotted along side vacuole and glial change 109

Figure 3.20 No BBB breakdown is seen at any time point in *SOD1*^{G93A} mice 113

Figure 3.21 – Imaging of VCAM-1 expression in the brains of *SOD1*^{G93A} mice and wild type controls at 120 days, and positive IL-1β-injected controls. 114

Figure 3.22 – Representative images of VCAM-1 immunohistochemistry in the sensorimotor cortex, spinal cord and cranial nuclei 115

Figure 4.1 – IL-1β expression in the sensorimotor cortex, brainstem, cervical spinal cord and lumbar spinal cord in *SOD1*^{G93A} and wild type control mice 137

Figure 4.2 – TNF-α expression in the sensorimotor cortex, brainstem, cervical spinal cord and lumbar spinal cord in *SOD1*^{G93A} and wild type control mice 139

Figure 4.3 – IFN-γ expression in the sensorimotor cortex, brainstem, cervical spinal cord and lumbar spinal cord in *SOD1*^{G93A} and wild type control mice 140

Figure 4.4 – CXCL-10 expression in the sensorimotor cortex, brainstem, cervical spinal cord and lumbar spinal cord in *SOD1*^{G93A} and wild type control mice 142

Figure 4.5 – Representative images of ICAM-1 immunohistochemistry in the trigeminal, facial and hypoglossal nuclei in *SOD1*^{G93A} and wild type mice . 144

Figure 4.6 – Representative images of ICAM-1 immunohistochemistry in the cervical and lumbar spinal cord and sensorimotor cortex in *SOD1*^{G93A} and wild type mice 145

Figure 4.7 – Quantification of ICAM-1 optical density in the sensorimotor cortex, brainstem and spinal cord of *SOD1*^{G93A} and wild type mice 146

Figure 4.8 – Representative images of E-selectin immunoreactivity in *SOD1*^{G93A} and wild type mice 148

Figure 4.9 - Representative images VAP-1 immunoreactivity in *SOD1*^{G93A} and wild type mice 149

Figure 5.1 – Steroid structure 156

Figure 5.2 – Example of a neuron defined as morphologically normal and an abnormal neuron with significant vacuolation 163

Figure 5.3 – Behaviour and weight data for the 2B3-201 study 166

Figure 5.4 – Representative T_2 MR images of the cranial motor nuclei in the 2B3-201 study 169

Figure 5.5 – Quantification of T_2 intensity in the midbrain/brainstem motor nuclei in the 2B3-201 study 170

Figure 5.6 – Light micrographs of sections of trigeminal, facial and hypoglossal nuclei, and ventral spinal cord from the 2B3-201 study, stained with H&E 176

Figure 5.7 – Quantification of vacuolation in the trigeminal, facial and hypoglossal nuclei from the 2B3-201 study 177

Figure 5.8 – motor neuron counts in the trigeminal, facial and hypoglossal nuclei, and the lumbar spinal cord (ventral horn) from the 2B3-201 study 178

Figure 5.9 – Photomicrographs of GFAP staining in the cranial motor nuclei and spinal cord of mice in the 2B3-201 study 181

Figure 5.10 – Quantification of GFAP staining intensity and astrocyte counts in the cranial motor nuclei and spinal cord of mice from the 2B3-201 study 182

Figure 5.11 - Photomicrographs of Iba1 staining in the cranial motor nuclei and spinal cord of mice in the 2B3-201 study 185

Figure 5.12 - Quantification of Iba1 staining intensity and microglia counts in the cranial motor nuclei and spinal cord of mice from the 2B3-201 study 186

Figure 6.1 – Motor behaviour and survival data of *SOD1*^{G93A} mice housed in a 'dirty' and a 'clean' facility 197

Figure 6.2 – Schematic representation of different components of the inflammatory response in *SOD1*^{G93A} mice 205

Table 1.1 - Animal models of ALS 19

Table 1.2 - Common metabolites measured by ^{1}H MRS and their physiological and pathological relevances 47

Table 2.1 - Reagents and concentrations for PCR mastermix for genotyping 52

Table 2.2 - Sense and antisense primers for *SOD1*^{G93A} transgene and *IL-6* internal control for genotyping 52

Table 2.3 - Details of the type of tissue, washes, and antibodies used for immunohistochemistry. 60

Table 2.4 - Reaction mixture for qRT-PCR using Primer Design asssays (GAPDH, IL-1β and TNF-α) 67

Table 2.5 - Reaction mixture for qRT-PCR using Invitrogen primers (20ng/μL) (IFN-γ and CXCL-10) 67

Table 2.6 - Primer sequences and probe details for the PCR assays 67

Table 3.1 - Effect size (Cohen's d) for the signal intensity in *SOD1*^{G93A} compared to wild type mice from 40 to 120 days 91

Table 3.2 - Effect size (Cohen's d) for T_2, MTR and ADC sequences at 120 days in brainstem motor nuclei 93

Chapter 1 : Introduction

1.1 Background to disorders of the motor system

1.1.1 The motor neuron diseases

The term “motor neuron disease” (MND) can be an ambiguous one, owing to two different levels of explanation associated with it. In its true sense, MND describes a group of related disorders that are united by degeneration of one or more of three main motor neuron pools: i) ventral horn of the spinal cord; ii) cranial motor nuclei; iii) motor cortex. However, in popular use, and occasionally in the scientific literature, a more restricted definition is used, which is analogous to amyotrophic lateral sclerosis (see below). To avoid confusion, MND is only used here in the broader categorical sense and, wherever appropriate, the more specific term ‘amyotrophic lateral sclerosis’ is used.

There are three main MNDs, which are defined based on the specific populations of motor neurons that are affected. There are two classes of motor neurons in the motor pathway: upper motor neurons (UMN), which have cell bodies in the motor cortex and cranial motor nuclei, and these project onto lower motor neurons (LMN) in the cranial motor nuclei and ventral horn of the spinal cord; LMNs project from the CNS to muscle fibres, and are ultimately responsible for causing muscular contraction.

Primary lateral sclerosis is a disorder that affects UMNs selectively, causing UMN signs such as spastic paraparesis. The disease course in primary lateral sclerosis can be slow, with patients affected for over a decade (Pringle et al., 1992). In contrast, progressive bulbar atrophy and progressive spinal atrophy affects only the LMN pool, with degeneration of neurons from the cranial motor nuclei and spinal cord respectively. These patients present with LMN signs such as muscle wasting (amyotrophy) and weakness (Hu et al., 1998, Gamez et al., 1999). Amyotrophic lateral sclerosis (ALS),

affects both the UMN and LMNs, and as such is characterised by both UMN and LMN signs.

1.1.2 Other disorders of the motor neuron system

In additions to the MNDs described above, there are also many MND “mimic” diseases. It is very important that these mimic disorders are excluded when coming to a diagnosis of MND, as the disease course is often very different, and as specific treatments become available, it is important to avoid mis-treatment.

Spinal muscular atrophy is an autosomal recessive genetic disorder that affects the LMNs of the spinal cord, causing reduced muscle tone, denervation and weakness. Often a disease of very early childhood, spinal muscular atrophy can also have a milder phenotype (type IV) that only affects patients later in life, and therefore may be confused with MND. Differentiation from MND is often on the basis on electromyography (Buchthal and Olsen, 1970, Emery et al., 1976). Spinal muscular atrophy is caused by a mutation, deletion or rearrangement in the survival motor neuron 1 (*SMN1*) gene (Lefebvre et al., 1995), and because of this, there is hope of forthcoming gene therapy.

Kennedy’s disease is another genetic neuromuscular disorder, caused by a polyglutamine (CAG) repeat expansion in the androgen receptor gene. The presentation of the disease is weakness, muscular atrophy and fasciculation with a predominance for facial muscles, due to degeneration of LMNs in the spinal and bulbar regions (Sperfeld et al., 2002).

In contrast to the conditions above, multifocal motor neuropathy is a peripheral nerve disorder (Chad et al., 1986, Roth et al., 1986). The clinical manifestation is progressive distal muscle weakness, typically affecting the arm muscles. The prevalence of multifocal motor neuropathy has been estimated to be around 1-2 per 100,000 (Nobile-Orazio, 2001). There is a suggestion of an auto-inflammatory component to this disease,

which has led to a number of therapeutic strategies based on manipulating the immune system (Pestronk et al., 1989, Feldman et al., 1991).

1.2 Amyotrophic lateral sclerosis

Amyotrophic lateral sclerosis (ALS) (also known as Lou Gehrig's disease in the USA and Charcot's disease in Europe) is the most prevalent subtype of MND. The annual incidence of ALS is around 1.6 new cases per 100,000 people, resulting in around 5,000 new cases per year in the UK. The prevalence of the disease has been estimated at around 4 per 100,000, which translates to around 12,000 people afflicted with the disease at any given time in the UK (Hirtz et al., 2007). There is currently no effective treatment, other than the mild effect of Riluzole (Miller, 2003, Miller et al., 2003), which is thought to act by reducing glutamate excitotoxicity indirectly through blockade of tetanus toxin (TeTX)-sensitive sodium channels, and subsequent reduction of calcium influx. The age of onset of this disorder is relatively early, at around 50-60 years of age, with a male bias of 1.3 (Hirtz et al., 2007). However, our knowledge of the population figures of ALS is mostly restricted to European populations, and those that are European in origin (e.g. US, Canada). More work needs to be carried out in African and Asian populations to put the disease in a worldwide context.

1.2.1 Symptoms and diagnosis

ALS is characterized pathologically by a progressive dysfunction and degeneration of both UMNs from the cortex and brainstem (including those making up the corticospinal and corticobulbar tracts), and LMNs from the ventral roots of the spinal cord and cranial nerves. This degeneration causes spasticity, hyperreflexia, coordination problems, stiffness, Babinsky reflex and bulbar symptoms (UMN), and fatigue, weakness, muscle cramps, muscular atrophy, fasciculation, fibrillations, suppression of reflexes, hypotonoia and paralysis (LMN) (Mulder et al., 1986, Brown, 1995, Shaw, 1999, Cleveland and Rothstein, 2001, Rowland and Shneider, 2001, Talbot, 2002). The cause of death of ALS is normally failure of respiratory muscles, which typically occurs 3-5

years after disease onset, although this is hugely variable, with a small subset of patients surviving more than 10 years post-onset (Turner et al., 2002, Turner et al., 2003). Cell death is typically seen in the ventral horn of the spinal cord, motor cortex and cranial motor nuclei V (trigeminal), VII (facial) and XII (hypoglossal) (DePaul et al., 1988), whereas motor neurons controlling the bladder (Onuf's nucleus in the brainstem) and eye movements (motor nucleus III, occulomotor) are typically spared.

Diagnosis of ALS is made with a combination of positive evidence for the symptoms of the disease, and an absence of evidence for other diseases that may show a similar presentation. This latter point is crucial, as the treatment options often differ significantly depending on the underlying pathology. The current standard for diagnosis of ALS is the El Escorial criteria from the World Federation of Neurology (Brooks, 1994). The following features are required for positive diagnosis of ALS:

1) Signs of LMN degeneration, as defined above. This needs to be in one of four regions – bulbar, cervical, thoracic or lumbosacral.
2) Signs of UMN degeneration, as defined above. This also needs to be in one of the four regions of the neuraxis in 1), but is best seen in the bulbar, cervical and lumbosacral regions.
3) Progressive spread of symptoms within or between regions within a reasonable timeframe (e.g. 12 months).

In addition to the positive evidence, other confounding conditions need to be excluded from the diagnosis. Therefore the criteria also asks for an absence of:

1) Electrophysiological evidence (e.g. electromyography) of any other pathologies that could explain the pattern of UMN and LMN signs (e.g. spinal muscular atrophy), and
2) Neuroimaging evidence (e.g. MRI) that could explain the overall clinical and electrophysiological data, (e.g. syringomyelia and syringobulbia)

Follow-ups are typically performed every 6 months to determine disease progression. Patients are defined as “suspected ALS”, “possible ALS”, “probable ALS” and “definite ALS”, depending on the extent of the neuraxis affected. In both probable and definite ALS, there needs to be UMN and LMN signs in three of the four regions, with the crucial feature determining a diagnosis of definite ALS being the absence of neuroimaging, electrophysiological or laboratory tests indicating other disorders. Furthermore patients that meet the topographical criteria for probably or definite ALS, but do not progress significantly in a 12 month period, are designated as possible ALS until some change is seen.

1.2.2 Genetics of ALS

Whilst the majority of ALS patients are defined as sporadic (sALS), in that they occur apparently randomly in the population (Charles and Swash, 2001, Chio et al., 2008), around 10% of cases are defined as familial (fALS), showing an autosomal dominant or autosomal recessive inheritance pattern, with varying degrees of penetrance. A number of genes have been linked to both familial and sporadic ALS, including *SOD1*, *TARDBP*, *FUS*, *OPTN, VCP*, *ALS2*, *SETX*, *VAPB* and *dynactin,* and are discussed briefly below. Recently a breakthrough in the field led to discovery of the gene locus *C9ORF72* as an important genetic contributor to the disease. Distribution of genetic causes for both sALS and fALS is shown in **Figure 1.1**.

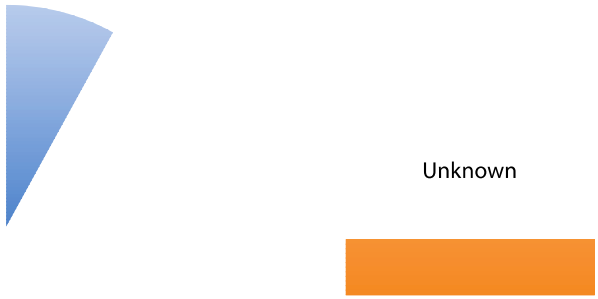


Figure 1.1 – Relative prevalence of genetic causes of sporadic and familial ALS in Caucasian populations.

In sporadic ALS, the majority of cases are of unknown genetic origin, but a substantial number carry novel mutations, or mutations with low penetrance, in genes implicated in familial ALS. Around 8% of sporadic cases carry mutations in *C9ORF72*, with only a very small number of cases ~2% due to a combination of *SOD1*, *TARDBP*, *FUS* and even more rare gene mutations.

In familial ALS, the largest genetic cause is at the *C9ORF72* locus (~40%), followed by *SOD1* (20%). A much smaller group of patients carry a mutation in *TARDBP*, *FUS* or other genes (~10% total), with around 30% of cases of unknown genetic origin.

1.2.2.1 Cu/Zn Superoxide dismutase-1 (SOD1)

Around 20% of fALS cases are due to a mutation in the Cu/Zn superoxide dismutase (*SOD1*) gene, located on human chromosome 21, which results in an autosomal dominant degenerative disorder (Rosen, 1993, Harris, 1998). The *SOD1* gene codes for a soluble antioxidant enzyme that is present in the cytosol and mitochondrial intermembrane space. Neurons, endothelial cells, macrophages and neutrophils produce superoxide (O_2^-) and nitric oxide (.NO), which combine to form peroxynitrite ($ONOO^-$), a powerful oxidizing agent that can cause damage to cells (Radi et al., 1991). The SOD1 enzyme catalyses the dismutation of superoxide into oxygen and hydrogen peroxide (H_2O_2) (Beal, 1996). *SOD1* mutations do not seem to contribute significantly to sALS: various studies quote a figure of around 1%, but this is uncorrected for the

inherent bias in screening clinical samples, as many of these could be explained by *de novo* mutations (Alexander et al., 2002) or low penetrance (Hayward et al., 1996).

To date over 125 mutations have been found in the *SOD1* gene, covering all 5 exons, with all but 11 causing overt disease (Pasinelli and Brown, 2006). Most of the mutations are point mutations, but 12 are nonsense mutations (Andersen et al., 2003). This does not seem to be a simple loss-of-function mechanism, as whilst some mutations impair enzymatic activity, others retain full function, and there is no simple relationship between enzymatic activity and disease progression. However, each type of mutation has a fairly stereotyped disease progression (Andersen et al., 1997, Radunovic et al., 1997, Yamanaka and Cleveland, 2005). For example, the most common mutation in Northern America, the A4V mutation, is characterized by a short survival (~1 year) and limited upper motor neuron involvement (Cudkowicz et al., 1998). In contrast, patients homozygous for D90A mutations in the Scandinavian population (heterozygocity is benign in this group) are characterized by a slowly progressing phenotype, with survival in excess of a decade (Andersen et al., 1996). Interestingly, patients heterozygous for D90A outside of Scandinavia develop classical ALS with a survival of 3-5 years, suggesting the presence of interacting alleles in other populations (Pasinelli and Brown, 2006).

Pathologically, *SOD1* patients are defined by ubiquitinated protein inclusions that are immunoreactive for SOD1 protein, but not for TDP-43 or FUS (see below) (Mackenzie et al., 2007). This suggests a level of heterogeneity in the disease, and has led to much debate over the *SOD1* animal models, as the protein pathology is not reflective of the majority of ALS cases. This theme is returned to in the General Discussion.

1.2.2.2 Tar DNA-binding protein-43 (TDP-43)

Mutations in the *TARDBP* gene account for around 4% of all fALS cases and around 1.5% of all sporadic cases (Mackenzie et al., 2010). The gene is located on chromosome 1p36.2, which encodes the protein TDP-43, a protein that is able to bind RNA, DNA and

other proteins and is crucially involved in RNA processing (Buratti et al., 2001, Wang et al., 2004). This important role is underscored by the fact that knockout mice are developmentally lethal (see 1.3.3 below).

Around 40 mutations have been discovered to date in the *TARDBP* gene. Pathologically, patients with TDP-43 mutations are characterized by ubiquitinated inclusions of aggregated TDP-43 protein in motor neurons and glia in the spinal cord, brainstem and motor cortex (Mackenzie et al., 2007). The protein has far broader relevance in ALS, though, as abnormal TDP-43 deposition occurs in almost all other cases of fALS and sALS that are not immuno-reactive for SOD1 or FUS (Mackenzie et al., 2010).

It was recently discovered that TDP-43 plays an important role in fronto-temporal lobar dementia (FTLD) as well as ALS, illustrating a pathological link between these two diseases (Neumann et al., 2006). This is consistent with the clinical picture, as frontal lobe symptoms (impulsivity, aggression, personality change) are often described in ALS patients (Lomen-Hoerth et al., 2002, Murphy et al., 2007a, Murphy et al., 2007b, Mackenzie et al., 2010).

1.2.2.3 FUS

Mutations in the gene *fused in sarcoma* (*FUS*) have been identified in around 3% of fALS and <1% of sALS cases (Mackenzie et al., 2010). Like TDP-43, FUS has an important role in RNA processing (Janknecht, 2005, Buratti and Baralle, 2008), which has led researchers to suggest that anomalies in RNA processing may be an important theme in ALS pathogenesis (Lagier-Tourenne and Cleveland, 2009). Under normal conditions, FUS is found in both the nucleus and the cytoplasm, and is transported continuously between these compartments (Zinszner et al., 1997, Andersson et al., 2008); in patients it aggregates in the cytosol and there is a corresponding depletion of nuclear FUS.

Patients with *FUS* mutations may present with classical ALS symptoms or may present with a more atypical phenotype (Mackenzie et al., 2010). Because of the scarcity of the disorder, there are only a few reports of the pathology seen in this disease, based on very small sample sizes (Kwiatkowski et al., 2009, Vance et al., 2009, Blair et al., 2010, Hewitt et al., 2010, Rademakers et al., 2010, Suzuki et al., 2010, Tateishi et al., 2010a). However, *FUS* ALS patients show degeneration of motor neurons in the spinal cord, and to a lesser degree brainstem, with either cytoplasmic inclusions of ubiquitinated FUS protein, or increased cytoplasmic FUS. As is the case for TDP-43, many FTLD cases are associated with FUS pathology (Mackenzie et al., 2008, Roeber et al., 2008).

1.2.2.4 OPTN

Mutations in the *optineurin* (*OPTN*) gene were originally discovered to be one of the genetic causes for primary open-angle glaucoma (Rezaie et al., 2002, Allingham et al., 2009), but more recently research has shown the gene to be mutated in a very small number of ALS cases. The initial reports of *OPTN* mutations in ALS were from Japanese populations (Maruyama et al., 2010, Iida et al., 2012), but *OPTN* mutations are extremely rare in Caucasian populations (Sugihara et al., 2011).

Pathologically, *OPTN*-ALS cases are characterized by ubiquitinated OPTN protein aggregates. OPTN staining occurs in aggregates of a small fraction of TDP-43-positive sALS cases (Hortobagyi et al., 2011, Osawa et al., 2011), and there is some suggestions that OPTN may contribute to other degenerative diseases, although this is currently contentious (Hortobagyi et al., 2011, Osawa et al., 2011).

1.2.2.5 VCP

Valosin-containing protein (VCP) is a protein encoded by the *VCP* gene, and is an ATPase-associated protein implicated in endoplasmic reticulum-associated degeneration (Weihl et al., 2009). Mutations at this locus were originally discovered to cause an extremely rare condition called inclusion body myopathy with Paget's disease

of bone and fronto-temporal dementia. However, recently a number of families were reported with mutations in the *VCP* gene, which presented with typical ALS (Johnson et al., 2010). It is estimated that *VCP* mutations may occur in around 1-2% of familial ALS cases and a very small proportion of sALS (<1%) (Abramzon et al., 2012). *VCP*-related conditions are characterized by TDP-43-positive protein pathology (Weihl et al., 2009).

1.2.2.6 C9ORF72

A number of linkage and genome-wide association studies conducted over the past 6 years indicated a locus on chromosome 9p21 linked with ALS, from a number of regions including Sweden (Morita et al., 2006), the Netherlands (Vance et al., 2006), Finland (Laaksovirta et al., 2010) and South Wales (Pearson et al., 2011). Penetrance for the disease at this locus seemed to be variable between kindreds, ranging from around 20% in the Dutch kindred, to nearly 100% in the Gwent (South Wales) kindred.

Recently, this locus was identified as the chromosome 9 open reading frame 72 (*C9ORF72*) (DeJesus-Hernandez et al., 2011, Renton et al., 2011), due to a hexonucleotide repeat expansion in the promoter region of the first intron. Expansions at this locus accounted for around 46% of fALS cases in Finland, and 38% outside of Finland (Renton et al., 2011). Whilst this was lower in the second study (22.5%) (DeJesus-Hernandez et al., 2011), this still accounts for the largest group of fALS cases for any other gene, including *SOD1*. A large proportion of sALS cases also have a repeat expansion (~21% in the Finish population), linking fALS with sALS.

So far, the function of the C9ORF72 gene product has not been elucidated. However, some interesting suggestions have been made from recent findings. For example, sequence analysis has revealed that the C9ORF72 product is a differentially expressed in normal and neoplastic cells (DENN) protein homologue (Zhang et al., 2012, Levine et al., 2013), suggesting that it may act as a guanine nucleotide exchange factor for small GTPases. Therefore one hypothesis is that it is involved in aspects of membrane trafficking, such as exo- and endocytosis. Pathologically, *C9ORF72* cases are

characterized by ubiquitinated, TDP-43 positive protein inclusions, especially in the cerebellum and the dentate gyrus (Murray et al., 2011b, Snowden et al., 2012).

1.2.2.7 Other genetic loci

In addition to the genes described above, even rarer ALS cases have been identified with genetic mutations at other loci. *Alsin*, *dynactin* and *VAMP-associated protein B*, three genes involved in cellular transport, have been associated with ALS (Yang et al., 2001, Puls et al., 2003, Pasinelli and Brown, 2006). In addition, sentaxin, a protein involved in RNA processing has also been linked with ALS (Chen et al., 2004, Chen et al., 2006), which provides more evidence for the faulty RNA processing theme to ALS pathogenesis.

1.2.3 Disease mechanisms

A number of disease mechanisms have been proposed so far, including protein aggregation, increases in reactive oxygen species (ROS), glutamate or intracellular calcium, and mitochondrial degeneration, either singly or in combination (Viner et al., 1996, Keller et al., 1997). The degeneration seen in the disease is accompanied by active gliosis (Leigh and Swash, 1991), which may interact with the degenerative pathology (see 1.4.3 and 1.4.4). In addition, the disease often presents with neurofilament abnormalities and axonal spheroids (Carpenter, 1968, Hirano et al., 1984, Gonatas et al., 1992), as well as Wallerian degeneration and atrophy of myelinated nerve fibres (Delisle and Carpenter, 1984).

1.2.3.1 Protein aggregation

Almost all neurodegenerative diseases are characterized by aggregation of proteins in tissue, either intra- or extra-cellularly, and the characterization of specific proteins within the aggregates has been the focus of the pathology of these diseases for some time. In fact the pattern of protein staining within aggregates has been used to differentiate and classify diseases. All types of ALS have protein aggregation, although as discussed

above, the particular proteins present in inclusions will depend on the disease-causing mutation (see 1.2.2). In the case of *SOD1* ALS, intracellular aggregates of mutated SOD1 protein appear before disease onset, and increase throughout the disease (Bruijn et al., 1998). The role of the aggregates in the disease process is likely to be complex, involving a loss of the normal protein function, possible toxicity of the aggregated species, and disruption of normal cell function due to the aggregation.

1.2.3.2 Reactive oxygen species (ROS)

Discovery of the involvement of *SOD1* in ALS quickly led to the hypothesis that impairment of the metabolism of ROS may have a role in cellular damage in ALS. Disruption of the normal enzymatic activity of the SOD1 protein could result in increased concentrations of hydroxyl radicals and/or peroxynitrite (Beckman et al., 1993, Wiedau-Pazos et al., 1996), which would lead to oxidative damage and potentially cell death. This hypothesis is supported by the finding that 3-nitrotyrosine levels (a marker of cellular damage from peroxynitrite) are increased both in *SOD1* models and human patients (Beal et al., 1997, Bruijn et al., 1997a). However, many animal models of *SOD1* ALS show characteristic pathological change despite unaltered or even enhanced enzymatic function (Gurney et al., 1994, Bruijn et al., 1997b). Therefore, if ROS are a contributor to the disease mechanism, this is clearly not the only or main mechanism. In addition, microglial activation can result in up-regulation of NADH oxidase and increased production of ROS (Lucas et al., 2006, Block and Hong, 2007).

1.2.3.3 Glutamate excitotoxicity

Increased glutamate activity and intracellular calcium are intimately connected; an increase in the release of glutamate by the pre-synaptic terminal, or an increased sensitivity for glutamate at the post-synaptic terminal will cause enhanced opening of ionotropic receptors, and an excessive influx of sodium and calcium ions. Calcium homeostasis is crucial, as many important cellular functions are dependent on the level of intracellular calcium, so a disruption of this homeostasis can be lethal for the cell. A

large number of ALS cases have increased levels of glutamate in the cerebrospinal fluid (CSF), and glutamate levels are correlated with disease severity (Spreux-Varoquaux et al., 2002).

The protein glutamate transporter-1 (GLT-1), otherwise known as excitatory amino acid transporter-2, is a protein expressed on astrocytes, and is involved in the clearance of glutamate from the synaptic cleft, in order to prevent glutamate-mediated excitotoxicity. GLT-1 levels are decreased in both human patients and preclinical models of ALS (Rothstein et al., 1995, Bruijn et al., 1997b, Howland et al., 2002). Whilst glutamate excitotoxicity is more commonly due to overstimulation of *N*-methyl-*D*-aspartic acid (NMDA) receptors, motor neurons seem to be more vulnerable to α-amino-3-hydroxy-5-methyl-4-isoxazole propionic acid (AMPA) receptor-mediated excitotoxicity (Van Den Bosch et al., 2006).

1.2.3.4 Mitochondrial dysfunction

Mitochondria are essential to cell survival; they produce adenosine triphosphate (ATP), which is essential for energy-dependent cellular processes, and involved in maintaining calcium homeostasis. Alterations in the structure of mitochondria can be seen in human cases and animal models, and mitochondrial degeneration is thought to be the cause of vacuolation (Afifi et al., 1966, Takenaka et al., 1990, Dal Canto and Gurney, 1994, Niessen et al., 2006).

In terms of *SOD1*-related ALS, the link with mitochondria is becoming increasingly clear. It is surprising that SOD1 would be required to protect the mitochondria from oxidative damage, given the presence of MnSOD (SOD2) within the mitochondria, but there is now little doubt of its importance. In non-pathological conditions, SOD1 is transported into mitochondria, where it is found in greatest concentration in the intermembrane space (Liu et al., 2004, Vijayvergiya et al., 2005). A number of strands of evidence show that mitochondrial SOD1 is important in protecting the cell from oxidative damage (O'Brien et al., 2004, Aquilano et al., 2006, Fischer et al., 2011). It seems that *SOD1*

ALS results in aggregates and oligomers of SOD1 in the intermembrane space, either causing damage directly through aggregate formation, or by loss of the protective dismutase activity (Deng et al., 2006, Ferri et al., 2006).

Non-*SOD1*-linked ALS has also been linked with mitochondrial dysfunction and degeneration (Huang et al., 2010, Shan et al., 2010). However, the mechanisms of this have not been explored to the same extent as for *SOD1*-mediated mitochondrial damage.

1.2.4 Therapeutic interventions in ALS

To date, around 200 compounds have been trialled in preclinical models of ALS, a significant number of which have shown promise to treat the disease (Turner and Talbot, 2008). However, only Riluzole has translated to therapeutic efficacy in the clinic thus far. Some of the reasons for this are discussed in the Discussion.

1.2.4.1 Anti-oxidants

Various compounds with antioxidant properties have been trialled in ALS models. Catalase, ginseng and vitamin E conferred a mild increase in age of onset with limited effect on survival time (Gurney et al., 1996, Reinholz et al., 1999, Jiang et al., 2000). However, effects are often different between high and low copy number strains (Reinholz et al., 1999). A number of other antioxidants increased survival but not onset, including nitric oxide synthase (NOS) inhibitors, creatine, synthetic SOD/catalase and red wine (Facchinetti et al., 1999, Klivenyi et al., 1999, Jung et al., 2001, Amodio et al., 2006), whereas others increased age of onset in addition to survival, like green tea, celastrol, and Neu2000 (Kiaei et al., 2005, Koh et al., 2006, Shin et al., 2007).

1.2.4.2 Anti-glutamatergics

Riluzole is still the only effective treatment that has passed clinical trials and is used for ALS treatment. Riluzole is thought to act by blocking TeTX-sensitive sodium channels

present on damaged neurons and, therefore, reduces excess calcium entry into the cell, thereby inhibiting glutamate release (Song et al., 1997). In addition, up-regulation of astrocyte GLT-1 by ceftriaxone and GPI-1046, application of glutamate receptor antagonists, and inhibitors of glutamate carboxypeptidase II (an enzyme involved in the conversion of *N*-acetylaspartylglutamate to glutamate and *N*-acetylaspartate) have all shown some therapeutic effect in preclinical models of ALS (Ghadge et al., 2003, Van Damme et al., 2003, Rothstein et al., 2005, Ganel et al., 2006).

1.2.4.3 Anti-aggregation

A number of studies have attempted to capitalise on the heat shock proteins to ameliorate the protein aggregation. Heat shock proteins are stress proteins that are involved with folding and unfolding, and transportation to the proteasome for degradation (Schwartz, 1990, Morimoto, 2011). Arimoclomol is a drug that was developed as a treatment of ALS (and other degenerative diseases characterized by aberrant protein folding) by up-regulating the heat shock protein response. When given to transgenic mice, an increase in survival was seen (Kieran et al., 2004), although as pointed out in Turner and Talbot (2008), a direct association between protein aggregation and the heat shock protein was not demonstrated. Furthermore, it is unclear from this study whether treatment with arimoclomol during clinically relevant time points would yield a therapeutic effect. However, it was shown subsequently that arimoclomol treatment, either early or late in the disease process, provided a therapeutic effect, and that it was associated with a reduction in protein aggregation (Kalmar et al., 2008). Using a more specific mechanism, exogenous delivery of heat shock protein-70 gave some protection in a *SOD1* mouse model (Gifondorwa et al., 2007).

1.2.4.4 Anti-apoptotics

The ultimate cause of cell death in neurodegenerative conditions is activation of the apoptotic pathway. Description of the mechanisms of apoptosis, and its involvement in ALS is beyond the scope of this thesis, but there are excellent reviews on this topic

(Sathasivam et al., 2001, Sathasivam and Shaw, 2005, Elmore, 2007). Lithium has been shown to reduce apoptosis in other neurological conditions (Li et al., 2010), and lithium administration increased age of symptom onset when injected systemically in ALS mice (Shin et al., 2007). zVAD-fmk, which is a general caspase inhibitor, also increased age of onset, as well as disease duration when injected intrathecally (Li et al., 2000). Other successful apoptosis-related mechanisms in ALS models include rasagiline, Janus kinase inhibitors, phenylbutyrate and valproate (Trieu et al., 2000, Sugai et al., 2004, Waibel et al., 2004, Ryu et al., 2005).

1.2.4.5 Growth factors

Promoting the protective response afforded by growth factors has been another source of therapeutic strategies in ALS. Administration of growth factors or substances upregulating growth factor pathways, including vascular endothelial growth factor (VEGF), basic fibroblast growth factor (bFGF), AIT-082 or $p75^{NTR}$ antagonists peripherally (orally and intraperitoneal) has been mostly unsuccessful in reducing symptoms (Upton-Rice et al., 1999, Turner et al., 2004a, Jiang et al., 2006, Zheng et al., 2007). More specific delivery into the CNS has led to better therapeutic effect for activity-dependent neurotrophic factor (ADNF) and insulin-like growth factor-1 (IGF-1) (Nagano et al., 2005, Chiba et al., 2006).

1.2.4.6 Steroid compounds

A number of studies have investigated whether sex hormones alter the disease process in *SOD1* rodent models. In human ALS, males are more susceptible to develop the disease compared to females, and in *SOD1* rodent models, males tend to progress to death faster than females. In human ALS, low index finger : ring finger ratio, a feature of high testosterone exposure *in utero,* confers motor neuron vulnerability later in life, suggesting a negative role of sex hormones in ALS (Vivekananda et al., 2011). Two studies investigated the effect of gonadectomy, on male and female *SOD1* mice respectively. Gonadectomy, and the resultant decrease in serum androgen levels had

no effect of disease course in male *SOD1* rats, nor did administration of the protective neurosteroid dehydroepiandrosterone (DHEA) (Hayes-Punzo et al., 2012), which suggests that the influence of sex hormones on disease progression in *SOD1* rodent models is not testosterone-driven. Similarly, anabolic-androgenic steroids, which mimic the effect of testosterone and dihydrotestosterone, had very limited effect on the molecular profile of *SOD1* mice, although it did exacerbate the increase in TGF-β1 seen in *SOD1* muscle tissue (Galbiati et al., 2012). In clinical populations, low levels of free testosterone have been reported (Militello et al., 2002), as well as higher levels of progesterone, which seem to be associated with better outcomes in ALS patients (Gargiulo Monachelli et al., 2011). This is supported by preclinical findings that progesterone administration is protective in the Wobbler mouse (Groeneveld et al., 2004). On the other hand, ovariectomy increased progression to death after disease onset, which was rescued by administration of 17β-estradiol (Choi et al., 2008), suggesting a protective role of oestrogens in *SOD1* pathogenesis.

There is also some evidence that corticosteroids can alter the disease in *SOD1* mice (Gonzalez Deniselle et al., 1996, Deniselle et al., 1999, Gonzalez Deniselle et al., 1999a, Gonzalez Deniselle et al., 1999b, Gonzalez Deniselle et al., 2001, Groeneveld et al., 2004, Bordet et al., 2007, Fidler et al., 2011, Roozendaal et al., 2012, Sunyach et al., 2012), although attempts to use corticosteroid compounds in a therapeutic capacity have been limited, both in preclinical models and in clinical populations. Given the relevance of corticosteroid treatments in ALS to this thesis, this literature is discussed further in Chapter 5.

1.2.4.7 Non-steroidal anti-inflammatory drugs

A number of non-steroidal compounds with anti-inflammatory or immunosuppressant activities have been successful in protecting neurons and increasing survival in ALS models. Cyclooxygenase-2 (COX-2) is a very important molecule in the production of inflammation and pain, and COX-2 inhibitors have had therapeutic effects in animal

models, reducing inflammation and prolonging life, as have more general immunosuppressors such as thalidomide (and thalidomide derivatives), and cyclosporin (Drachman et al., 2002, Karlsson et al., 2004, Klivenyi et al., 2004, Kiaei et al., 2006). Glycogen synthase kinase and matrix metalloproteinase 9 (MMP-9) inhibitors showed a beneficial therapeutic effect when administered pre-symptom onset (Lorenzl et al., 2006, Koh et al., 2007).

1.3 Preclinical models of ALS

A number of animal models of ALS are currently available, which are summarized in **Table 1.1**. By far the most commonly used is the *SOD1* transgenic model, in particular the G93A variant.

Model (Species)	Gene	Presentation	Inclusion pathology	Reference
$SOD1^{G93A}$ (mouse)	Superoxide dismutase (SOD1). Expression 11 x endogenous levels. Glycine – Alanine point mutation	Symptom onset ~ 90 days with hind limb tremor, progression to death ~ 4 months. Golgi fragmentation, mitochondrial vacuolation days 60-80. Reactive gliosis preceding symptom onset	SOD1 ubiquitinated aggregates – no TDP43 pathology	(Gurney, 1994)
$SOD1^{G37R}$ (mouse)	SOD1. Expression 14.5 x endogenous levels. Glycine – Arginine point mutation	Symptom onset around 4-6 months. Pathology otherwise similar between these models.	SOD1 ubiquitinated aggregates – no TDP43 pathology	(Wong et al., 1995)
$SOD1^{G85R}$ (mouse)	SOD1. Expression below (20-90%) endogenous levels. Glycine – Arginine point mutation	Late symptom onset (sometimes >8 months) but very aggressive progression with degeneration of ~40% of motor neurons in 2 weeks.	SOD1 ubiquitinated aggregates – no TDP43 pathology	(Bruijn et al., 1997b)

$SOD1^{G93A}$ (rat)	SOD1. Expression 2.5 x endogenous levels. Glycine – alanine point mutation.	Reduced motor activity around 110 days, with hind limb weakness and weight loss around 123 days. Motor neuron loss and gliosis around clinical onset.	SOD1 ubiquitinated aggregates – no TDP43 pathology	(Nagai et al., 2001)
$TDP43^{A315T}$ (mouse)	TAR DNA binding protein 43 (TDP43). Expression 3 x above endogenous levels.	Motor symptom onset around 90 days. Axonal degeneration is seen without overt cell loss. Reactive gliosis is also present.	Ubiquitinated inclusions, but only very rare phospho-TDP43 inclusions.	(Wegorzewska et al., 2009)
$VAPB^{P56S}$ (mouse)	VAPB. Proline – Serine point mutation.	No overt motor phenotype.	Cytoplasmic TDP43 positive inclusions in spinal motor neurons from 18 months.	(Tudor et al., 2010)
Model (Species)	**Gene**	**Presentation**	**Inclusion pathology**	**Reference**
Legs at odd angles (LOA)	Dynein heavy chain 1. Carries missense mutation caused by random mutagenesis with *N*-ethyl-*N*-nitrosourea.	Slowly progressing motor symptoms but no significant reduction in lifespan. Degeneration of anterior horn motor neurons around 16 months. Cranial motor nuclei abnormalities and impairment of retrograde transport.	Ubiquitinated inclusions, also contain SOD1, cyclin-dependent kinases and neurofilament	(Hafezparast et al., 2003)
Wobbler	Vsp54. Carries missense mutation caused by random mutagenesis by *N*-ethyl-*N*-nitrosourea, with L976Q mutation.	Early onset motor abnormalities, as well as degeneration and loss of spinal and cortical motor neurons by week 4. Activation of micro- and astroglia also present. Degeneration is, however, biased towards cervical rather than lumbar cord	Neurofilament heavy chain, ubiquitinated inclusions.	(Pioro et al., 1998) (Schmitt-John et al., 2005)

Table 1.1 – Animal models of ALS

1.3.1 *SOD1* transgenic models

Findings of *SOD1* mutations in ALS patients soon led to the development of *SOD1* animal models. Initial attempts focused on targeted deletion of the *SOD1* gene, but mice lacked an obvious MND phenotype (Reaume et al., 1996, Ho et al., 1998). Whilst subsequent studies have shown that there is some effect on the motor system in these mice, including increased susceptibility to axonopathy, denervation and muscular atrophy (Flood et al., 1999, Shefner et al., 1999), typical ALS pathology and phenotype was not seen. Therefore a simple loss-of-function mechanism appears to be over-simplistic in accounting for ALS pathogenesis.

Taking a different approach, many transgenic animal models have been created where 12-15kb fragments of the mutated human gene have been expressed using the endogenous mouse promoter and regulatory elements (Gurney, 1994, Ripps et al., 1995, Wong et al., 1995). There are currently 15 of these models in usage, including a L126X truncation (Wang et al., 2005b, Deng et al., 2006), strains with mutations in the copper-binding domain, and mice expressing the mutated murine protein (Ripps et al., 1995). More recently a *SOD1*^{G93A} rat model has also been created. Each of these models differ, not only in the particular mutation used, but also in the copy number of the human gene introduced into the mouse genome, and as a result they all exhibit different levels of mutant protein expression, and therefore dismutase activity. Because of this, the age of onset and rate of progression differs, often substantially, between different strains. However, each of the models display clear symptoms of ALS, and associated pathology. These animals have been well evaluated biochemically (Gurney, 1994, Hafezparast et al., 2003, Kaspar et al., 2003, Kieran et al., 2005, Teuchert et al., 2006, Niessen et al., 2007) and behaviourally (Weydt et al., 2003, Dobrowolny et al., 2005, Schutz et al., 2005), but the specific pathological mechanisms that lead to selective motor neuron loss remain enigmatic.

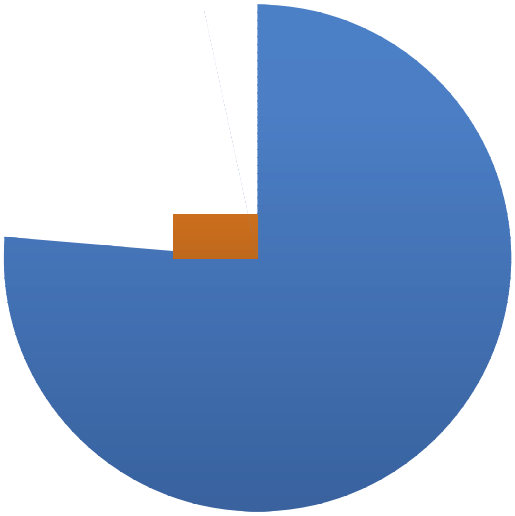


Figure 1.2 – Pie chart illustrating the popularity of different *SOD1* rodent models, as defined by PubMed search hits

The vast majority of studies using *SOD1* transgenic models use the *SOD1*^{G93A} mouse (76%), followed by the mouse *SOD1*^{G37R} (7%) and mouse *SOD1*^{G85R} (7%) Other models, including the *SOD1*^{G93A} rat (3%) are rarely used.

SOD1^{G93A} is by far the most commonly used animal model in the literature, followed by *SOD1*^{G37R} and *SOD1*^{G85R} (see **Figure 1.2**). The *SOD1*^{G93A} mouse has 25 copies of the mutant transgene, and is characterized by onset of motor symptoms at around 90 days of age, usually demonstrated by abnormal paddle reflex on tail suspension, and reduction in motor performance using the rotarod, progressing to paralysis and death at around 130-140 days (Gurney, 1994). Decrease in the size of spinal cord motor neurons has been noted as an early disease feature, starting around 60 days (Bendotti and Carri, 2004, Turner and Talbot, 2008), occurring just after loss of neuromuscular junctions (Turner and Talbot, 2008). Reactive gliosis is seen, both in the spinal cord and the brainstem (see sections 1.4.3 and 1.4.4 below), starting around symptom onset and increasing as the disease develops (Hall et al., 1998, Keller et al., 2009). Other significant disease features include mitochondrial vacuolation (Dal Canto and Gurney, 1994), fragmentation of the Golgi apparatus (Mourelatos et al., 1996) and aggregation of ubiquitinated SOD1 protein (Johnston et al., 2000).

Involvement of the UMN system has been contentious until recently (Leichsenring et al., 2006), but a number of studies have now shown that there is involvement of UMNs in *SOD1* pathogenesis (Zang and Cheema, 2002, Petrik et al., 2007, Kassa et al., 2009). Comparing to the time of onset for neuromuscular and spinal shrinkage, this is consistent with the idea of a “dying-back” pathology which has been suggested by a number of researchers (Fischer et al., 2004). Also this may not be restricted to just the descending corticospinal neurons, as changes have also been found in the number and distribution of inhibitory interneurons in the sensorimotor cortex of fALS mice (Minciacchi et al., 2009). However, some features of pathology that have been confirmed in the motor neurons of the spinal cord, such as protein aggregation and mitochondrial vacuolization (Bendotti and Carri, 2004, Turner and Talbot, 2008), are less clear in the cortex.

Another high copy number line, *SOD1*^{G37R} (Wong et al., 1995), has the highest level of dismutase activity. Conversely, it has a slightly later disease onset compared to the

G93A line, but otherwise has a very similar presentation, including mitochondrial vacuolation, which is typically not seen substantially in lower copy number *SOD1* lines or human patients (Sasaki et al., 1998). It may be that some features such as vacuolation are due to the large overexpression of mutant protein, and because of this a number of lower copy number lines have been developed, including the *SOD1*^{G85R} line (Bruijn et al., 1997b). The *SOD1*^{G85R} mouse is characterized by a late onset disease, but with a very aggressive course, progressing very quickly to death after disease onset. Interestingly this is despite mutant SOD1 activity below that of endogenous SOD1 levels, so is more "physiological" in the induction of disease.

A transgenic rat model has also been created, carrying the G93A mutation (Nagai et al., 2001). Despite having a much lower level of dismutase activity compared with the G93A mouse model (2.5 time endogenous levels compared to around 11 times), it shares many characteristic features, although slightly delayed; motor weakness and cell loss start from around 110 days. This model is nowhere near as popular as the mouse model (see **Figure 1.2**), but its larger size may be attractive for some applications (e.g. better spatial resolution relative to total brain size in MRI, greater mRNA yield for real-time PCR).

1.3.2 Models created by mutagenesis

Two early models of motor neuron disease were created by mutagenesis using *N*-ethyl-*N*-nitrosourea (ENU). Wobbler mice develop muscular atrophy with associated weakness and shaking, predominantly affecting the forelimbs, starting around 4 weeks of age (Andrews et al., 1974, Duchen, 1978). For a number of decades, the genetic defect in this model remained elusive, but an L976Q missense mutation in the *Vsp54* gene has been identified as the wobbler genetic defect (Schmitt-John et al., 2005).

The second mouse created by ENU mutagenesis is the legs at odd angles (LOA) mouse (Hrabe de Angelis et al., 2000, Rogers et al., 2001). Homozygous mice are more severe than heterozygous, dying within 24 hours of birth, but both are characterized by a severe

motor phenotype, with cramping atrophy and motor dysfunction. Subsequent studies identified a mutation in the gene encoding dynein heavy chain, resulting in an axonal transport dysfunction (Hafezparast et al., 2003).

1.3.3 *TDP-43* models

Much effort has been put into creating physiological models of TDP-43-positive ALS and ALS/FTD recently, due to the presence of TDP-43 inclusions in protein inclusion in the majority of ALS cases (both familial and sporadic). However, whilst *SOD1* models began appearing in the literature within a year or so of the discovery of the importance of *SOD1* in fALS, *TDP-43* models took significantly longer (Wegorzewska et al., 2009, Shan et al., 2010, Stallings et al., 2010, Tsai et al., 2010, Wils et al., 2010, Xu et al., 2010), in part because high levels of TDP-43 confer cellular toxicity (Ayala et al., 2008, Zhang et al., 2009, Ash et al., 2010). A number of different promoters and inducible transgenic approaches have been attempted to circumvent this issue. A number of studies used the mouse prion promoter to drive expression of the mutant protein (Wegorzewska et al., 2009, Stallings et al., 2010, Xu et al., 2010). Mice develop pathological changes in relevant motor regions, the time course of which is dependent on transgene expression; expression ~3 times endogenous levels results in disease onset at approximately 3 months (Wegorzewska et al., 2009). Other approaches used the Thy1.2 (Shan et al., 2009, Wils et al., 2010) or CamKII promoter (Tsai et al., 2010), or a tetracycline-inducible rat model (Zhang et al., 2009) to similar effect.

However, all of the current TDP-43 models lack validity as models of ALS. The main incentive of creating these models is to mimic the protein pathology seen in the majority of ALS cases. Despite carrying a mutation in the *TDP-43* gene, these models either show no obvious TDP-43 protein pathology or only show rare inclusions. Also, in many of the cases, despite there being pathology in motor regions, there is no overt cell loss (Shan et al., 2010, Xu et al., 2010). Approaches focusing on integrating whole genes

and regulatory elements into the genome, instead of smaller cDNA fragments (as is the case for all the models cited above) are the current focus of model development.

1.3.4 *FUS* models

Given the relevance of the FUS to cancer research, *FUS* knockout mice were created before the discovery of the importance of *FUS* in ALS (Hicks et al., 2000, Kuroda et al., 2000). Knockout mice were born smaller than wild type mice, had problems with suckling and died within 16 hours of birth, showing that FUS activity is important for normal developmental processes.

Transgenic rats have also been created, overexpressing a R521C mutation, which replicated many of the core features of ALS (Huang et al., 2011). Transgenic rats presented with motor symptoms, and spinal motor axon degeneration, muscle atrophy, denervation of the neuromuscular junction (NMJ), and degeneration of motor neurons in the brain. Pathologically, ubiquitinated inclusions are seen in the brain and spinal cord.

1.3.5 Non-murine models

In addition to the mouse and rat models discussed above, genetic mutant models of ALS exist in other species. Models have been created in *D. melanogaster*, *C. elegans* and *D. rerio* for *SOD1* (Watson et al., 2008, Wang et al., 2009, Ramesh et al., 2010), *TDP-43* (Lu et al., 2009, Laird et al., 2010, Liachko et al., 2010) and *FUS* (Bosco et al., 2010, Lanson et al., 2011, Murakami et al., 2012). *C, elegans* models have been used particularly in genetic screening, because they allow for high-throughput testing (Silva et al., 2011), and *D. melanogaster* models have been used to elucidate basic protein physiology (Watson et al., 2008). Because of species differences in the physiology and anatomy of motor pathways, they tend not to be used for wider applications. In light of this, and the lack of relevance for this thesis, these models will not be discussed further.

1.4 Inflammation and neuro-vasculature

Neuroinflammation is a multifaceted and complex interacting system involving many different cell types, which together determine the inflammatory environment in the CNS. Whilst the CNS has very different immunological characteristics compared to other organs, signalling nonetheless occurs both ways across the BBB. The general scheme of this process is shown in **Figure 1.3**.

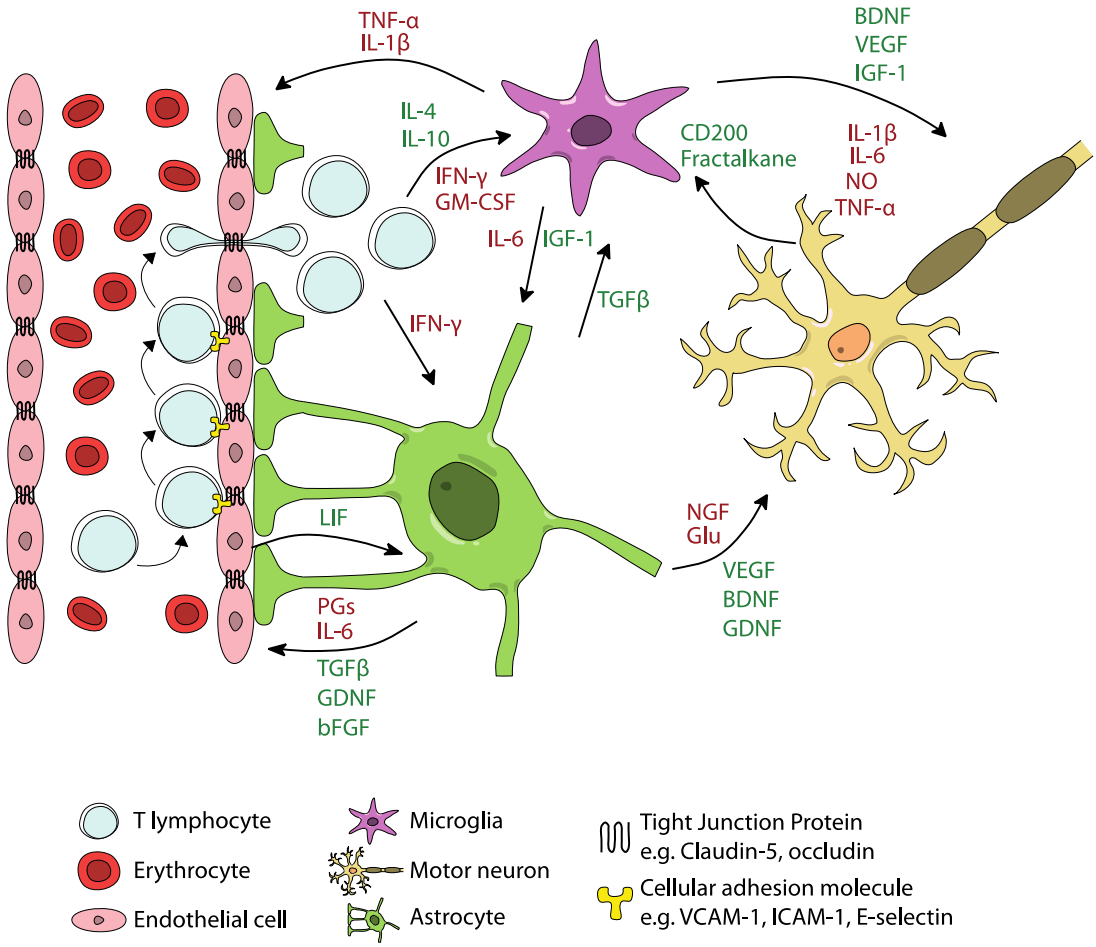


Figure 1.3 – Inflammatory cellular interactions in the CNS

Activation of the endothelium by the release of cytokines such as IL-1β and TNF-α from microglia causes expression of cellular adhesion molecules (CAMs) on the luminal wall of the blood vessels, which attracts circulating leukocytes to roll, and bind to the endothelium, and then migrate into the surrounding CNS parenchyma. Once in the CNS, lymphocytes release various pro- and anti-inflammatory molecules, which can change the activation state of resident microglia and astrocytes, which in turn release diffusible factors that can act on neurons.

1.4.1 The blood-brain barrier

The brain is a highly vascularized organ, owing to its huge metabolic demands. The blood-brain barrier (BBB)[1] is a specialised region of vasculature that separates the periphery from the CNS. It comprises a number of cell types, which act in concert to provide particularly selective permeability characteristics. Like all blood vessels, the BBB is made up of endothelial cells, held together by junction proteins. However, unlike other vessels in the body, the BBB is devoid of fenestrations (which allow substances to cross the endothelial cell layer in other tissues), and have tight junctions between endothelial cells, made up of tight junction proteins (TJPs) including claudin-5 and occludin, which occlude the paracellular pathway into the CNS for many molecules and cell types (Bazzoni and Dejana, 2004). Because of this, only very small (<400 Da) and very lipophilic molecules are able to cross the barrier in either direction (Zlokovic, 2008). There are only a very small number of lymphocytes in the healthy CNS, which is partly responsibly for the CNS being considered “immunologically privileged”.

There is evidence suggesting that BBB stability is maintained through interaction with two other important cell types at the BBB – pericytes and astrocytes. Pericytes differentiate from vascular smooth muscle cells and share a basement membrane with endothelial cells. They are in close contact with endothelial cells, and various types of junction connect the two cell types (von Tell et al., 2006). Similarly, astrocytes have “end-feet” processes that are in close contact with endothelial cells. Whilst the mechanisms are unclear, both astrocytes and pericytes seem to be involved in promoting BBB characteristics and are important for stability (von Tell et al., 2006, Zlokovic, 2008). This may be partly mediated through release of growth factors (Dore-Duffy and LaManna, 2007).

[1] The CNS has a number of barriers, which are often considered separately in the literature, including the blood-brain, blood-spinal cord and blood-CSF barriers. In this thesis, the term BBB is used as a general term for blood-brain and blood-spinal cord barrier. Blood-CSF barrier is used separately where relevant.

During inflammation in the CNS, cytokines such as tumour necrosis factor(TNF)-α and interleukin(IL)-1β are released, which cause transcriptional alterations in endothelial cells, leading to the expression of cellular adhesion molecules (CAMs), primarily intercellular adhesion molecule(ICAM)-1, vascular cellular adhesion molecules(VCAM)-1 and E-selectin (Haraldsen et al., 1996). At post-capillary venules, these CAMs are bound by receptors on leukocytes (LFA-1, VLA-4 and SLe^x respectively), leading to rolling (selectin-dependent), adhesion (ICAM-1- and VCAM-1-dependent) and transport into the CNS (PECAM and ICAM-1 dependent) at sites of injury (Shimizu et al., 1991, Barten and Ruddle, 1994, Muller, 1995, Verbeek et al., 1995, Wong et al., 1999).

There is some debate as to the mechanism of lymphocyte migration across the BBB, but there is evidence for both paracellular transport (Marchesi, 1961, Wong et al., 1999, Muller, 2003), and transcellular transport through endothelial cells using an F-actin and caveolin-based mechanism (Feng et al., 1998, Wong et al., 1999, Millan et al., 2006). Once the endothelial cell layer has been breached, leukocytes then need to traverse pericytes and the basement membranes, which is achieved by transcellular transport through the pericytes (Feng et al., 1998), and/or proteolysis of the basement membrane (Janoff and Zeligs, 1968, Uitto et al., 1980). Little is known about transport around/through astrocyte end-feet, but whilst transcellular transport is certainly possible, like pericytes, astrocyte end-feet do not form a complete barrier, so paracellular transport seems more likely in this situation. However, it should be noted that most invading leukocytes occupy the perivascular cuff and do not pass any of these secondary barriers (Bechmann et al., 2007).

The BBB also allows the selective transport of certain molecules, both in normal and disease states. In terms of transport into the CNS, many molecules that are important in biochemical pathways have specific transport mechanisms, such as the glucose transporter (Glut-1) to transport glucose as an energy source (Simpson et al., 2007), and excitatory amino acid transporters for glutamate and aspartate (Zlokovic, 2008). Similarly, various substances can be transported back out of the CNS, into the

vasculature, by efflux pumps such as p-glycoprotein (Loscher and Potschka, 2005). This has particular relevance for drug administration, as these pumps transport potentially toxic, lipophilic metabolites out of the CNS, and are thought to underlie the phenomenon of multi-drug resistance.

The characteristics of the BBB can be altered in disease states, by changes in the expression of TJPs (and subsequent changes in permeability), activation of CAMs (and subsequent infiltration of leukocyte populations) or alterations of transporters/pumps. This can be investigated experimentally by administration of substances into the vasculature, and testing whether they are able to gain access to the CNS. For example, large and hydrophilic molecules such as IgG or serum proteins will only be present in the CNS in extremely low concentrations in normal conditions, so positive areas of staining highlight areas of BBB compromise. For a detailed review of the BBB in disease, see Zlokovic (2008).

1.4.2 Inflammatory cellular interactions in the CNS

On entering the CNS, the three main cell types that the lymphocyte encounters are astrocytes, microglia and neurons, and through release of diffusible factors, lymphocytes can communicate directly, or indirectly, with all three of these cell types, altering their gene transcription and function. In addition, these cells can signal back to the endothelium, altering local permeability to specific cells or molecules (see Figure 1).

Microglia are the resident macrophages of the CNS, and have two distinct roles: firstly a supporting role for neurons in concert with astrocytes; and secondly an immunological role. At rest, microglia have a surveying role in the CNS, as they contain a number of pattern recognition molecules such as Toll-like receptors (TLR), which can alter microglial phenotype by interacting with their ligand. Recent work has reclassified activated microglia into M1-like and M2-like, in homage to the peripheral macrophage classification system (Gordon, 2003, Henkel et al., 2009). A ‘classically activated’, or M1-like phenotype, is induced by activation of microglia by pro-inflammatory molecules

such as lipopolysaccharide (LPS) and interferon(IFN)-γ. This results in transcriptional upregulation of genes that are pro-inflammatory and/or cytotoxic: pro-inflammatory cytokines, such as IL-1β and TNF-α are produced (Henkel et al., 2009), which can promote pro-inflammatory phenotypes in other cells; excess ROS, such as superoxide, are produced, which can damage the cell membranes of nearby cells; and MMPs are released, which degrade components of the extracellular matrix, and can lead to blood-borne immune cells infiltrating the CNS.

On the other hand, anti-inflammatory cytokines such as IL-4 and IL-10 can lead microglia to adopt an 'alternatively activated', or M2-like state (Martinez et al., 2006, Zhao et al., 2006), which augments a neuroprotective environment. Specifically, release of growth factors such as IGF-1 allow neuronal outgrowth and support of other glia (Isgaard et al., 2007), and anti-inflammatory cytokines like IL-10 are released, further augmenting a protective phenotype in neighbouring cells.

The degree of inflammatory output from microglia is tightly regulated by both intrinsic factors (Streit, 2002) and by cross-talk between neurons and glia. Motor neurons, in particular, suppress the neurotoxic capacity of microglia via both fractalkine and CD200 (Hoek et al., 2000, Cardona et al., 2006). Auto-activation by microglia has been shown, as well as activation by infiltrating neutrophils or lymphocytes (Li et al., 2007, Mosser and Edwards, 2008). To add more complexity, release of pro-inflammatory cytokines by M1 microglia has recently been suggested to promote an M2 phenotype, the 'destroy and clean up' hypothesis of microglial function (David and Kroner, 2011).

Astrocytes are the most populous cell type in the CNS. In addition to their obvious structural role, they are also intimately involved in the homeostasis of the extracellular environment, influencing neuronal excitability by modulating the levels of ions and neurotransmitters, and influencing neuronal health by releasing growth factors (Bezzi and Volterra, 2001, Aschner et al., 2002). Given the proximity to the vasculature, the astrocyte is ideally placed to transmit signals from the periphery to the CNS and vice

versa. Various inflammatory signals activate astrocytes, causing morphological changes and up-regulation of glial fibrillary acidic protein (GFAP), and a change in gene transcription (Pekny and Nilsson, 2005). The downstream signalling pathways after activation are mediated by NFκB (Brambilla et al., 2005) and could therefore be considered as inflammatory in nature. The cross-talk between microglia and astrocytes is important in terms of generating not only a central inflammatory response, but also in potentiating a parenchymal invasion of peripheral immune cells through release of substances that activate the endothelium. In addition, astrocytes are an important component of the BBB as mentioned above, and *in vitro* studies suggest that astrocytes are capable of releasing a number of inducing factors that can act on endothelial cells, such as transforming growth factor(TGF)-β, glial-derived neurotrophic factor (GDNF) and bFGF (Igarashi et al., 1999, Lee et al., 2003).

The following sections will apply our current knowledge of these processes to immune activation in the CNS in models of ALS.

1.4.3 Role of astrocytes in ALS

Whilst ALS is typically thought of as a disease affecting upper and lower motor neurons, numerous studies have illustrated that the pathology in this condition is non-cell autonomous; degeneration and death of motor neurons, and associated neurological symptoms, requires mutant *SOD1* expression in other cell types in addition to neurons (Pramatarova et al., 2001, Jaarsma et al., 2008). Expression of the mutant SOD1 protein in neurons and glia together is sufficient to cause cellular toxicity to the neurons, resulting in neuronal degeneration and eventual cell death (Clement et al., 2003, Beers et al., 2006, Boillee et al., 2006, Di Giorgio et al., 2007, Nagai et al., 2007, Yamanaka et al., 2008). This has been shown using both cell culture and *in vivo* experiments, and illustrates the importance of both astrocytes and microglia in ALS.

In response to injury in the brain, astrocytes become activated. Whilst it is often unclear what exactly is meant by ‘astrocytosis’ or ‘gliosis’, a typical marker is up-regulation of

the intermediate filament GFAP, and the accompanying morphological change, with hypertrophic nuclei and increased prominence of processes (Pekny and Nilsson, 2005). This feature has been noted in both *SOD1* mice and human ALS cases, both in the spinal cord, and brain motor regions (Kushner et al., 1991, Hirano, 1996, Hall et al., 1998, Nagata et al., 1998, Petrik et al., 2007, Kassa et al., 2009). However, the onset of astrocyte activation is necessarily unclear in human cases, and varies between transgenic murine strains (earlier in mouse G85R and rat G93A, later in mouse G93A) (Bruijn et al., 1997b, Hall et al., 1998, Alexianu et al., 2001, Nagai et al., 2001). Using a GFAP-luciferase reporter mouse, Kassa et al. (2009) found that the pattern of astrocyte activation even within one mouse model is complex, increasing and decreasing in waves at different times, at different levels of the neuraxis. Interestingly this study showed that the initial change in GFAP expression is actually peripherally in Schwann cells, rather than centrally as may have been predicted.

Knowing when and where astrocytes become activated in the CNS is useful, but further understanding is needed regarding the functional consequences of this activation (e.g. how does it lead to neuronal death? What other cell types does it affect?). In one recent study, Diaz-Amarilla et al. (2011) created primary astrocyte cultures from symptomatic *SOD1* rat spinal cords in order to better understand the phenotype of “aberrant astrocytes”. This identified a subset of astrocytes in symptomatic rats that show high proliferation, expression of GFAP and other astrocyte markers, but which show an absence of GLT-1. Care must be taken when interpreting glial cell culture data, however, as many cell types, including astrocytes, undergo transcriptional changes when removed from the physiological cell environment and cultured. These data are consistent with findings of a decrease in GLT-1 expression around the time of spinal motor neuron loss in *SOD1* models (Howland et al., 2002, Bruijn et al., 2004). GLT-1 is involved in uptake of excess glutamate at astrocyte end-feet, so this decrease could be the cause of glutamate excitotoxicity noted in the disease (Rothstein et al., 1992, Cleveland and Rothstein, 2001). Indeed, glutamate levels are elevated in the CSF of a

large proportion of patients with sporadic ALS (Spreux-Varoquaux et al., 2002), and Riluzole – a TeTX-sensitive Na-channel blocker, which prevents glutamate release by preventing calcium influx – is the only drug to offer any therapeutic effect so far in ALS patients (Meininger et al., 2000, Van Den Bosch et al., 2006). Aberrant astrocytes also seem to produce soluble factors that are toxic to co-cultured motor neurons (Nagai et al., 2007, Di Giorgio et al., 2008, Marchetto et al., 2008, Diaz-Amarilla et al., 2011), but these are, as yet, mostly unidentified.

Activated astrocytes may also affect motor neurons via reduced release of trophic factors, which normally promote neuronal survival. Both *in vivo* and *in vitro,* a number of trophic factors, including brain-derived neurotrophic factor (BDNF), GDNF and vascular endothelial growth factor (VEGF) have been shown to rescue motor neurons from various forms of insult (Ekestern, 2004, Van Den Bosch et al., 2004, Van Den Bosch and Robberecht, 2008). Reducing VEGF levels by deleting the hypoxia response element (HRE) of the *VEGF* gene in mice (Oosthuyse et al., 2001) caused motor neuron degeneration reminiscent of *SOD1* models. More solid evidence for the role of VEGF in ALS came from a study showing that a haplotype associated with low VEGF levels in humans conferred vulnerability for motor neuron degeneration, and deleting the HRE in the *VEGF* gene in *SOD1* mice aggravated the disease (Lambrechts et al., 2003). Astrocytes are an important source of VEGF, at least in culture models, and there is evidence that astrocyte-derived VEGF can have a direct effect on motor neurons, in addition to affecting them indirectly via their known vascular effects (Van Den Bosch et al., 2004). However, VEGF was shown not to affect the motor neuron response to excitotoxicity. Another caveat is that levels of VEGF were not significantly different in mutant *SOD1* and control mice, either in whole spinal cord or specifically in glial cells, nor was there any difference in cultured mutant *SOD1* motor neurons compared to control motor neurons in response to excitotoxicity (Van Den Bosch et al., 2004).

Therefore, the involvement of trophic factors in ALS is currently poorly understood. For example, depending on the chemical environment, nerve growth factor (NGF), or rather

its precursor form, pro-NGF, which is typically thought of as beneficial for neuron survival (Diener and Bregman, 1994), can induce apoptosis in cultured motor neurons, perhaps through the action of the receptor p75 (Pehar et al., 2004, Domeniconi et al., 2007).

1.4.4 Role of microglia in ALS

Microglia are also significant contributors to the pathology of ALS. Indeed, just as selective expression experiments have shown astroglia to be important for driving the pathology, mutant SOD1-related damage in microglia seems to be important in ALS, particularly in driving later disease progression (Beers et al., 2006, Boillee et al., 2006). Expression of mutant SOD1 in microglia alone is not sufficient to cause significant motor neuron death, but transplantation of wild type microglia in *SOD1* transgenic mice delayed disease progression significantly, showing some capacity of mutant SOD1-expressing microglia to drive the disease process. Both preclinical and human studies have shown the activation of microglia in pathologically relevant areas of the CNS such as the ventral horns of the spinal cord, and the brainstem (Engelhardt and Appel, 1990, Hall et al., 1998, Alexianu et al., 2001, McGeer and McGeer, 2002, Turner et al., 2004b).

Whilst the source of this activation is poorly understood at present, it is very likely to be due to altered level of CNS cytokines. Indeed, levels of TNF-α and the TNF-R are increased just before disease onset in *SOD1* mice, around the same time as microglial activation, and this expression increases as the disease progresses (Elliott, 2001, Hensley et al., 2002). IL-6 and IFN-γ are also upregulated in the *SOD1* mouse model (Hensley et al., 2003), which the authors hypothesise could interact with TNF-α in activating glial cells, including microglia.

Another potent activator of microglia, at least *in vitro*, is the mutant SOD1 protein itself. In addition to the validated effects of endogenous microglial mutant SOD1 protein, evidence from cell culture shows that application of exogenous mutant SOD1 can increase the production of pro-inflammatory cytokines and free radicals (Zhao et al., 2010). Presence of mutant SOD1 also causes reduced expression of neurotrophic

factors such as IGF-1 and BNDF, which may amplify the action of cytokines on vulnerable motor neurons. Response of microglia to mutated SOD1 may be through CD14, which is a pattern recognition receptor for mis-folded proteins, as mutations in SOD1 would change the protein tertiary structure (Furukawa et al., 2006). CD14 has the co-receptors TLR2 and TLR4. Like LPS, mutant SOD1 protein is able to bind to CD14, and blocking this pathway, either using antibodies raised against TLR2/4 or CD14, or by using CD14-/- microglia, attenuated the neurotoxic, and augmented the neuroprotective potential of microglia in culture (Zhao et al., 2010). This is relevant *in vivo* as CD14 expression is increased in the spinal cords of *SOD1* mice and ALS patients (Henkel et al., 2004, Henkel et al., 2006).

Another mechanism of microglial activation could be the loss of restraint imposed by other cell types, which normally restricts the M1 phenotype of microglia. As mentioned above, neurons produce fractalkine and CD200 (OX2), which prevent microglia from becoming neurotoxic (Hoek et al., 2000, Cardona et al., 2006). Microglia express the receptor for fractalkine (CX3CR1), and *CX3CR1* knockouts show a deregulated microglial response, and increased cell-autonomous toxicity in response to LPS. Moreover, mutant m*SOD1*$^{+/-}$*/CX3CR1*$^{-/-}$ mice showed increased microglial activation and motor neuron death (Hoek et al., 2000, Cardona et al., 2006).

However, it is still unclear whether microglial activation is beneficial or detrimental, and it is possible that the role changes at different points of the disease. Initial reports suggested that microglial activation is cytotoxic and therefore drives the disease process, but attempts to ameliorate disease progression by attenuating the microglial response were mostly unsuccessful (Henkel et al., 2009, Appel et al., 2010, Polazzi and Monti, 2010). Other studies have recently shown that activated microglia could have a protective capacity in CNS damage, including motor neuron death, through the release of anti-inflammatory cytokines and growth factors such as IL-4, IL-10, BDNF and IGF-1 – factors consistent with an M2 phenotype (Lalancette-Hebert et al., 2007, Simard and Rivest, 2007, Zhao et al., 2010). Therefore, whilst “activation” of microglia has been an

accepted feature of disease for some time now, it has not been clear whether this is protective or destructive (Moisse and Strong, 2006). As is discussed in the section below, microglia may adopt an M1 or M2 phenotype at different times in the disease, which could depend largely on chemical communication with infiltrating T cells. To add to this complexity, regional differences in glia- and lymphocyte-produced cytokines and growth factors may result in populations of glia with different phenotypes and function in different parts of the CNS (Beers et al., 2011). This may explain why the lumbar cord is particularly vulnerable in animal models of ALS, leading to the hind-limb onset seen in the disease.

1.4.5 Role of lymphocytes in ALS

T lymphocytes have been highlighted as important immune cells in both human ALS and animal models. Increased presence of CD4+ lymphocytes, and decreased regulatory T cells (Tregs) have been noted in the blood of ALS patients (Zhang et al., 2005, Mantovani et al., 2009), and a decrease in naïve T cells and an increase in memory T cells seen in patients compared to age matched controls (Banerjee et al., 2008). In mouse models, at the end stage of disease, there was a significant change to peripheral immune cells, with significantly reduced spleen size and weight, as well as lymphocyte numbers in *SOD1* compared to control mice (Banerjee et al., 2008). Within the CNS, though, there is significant T cell infiltration, in both humans and mouse models (Engelhardt et al., 1993, Alexianu et al., 2001). In contrast, B lymphocytes seem to contribute little to the development of the disease, as mice expressing mutant *SOD1*, but deficient for B lymphocytes, still develop ALS (Naor et al., 2009), and B lymphocytes are not typically found in the spinal cord in human patients (Engelhardt et al., 1993).

Microglia in ALS are influenced by chemical mediators released from infiltrating T-cells. From a relatively early stage in the disease (10 weeks) *SOD1* mice showed an infiltration of $CD4^+$ T cells, and microglia typical of an M2 state (e.g. increased secretion of IGF-1), as well as a general increase in mRNA of neuroprotective genes and a decrease in

mRNA of pro-inflammatory genes in the spinal cord (Beers et al., 2008, Chiu et al., 2008) Moreover, mice expressing mutant *SOD1* but with no functional $CD4^+$ T-cells (mutant *SOD1/RAG2*$^{-/-}$) were shown to display an accelerated disease progression, further supportive of a protective T-cell-microglial dialogue that increases the proportion of M2-type microglia (Tiemessen et al., 2007, Beers et al., 2008, Henkel et al., 2009). To strengthen this argument, restoration of $CD4^+$ cells in mutant *SOD1*$^{+/-}$*/RAG2*$^{-/-}$ mice by bone marrow transplantation prolonged survival (Beers et al., 2008). Additionally, the interaction between infiltrating T lymphocytes and microglia seems to rely on the activation state of the lymphocytes; SOD1 mice given donor lymphocytes showed an ameliorated disease course and increased survival for activated, but not naïve T lymphocytes. In addition, introducing activated Tregs increased time to disease onset, whereas activated T effector cells (Teff) increased the time from symptom onset to death (Banerjee et al., 2008).

However, in later stages of disease, microglia seem to adopt an M1 phenotype, producing pro-inflammatory molecules such as IL-1β and TNF-α, as well as other neurotoxic substances such as ROS (Hall et al., 1998, Alexianu et al., 2001, Beers et al., 2008). This is consistent with an infiltration of cytotoxic CD8+ cells in later stages of the disease, leading the authors to suggest a framework whereby T cell-microglia interactions (primarily driven by CD4+ cells) earlier in the disease promotes a neuroprotective, M2 phenotype, whereas T cell-microglia interactions later in the disease (driven mainly by CD8+ cells) promotes an M1 phenotype, thereby causing neuronal damage (Beers et al., 2008).

However, contradictory work using the same double mouse strain (mutant *SOD1*$^{+/-}$*/RAG2*$^{-/-}$) has shown that *SOD1* animals lacking any functional mature lymphocytes show delayed disease progression (Tada et al., 2011) suggesting a harmful effect of lymphocytes. This discrepancy could be due to a number of factors. Given that the interaction with microglia will depend in a large part on the basal activation level of the microglia, differences in transgene number could change the nature of the

cellular interaction. As these mice are known to lose copies of the transgene through successive generations, this is a distinct possibility. Secondly, given that the interaction also depends on the activation state of lymphocytes (Banerjee et al., 2008), environmental factors that would change the state of the immune system, such as exposure to pathogens, may also interact with this communication. These experiments need to be carried out before we can resolve this problem, and discover the influence (positive or negative) that lymphocytes have in *SOD1* ALS pathology.

1.4.6 Neurovascular changes in ALS

A number of early clinical observations illustrated that the vascular barriers may be affected in ALS pathology. Annunziata and Volpi (1985) and Leonardi *et al.,* (1984) showed that serum components were present in the CSF of ALS patients. Similar findings were found in the spinal cord and motor cortex of ALS patients (Donnenfeld et al., 1984), suggestive of permeability changes at the BCSFB and BBB respectively.

More recently, a number of laboratories have attempted to probe this issue further in *SOD1* rodent models of ALS. In line with the clinical observations cited above, studies have shown functional permeability changes, with leakage of substances from the blood into the CNS. Injection of Evans blue i.v., a staple marker of vascular permeability, showed increased permeability in symptomatic *SOD1*^{G93A} mice in the brainstem and spinal cord, both early and late in the disease (Garbuzova-Davis et al., 2007b). However, this is only found later in the disease in *SOD1*^{G93A} rats (Nicaise et al., 2009a). Nonetheless, this permeability increase has also been shown using an MRI measurement; Gd-DTPA injected i.v. was detected in the brain in close proximity to the lateral ventricles in postsymptomatic *SOD1*^{G93A} rats (Andjus et al., 2009). Other blood components, including IgG and hemosiderin (a haemoglobin-related molecule) have also been shown to be present in the spinal cord of a number of different *SOD1* mice and rats, further indicative of permeability changes and microhemorrhages, which apparently happens before expression of inflammatory molecules and CAMs that affect

the endothelium (Zhong et al., 2008, Nicaise et al., 2009a). There is also evidence for decreased capillary length, diameter and perfusion in the spinal cord of pre- and post-symptomatic *SOD1* mice (Zhong et al., 2008, Miyazaki et al., 2011). These findings are supported by human clinical studies using SPECT and perfusion MRI, which has shown frontal and/or parietal hypoperfusion (Beall et al., 1998, Kumar and Abdel-Dayem, 1999, Rule et al., 2010), which correlates with disease severity (Rule et al., 2010). However, not all the preclinical data is consistent with human studies, as in a human MRI study, no evidence of microbleeds was found using T_2* MRI (Verstraete et al., 2010).

Electron microscopic studies have shown changes to the BBB and BSCB in symptomatic *SOD1*^{G93A} mice (Garbuzova-Davis et al., 2007a). At both early and late disease stages, the authors noted degenerating endothelial cells and astrocytes, swollen astrocyte end-feet, mitochondrial degeneration in endothelial cells, damage to the basement membrane, and extracellular oedema in the brainstem motor nuclei and spinal cord. The swelling and oedema may be in part generated by aquaporin-4 channels (Nicaise et al., 2009b, Nicaise et al., 2010). There was also sign of capillary rupture in the brainstem. These structural changes from electron microscopy are corroborated by a change in the collagen IV and agrin expression, suggesting a dysfunction of the basement membrane (Nicaise et al., 2009a, Miyazaki et al., 2011).

A number of reports have now been published of alterations in TJP, either based on mRNA or protein quantification. Analysis of both whole tissues and isolated capillaries from various *SOD1* mice have shows a reduction of claudin-5, occludin and Zonula occludens-1 protein concentration long before the onset of symptoms, which is not dependant on mutant SOD1 activity (Zhong et al., 2008, Miyazaki et al., 2011). As mentioned above, claudin-5 and occludin are two important TJPs, and Zonula occludens-1 is a molecule that binds to the intracellular portions of the TJPs, anchoring them to the cytoskeleton. Decreased levels of the endothelial markers Glut-1 was also demonstrated through immunofluorescence (Garbuzova-Davis et al., 2007b), which the authors suggest may reflect altered vascular permeability, although the mechanism by

which this occurs is not readily apparent. This finding has also not been confirmed in isolated brain capillaries (Zhong et al., 2008).

The vascular endothelium becomes activated in mouse models of ALS, with expression of CAMs. ICAM-1, which is intimately involved in leukocyte transport (1.4.1), and melanoma cellular adhesion molecule (MelCAM) have been demonstrated to be up-regulated, and PECAM down-regulated, using both PCR and/or immunohistochemistry/Western bot (Alexianu et al., 2001, Garbuzova-Davis et al., 2007b, Zhong et al., 2008), although one study highlighted this as being a late feature of the disease (Zhong et al., 2008), whereas another shows ICAM-1 activated early in the disease (Alexianu et al., 2001). Equally, human studies have been inconsistent; one study finding elevated soluble selectin levels in ALS (Ikeda et al., 2000), and another study finding no difference between ALS patients and controls in soluble selectin or ICAM-1 levels (Rentzos et al., 2005). Moreover, monocyte chemoattractant protein(MCP)-1 and COX-2, which are both involved in increasing vascular permeability, are up-regulated at the mRNA and protein level in symptomatic mice from various *SOD1* transgenic lines (Zhong et al., 2008). Finally, a recent study suggests that an important molecule in the CNS efflux mechanism, p-glycoprotein, is up-regulated in *SOD1*^{G86R} mice. This may have important implications for treatments, as p-glycoprotein appears to confer multiple drug resistance, and may go some way to explaining the lack of efficacy of some drug treatments in the ALS mouse models, due to increased clearance from the CNS (Boston-Howes et al., 2008).

1.5 Magnetic resonance imaging (MRI) in ALS

Magnetic resonance imaging (MRI) is based on the interaction between the intrinsic spin of atomic nuclei and an applied magnetic field. All elements except for argon and cerium have at least one isotope that possesses a spin, with the value of the spin depending on the composition of the nucleus: if the number of protons and the number of neutrons is both even (e.g. ^{40}Ar) there is no overall spin; if the sum of protons and neutrons is

odd, there is a spin of ½ (e.g. ^{1}H); if the number of protons and the number of neutrons are both odd (e.g. ^{14}N), there will be a spin of 1. The principals of nuclear magnetic resonance apply to all nuclei that possess a spin, and indeed MR spectroscopic studies use a number of nuclei to probe biological samples, including ^{13}C and ^{31}P. Due to the high abundance of ^{1}H from the high proportion of water in tissue, this is the most commonly used nucleus, and we will therefore restrict discussion to ^{1}H MRI from here onwards. A discussion of the physical basis of MRI, and the sequences discussed here, is presented in the Appendix.

MRI offers unrivalled potential to study the evolution and progression of neurological disease *in vivo*. Rapid developments in both the acquisition and post-processing of images mean that a range of techniques to study both grey and white matter pathology can now be applied to rodent models of ALS.

1.5.1 T_1 and T_2(*)-weighted MRI

'Standard' T_1 and T_2-weighted MRI sequences can produce high resolution structural images differentiating grey and white matter, with T_2-weighting (and related sequences), having particular sensitivity for white matter pathology.

Automated volumetric analysis, known as voxel-based morphometry can be undertaken to study regional grey and white matter changes and has become a standard technique in clinical practice for other neurodegenerative diseases, particularly Alzheimer's disease and Huntington's disease.

In human ALS, despite post-mortem neuropathological evidence for widespread extra motor involvement, MRI volumetric changes in these regions are less consistent (Chang et al., 2005, Kassubek et al., 2005), though involvement of the right precentral gyrus was a consistent finding in a meta-analysis (Chen and Ma, 2010).

A voxel-based morphometry study in the *SOD1* mouse model of ALS revealed more widespread volumetric change in various CNS regions, including motor and

somatosensory cortices, substantia nigra *pars compacta*, striatum, internal capsule and hippocampus (Petrik et al., 2007). This study also found a decrease in total grey and total white matter in the lumbar spinal cord. Similar results were found using MR microscopy of post-mortem tissue from a putative mouse model of Guamanian ALS-Parkinson's-Dementia complex, with additional evidence of apoptosis (Wilson et al., 2004). Another application of this type of MRI sequence has been to quantify changes in the volume of hindlimb muscles as a biomarker for disease progression. Significant changes were noted from 11 weeks, over 10 days before symptom onset in *SOD1* mice (Brooks et al., 2004).

1.5.2 MRI relaxometry

An approach which does not require such high spatial resolution is termed relaxometry (a technique applicable to T_1, T_2 and T_2*), and is typically performed using a region-of-interest (ROI) rather than a whole-brain approach. In relaxometry, the assumption is that changes in the biophysical water environment or metal load (e.g. iron content) within a given tissue alter the relaxation rate of the proton magnetic moment (Helpern et al., 2004).

Using measures of T_2 relaxation, increased relaxation times have been observed in various motor nuclei (V, VII and XII) and the substantia nigra, as well as the ventral portion of the spinal cord of the *SOD1* mouse (Angenstein et al., 2004, Zang et al., 2004, Niessen et al., 2006) starting from around 80 days of age. This approach was found to be superior to other MR measures, including measurement of the apparent diffusion coefficient (ADC) (Niessen et al., 2006). Similar findings have been reported in ALS patients, with hypointensities evident on T_1-weighted images and hyperintensities on T_2-weighted and proton density images along the corticospinal tract (Waragai, 1997, Ellis et al., 1999).

The source of this signal change is not entirely clear at present. Unlike the MRI contrast seen in amyloid-β plaques in Alzheimer's disease (Benveniste et al., 1999, Falangola et

al., 2005), there does not seem to be significant iron deposition in *SOD1* mice, although abnormal relaxometry, interpreted as iron deposition along the corticospinal tract, has been reported in human ALS (Langkammer et al., 2010). However, it now seems likely that water-filled vacuolation accounts for this signal change in *SOD1* mice (Angenstein et al., 2004, Bucher et al., 2007). Such vacuolation is a downstream effect of mutant SOD1 expression (Kong and Xu, 1998, Higgins et al., 2003), possibly mediated through mitochondrial dysfunction (Jaarsma et al., 2000, Mattiazzi et al., 2002), one of several current themes in human ALS pathogenesis (Rothstein, 2009). As a caveat to this, human studies have so far concluded that corticospinal tract T_2 hyperintensities in isolation are neither sensitive nor specific enough for ALS (Peretti-Viton et al., 1999), as hyperintensities are seen in control subjects, and there is no correlation between disease severity and corticospinal tract hyperintensity. As yet no systematic study has been carried out in animal models to address this issue, nor has any quantitative analysis been performed.

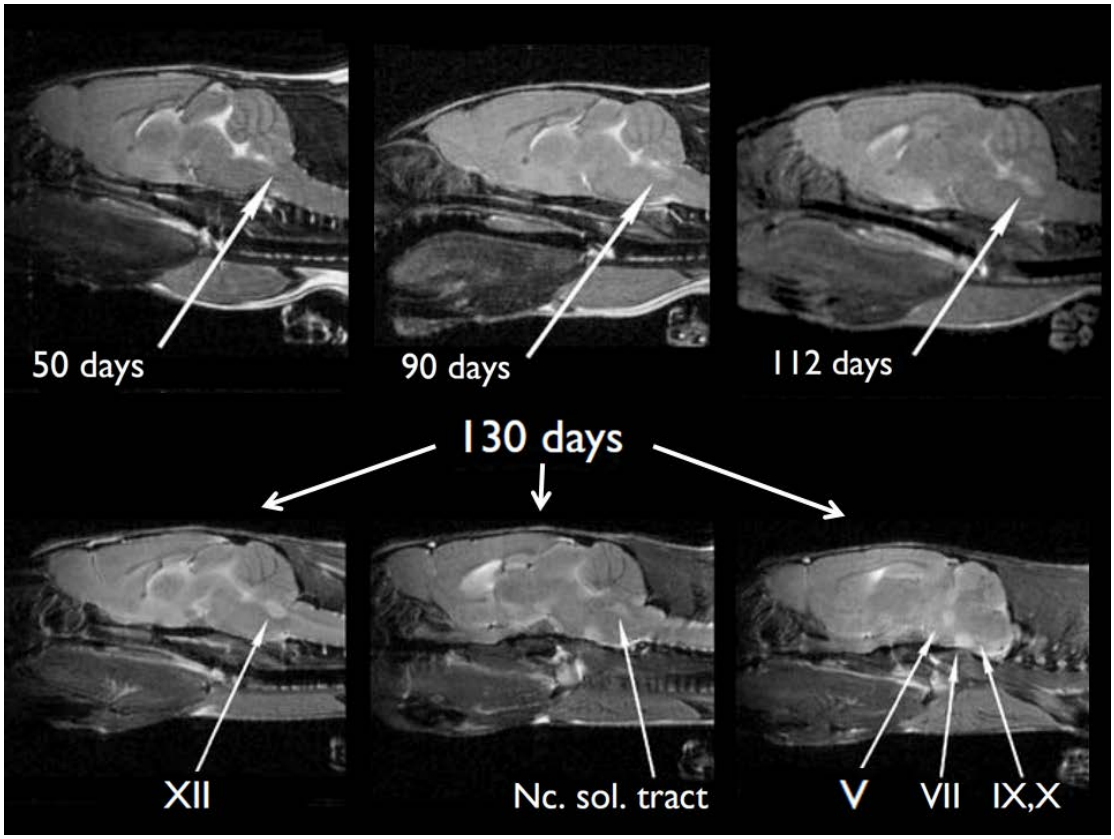


Figure 1.4 - T_2-weighted MRI of a transgenic *SOD1*^{G93A} mouse.

Hyperintensity develops in the hypoglossal nucleus (arrows, top panel) in the model at 50 days (pre-symptomatic), 90 days (early symptomatic) and 112 days (established disease). At 130 days (late stage disease), hyperintensity has developed in multiple brainstem nuclei (bottom panel with arrows), including the hypoglossal (XII), nucleus of the solitary tract (Nc. sol. tract), trigeminal (V), facial (VII), glosspharyngeal (IX), and vagus (X).

(Figure modified from Angenstein et al. (2004) [used with permission]).

1.5.3 Diffusion-weighted and tensor imaging

In ALS animal models, whilst change in the apparent diffusion coefficient (ADC) appears to correlate with disease progression, it is a much less sensitive measure than T_2-weighted imaging (Niessen et al., 2006), which may be explained by the fact that ADC is a non-directional diffusion measure. Despite this, scanning time in this study was 108 minutes at 4.7T, and for diffusion imaging to be reliably used in mouse models, scanning time has to be reduced significantly. Despite its considerable promise as a biomarker in ALS patients (Turner et al., 2011 epub), issues relating to long acquisition time and spatial resolution mean that diffusion-weighted (DWI) and -tensor imaging (DTI) have not been easily translated to rodents. However, in a model of Alzheimer's disease (Sun et al., 2005), DTI enabled separation of axonal damage (axial diffusivity, $\lambda_{||}$) from demyelination due to Wallerian degeneration (radial diffusivity, $\lambda_{\perp}$) (Song et al., 2002, Song et al., 2003, Song et al., 2005). This phenomenon has been noted in a DTI study of ALS patients (Filippini et al., 2010), where consistent increase in $\lambda_{\perp}$ in the corpus callosum was interpreted to reflect secondary demyelination reported in historic post-mortem study (Smith, 1960).

Furthermore, two studies have reported successful acquisition of full DTI data sets in *SOD1* mice, with reduced fractional anisotropy (FA), ADC and $\lambda_{||}$, and an increase in $\lambda_{\perp}$ found in the lumbar spinal cord of *SOD1* mice (Kim et al., 2010, Underwood et al., 2011). Similarly, ADC was reduced in both the cervical spinal cord and brainstem, and $\lambda_{||}$ was reduced in the cervical spinal cord in *SOD1* mice (Kim et al., 2010). Axonal damage and demyelination were confirmed by immunohistochemistry and electron microscopy.

1.5.4 MR Spectroscopy

MR spectroscopy (MRS) can provide quantitative measures of tissue metabolite levels, and with higher magnetic field strengths it is possible to delineate closely-related metabolites, which might include those with more specific relevance to ALS pathogenesis (e.g. glutamate and glutamine). Although several nuclei can potentially be

used in MRS (e.g. ^{19}P, ^{13}C), proton (^{1}H) MRS is the most widely studied, revealing consistent motor and extra-motor pathology in human ALS (reviewed in (Turner et al., 2009)). The more common metabolites quantified using MRS are listed in Table 3.

In support of a pivotal role for glutamatergic excitotoxicity in ALS pathogenesis (Rothstein, 2009), the MRS tissue concentration of glutamate was found to be higher in late-phase (c.115 days) *SOD1* mice compared to controls (Andreassen et al., 2001). In a study at very high field strength (14.1T), a very early (37 days) reduction in N-acetyl aspartate (NAA) was also observed, with a later pre-symptomatic reduction in levels of glutamine and γ-aminobutyric acid (GABA) in the spinal cord of *SOD1*^{G93A} mice (Niessen et al., 2007). Another study using Wobbler mice confirmed the reduction in NAA in a large ROI spanning the parasaggital and frontal neocortex (Pioro et al., 1998). Reduction in NAA seems likely to be a non-specific feature of neurodegenerative disorders, having also been found in mouse models of Alzheimer's disease (Dedeoglu et al., 2004, von Kienlin et al., 2005), prion disease (Broom et al., 2007) and Huntington's disease (Jenkins et al., 1993, Jenkins et al., 1998).

Metabolite	Main function(s)	Potential pathogenic link to ALS	References
N-acetyl aspartate (NAA)	Localized within neurons and myelin sheaths, decreasing levels thought to be indicative of neuronal damage / dysfunction.	Non-specific marker of neuronal loss	(Birken and Oldendorf, 1989, Kantarci et al., 2003)
Total choline (Cho)	Components of cell membranes, so increases may reflect increased membrane turnover or damage. Also a pre-cursor for acetyl-choline. Concentration higher in glia than neurons, so may also serve as measure of gliosis.	Non-specific marker of neuronal loss	(Smith et al., 2003)
Total creatine (tCr)	Important energy metabolite, so linked to oxidative phosphorylation and mitochondrial function. Changes may indicate impaired energy metabolism.	Non-specific marker of neuronal loss	(Bottomley et al., 1997)
Glutamate (Glu) Glutamine (Gln)	Glu is the main excitatory neurotransmitter. Increases may indicate excito-toxic damage. Gln is a precursor of Glu, mainly present in astrocytes before transported to neurons to be converted to Glu. Increases in Gln and decreases in Glu may suggest Gln-Glu cycling.	Excitotoxicity	(Magistretti et al., 1999, Jenkins et al., 2000)
Taurine (Tau) Myo-inositol (mIns) Scyllo-inositol (sins)	Major osmolytes in the brain, involved in volume regulation. Increases may be due to osmotic stress, e.g. as a result of atrophy. The inositols are present at much higher concentrations in glia than neurons, so can be measures of gliosis.	Glial interactions e.g. neuroinflammation or apoptosis	(Thurston et al., 1989, Brand et al., 1993)

Table 1.2 – Common metabolites measured by ^{1}H MRS and their physiological and pathological relevance

1.6 Aims of this thesis

The broad aim of this thesis is to deepen our understanding of the inflammatory and vascular changes that occur throughout the neuraxis in *SOD1*^{G93A} mice, which is the most commonly used preclinical model of familial ALS. Whilst many papers have now been published highlighting the important role inflammatory processes seem to play in the development of ALS, these tend to be mostly spinocentric, so knowledge of inflammatory mechanisms in the brain is still limited. Vascular changes are relatively unexplored in *SOD1* preclinical models, and indeed in the disease as a whole. We take a multidisciplinary approach here, investigating changes *in vivo* with magnetic resonance imaging (MRI), and *ex vivo* with immunohistochemistry and real-time polymerase chain reaction (RT-PCR).

The search for biomarkers is a booming area of research into degenerative conditions of the brain. As well as giving us insight into the biology of a disease as it unfolds, they provide us with an objective method of quantifying disease progression, and also to measure disease modification with potential drugs. MRI is frequently employed for this purpose, as the emergence of different techniques over the previous few decades, coupled with increasing availability of higher magnetic fields and small rodent machines, now allow us to probe a wide array of biological questions in more and more detail. The most robust change shown so far using MRI in both human and rodent models of ALS is a gain of signal intensity in motor areas of the central nervous system (CNS) (corticospinal tract in humans, brainstem motor nuclei in rodent models) (Waragai, 1997, Ellis et al., 1999, Angenstein et al., 2004, Niessen et al., 2006). Work in preclinical models often use lengthy scans (in excess of 1 hour) in order to achieve sufficient sensitivity and spatial resolution, but this would make MRI a very expensive biomarker to treat disease progression, and would limit the number of different scans that could be employed in a scanning session (thereby reducing the amount of biological information available to the experimenter). This biomarker requires optimization, in order to reduce the scanning time, but still retain as much of the sensitivity for disease progression as possible.

A second MRI biomarker, which is often used in multiple sclerosis but has only found limited application in ALS thus far, is the contrast agent gadolinium-diethylenetriamine penta-acetic acid (Gd-DTPA). Injection of this contrast agent into the circulation allows imaging of areas of BBB breakdown *in vivo*, as the contrast agent passes through the vascular system in normal conditions, causing no signal change in the brain parenchyma. However, when the barrier is compromised, the contrast agent is able to pass into the brain parenchyma around the area of damage, which results in marked signal change on T_1-weighted images. This technique has been used in a transgenic rat model of ALS, and results show Gd-signal intensity at the end of the disease. The potential of this tracer to shed light on disease progression at earlier disease stages has not been established, nor has it been explored so far in the more common mouse transgenic lines.

Neural inflammation occurs in many diseases affecting the CNS, and often significantly modifies the degenerative pathology. A large body of evidence has shown that microglia and astrocytes become activated before the onset of symptoms in ALS mouse models, and play a part in the pathology in human cases. Less is known about vascular changes, although work in preclinical models suggests that a number of changes may take place at the level of the CNS vasculature. Firstly, studies have reported infiltration of T lymphocytes in key areas of pathology in ALS rodent models. This is presumably associated with expression of cellular adhesion molecules such as ICAM-1 and VCAM-1 on the endothelial cells, but little is currently understood of this mechanism. Studies have also suggested an increase in permeability of the barrier, and also down-regulation of TJPs, which play a key role in maintaining barrier characteristics. All of this information, however, is strongly biased to the spinal cord – much less is known about the changes in the forebrain (especially sensorimotor cortex).

Many different types of therapies have been attempted with ALS patients and preclinical models, but only Riluzole has been shown to have any significant effect on the disease thus far, and even this has limited efficacy. Due to the mounting evidence for the important role of inflammatory mechanisms in ALS, compounds that target inflammatory pathways

have been used and shown to be effective in ALS mice, including MMP inhibitors, non-steroidal anti-inflammatory drugs, antibiotics and steroids. However, there is only limited BBB permeability for many of the compounds used, so deepening our understanding of barrier changes in the disease will also have knock-on consequences to drug design and development, to increase availability of drugs for the areas of pathology.

1.6.1 Aims and hypotheses

In this thesis, I explore the following hypotheses:

1) That shorter T_2 sequences will show sensitivity for disease progression in *SOD1*^{G93A} mice, detecting pathological changes at least as early (80 days) as previous studies with longer sequences, to allow T_2 MRI to be used as a cost-effective biomarker in drug trials
2) That other sequences sensitive to water content of tissue will shed light on the physical basis of T_2 signal change
3) That BBB breakdown occurs in multiple areas of the CNS in *SOD1*^{G93A} mice. This will be investigated both *in vivo* with MRI, and *ex vivo* using immunohistochemistry / histology
4) That astrocytes and microglia will be activated in *SOD1*^{G93A} mice, as shown in previous studies, and that this activation will vary both spatially and temporally.
5) That CAMs are expressed on the neuro-vasculature in *SOD1*^{G93A} mice. Specific involvement of a number of CAMs will be investigated both *in vivo* using MRI, and *ex vivo* using immunohistochemistry. This will be related to the transcriptional regulation of pertinent cytokines and chemokines using qRT-PCR.
6) That the steroid methylprednisolone will modify the disease process in *SOD1*^{G93A} mice, when targeted specifically to the CNS using a PEGylated, glutathione-modified liposome

Chapter 2: Materials and methods

2.1 Animals

Breeding pairs of transgenic B6SJL-TgN(SOD1-G93A)1Gur mice (*SOD1*^{G93A}) were purchased from The Jackson laboratory (Bar Harbor, ME, USA), and a breeding colony established in Oxford, maintained on a C57B/6J background. Founder mice were crossed onto the C57B/6J background for 10 generations to ensure stability of phenotype. Female *SOD1*^{G93A} mice only were used for experiments to reduce variation due to gender differences, with female non-transgenic littermates as a control group. Male *SOD1*^{G93A} were used for breeding purposes. All breeding and experiments performed obtained home office approval (license numbers 30/2524 or 30/2533), and all efforts were made to reduce animal numbers and refine techniques. All mice were housed in individually ventilated cages, and given access to food and water *ad libitum*. Due to possible interaction with pathology, no toys or exercise wheels were placed in cages. Founder mice

2.2 Reagents and kits

The RNeasy® Mini kit and RNeasy® MinElute Cleanup kit was purchased from Qiagen for RNA extraction. Superscript® III, RNaseOUT™, dNTPs and random primers used for reverse transcription, and DNase I were purchased from Invitrogen. The VCAM-MPIO was generously donated by Dr Robin Choudhury, Department of Cardiovascular Medicine, University of Oxford. All other reagents were purchased from Sigma unless otherwise stated.

2.3 Genotyping

DNA was extracted from 1mm tail clips using DirectPCR Lysis Reagent from Viagen (York, UK). Clips were incubated with 500µL of lysis reagent with 1mg/ml proteinase K at

55°C overnight. Crude lysates were placed in racks in a waterbath at 85°C for 45 minutes. The crude DNA sample was used in a standard PCR reaction using Taq DNA polymerase. Full details of the mastermix used for genotyping are given in **Table 2.1**. below. The primers for hSOD1^{G93A} and IL-6 are provided in **Table 2.2**. Samples were incubated initially for 3 minutes at 95°C. This was followed by 35 cycles with a denaturation temperature of 95°C for 30 seconds, an annealing temperature of 60°C for 30 seconds and an elongation temperature of 72°C for 45 seconds. The final elongation was at 72°C for 2 minutes, and then samples were placed on ice.

Reagent	Amount / reaction
10x PCR buffer	1.0 µL
2.5mM dNTP	0.8 µL
hSOD1^{G93A} forward primer	0.6 µL
hSOD1^{G93A} reverse primer	0.6 µL
IL-6 forward primer	0.4 µL
IL-6 reverse primer	0.4 µL
Taq DNA polymerase	0.04 µL
PCR grade water	4.16 µL
DNA	2.0 µL

Table 2.1 - Reagents and concentrations for PCR mastermix for genotyping

	Forward primer (5'-3')	Reverse primer (3'-5')
hSOD1^{G93A}	CAT CAG CCC TAA TCC ATC TGA	CGC GAC TAA CAA TCA AAG TGA
IL-6	CTA GGC CAC AGA ATT GAA AGA TCT	GTA GGT GGA AAT TCT AGC ATC ATC C

Table 2.2 – Sense and antisense primers for *SOD1*^{G93A} transgene and *IL-6* internal control for genotyping

For gel electrophoresis, 1.7µL of blue DNA loading dye (New England Biolabs) was added to each sample, and these were pipetted into a 2% agarose gel in TAE buffer (4.84g Tris base, 1.142ml glacial acetic acid, 2ml 0.5M EDTA, made up to 1L with H_2O). This was run along with 1µL 100bp ladder (New England Biolabs) in 7.3µL TAE buffer and 1.7µL loading dye for reference. This results in a strong band of 324bp in non-transgenic

littermates, but a strong band of 236bp in addition to a weaker band at 324bp for *SOD1*^{G93A} mice, shown in **Figure 2.1**.

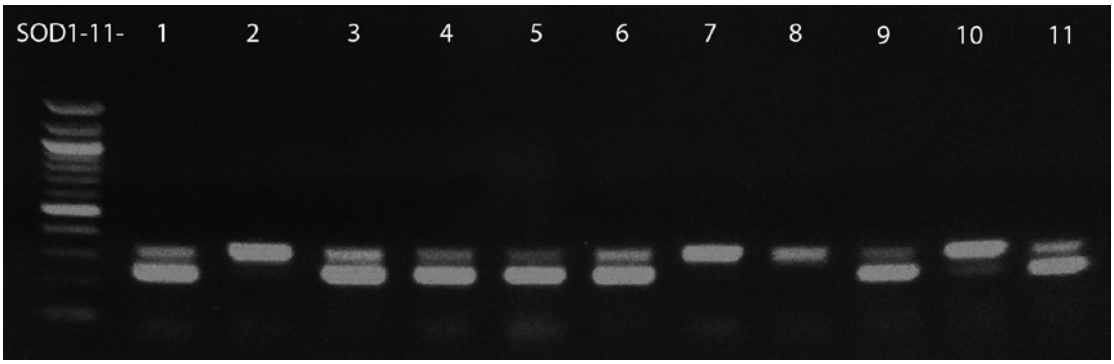


Figure 2.1 - Gel picture from genotyping of SOD1-11-1 to SOD1-11-11

There is a clear distinction between non-transgenic (S1-11-[2,7,8,10]) and *SOD1*^{G93A} (S1-11-[1,3,4,5,6,8,11]) mice. Non-transgenic mice have a single band at 324bp (IL-6), but in addition to this, *SOD1*^{G93A} mice have a band at 236bp.

2.3.1 Protein confirmation of genotyping

With mice used for immunohistochemistry, genotyping was confirmed using immunofluorescence. Spinal cords were perfused and post-fixed with 4% PFA. These were then embedded in OCT, and 10µm sections of spinal cord were cut using a cryostat at -20°C. A rabbit polyclonal antibody against *hSOD1* protein (with no mouse cross reactivity) from Abcam (ab52950) was applied 1:200 to the tissue sections. A goat anti-rabbit biotinylated secondary antibody (Vector labs) was used to bind to this primary antibody, and then streptavidin-conjugated Texas Red (Vector labs) was used for fluorescent detection. Between each of the antibody steps, sections were washed 3 times with phosphate buffered saline (PBS) solution. Presence of human protein was seen in all *SOD1*^{G93A} mice, particularly in the ventral horn of the spinal cord (see **Figure 2.2**).

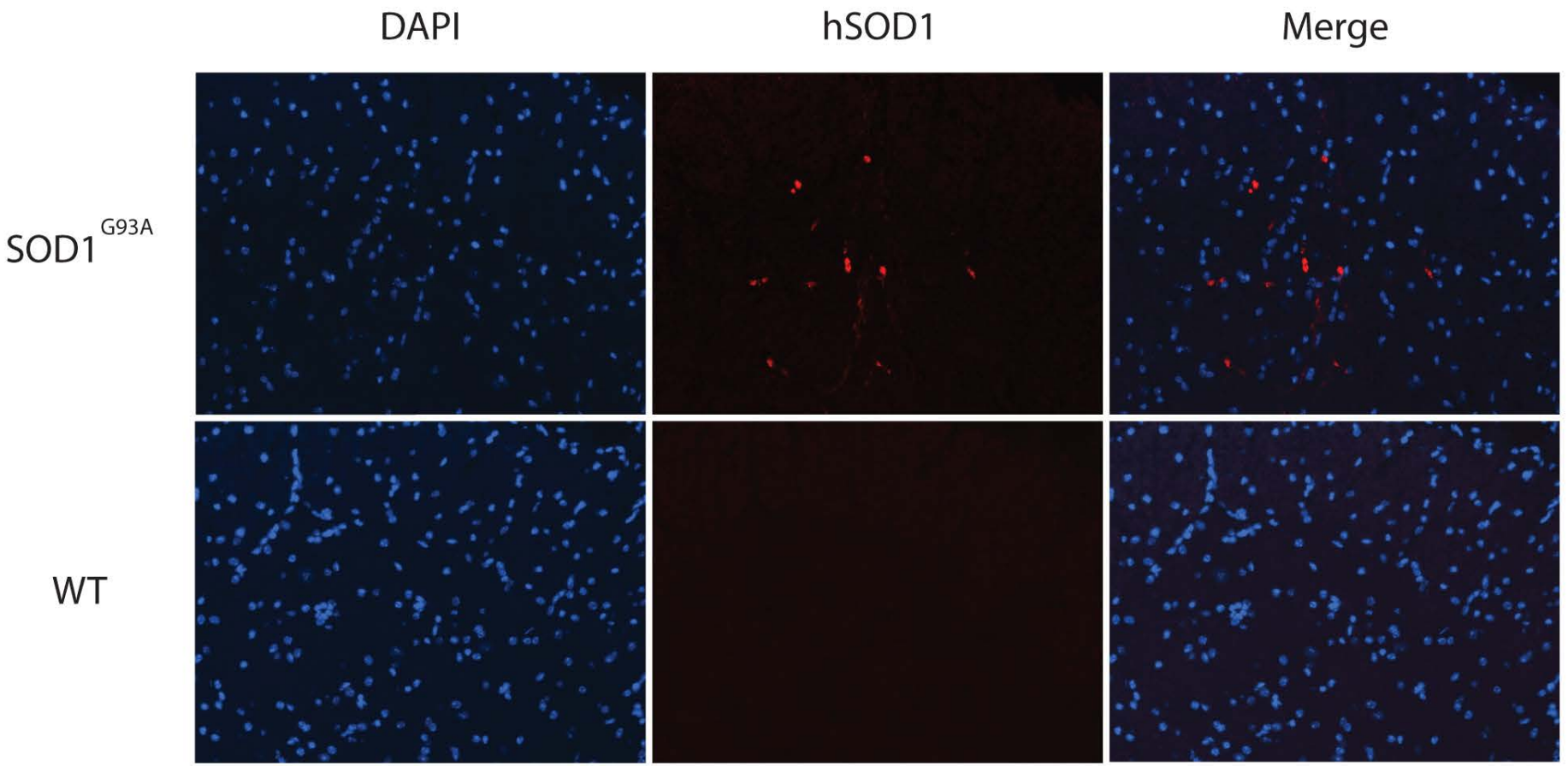


Figure 2.2 - Immunofluorescent images for DAPI (blue) and human SOD1 protein (red).

All of the *SOD1*^{G93A} mice tested showed deposits of hSOD1 protein in the ventral horn of the spinal cord (top row). No such fluorescence was seen in wild type mice (bottom row).

2.4 *In vivo* procedures

2.4.1 Anaesthesia

All animals undergoing tail vein cannulation, MRI or intracerebral injections were anaesthetised using isofluorane (IsoFlo®, Abbot Laboratories, Maidenhead, UK). 2.5% isofluorane was used for induction, maintained between 1-2% by monitoring respiration and/or temperature. For intracerebral injections, O_2 was used with a flow rate of 1.5L/min. For cannulation and MRI, 30% O_2 and 70% NO_2 was used, with a flow rate of 1.5L/min. A fluovac scavenging system was used to remove excess anaesthetic agent (International Market Supply, UK).

2.4.2 MRI protocols

Mice were scanned using a 7 Tesla magnet with a Varian Inova spectrometer (Varian). Mice were secured with a tooth bar, and head fixed in place to reduce motion artefacts. VCAM-MPIO was administered by intravenous tail injection. Gd-DPTA was administered intravenously through a cannula placed in the tail vein prior to scanning. Details of sequences and analysis are provided in 3.3 and 5.3.

2.4.3 Behavioural testing

2.4.3.1 Rotarod

Motor behaviour was tested using the rotarod apparatus (Ugo Basile, Italy). An accelerating paradigm was used, starting at 4 rotations/min, accelerating gradually to a final speed of 40 rotations / min, for up to 5 mins. Mice were placed on the apparatus 2 at a time, and three separate measures were made: firstly, the time when mice first made a footfall was noted; secondly, after slipping, mice occasionally hold on and spin on the apparatus, so the time for “double spin” was noted, i.e. when mice made two complete spins of the apparatus; lastly, the “final fall” was noted, which was when the mice fell off

the apparatus (or mice received a score off 300 seconds for staying on for the duration of the test). For initial foot fault, if the first slip involved a double spin, the score would default to “double spin”. For both first foot fault and double spin, if the first fault involved falling off the apparatus, both of these scores defaulted to “final fall”. Three trials were given per mouse per time point. For final fall and double spin, the best score of the three trials was used, consistent with previous studies (Weydt et al., 2003); the mean score was taken for foot fault, owing to the much greater variability in measures.

2.4.3.2 Weight

Prior to testing on the rotarod, all mice were weighed using sensitive digital scales.

2.4.4 Intracerebral injections

Positive control tissue was created, both for the inflammatory immunohistochemistry (striatal IL-1β injection) and VCAM-MPIO experiment (sensorimotor cortex IL-1β injection). Details of this procedure are provided in 3.3.6.

2.4.5 Intravenous injections

For the drug study, mice were injected from 60 days, every 7 days until 116 days, either with saline (50µL), methylprednisolone (10 mg/kg bodyweight), or liposomally packaged methylprednisolone (10 mg methylprednisolone/kg bodyweight). For administration of VCAM-MPIO, mice were injected with the contrast agent into the tail vein 1 hour prior to scanning. Details of the injection procedure are provided in 3.3.4.

2.5 Histology

2.5.1 Gelatinising slides

Blank slides were washed with 10% Decon (Decon laboratories Ltd, Sussex, UK), then were washed 3 times in tap water, followed by 3 times in distilled water. These were then dried overnight and coated in 0.05% potassium sulphate and dried overnight at 37°C.

2.5.2 Fixative preparation for histology

For 100ml of Paraformaldehyde/Lysine/Periodate $(PLP)_{light}$ fixative, 1.37g of lysine HCL was dissolved in 37.5ml H_2O. 180mg of di-sodium hydrogen orthophosphate di-hydrate (Sørrenson's salt) was then dissolved in 10ml H_2O, and this was added to the lysine until pH 7.4. 2g of paraformaldehyde was dissolved in 20ml of H_2O at 60°C, using 10M sodium hydroxide to aid dissolving. To make final solution, the lysine/Sørrenson solution was added to the paraformaldehyde solution, and 214 mg of sodium periodate was added, and 100 µL of 25% gluteraldehyde solution. This gave a final concentration of 75mM lysine HCL, 10mM di-sodium hydrogen orthophosphate, 10mM sodium periodate, 2% PFA, 0.05% gluteraldehyde.

For 100ml of 4% paraformaldehyde (PFA), 4g of PFA powder was dissolved in 100ml 0.1M phosphate buffer at 60°C, using 10M sodium hydroxide to facilitate dissolving.

2.5.3 Tissue preparation

Mice were injected with 100µL pentobarbitone (Pharmasol). After loss of hind limb reflex, the thoracic cavity was exposed, and a cut made in the right atrium of the heart. A 21-gauge needle was placed in the left ventricle of the heart, and the mouse was transcardially perfused with saline with 5,000 U/L heparin until the liquid exiting the heart was clear, and then fixed with PLP_{light}. Tissue was then removed, and either taken as whole brain and spinal cord segments (whole cervical, whole lumbar), or further dissected in half. Details of this are given in the specific result chapters.

The tissue for frozen IHC was post-fixed for 4 hours in PLP_{light}, and then put into 30% sucrose solution until the tissue sank to the bottom. Tissue was then snap frozen in isopentane, chilled on dry ice, in TissueTek optical coating compound (OCT) (Bayer Plc, Newbury, UK), and stored for use at -20°C. The tissue for paraffin IHC was post-fixed in 4% PFA for 24 hours, and then processed for wax embedding. Tissue was placed in 70% ethanol for 20 minutes on a shaker, followed by 70%, 80%, 90%, and 100% ethanol for 1.5 hours, followed by 100% ethanol overnight for dehydration. The next day, tissue was placed in histo-clear (National Diagnostics, Georgia, USA) twice, for 4 hours each, followed by an overnight incubation in histo-clear. Finally, tissue was placed in wax twice for 2 hours each, and then embedded in wax (brain and spinal cord sections separately). These were then stored at room temperature.

2.5.4 Tissue sectioning

Frozen tissue was cut using a cryostat (Leica CM1850, Leica Microsystems, Milton Keynes, UK) set to -20°C. 10µm sections were collected onto gelatinized slides. These were left to dry overnight at room temperature, before being stored at -20°C before use.

Paraffin-embedded tissue was cut using a microtome (Leica Reichert-Jung 2035, Leica Microsystems, Milton Keynes, UK). 10µm sections were collected onto SuperFrost® Plus slides (Fisher Scientific, Loughborough, UK). These were kept at 37°C overnight, and then stored at room temperature before use.

2.5.5 Immunohistochemistry

To prepare tissue for immunohistochemistry, frozen sections were removed from the freezer, and placed at 37°C for 20 minutes and then placed in PBS. Wax sections were placed at 65°C for 20 minutes, then washed 3 times in xylene solution to de-wax, and taken through decreasing grades of ethanol (100%, 100%, 95% 70%) to re-hydrate the tissue, and then placed in PBS. Antigen retrieval was performed on all wax tissue, by boiling in citrate buffer for 15 minutes using a microwave. Tissue was subsequently

allowed to cool, and then placed in room temperature PBS. From this point, previously frozen, and previously wax tissue joined a common protocol.

Endogenous peroxidase activity was blocked by placing slides in methanol with 0.3% H_2O_2 for 20 mins on a shaker, and then washed 3 times in PBS. Next, a protein block was used by applying 10% serum diluted in PBS to the tissue, using serum from the species that the secondary antibody was raised in (e.g. horse serum for horse-anti-goat IgG) for 1 hour. Primary antibody was then added, at the relevant concentration, either diluted in PBS or PBST, either at 4°C or 24°C, for a time that was optimized for the individual antibody. Slides were then washed 3 times with either PBS or PBS tween. The secondary antibody was then added, diluted 1:100 in PBS or PBST, for 1 hour, and then washed 3 times with PBS. Vector Elite ABC was added (Vector Labs), after the A and B solutions were diluted 1:100 each in PBS 30 - 60 minutes prior to adding to the tissue, and this was incubated for 45 minutes, after which the tissue was washed 3 times in PBS. The development solution was made up by adding 5g diaminobenzidine (DAB) powder and 250µL 30% H_2O_2 to 250mL 0.1M phosphate buffer. Slides were placed in development solution, checked intermittently under the microscope, and washed 3 times in 0.1M phosphate buffer once adequate reaction product had formed.

Haematoxylin counterstain was used as follows: slides were placed in Harris' haematoxylin solution for 5 minutes, differentiated in acidified 70% ethanol (1% HCl), and then placed in tap water for 5 minutes on a shaker.

Slides were then dehydrated by taking through increasing grades of ethanol (80%, 95%, 100%, 100%), and then placed in xylene for 15 minutes as a clearing agent. Slides were mounted to coverslips with DPX mounting medium, and allowed to air dry at room temperature.

Antigen	Tissue	Wash	Primary antibody	Secondary antibody
GFAP	Wax	PBST	Rabbit (Invitrogen) 1:1,000	Goat anti rabbit (Vector) 1:100
Iba-1	Wax	PBST	Goat (Abcam) 1:500	Horse anti Goat (Vector) 1:100

VCAM-1	Frozen	PBS	Rat (Camb. Bio.) 1:200	Goat anti rat (Vector) 1:100
ICAM-1	Frozen	PBS	Rat (Abcam) 1:500	Goat anti rat (Vector) 1:100
E-selectin	Frozen	PBST	Chicken (R&D) 1:50	Goat anti chicken (R&D) 1:20
VAP-1	Frozen	PBST	Rat (Abcam) 1:100	Goat anti rat (Vector) 1:100

Table 2.3 – Details of the type of tissue, washes, and antibodies used for immunohistochemistry.

2.5.6 Haematoxylin and Eosin (H&E)

A haematoxylin & eosin (H&E) stain was used as a histological investigation of tissue vacuolation, and for neuron counts. The haematoxylin stain was carried out, exactly as described above in 2.5.5. Following this, slides were placed in eosin Y solution for 5 minutes, and then rinsed in running tap water for 20 minutes. The slides were then taken through increasing grades of ethanol (80%, 95%, 100%, 100%) to dehydrate the tissue, and then placed in xylene for 15 minutes and mounted to cover slips using DPX mounting medium.

2.5.7 CNS regions analysed

For the *SOD1*^{G93A} immunohistochemistry, a number of different CNS regions were studied, specifically the sensorimotor cortex **Figure 2.3**, trigeminal (V) nucleus (**Figure 2.4**), facial (VII) nucleus (**Figure 2.5**), hypoglossal (XII) nucleus (**Figure 2.6**), and the ventral horn of the spinal cord (cervical and lumbar regions) (**Figure 2.7**). The histological definitions of each region, defined from H&E staining, is indicated on the histological images in each case.

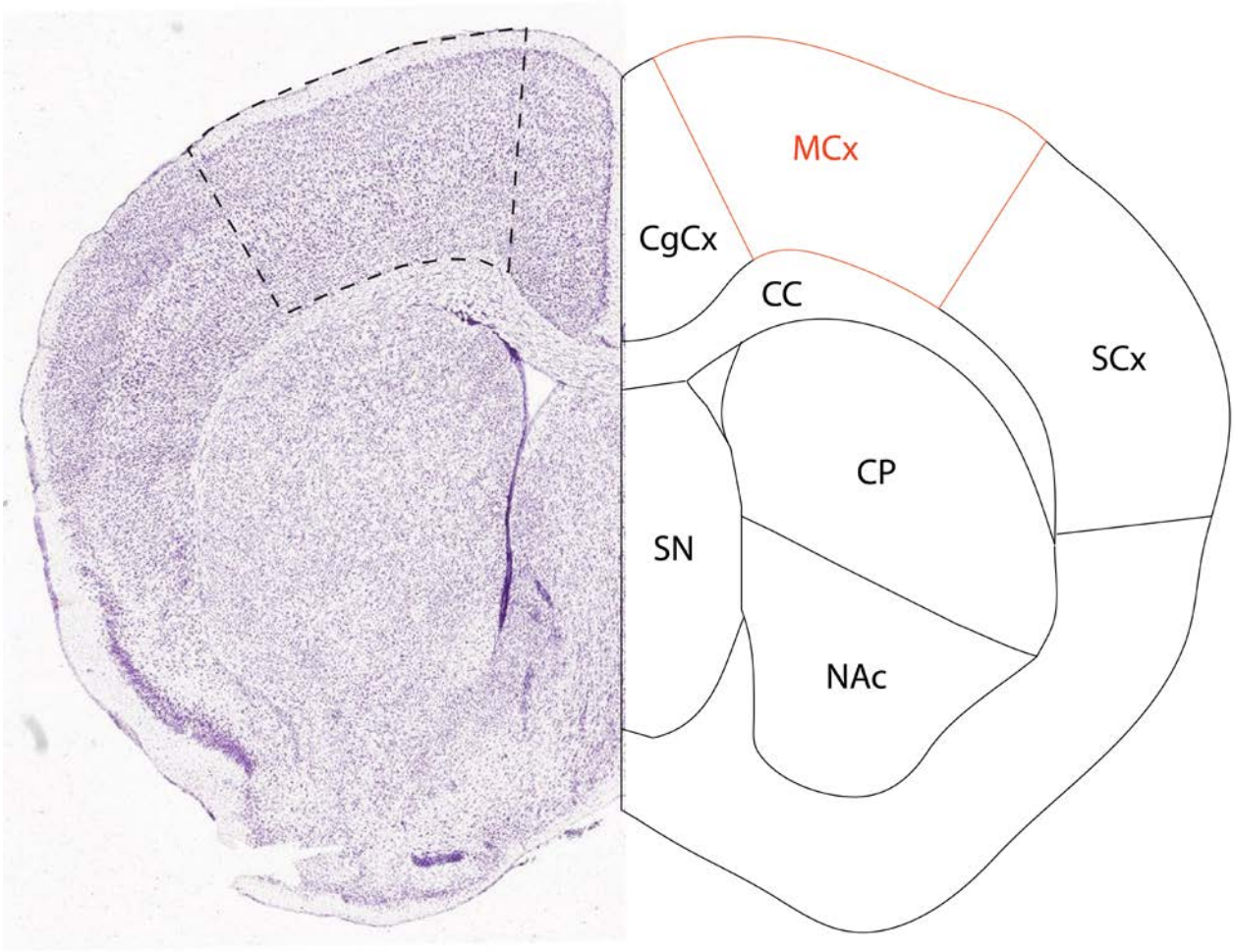


Figure 2.3 - Diagram illustrating the position of the motor cortex

The region specified for analysis is identified on the left hand image by a dotted area

Key: MCx = motor cortex; SCx = somatosensory cortex; CgCx = cingulate cortex; CC = corpus callosum; CP = caudoputamen; NAc = nucleus accumbens; SN = septal nucleus

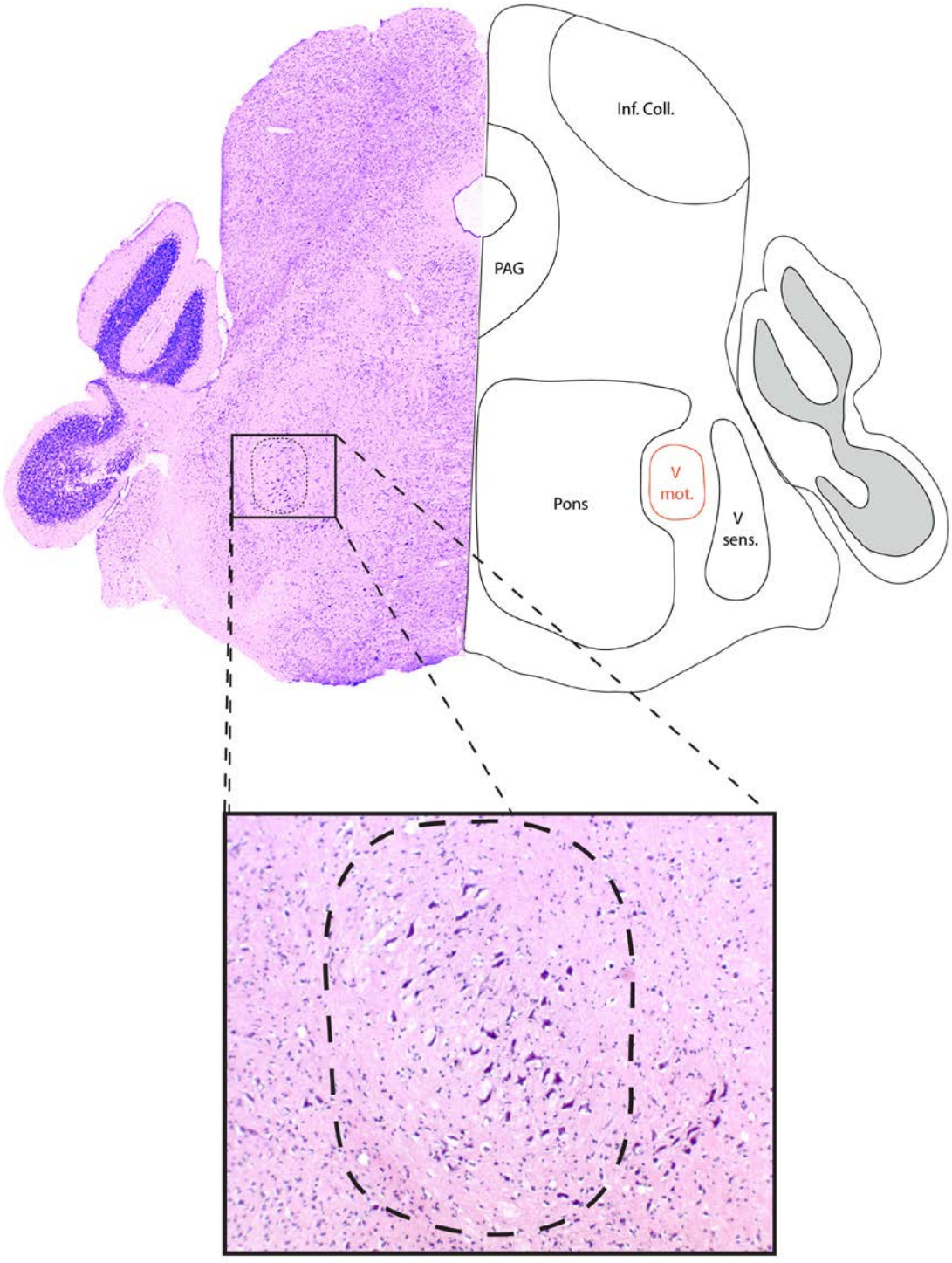


Figure 2.4 – Diagram illustrating the position of the trigeminal nucleus (MN V)

The region specified for analysis is identified on the left hand image by a dotted area

Key: Inf. Coll. = inferior colliculus; PAG = periaqueductal grey; V mot. = trigeminal motor; V sens. = trigeminal sensory

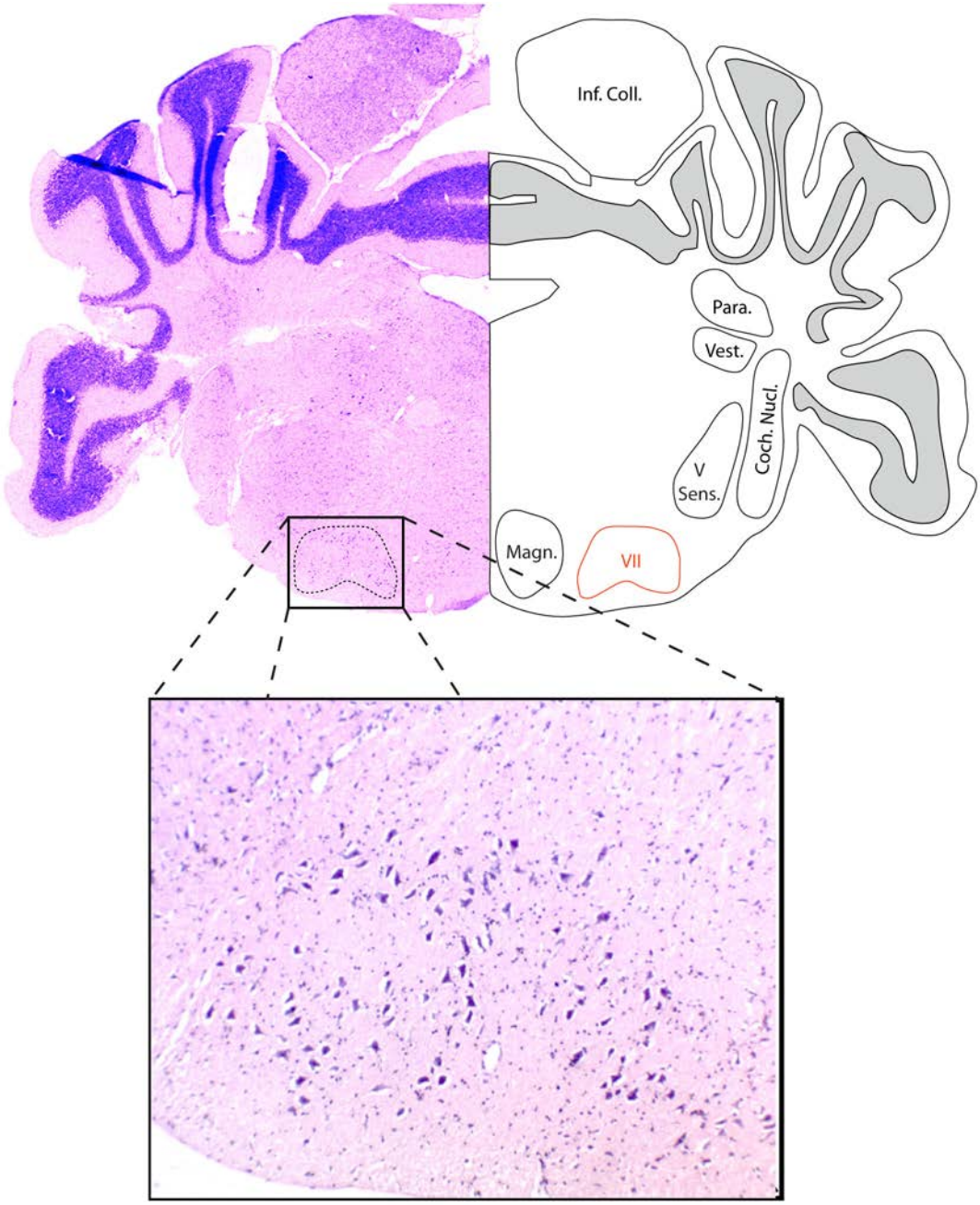


Figure 2.5 - Diagram illustrating the position of the facial nucleus (MN VII)

The region specified for analysis is identified on the left hand image by a dotted area

Key: Inf. Coll. = inferior colliculus; Para. = parabrachial nucleus; Vest. = vestibular nucleus; Coch. = cochlear nucleus; V. sens = trigeminal Sensory; VII = trigeminal nucleus; Magn. = magnocellular reticular nucleus.

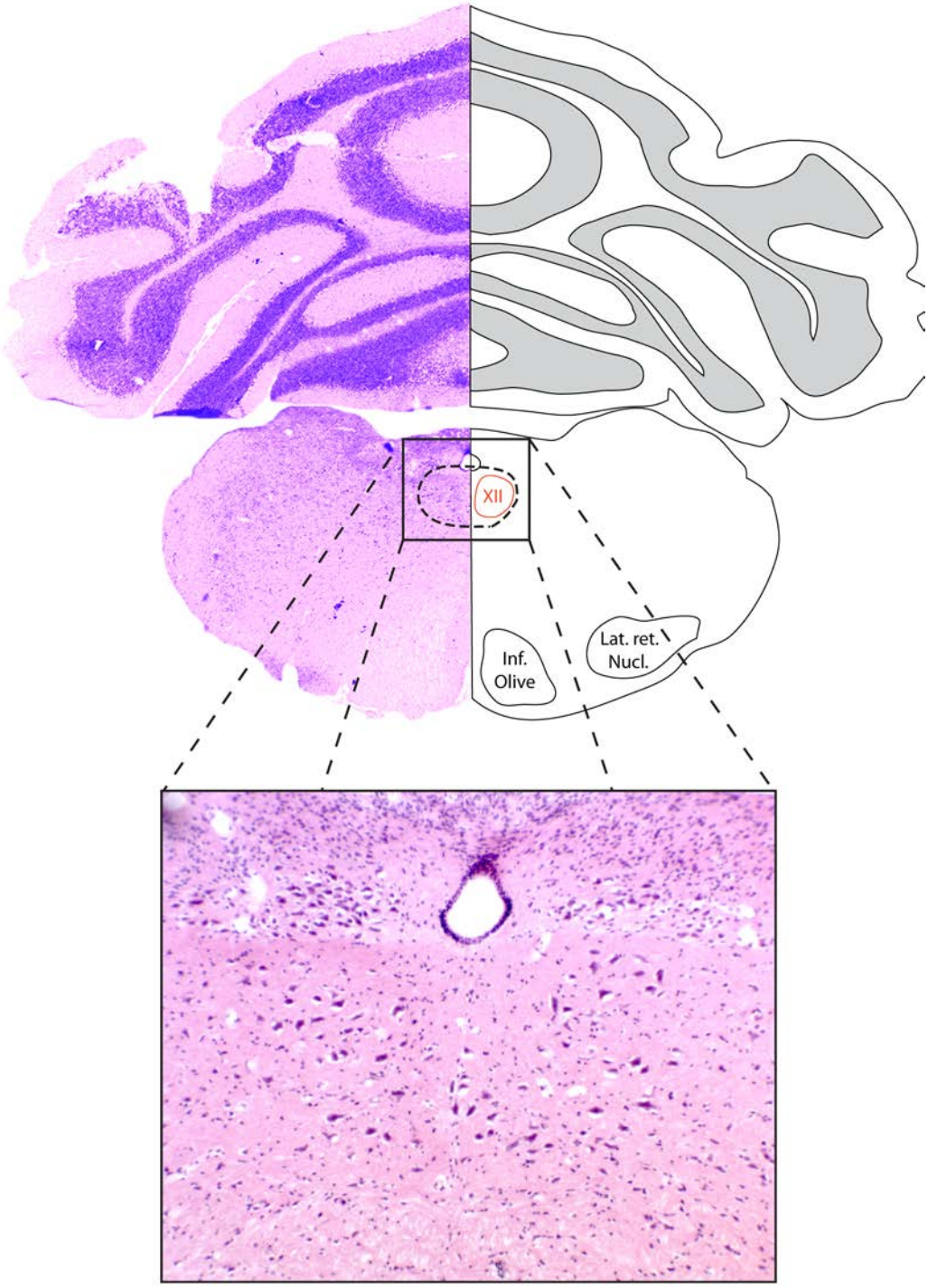


Figure 2.6 - Diagram illustrating the position of the hypoglossal nucleus (MN XII)

The region specified for analysis is identified by a dotted area

Key: XII = Hypoglossal nucleus; Inf. Olive = inferior olivary complex; Lat. ret. Nucl. = lateral reticular nucleus

Figure 2.7 - Diagram illustrating the position of the ventral horn of the spinal cord (lumbar)

The region specified for analysis is identified on the left hand image by a dotted area

Key: DCMLS = dorsal column medial lemniscal system; LCST = lateral corticospinal tract; ACST = Anterior corticospinal tract; RtS = Reticulospinal tract; RST = rubrospinal tract; SCbT = spinaocerebellar tract; LSThalT = lateral spinothalamic tract; MSThalT = medial spinothalamic tract; VST = vestibulospinal tract; OST = olivospinal tract; SOT = spinoolivary tract.

2.5.8 Analysis of immunohistochemistry/histology

Specific details of the method used for analysis are provided in the three result chapters.

2.6 Quantitative polymerase chain reaction (qRT-PCR)

2.6.1 Tissue preparation

Mice were deeply anaesthetised with 100μL of pentobarbitone, and after loss of hind limb reflex were killed by cervical dislocation. Mice were decapitated at the level of the upper cervical vertebrae, and the brain and spinal cords were dissected out. The sensorimotor cortex, brainstem, cervical spinal cord and lumbar spinal cord were then further dissected,

and collected in DNase/RNase-free eppendorfs on dry ice. Samples were kept at -80°C until ready to be used.

2.6.2 RNA isolation and cDNA conversion

RNA was purified using the Qiagen RNeasy mini kit according to manufacturer's instructions, and RNA was eluted in 20µL DNAse/RNase-free water. Concentration and quality of RNA was measured using a Nanodrop spectrophotometer (Thermo scientific), with only RNA concentration higher than 40ng/µL, with a 260:280 ratio greater than 1.95, used for downstream analysis.

RNA was converted to cDNA using Superscript III (Invitrogen) reverse transcription system. For each of the RNA samples, 400ng of total RNA was used, made up to 11µL with DNase/RNase-free water. 1µL random primers (250ng/µL), and 1µL dNTPs (10mM) was added to the RNA/water mixture, and the samples were placed in a 65°C oven for 5 minutes, then placed on ice for a further 5 minutes. To each tube, 4µL first strand buffer, 1µL DTT (0.1M), 1µL Superscript III® enzyme (200 units/µL) and 1µL RNaseOUT® (40 units/µL) was added, the samples were mixed thoroughly, and left at room temperature for 5 minutes. The samples were then incubated at 50°C for 1 hour to allow the enzymatic reaction to occur, and incubating at 70°C for 15 minutes stopped the reaction by denaturing the enzyme. Each 20µL of resulting DNA was diluted to half the concentration by addition of 20µL DNAse/RNAse-free water.

2.6.3 Setup and reagents

qRT-PCR was performed using the light cycler 480® PCR machine (Roche), using Roche mastermix. PCR was performed for the following genes: GAPDH (housekeeping gene); IL-1β; TNF-α; IFN-γ; CXCL-10. For GAPDH, IL-1β and TNF-α, assays were obtained from Primer Design (Southampton, UK). For IFN-γ and CXCL-10, primers were designed using the assay design centre (Roche), and ordered from Invitrogen. The primer design assays contain the primers and probes required for qRT-PCR, whereas for IFN-γ and CXCL-10,

appropriate probes were used (Universal probe library, Roche). Reaction mixture for the primer design assays is shown in **Table 2.4** and for Invitrogen primers in **Table 2.5**. A list of primer sequences and probe numbers (where relevant) is given in **Table 2.6**.

Component	Per reaction
Primer/probe mixture	1μL
Mastermix	5μL
Water	3μL
cDNA	1μL

Table 2.4 – Reaction mixture for qRT-PCR using Primer Design assays (GAPDH, IL-1β and TNF-α)

Component	Per reaction
Forward primer	0.1μL
Reverse primer	0.1μL
Probe	0.1μL
Mastermix	5μL
Water	3.7μL
cDNA	1μL

Table 2.5 – Reaction mixture for qRT-PCR using Invitrogen primers (20ng/μL) (IFN-γ and CXCL-10)

Gene	Primer sequence	Probe
GAPDH	F: N/A* R: N/A*	N/A
IL-1β	F: CAA CCA ACA AGT GAT ATT CTC CAT R: GGG TGT GCC GTC TTT CAT TA	N/A
TNF-α	F: AGC CAG GAG GGA GAA CAG A R: CAG TGA GTG AAA GGG ACA GAA C	N/A
IFN-γ	F: ATC TGG AGG AAC TGG CAA AA R: TTC AAG ACT TCA AAG AGT CTG AGG TA	#21
CXCL-10	F: GCT GCC GTC ATT TTC TGC R: TCT CAC TGG CCC GTC ATC	#3

Table 2.6 – Primer sequences and probe details for the PCR assays

* Sequence information is not available on this product for commercial reasons

For each of the genes, all samples were run, along with a standard curve. The most concentrated standard curve was made up using a mixture of random RNA samples, reverse transcribed using 5μg total RNA. Dilutions were made using half of the previous sample and the same volume of water, to make a 6-point standard curve. For the PCR reaction, the reaction mixture was pipetted into a 384 well PCR plate, and sealed with plastic plate foils. The plate was spun at 1,000rpm for 5 minutes to spin the samples to the bottom of the wells. The plate was placed in the PCR machine and heated to 95°C for 5 minutes as a pre-incubation. Following the pre-incubation, 50 cycles of the following sequence was used: 95°C for 15 seconds, followed by 60°C for 60 seconds. Finally the samples were cooled down to 40°C to end the PCR.

2.6.4 PCR analysis

For each of the genes, including the housekeeping gene, a standard curve was constructed by plotting the cycle numbers on a logarithmic scale. A line of best fit was placed on the graph, with linear equation. An example standard curve is shown in **Figure 2.8**.

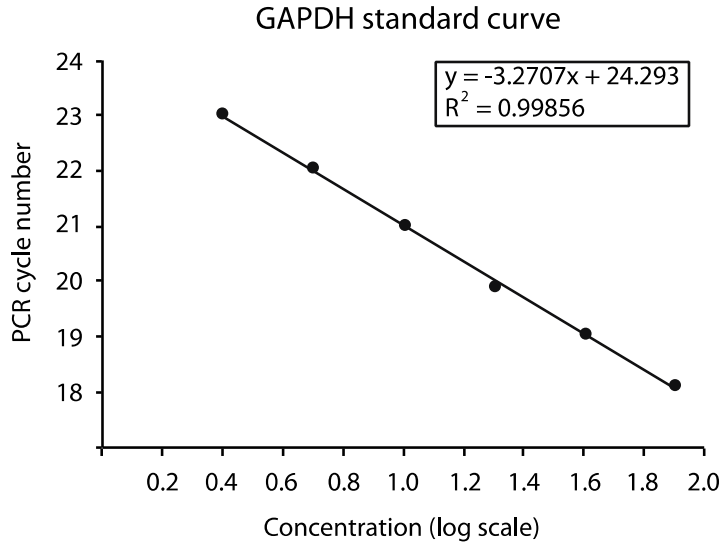


Figure 2.8 – Example standard curve (GAPDH) with line of best fit and linear equation

For each sample and each gene, an average cycle number of was calculated from the duplicates, and this was converted into an expression level by using the m and c values from the linear equation, and converting back to a linear scale (10^X). For each gene of interest, the value for each sample was divided by the value for GAPDH for that sample, thereby calculating a relative expression level, normalized to GAPDH.

Chapter 3: MRI investigation of vascular changes in relation to neurodegeneration in *SOD1*^{G93A} mice

3.1 Aims of this chapter

This chapter is focused on MRI biomarkers of disease in *SOD1*^{G93A} mice. In one group of mice, a T_2–weighted sequence was used to replicate previous studies investigating brainstem pathological changes in *SOD1*^{G93A} mice, but at higher field strength and with a very short acquisition time, to minimize scanning time and therefore costs for pre-clinical trials. Changes on T_2-weighted images were compared to those seen on T_1-weighted images throughout the lifespan of the mice (40, 60, 80, 100 and 120 days), cross-sectionally with 4 *SOD1*^{G93A} and 4 wild type mice at each time point. In addition, a superparamagnetic contrast agent recognising VCAM-1 (VCAM-MPIO) was used to investigate vascular activation, and Gd-DTPA for vascular permeability, from 40 to 120 days. In a second group of mice diffusion-weighted and magnetization transfer data was acquired in addition to T_2 at 120 days, to probe the physical basis to the T_2 MRI changes in more detail by using other sequences sensitive to water content of tissue. Brains and spinal cords of mice were extracted at each time point to stain for IgG, to corroborate Gd-DTPA findings, and VCAM-1, to corroborate the VCAM-MPIO findings. Nissl staining was also carried out to align MRI changes with neuronal structural tissue changes, and astrocyte and microglia activation were measured by staining for GFAP and Iba1 respectively.

3.2 Introduction

The most commonly used model of ALS is the transgenic rodent over-expressing the human Cu/Zn superoxide dismutase (*SOD1*) gene (Gurney et al., 1994). Whilst its limitations are well established, *SOD1* mice nonetheless have a predictable disease progression and pathology and recapitulate many of the core clinical features of the

human disorder (Turner and Talbot, 2008). As such the model has great potential to test candidate disease-modifying agents, though it is recognised that this must be within an optimized and standardized framework (Ludolph et al., 2010). To date there have been nearly 200 compounds tested using various *SOD1*-based rodent models, although it must be noted that there has been poor translation to therapeutic use in the clinical population (Turner and Talbot, 2008). Behavioural amelioration has been the primary biomarker in such trials, but a biomarker that offers more direct insight into the biology of the disease would contribute to a better understanding of the therapeutic mechanism. A host of potential biomarkers now exist in ALS (summarised in Turner et al. (2009)), and MRI is increasingly taking centre stage in the biomarker literature, both in humans (Turner, 2011) animal models (Evans et al., 2012). Choosing the most sensitive biomarkers to the pathology in question is critical for recognition of promising drugs and therapies in future trials. However, a competing demand in trial design in that of costing – trials in general, and those using MRI in particular, are very expensive, so it is important to streamline the study as much as possible. This will either allow the trial to be performed as quickly (and therefore as cheaply) as possible, and/or to allow additional data to be collected in a given time frame.

The rotarod is a common measure of motor performance in mouse models (Kalueff et al., 2007), including *SOD1* mice. Studies typically measure the time taken to fall off the rotarod, either using a constant speed paradigm (Weydt et al., 2003, Miana-Mena et al., 2005) or an accelerating paradigm (Fischer et al., 2004). Typically, the accelerating paradigm is more sensitive to motor behavioural problems than the constant speed paradigm (Fischer et al., 2004). However, there are potentially motor signs that precede the final fall, which could give further insight into the disease mechanism. For example, mice typically stumble a number of times much earlier than the final fall, so this might be a more sensitive measure of motor problems. Similarly, some mice will grip onto the apparatus and spin repeatedly rather than falling off, which could provide additional information of motor performance. However, these measures are more experimenter-

intensive, as they require constant monitoring of the mice. Therefore, it should be determined how useful, if at all, these additional measures are compared with final fall, in order to weigh up whether they would be useful as behavioural biomarkers.

The most powerful MRI biomarker discovered so far in *SOD1* models of ALS is T_2-weighted MRI of the cranial motor nuclei. T_2 is a quantification of spin-spin relaxation, which is loss of transverse magnetization, due to relaxation in the longitudinal plane and loss of energy to neighbouring spins (see Appendix). T_2 relaxation time is significantly longer for water than fat, and so generates contrast for the detection of pathological fluid within biological tissues. A number of studies using *SOD1* ALS models have shown T_2 hyper-intensities in motor regions of the CNS, including the trigeminal, facial and hypoglossal nuclei (Angenstein et al., 2004, Zang et al., 2004, Niessen et al., 2006), which has been attributed to water-filled vacuolation (Bucher et al., 2007). T_2 MRI has been shown to be more sensitive than diffusion-weighted imaging for distinguishing between *SOD1* and wild type mice, with quantitative measurement of the apparent diffusion coefficient (ADC) (Niessen et al., 2006). However, other sequences that are thought to be sensitive to the macromolecule content of tissue, such as magnetization transfer (MT) sequences, have not been used in this model. An initial study by Angenstein et al. (2004) used a short T_2-weighted sequence taking 17 minutes, and they measured changes in intensity in the motor nuclei compared to a control region in the surrounding brainstem tissue. With the limited time points used in Angenstein et al. (2004), T_2 changes were only shown post-symptomatically (112 days). This was confirmed by a Zang et al. (2004), in which a significantly longer sequence was used taking 42 minutes for higher spatial resolution. In a more in-depth study, Niessen et al. (2006) acquired T_2 sequences using 16 spin echoes in order to create a T_2 map, which allows absolute quantification of T_2 relaxation in the tissue. Using this approach the authors found T_2 changes from 80 days onwards (just prior to symptom onset). However, the scanning time of this sequence was 1 hour 17 minutes, which firstly puts a high anaesthetic demand on sick animals, and secondly would generate high costs if used as a biomarker for preclinical trials. In this

chapter I aim to improve imaging, by producing good quality images that are sensitive to *SOD1* pathology, but using much shorter sequences, to allow high-throughput imaging.

A number of vascular abnormalities have been noted in *SOD1* rodent models, including functional BBB breakdown[2] (Garbuzova-Davis et al., 2007b, Zhong et al., 2008, Nicaise et al., 2009a), ultra-structural changes (Garbuzova-Davis et al., 2007a), and down-regulation of tight-junction proteins (Zhong et al., 2008, Miyazaki et al., 2011). These changes have important clinical implications, as BBB dysfunction allows inflammatory mediators and leukocyte populations to more readily enter the CNS, which can impact on the disease process. BBB deregulation may also have important implications for drug delivery when new pharmaceutical interventions are discovered. As yet, MR measures of vascular permeability have only been used by one group, using the *SOD1*^{G93A} rat (Andjus et al., 2009, Bataveljic et al., 2011). This work showed BBB breakdown in the "interbrain/midbrain" region around the lateral ventricles in *SOD1*^{G93A} rats, although the time course of this increased permeability is not known. However, this finding and the work discussed above in the *SOD1* mouse models using complementary approaches such as immunohistochemistry, western blots and electron microscopy, would lead us to hypothesise that gadolinium-based contrast agents should highlight BBB breakdown in this model (Garbuzova-Davis et al., 2008), and may provide a useful biomarker of disease progression. In this chapter I explore the use of MR measures of vascular permeability in the *SOD1*^{G93A} mouse model.

As discussed in the general introduction, a number of adhesion molecules are expressed on the vascular endothelium at sites of inflammation that are involved in the process of leukocyte recruitment into the CNS. This process involves three main steps: rolling, firm adhesion, and transport across the BBB (Shimizu et al., 1991, Barten and Ruddle, 1994, Muller, 1995, Verbeek et al., 1995, Wong et al., 1999). Vascular cellular adhesion molecule-1 (VCAM-1) is one such adhesion molecule, and is primarily involved in firm

[2] Note that a broader definition of "Blood-brain barrier" is being used in this thesis, which encompasses blood-brain barrier and blood-spinal cord barrier.

adhesion of leukocytes, including lymphocytes, which is demonstrated from both activation and antibody blocking experiments (Wong et al., 1999). In the classical immune-driven neurological disease, multiple sclerosis (MS), VCAM-1 is expressed on the brain vasculature, and is responsible for the lymphocyte infiltration seen in the brain parenchyma in MS lesions. Moreover, blockade of VCAM-1 both reduces the lymphocyte population within these lesions, and relieves symptoms (Yednock et al., 1992, Graesser et al., 2000). Our group has developed a contrast agent consisting of ~1μm microparticles of iron oxide (MPIO) which are conjugated to monoclonal anti-VCAM-1 antibodies. This contrast agent is detectable using T_2*-weighted MRI owing to the superparamagnetic properties of the iron oxide. This agent has been validated in a model of acute inflammation, achieved by injecting IL-1β into the striatum, which showed significant binding of the beads to areas of VCAM-1 expression (McAteer et al., 2007). This contrast agent has also been used in pre-clinical models of cerebral ischemia (Hoyte et al., 2010), brain metastasis (Serres et al., 2012) and MS (experimental autoimmune encephalomyelitis) (Serres et al., 2011). Importantly, in the latter two studies, the VCAM-MPIO contrast agent was shown to be sensitive to pathological changes in brain metastases and MS, and changes were detected far earlier than with standard clinical tools such as Gd-DTPA. In *SOD1* mouse models, the data on CAM expression is limited and conflicting. Alexianu et al. (2001), show an up-regulation in ICAM-1 expression early on in the disease, although this may be partly driven by ICAM-1 expression on microglia. However, Zhong et al. (2008) could not replicate this, and found ICAM-1 expression was only increased at very late stages of disease. No data is available at this stage on the expression level of VCAM-1 in ALS models. Therefore application of VCAM-MPIO in *SOD1*^{G93A} mice *in vivo* will significantly increase our understanding of the involvement of CAMs in *SOD1* pathology.

This chapter compares a number of behavioural and MRI biomarkers to determine those which of these is most sensitive to the disease pathology. Histological analysis was also carried out where relevant to corroborate MRI results.

3.3 Materials and Methods

3.3.1 Experimental groups

In one group of mice, 4 *SOD1*^{G93A} and 4 wild type mice were taken at each time point, and tested behaviourally (rotarod and weights), and scanned with T_2, T_1 (with and without Gd-DTPA) and T_2* (with administration of VCAM-MPIO) sequences. This was carried out at 40, 60, 80, 100 and 120 days, in different 8 mice at each time point. In a second group, 5 *SOD1*^{G93A} and 5 wild type mice were scanned at 120 days with T_2, diffusion-weighted imaging and magnetization transfer imaging. All mice (in both groups) were killed immediately following MRI scanning, and tissue collected for histology.

3.3.2 Behavioural testing

SOD1^{G93A} mice and wild type littermate controls were tested using the rotarod according to the protocol described in 2.4.3.1; time to foot fault, double spin, and final fall were noted. Mice were also weighed at each time point. Mice were tested at 40, 60, 80, 100 and 120 days of age. Behavioural measures were combined for mice scanned with MRI in this chapter (N=4, per group, per time point) and mice used for qPCR in Chapter 4 (N=5 per group, per time point). Therefore the data represent 9 *SOD1*^{G93A} and 9 wild type mice per time point, with different mice used at each time point (i.e. cross-sectional data).

3.3.3 VCAM-MPIO

VCAM-MPIO contrast agent, based on MyOne tosylactivated MPIO (1μm diameter - Invitrogen), was kindly donated by Dr Robin Choudhury, and was used for MRI detection of VCAM-1 protein *in vivo*.

3.3.4 MRI

SOD1^{G93A} mice and wildtype (WT) littermate controls were imaged at 40, 60, 80, 100, and 120 days of age (N=4 per group, per time point). Each mouse was injected *i.v.* with

VCAM-MPIO and scanned 1 hour later with a T_2*-weighted sequence for detection of MPIO binding. For i.v. injections mice were first placed in a heating chamber (37°C) to dilate the veins, and tails brushed with 70% ethanol. Mice were also infused *i.v.* with Gd-DTPA via a tail vein cannula, and scanned just before, and 5 minutes after injection with a T_1-weighted sequence to detect the Gd-DTPA. Additionally, mice were scanned with a T_2-weighted sequence to detect brainstem hyperintensities.

In a second experiment, wild type and *SOD1*^{G93A} mice were imaged at 120 days using the T_2-weighted sequence, and additionally magnetization transfer ratio (MTR) and apparent diffusion coefficient data were obtained (N=6 per group).

As a positive control for VCAM-1 up-regulation, 3 wild type mice were injected in the sensorimotor cortex with a bolus of human IL-1β. Mice were injected i.v. with VCAM-MPIO and Gd-DTPA 4 hours later, and scanned as above.

3.3.4.1 T_2-weighted MRI

Scanning parameters for the fast spin-echo multislice (fSEMS) T_2-weighted sequence were: TR = 3000 ms; TE = 61.92 ms; FOV = 25 x 25 mm; Matrix size = 128 x 128; number of slices = 11; averages = 2; slice thickness = 1mm; scanning time = 3 mins 12 sec. As described below, the T_2 slice selection was used as a template for all other scans. In order to orientate the scans consistently in space, the anatomy of the slice through the facial (VII) nucleus was scrutinized (see below) to ensure that a diamond shape of CSF was present in the 4th ventricle with a small amount of partial volume effect from adjacent brain tissue (red arrow), as well as CSF present medially and anteriorly to the cerebellar tissue (green arrow). Other slices were then defined relative to this, with slices 1mm apart as described above.

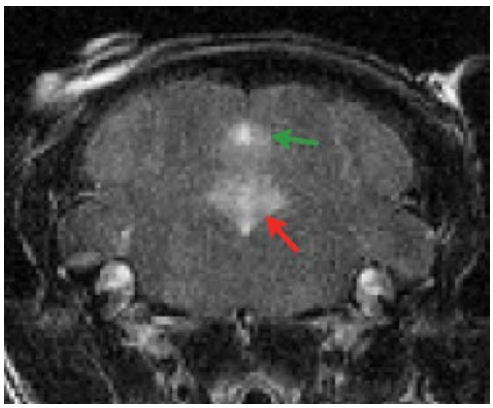


Figure 3.1 – Representative image illustrating the principle of slice selection

The slice through the facial (VII) nucleus was standardized for slice selection, with the other slices defined relative to this. For the facial nucleus slice, the region selected included a diagonal portion of 4th ventricle with some partial volume effect from surrounding brain tissue (red arrow), in addition to some partial volume effect from the CSF medial and anterior to the cerebellar tissue in this slice.

3.3.4.2 T_1-weighted MRI, and Gd-DTPA

Scanning parameters for the spin-echo multislice (SEMS) T_1-weighted sequence were: TR = 500 ms; TE = 20 ms; FOV = 25 x 25 mm; Matrix size = 128 x 128; number of slices = 11; averages = 2; slice thickness = 1mm; scanning time = 4 mins 16 sec. The same slice plan was used as for the T_2 weighted scan. For the Gd-DTPA experiment, a T_1-weighted scan was carried out immediately before and 5 mins following intravenous injection of Gd-DTPA contrast agent.

3.3.4.3 Apparent diffusion coefficient (ADC)

Scanning parameters for the diffusion weighted spin-echo multislice (SEMS) T_1-weighted sequence were: diffusion directions = 3 (readout, phase encoded, slice selection); array = 3; TR = 2000 ms; TE = 35.06 ms; duration of diffusion gradient = 12.5 sec; amplitude of diffusion gradient = 8.19 G/cm; FOV = 25 x 25 mm; matrix size = 128 x 128; number of slices – 11; averages = 1; slice thickness = 1mm; total scanning time = 12 min 48s each. The same slice plan was used as for the T_2 weighted scan. An ADC map was constructed from the 3 arrays for readout (ro), phase encoded (pe) and slice selection (sl), and the three ADC maps were added together to make an average ADC map.

3.3.4.4 Magnetisation transfer (MTR)

Scanning parameters for the T_1 magnetization transfer scan were: TR = 4489.5 ms; MTR flip angle = 8830; MTR pulse duration = 384 ms; offset = -1500 Hz; FOV = 25 x 25 mm; matrix size = 128 x 128; number of slices – 11; averages = 1; slice thickness = 1mm; total scanning time = 9 min 35 s each. The same slice plan was used as for the T_2 weighted scan. A scan was acquired without MTR pulse (pre-saturation) and with MTR pulse (saturation image). The scans were processed, with the saturation scan being subtracted from the pre-saturation scan, expressed as change from the pre-saturation scan.

3.3.4.5 T_2*-weighted MRI with administration of VCAM-MPIO

Scanning parameters for the 3-dimensional gradient echo (GE3D) T_2*-weighted sequence were: TR = 65 ms; TE = 7.5 ms; flip angle = 27°; FOV = 11.2 x 12.5 x 12.5 mm; matrix size = 96 x 192 x 256; averages = 2; scanning time = 40 mins. Scan was acquired 1 hour after intravenous injection of VCAM-MPIO contrast agent (16 µL diluted in 100 µL sterile saline).

3.3.4.6 MRI analysis

For Gadolinium T_1 scans, the pre-Gd image was subtracted from the post-Gd image, and expressed relative to the pre-Gd image. For T_1, T_2, ADC and MTR, ROIs were placed over the three motor nuclei (MN V, VII and XII), as well as a control region on the same slices as the nuclei (within the brainstem, but outside of the nuclei of interest), and intensities were measured as (ROI-control) / control. Standard ROIs were created for each nucleus, created by encapsulating the total area of hyperintensity on a standard 120 day *SOD1*^{G93A} image. This was then placed over each nucleus manually, using the standard 120 day image as a guide. An example of ROI placement for wild type and *SOD1*^{G93A} T_2 images is shown in **Figure 3.2**.

For analysis of the 3D T_2* data, whole brain, cortex and brainstem regions were segmented using ITK snap (http://www.itksnap.org/pmwiki/pmwiki.php). Within each of these regions, the number of hypointensities was calculated using Matlab (Mathworks®). Hypointensities were calculated as those voxels that were less than 65% of the mean intensity of all voxels in the tissue, and a cut-off of 20 voxels were used to omit larger structures (e.g. sinuses). By dividing the number of hypointensities by the number of voxels in the mask, the percentage of hypointense voxels was calculated.

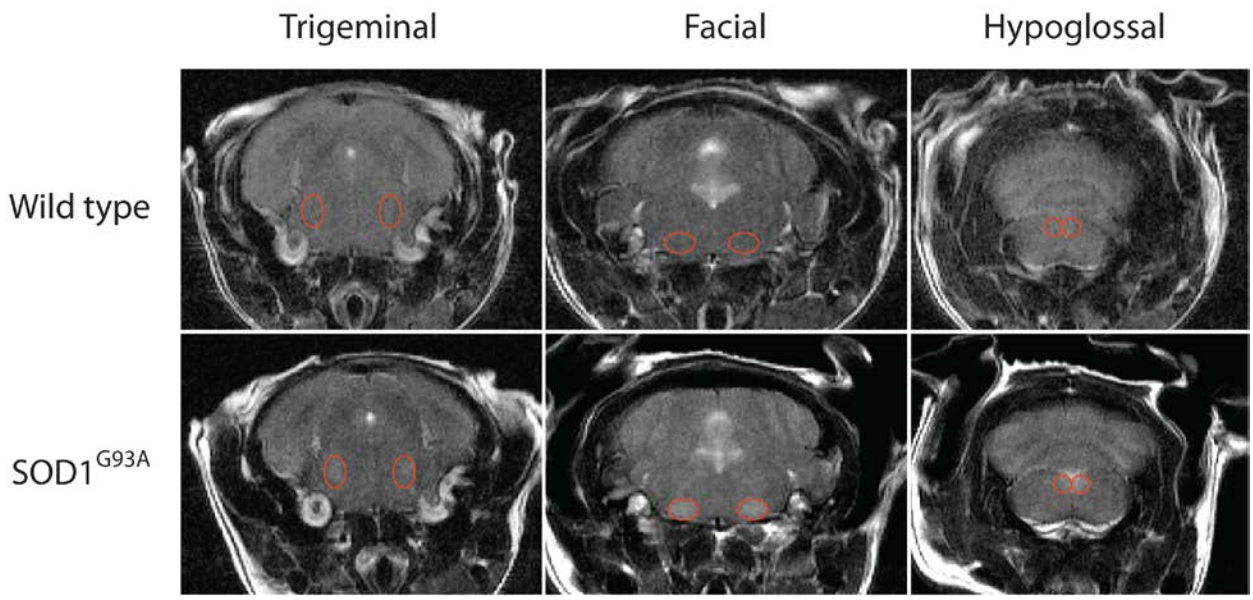


Figure 3.2 – Illustration of ROI placement for wild type and *SOD1*^{G93A} T_2 images

A standard 120 day *SOD1*^{G93A} image was used to create the ROI for each nucleus (bottom row). This image was then used to place the ROI over all other images, both *SOD1*^{G93A} and wild type (top row).

3.3.5 Immunohistochemistry

SOD1^{G93A} mice and control littermates were perfused fixed with heparinized saline followed by PLP_{light} solution. Brains were then cut down the midline, and the cervical and lumbar spinal cord dissected out and each segment split into 2, with half the tissue taken for frozen IHC, and the other half for paraffin IHC. The tissue was then prepared for cutting as described in 2.5.3.

Immunohistochemistry was carried out for mouse IgG, GFAP, Iba1 and VCAM-1 Information on source and dilution of antibodies can be found in 2.5.5, as can the immunohistochemistry protocol. Sections were counterstained using haematoxylin to investigate neuronal degeneration and vacuolation.

3.3.6 Intracerebral injections

For positive control tissue for inflammatory IHC, mice were injected into the left striatum with human recombinant IL-1β (1ng/μL). Mice were anaesthetised as described in 2.4.1, and placed on a stereotaxic frame. The head of the mouse was shaved, and a small incision made in the scalp to expose the skull. A small hole was then drilled above the striatum, and the desired solution injected 0.5mm anterior, 1.5mm lateral (left) and 2.5mm ventral to bregma (Paxinos), through a glass microcapillary (Drummand Scientific Company, Broomall, PA, USA). The solution was delivered gradually over 5 mins, and then left for a further 5 mins after injection. Following injection, the capillary was removed, and the incision was sutured closed. Mice were kept for 4 hours post-injection before processing for histology (see 2.5).

For positive control for the MRI, mice were instead injected bilaterally into the sensorimotor cortex, using Paxinos co-ordinates 0.5mm anterior, 1mm lateral (both left and right hemisphere), 0.5mm ventral to bregma. Otherwise the same procedure was followed as described above.

As a positive control for blood-brain barrier breakdown (paraffin sections only), mice were sham-injected in the left striatum with a large bore needle (21-gauge) in order to create a small amount of tissue damage and vascular leakage. Tissue for positive control was prepared as described in 2.5.

3.3.7 Immunohistochemistry analysis

For immunohistochemistry analysis, three sections of each region, 150μm apart, were photographed using Leica Firecam software (for the brainstem, the largest cross section of each nucleus was used, as well as a section 150μm anterior and 150μm posterior), using a 10x objective lens. Images were then analysed using ImageJ software. The background was subtracted from the image, and a colour deconvolution plugin was used to separate the image into DAB product and counterstain. The DAB product channel was converted to RGB, and thresholded by eye to remove the non-specific background signal. Finally, an ROI, with 500 unit diameter in ImageJ, was placed over the nuclei, or within the CNS region in the case of sensorimotor cortex and spinal cord, and the mean signal intensity was measured. This method is shown diagrammatically in **Figure 3.3**. As a proof of principal for the analysis, 5 sections were chosen with increasing strength of DAB staining (verified by blind rating by 5 people) from previous studies, and the calculation described here correctly distinguished between these sections.

For the analysis of vacuolation using H&E-stained tissue, photographs were taken of the largest cross-section of the nuclei (V, VII and XII), and sections 150μm anterior and posterior to this, using a 10x objective lens. Analysis was also performed using ImageJ. The background was subtracted, and the image was binarized, giving a value of 266 to pixels within vacuoles, and 0 to pixels outside of vacuoles. An ROI was then drawn around the area of vacuolation, and the total vacuolation was calculated from the product of the average vacuolation and area affected. Cell counts were performed within a standard ROI for all subjects (i.e. circle of diameter 500 units). This method is illustrated in **Figure 3.4**. As described above, for verification 5 sections of increasing vacuolation (verified by 5 people) were chosen, and the analysis was able to correctly rank them by quantification of vacuolation.

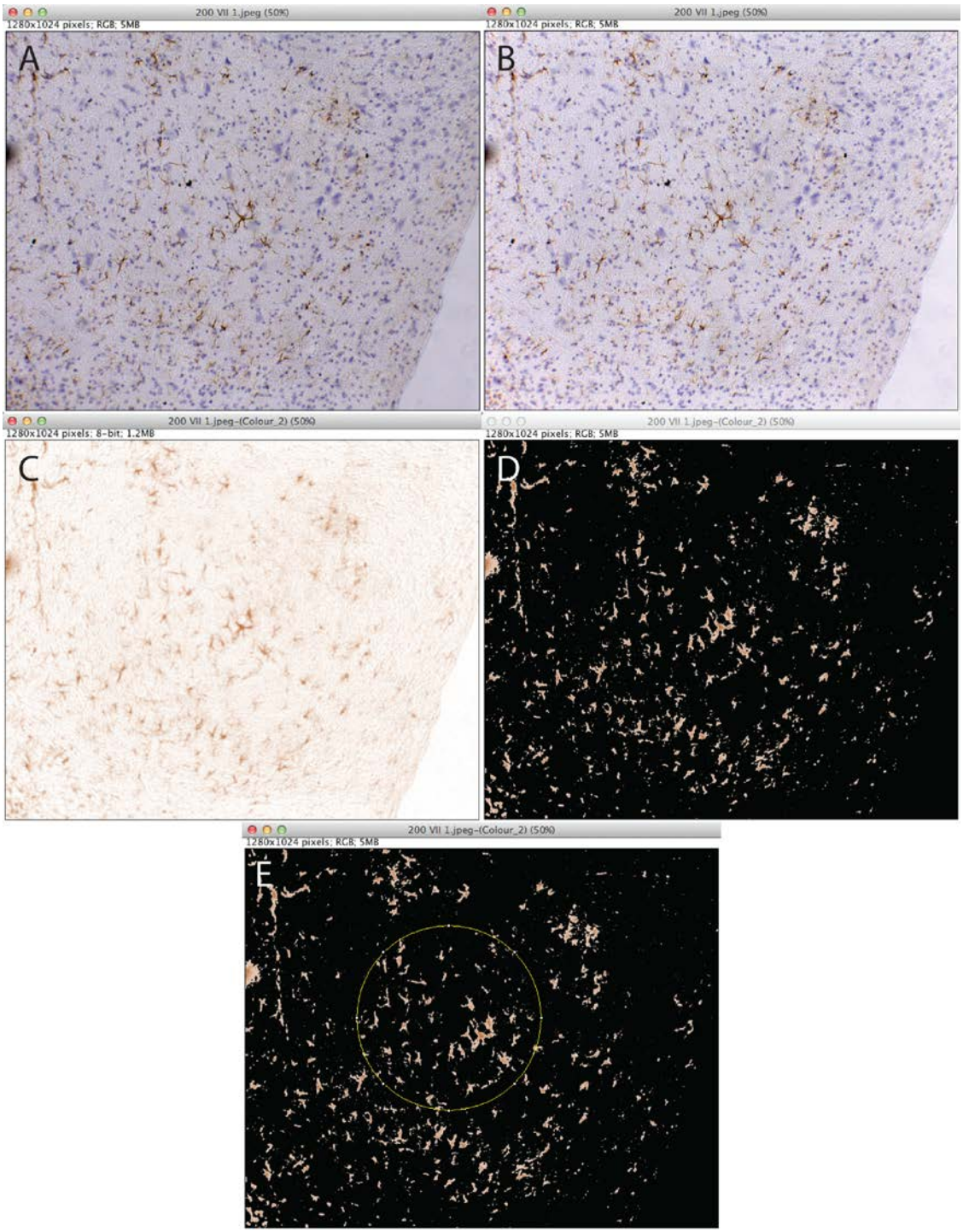


Figure 3.3 – Demonstration of the analysis method for immunohistochemistry

The original image was loaded in ImageJ (A), and the background was subtracted (B). Next a colour deconvolution plugin was used to isolate the drown DAB signal (C), and this was thresholded by eye to binarize the signal (D). Finally, a standard ROI of 500 units was placed over the region to be studied, using the original image as a guide (E).

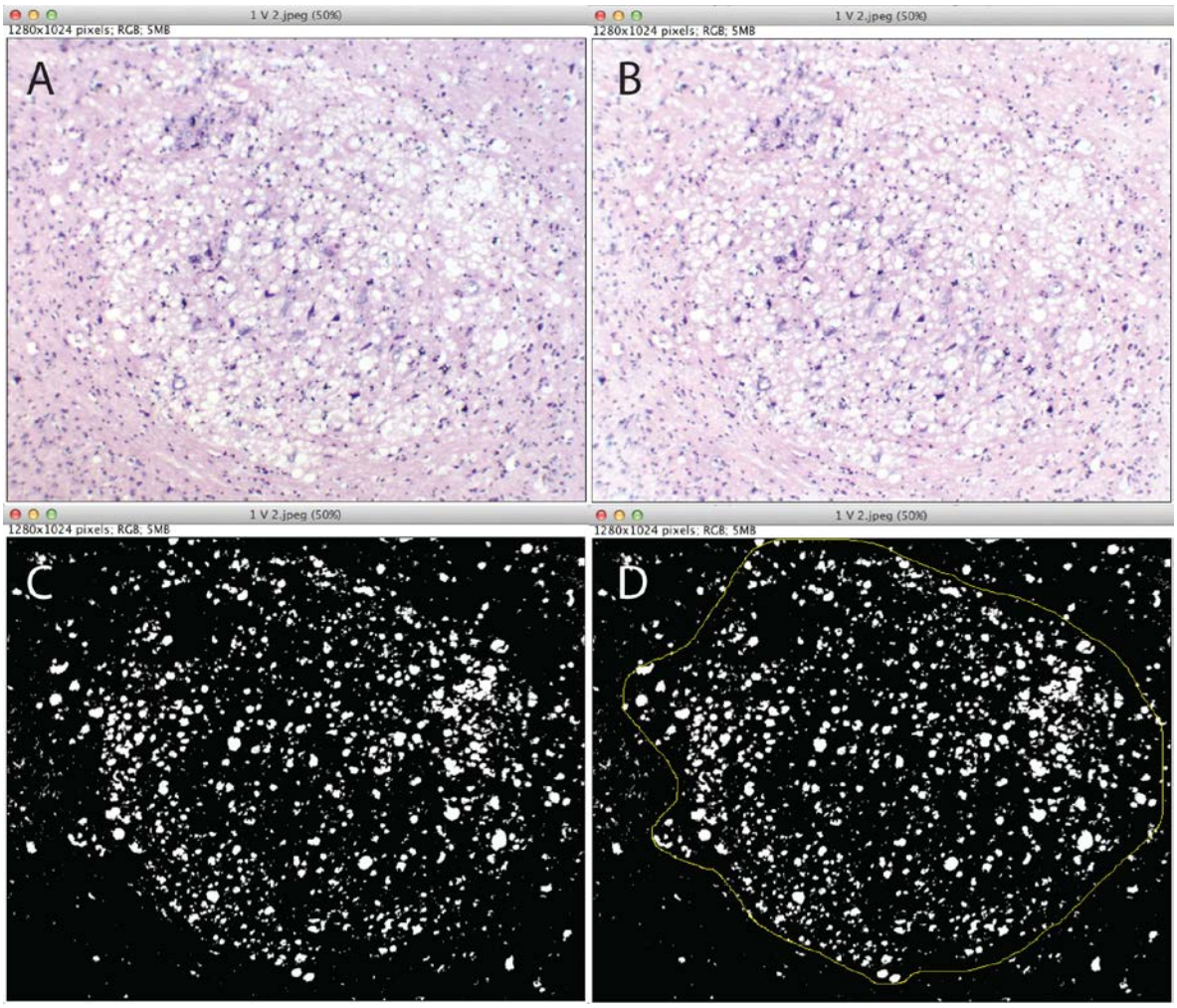


Figure 3.4 – Demonstration of the analysis method for vacuole quantification

The original image was loaded using ImageJ (A) and the background subtracted (B). The image was then binarized using the threshold function, assigning the vacuoles a value of 266 and the normal tissue a value of 0 (C) and an ROI was drawn around the area of vacuolation (D). From this the area affected and average vacuolation were measured, and these values used to calculate total vacuolation.

3.3.8 Statistical analysis

Changes in *SOD1*^{G93A} and wild type mice over time were investigated using a two-way ANOVA, with post-hoc Hulm-Bonferroni corrected t-tests to investigate all pairwise comparisons, using SPSS (SPSS inc.). Effect sizes were compared between measures using Cohen's *d,* calculated from the mean difference and standard deviation. Pearson's r was calculated for the correlation of T_2 hyperintensity in each brainstem nucleus with i) quantification of vacuolation ii) GFAP staining intensity and iii) Iba1 staining intensity. In

order to statistically compare the strength of each of the correlations with one another, r was converted to r' using Fisher's transformation:

$$r' = (0.5)\log_e\left[\frac{1+r}{1-r}\right]$$

A z score was then calculated using the formula:

$$z = \frac{r'_1 - r'_2}{\sqrt{\frac{1}{n_1 - 3} + \frac{1}{n_2 - 3}}}$$

Correlational analysis was carried out using Microsoft Excel.

3.4 Results

3.4.1 Behaviour / weights

For the three rotarod measures used – foot fault (**Figure 3.5**A), double spin (**Figure 3.5**B) and final fall (**Figure 3.5**C) – *SOD1*^{G93A} mice consistently underperformed compared to wild type littermates (significant main effect of genotype, $p<0.001$). Moreover, whilst wild type performance remained constant over time, *SOD1*^{G93A} performance showed a dramatic decrease over time (significant main effect of time-point, $p<0.001$; significant interaction between genotype, foot fault $p<0.05$, double spin and final fall $p<0.001$). A significant change from baseline performance (40 days) was seen for double spin and final fall at 100 days (double spin $p<0.01$, final fall $p<0.001$), and in all three measures at 120 days ($p<0.001$). In addition there was a trend for reduction from baseline for final fall at 80 days ($p=0.09$). Time taken to final fall was significantly different between *SOD1*^{G93A} and wild type mice at all time-points ($p<0.05$), and for double spin and first fall, time taken was significantly different between *SOD1*^{G93A} and wild type mice at 60, 100 and 120 days ($p<0.05$). Figure 1 shows the motor scores from the rotarod and weights throughout the lifespan of the mice (40 – 120 days). *p* values given reflect changes of subsequent time points from baseline (40 days).

The weight data (**Figure 3.5**D) showed the same pattern; *SOD1*^{G93A} mice were significantly lighter compared to wild type littermates at 100 days ($p<0.01$) and 120 days ($p<0.001$), with no significant difference in weight at earlier time points ($p>0.05$).

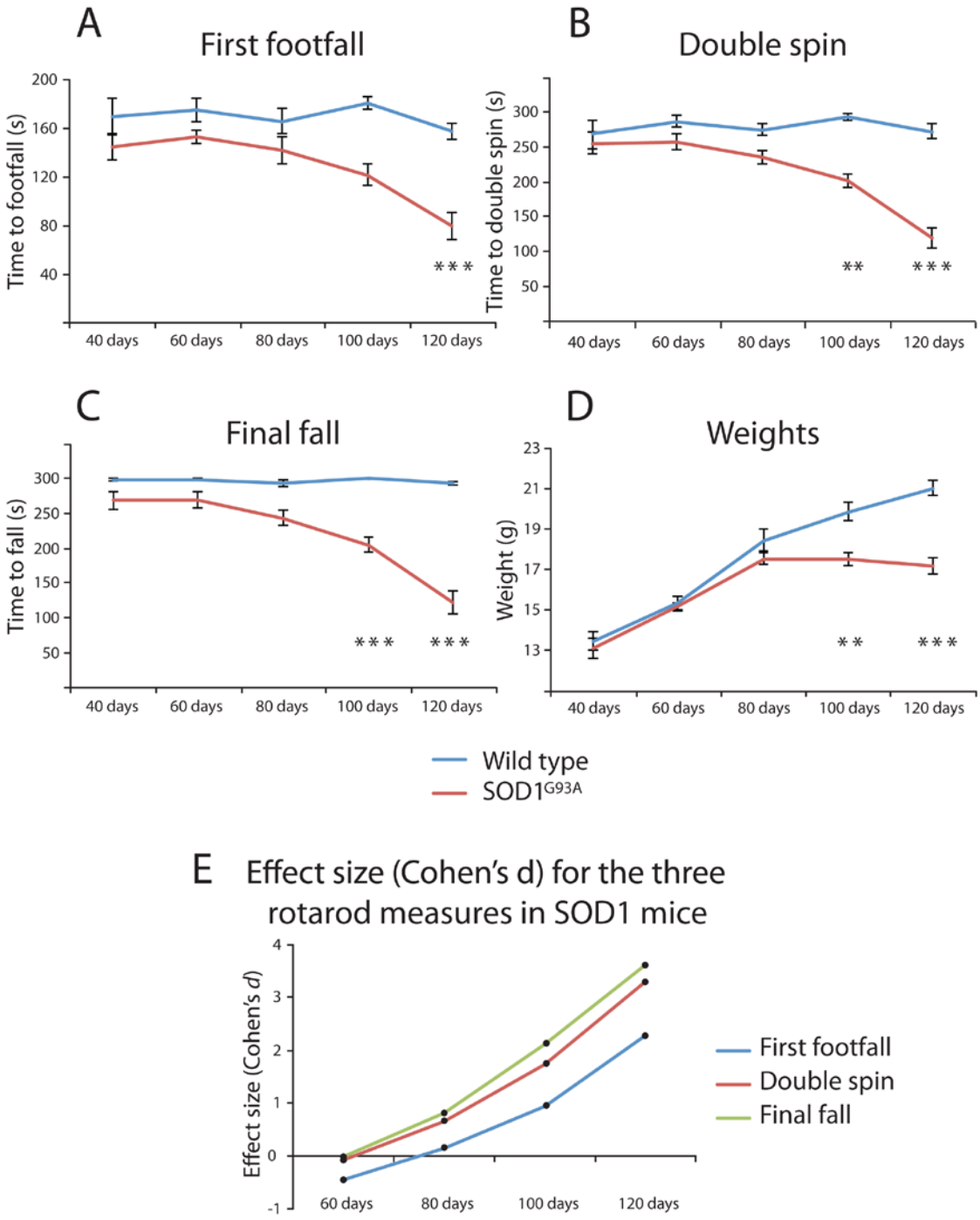


Figure 3.5 - Rotarod scores and weights across lifespan for *SOD1*^{G93A} and wild type littermates used in the MRI study.

All three behavioural measures show a gradual deterioration in motor score over time in *SOD1*, but not wild type mice. For foot fault (A), reduction from baseline was only significant at disease end-stage (120 days). However, for double spin (B) and final fall (C), there was a significant reduction from baseline in motor behaviour at 100 and 120 days. Weights show a stereotypical pattern (D), with wild type mice increasing in body weight in a linear fashion, but the *SOD1* group becoming significantly lighter at 100 and 120 days. Effect size increases for all three measures throughout the disease, but at each time point, final fall had a higher effect size compared with double spin or final fall. P values are for change from baseline.

* p<0.05; ** p<0.01; *** p<0.001. N = 9 per group

Effect size (Cohen's *d*) was calculated from the difference between subsequent time points and baseline (40 days) for each of the rotarod measures, which is illustrated in **Figure 3.5**E. Cohen's d describes the difference between means in terms of the respective standard deviations, so an effect size of 1 indicates a reduction from baseline of 1 standard deviation. Effect sizes increase for each of the measures throughout the lifespan of the *SOD1*^{G93A} mice, but at each time-point effect size is considerably greater for final fall and double spin compared to initial footfall, and final fall has a slightly greater effect size compared to double spin.

3.4.2 Investigating signal change with *in vivo* MRI

3.4.2.1 T_2-weighted imaging in the brainstem

T_2-weighted imaging revealed early and progressive degenerative change in all three motor nuclei (significant main effect of genotype, trigeminal $p<0.05$, facial $p<0.01$, hypoglossal $p<0.001$; significant main effect of time-point, trigeminal $p<0.01$, facial $p<0.001$, hypoglossal $p<0.01$; significant interaction between genotype and time-point, trigeminal $p<0.001$, facial $p<0.001$, hypoglossal $p<0.001$). I performed post-hoc t-tests and found a significant difference between *SOD1*^{G93A} and wild type in all three nuclei at 80 days (trigeminal $p<0.05$; facial $p<0.001$; hypoglossal $p<0.05$), 100 days (trigeminal $p<0.05$; facial $p<0.01$; hypoglossal $p<0.05$) and 120 days (trigeminal $p<0.05$; facial $p<0.01$; hypoglossal $p<0.01$), and a difference in the facial nucleus at day 60 ($p<0.01$) on post-hoc tests. The change in the facial nucleus was more dramatic than the other two nuclei, changing earlier in the disease (60 *vs*. 80 days), and with a greater effect size from 60 to 120 days (see **Table 3.1**). On a number of images, changes could also be noted by eye in the facial nucleus at day 40 and the hypoglossal nucleus at day 60, but this did not reach significance with a sample size of 4 ($p=0.15$). See **Figure 3.6**, **Figure 3.7** and **Figure 3.8** for representative T_2 images.

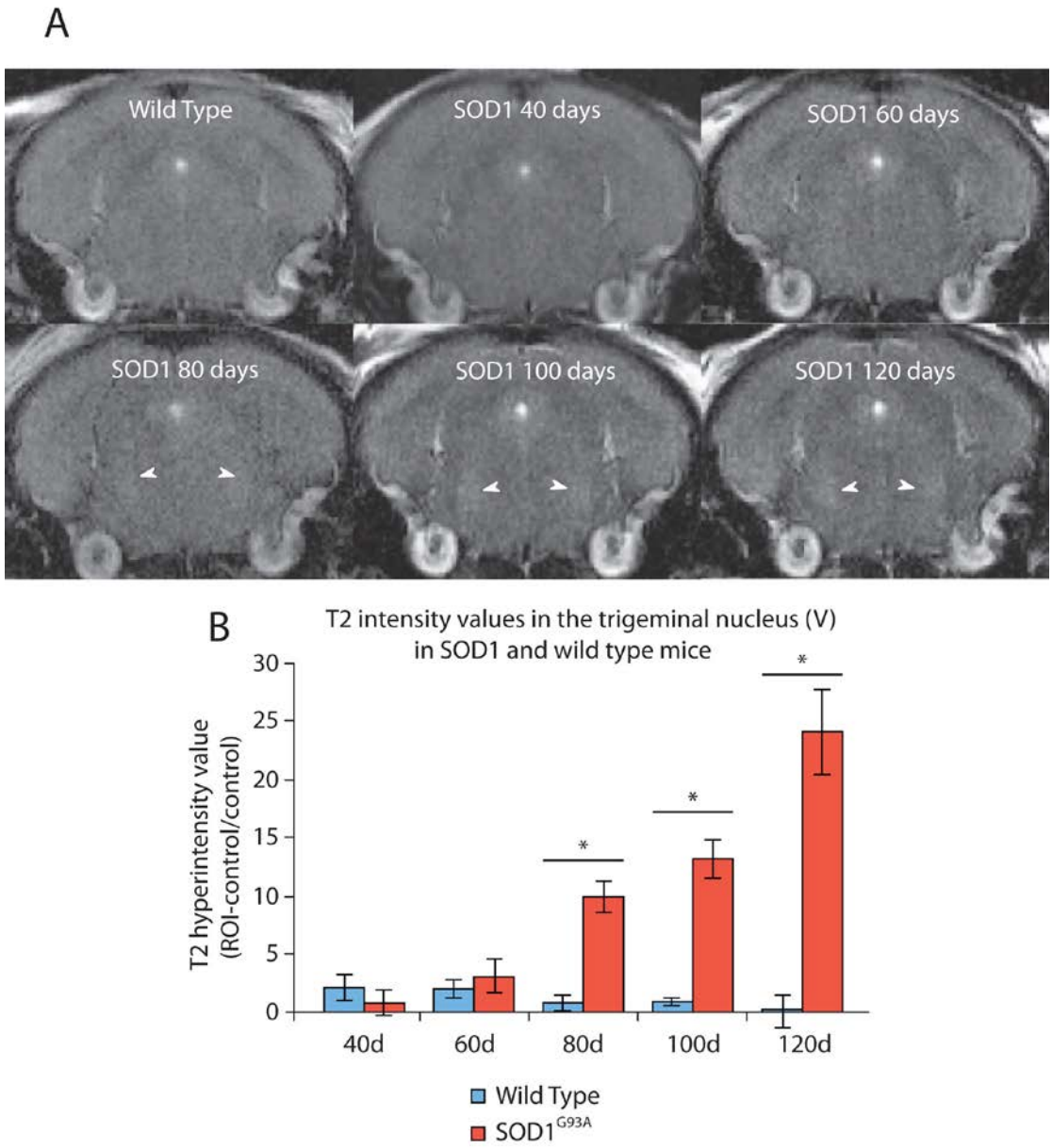


Figure 3.6 Comparison of *T2* signal intensity in the trigeminal nucleus (V) in *SOD1*^{G93A} and wild type mice

Representative T_2 images of the trigeminal nucleus (A) show a gradual increase in signal intensity, first noticeable at 80 days (arrows). Quantification of the T_2 signal intensity in an ROI over the trigeminal nucleus compared to a control region in the surrounding brainstem (B) shows a significant increase in signal intensity in *SOD1*^{G93A} compared with wild type mice at 80, 100 and 120 days.

* $p<0.05$. N=4 in each group

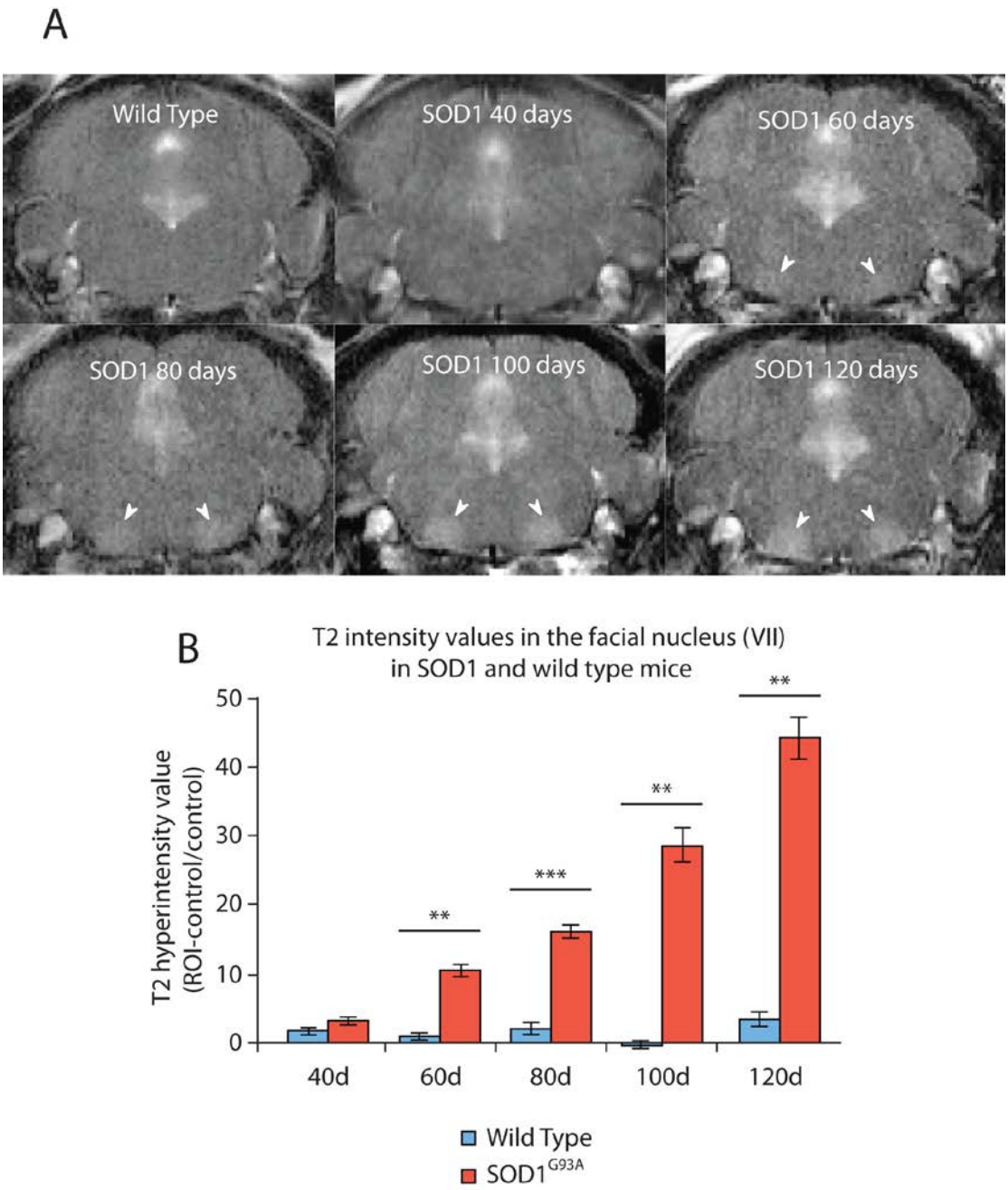


Figure 3.7 Comparison of T_2 signal intensity in the facial nucleus (VII) in *SOD1*^{G93A} and wild type mice

Representative T_2 images of the facial nucleus (A) show a gradual increase in signal intensity, first noticeable at 60 days (arrows). Quantification of the T_2 signal intensity in an ROI over the facial nucleus compared to a control region in the surrounding brainstem (B) shows a significant increase in signal intensity in *SOD1*^{G93A} compared with wild type mice at 60, 80, 100 and 120 days.

* p<0.05; ** p<0.01; *** p<0.001. N = 4 in each group

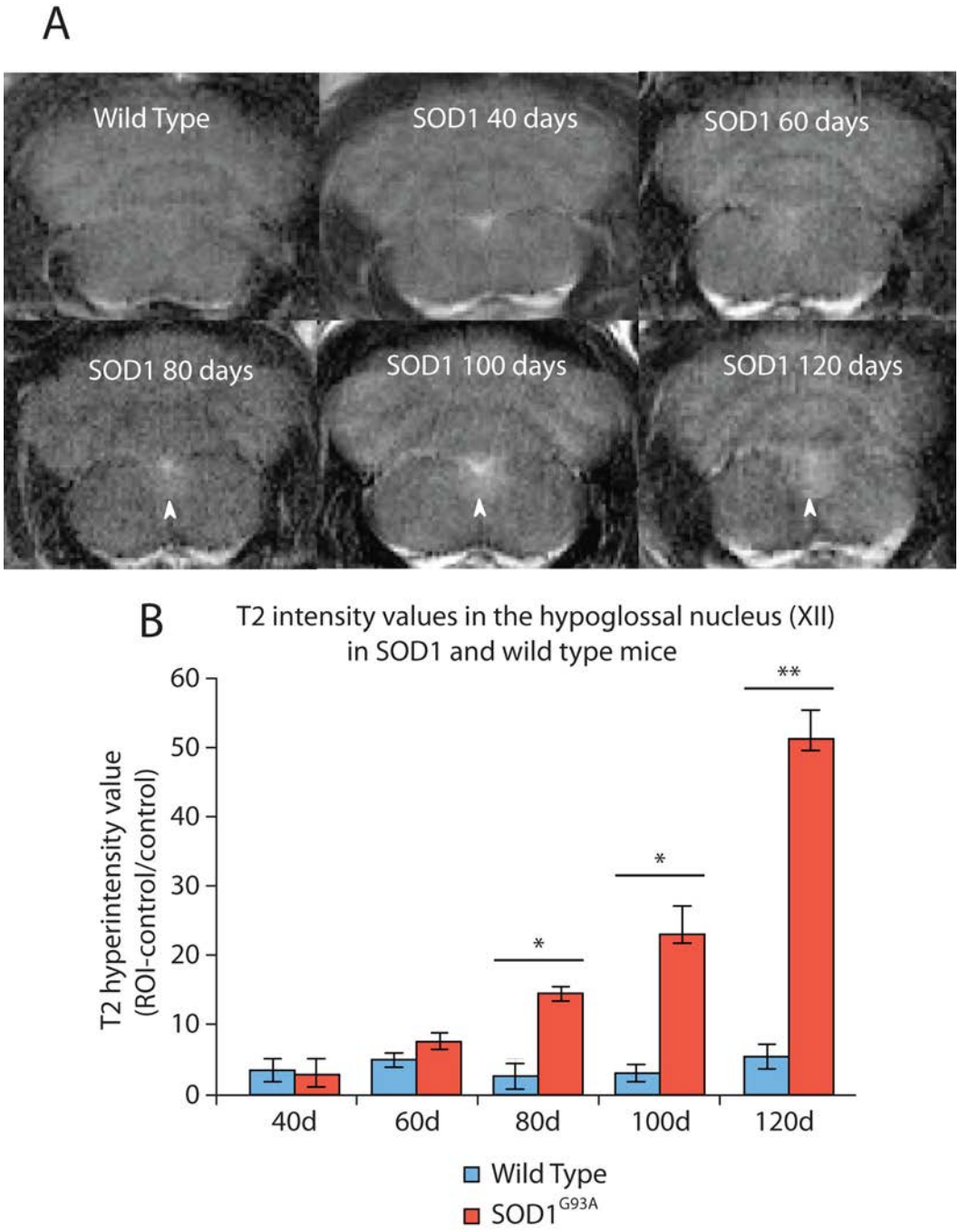


Figure 3.8 Comparison of T_2 signal intensity in the hypoglossal nucleus (XII) in *SOD1*^{G93A} and wild type mice

Representative T_2 images of the hypoglossal nucleus (A) show a gradual increase in signal intensity, first noticeable at 80 days (arrows). Quantification of the T_2 signal intensity in an ROI over the hypoglossal nucleus compared to a control region in the surrounding brainstem (B) shows a significant increase in signal intensity in *SOD1*^{G93A} compared with wild type mice at 80, 100 and 120 days.

* p<0.05; ** p<0.01; *** p<0.001. N = 4 in each group

	Trigeminal	Facial	Hypoglossal
40	-1.22	2.32	0.32
60	0.94	11.34	1.41
80	8.22	18.89	7.55
100	10.14	16.35	6.56
120	8.58	17.65	14.87

Table 3.1 – Effect size (Cohen's d) for the signal intensity in *SOD1*^{G93A} compared to wild type mice from 40 to 120 days

Effect size for the T_2 signal intensity in *SOD1*^{G93A} compared to wild type mice is markedly greater in the facial nucleus compared to the trigeminal or hypoglossal nuclei at all time-points. Effect sizes in the trigeminal and hypoglossal nuclei are mostly comparable.

3.4.2.2 T_2 signal change is not accompanied by T_1 signal change

A T_1-weighted sequence was used, with the same slice plan as the T_2 sequence above, in order to investigate whether changes to T_2 relaxation were accompanied by changes in T_1 relaxation. In comparison to the T_2 signal changes, no changes were seen between *SOD1*^{G93A} and wild type mice at any time-point using T_1-weighted MRI in any of the cranial nuclei (no significant main effect of genotype, $p>0.05$, or time-point, $p>0.05$, and no interaction between genotype and time-point, $p>0.05$). Representative images and quantification of T_1 signal intensity are shown in **Figure 3.9**.

3.4.2.3 Comparison of T_2 with ADC and MTR sequences

The relationship between T_2 signal changes and changes in other MRI measures, in particular MTR and ADC, was investigated at disease end-point (120 days). Although significant increases in T_2 signal intensity in all three brainstem motor nuclei (trigeminal and facial $p<0.001$, hypoglossal $p<0.01$) were seen as described above (arrows, A), both MTR and ADC maps showed a decrease in signal intensity in these nuclei, reflecting the different biological parameters measured by the sequences.

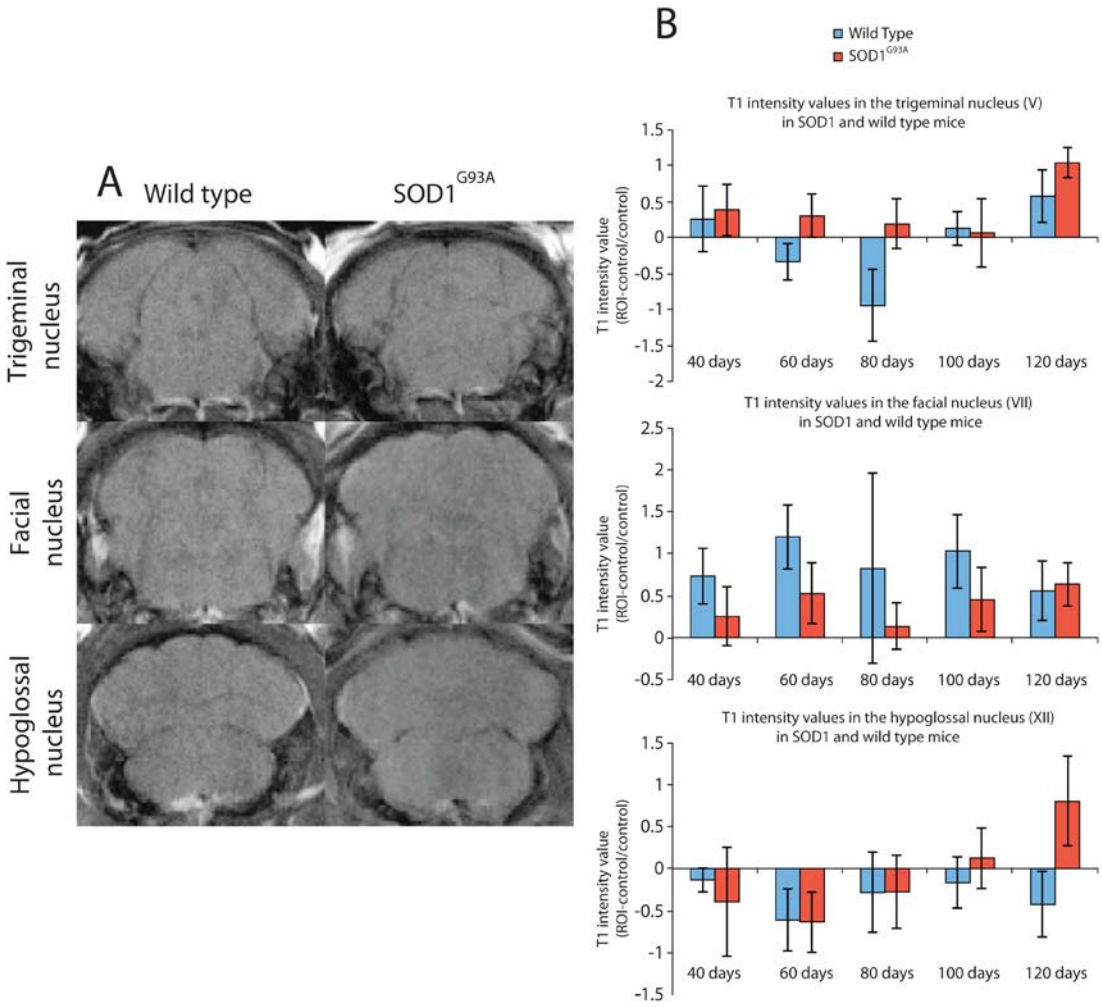


Figure 3.9 Comparison of T_1 signal intensity in the three motor nuclei in *SOD1*^{G93A} and wild type mice

Representative T_1-weighted images of the trigeminal, facial and hypoglossal nuclei (A) show homogenous T_1 signal intensity across the brainstem, with no noticeable changes in any of the nuclei. Quantification of the T_1 signal intensity in an ROI over each of the nuclei compared to a control region in the surrounding brainstem (B) shows no significant difference at any time-point.

N = 4 in each group

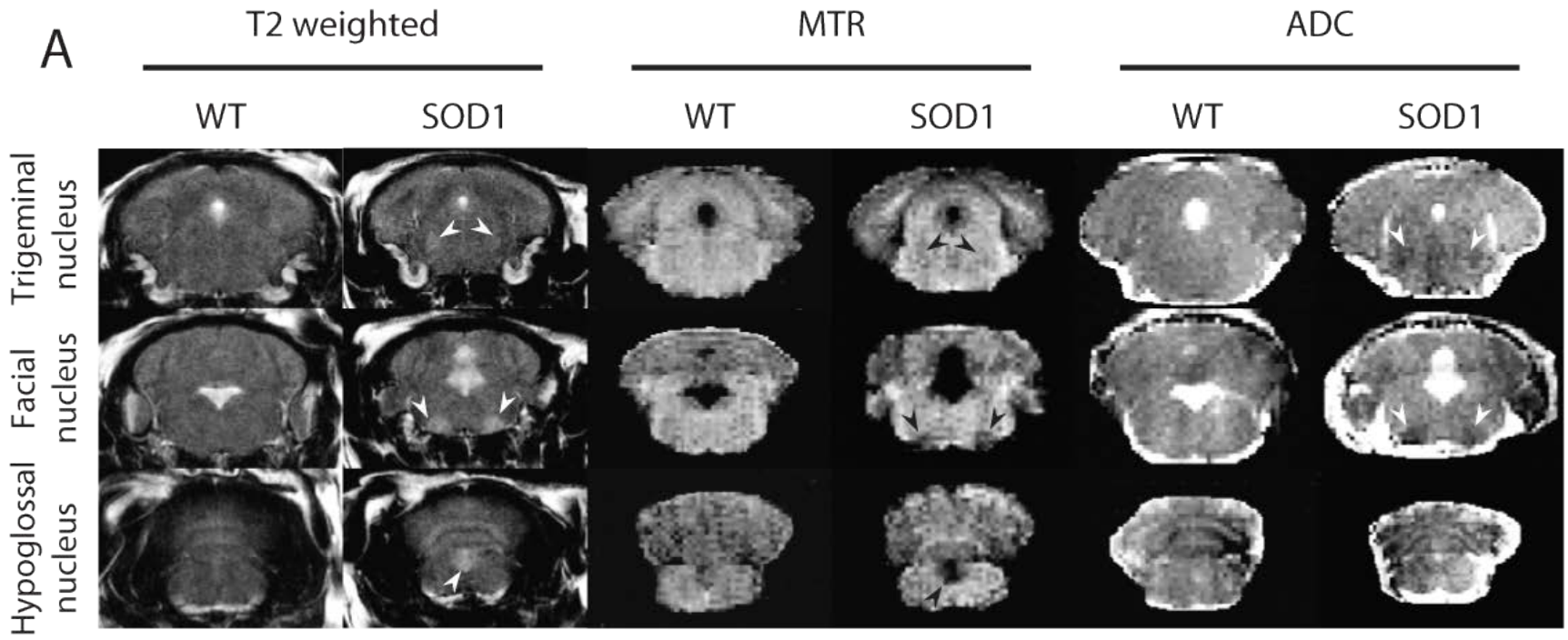
A significant decrease in MTR of the brainstem nuclei (trigeminal $p<0.05$, facial and hypoglossal $p<0.01$) was evident when compared to the control brainstem region, which can clearly be identified from the images (arrows, A). Similarly, a significant decrease in ADC of the nuclei was found (trigeminal $p<0.001$, facial and hypoglossal $p<0.01$). However, with the ADC maps, whilst changes in the trigeminal and facial nuclei are apparent in the images (arrows A, right hand panels), change in the hypoglossal nucleus is more masked by artefacts.

As a comparison of the three sequences, effect sizes were calculated for the difference between *SOD1*^{G93A} and wild type mice in the three nuclei, and the results of this are shown in **Table 3.2**. For all three nuclei, the effect size was greater for the T_2-weighted sequence. MTR and diffusion performed roughly the same across the brainstem nuclei, with a marginally greater effect size for MTR in the hypoglossal nucleus, and for ADC in the trigeminal nucleus. Effect size for all three parameters was lowest in the hypoglossal nucleus.

	T_2	MTR	ADC
Trigeminal	12.04	6.33	9.58
Facial	27.98	7.39	7.19
Hypoglossal	9.01	8.72	5.72

Table 3.2 – Effect size (Cohen's d) for T_2, MTR and ADC sequences at 120 days in brainstem motor nuclei

Comparison of effect size for changes in T_2 signal intensity, MTR and ADC in *SOD1*^{G93A} compared to wild type mice. Changes in T_2 signal intensity were markedly greater than MTR and ADC. Effect sizes for MTR and ADC were largely comparable, with marginally greater effect size for MTR in the hypoglossal nucleus, and for ADC in the trigeminal nucleus.


A
T2 weighted
MTR
ADC
WT
SOD1
WT
SOD1
WT
SOD1
Trigeminal nucleus
Facial nucleus
Hypoglossal nucleus

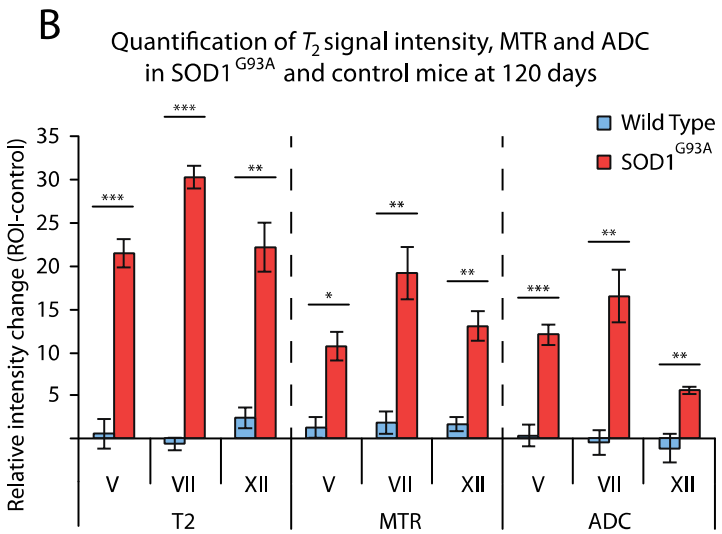


Figure 3.10 – Comparison of T_2 signal intensity, MTR and ADC in *SOD1*^{G93A} and control mice at 120 days.

Representative images from T_2, MTR and ADC MRI (A) show noticeable changes in all nuclei (arrows) except for the hypoglossal nucleus for ADC. Quantification of T_2 signal intensity, MTR and ADC in *SOD1*^{G93A} and control mice (B) indicate that significant changes occur in all three nuclei. Note that changes in ADC and MTR have been inverted for comparison with T_2 signal intensity changes.

V = trigeminal; VII = facial; XII = hypoglossal

* $p<0.05$; ** $p<0.01$; *** $p<0.001$, N = 6 in each group

3.4.3 Exploration of pathological changes using histology and immunohistochemistry

3.4.3.1 Vacuolation

Tissue sections of *SOD1*^{G93A} and wild type control mice were cut and stained with H&E at 40 – 120 days, in the trigeminal, facial and hypoglossal nuclei. From photographs of H&E stains, binary masks were created using Image J, and the amount of vacuolation in the tissue was calculated as described in the 2.5.8 above.

In all three nuclei, there was significantly greater vacuole pathology in *SOD1*^{G93A} compared with wild type mice (main effect of genotype, $p<0.05$; main effect of time point, $p<0.05$; interaction of genotype and time point, $p<0.05$). In the trigeminal nucleus (**Figure 3.11**, top row; **Figure 3.12**A), there was an increase in vacuolation at 60 days, that approached significance ($p=0.061$), and a significant increase in vacuolation at 80 ($p<0.05$), 100 and 120 days ($p<0.01$). In the facial nucleus (**Figure 3.11**, middle row; **Figure 3.12**B), there was also a borderline increase in vacuolation at 60 days ($p=0.079$), and significant vacuolation from 80 – 120 days of age ($p<0.01$). In the hypoglossal nucleus (**Figure 3.11**, bottom row; **Figure 3.12**C) there was an increase in vacuolation at 60 days, which was close to significance ($p=0.087$), and significant vacuolation from 80 – 120 days ($p<0.05$).

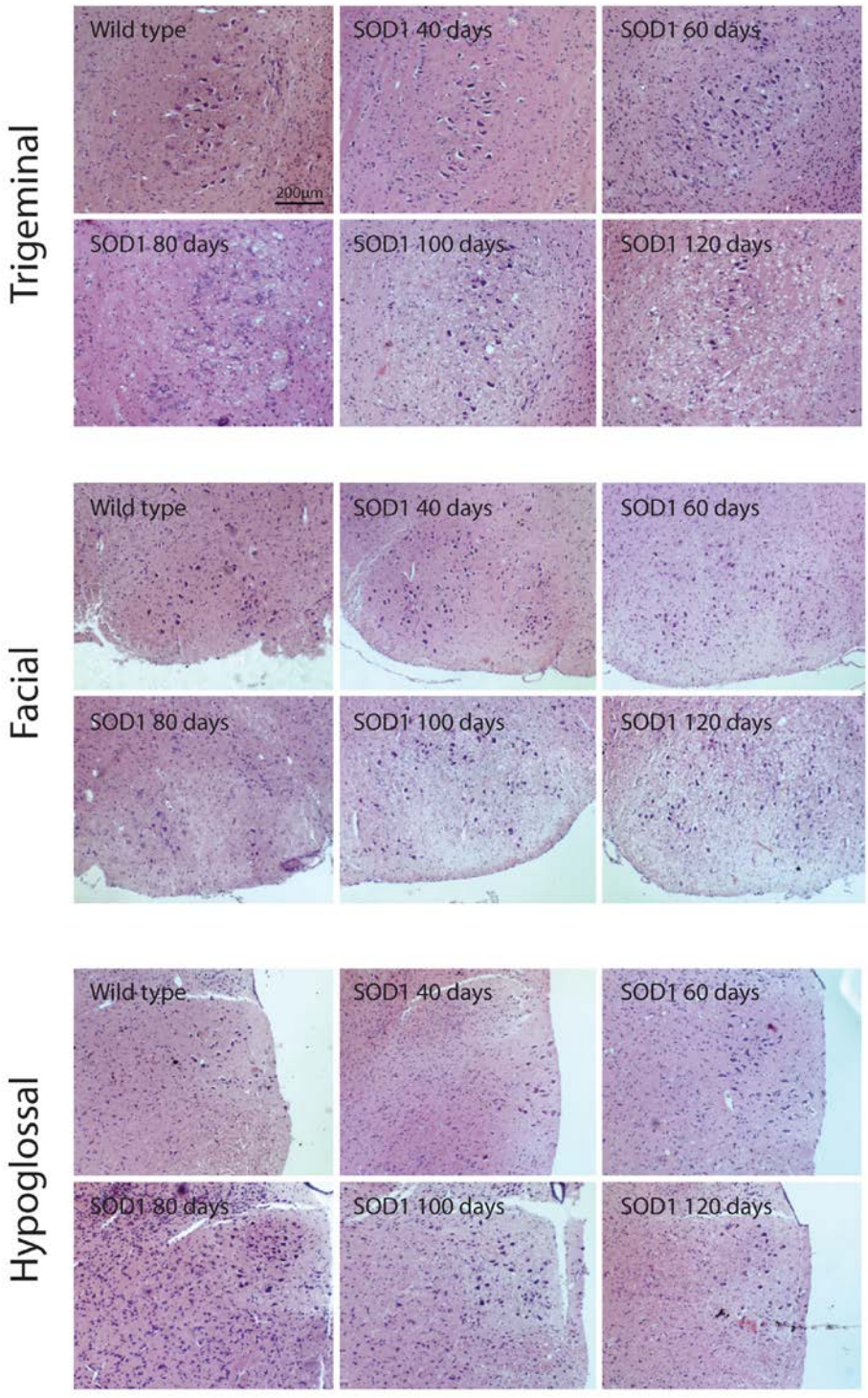


Figure 3.11 – Representative H&E images, showing the development of vacuolation in the trigeminal, facial and hypoglossal nuclei

Vacuoles developed in the tissue from 60 days in the facial nucleus (middle panels) and from 80 days in the trigeminal (top panels) and hypoglossal nuclei (bottom panels) in *SOD1*^{G93A} mice. No vacuoles were found in these regions in wild type littermates at any time point.

N = 4 in each group

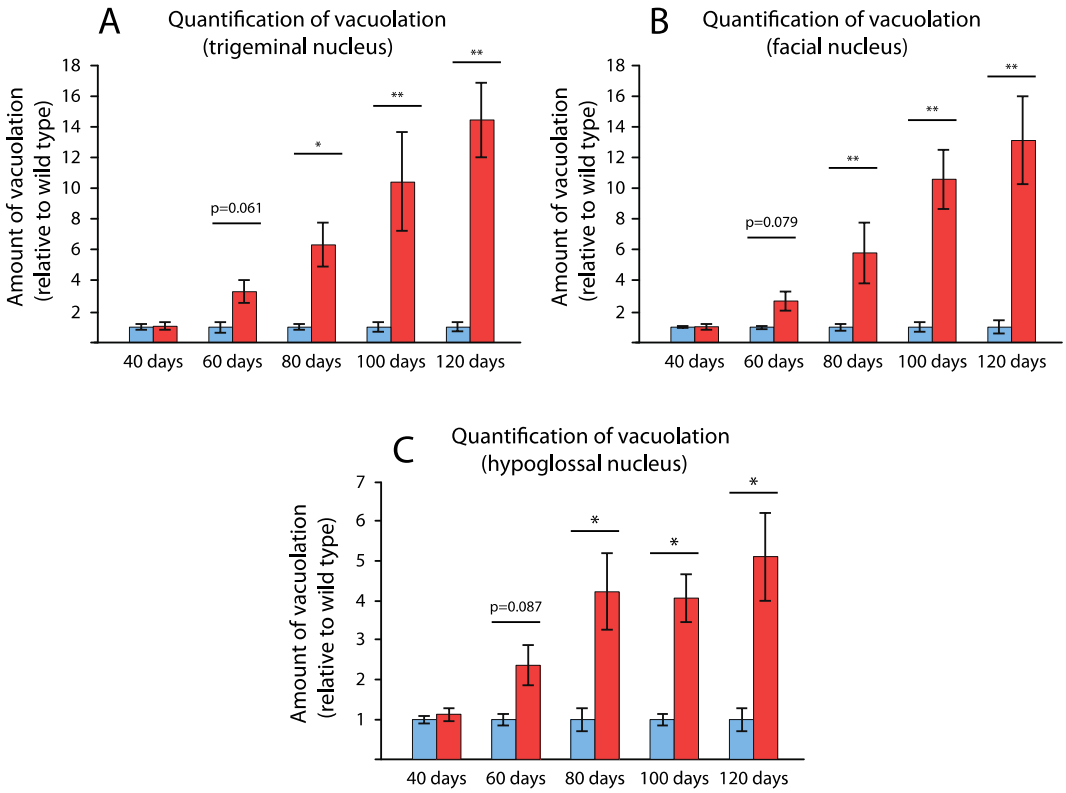


Figure 3.12 – Quantification of vacuolation in the trigeminal, facial and hypoglossal nuclei using ImageJ

Image J was used to quantify vacuolation by creating a binary mask from H&E images. Significant structural tissue alterations were noted from 60 days in the trigeminal, facial and hypoglossal nuclei in *SOD1*^{G93A} mice compared to wild type controls, and this increased steadily throughout the disease process.

* p<0.05; ** p<0.01; *** p<0.001, N = 4 in each group

3.4.3.2 GFAP

Sections of the cranial nuclei, and sensorimotor cortex and spinal cord, were also stained with antibodies against GFAP to measure phenotypic changes in astrocytes.

For all three nuclei, there was significantly stronger staining of GFAP for *SOD1*^{G93A} compared with wild type mice (main effect of genotype, $p<0.01$; main effect of time point, $p<0.05$; interaction between genotype and time point $p<0.01$). Within the trigeminal nucleus (**Figure 3.13**, top row; **Figure 3.15**B), GFAP immunoreactivity was significantly increased in *SOD1*^{G93A} mice from 100 days ($p<0.01$), but was also higher, although not significant, at 60 ($p=0.059$) and 80 days ($p=0.084$). In the facial nucleus (**Figure 3.13**, middle row; **Figure 3.15**C,) there was significantly higher GFAP immunoreactivity from 60 – 120 days of age ($p<0.01$). The increase in GFAP immunoreactivity in the hypoglossal nucleus (**Figure 3.13**, bottom row; **Figure 3.15**D) was slightly delayed with regards to the other two motor nuclei, with an increase in reaction product from 80 – 120 days ($p<0.05$).

In addition to changes in GFAP expression in the cranial motor nuclei, there was also an increase in GFAP immunoreactivity in the cervical and lumbar spinal cord (main effect of genotype, $p<0.01$; main effect of time point, $p<0.01$; interaction between genotype and time point, $p<0.01$). The lumbar cord (**Figure 3.14**, middle row; **Figure 3.15**F) was affected earlier, with significantly stronger GFAP staining at 60, 80, 100 ($p<0.05$) and 120 days ($p<0.01$) of age, whereas in the cervical cord (**Figure 3.14**, top row; **Figure 3.15**E) there was an increase in GFAP immunoreactivity at 80, 100 ($p<0.01$) and 120 days ($p<0.001$).

There was small difference in GFAP immunoreactivity in the sensorimotor cortex between *SOD1*^{G93A} and wild type littermates (**Figure 3.14**, bottom row). However, unlike the other regions studied, where most of the grey matter of the cranial nuclei and spinal cord stains very strongly for GFAP as the disease progresses, later in the disease in *SOD1*^{G93A} mice, focal regions of high GFAP staining appeared in the sensorimotor cortex, but this only

affected a small portion of the tissue. Therefore GFAP staining in randomly placed ROIs did not show any differences between the groups ($p>0.05$ – data not shown), but when instead an ROI was placed around the area of *highest* GFAP immunoreactivity in *SOD1*^{G93A} and wild type mice (**Figure 3.15**A), there was a morphological change in astrocytes for *SOD1*^{G93A} compared with wild type mice (main effect of genotype, $p<0.05$; main effect of time point, $p<0.05$; interaction between genotype and time point, $p<0.05$), due to an increase in staining at 100 ($p<0.05$) and 120 days of age ($p<0.01$).

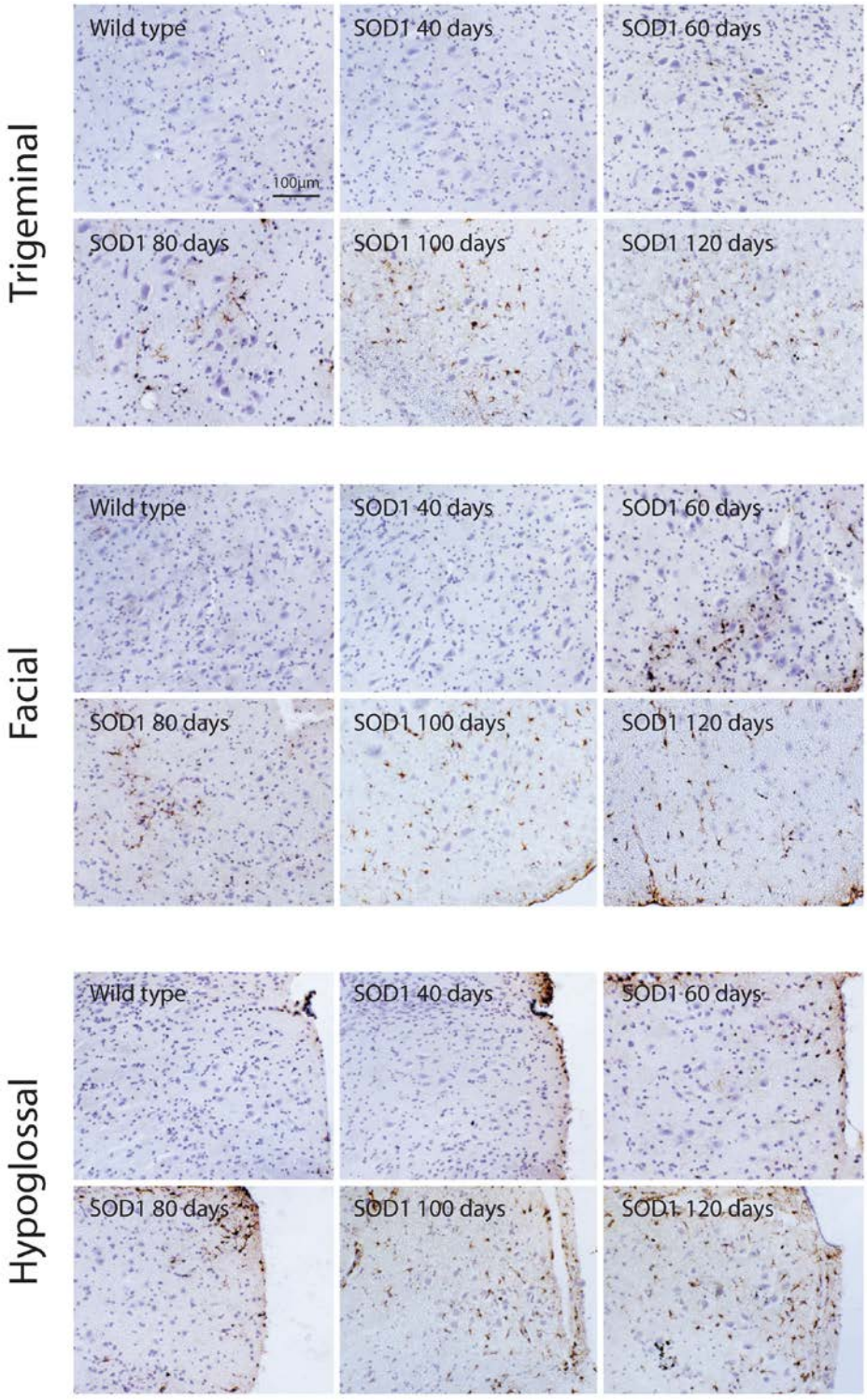


Figure 3.13 – Representative images of GFAP immunohistochemistry in the trigeminal, facial and hypoglossal nucleus

Immunoreactivity to GFAP was very low in wild type mice and 40 days *SOD1*^{G93A} mice in the grey matter of the trigeminal (top row), facial (middle row) and hypoglossal nuclei (bottom row). There was an increase in GFAP staining in the trigeminal and facial nuclei at 60 days, and in the hypoglossal nucleus at 80 days for *SOD1*^{G93A} mice, which became more prominent as the disease progressed.

N=4; scale bar applies to all images

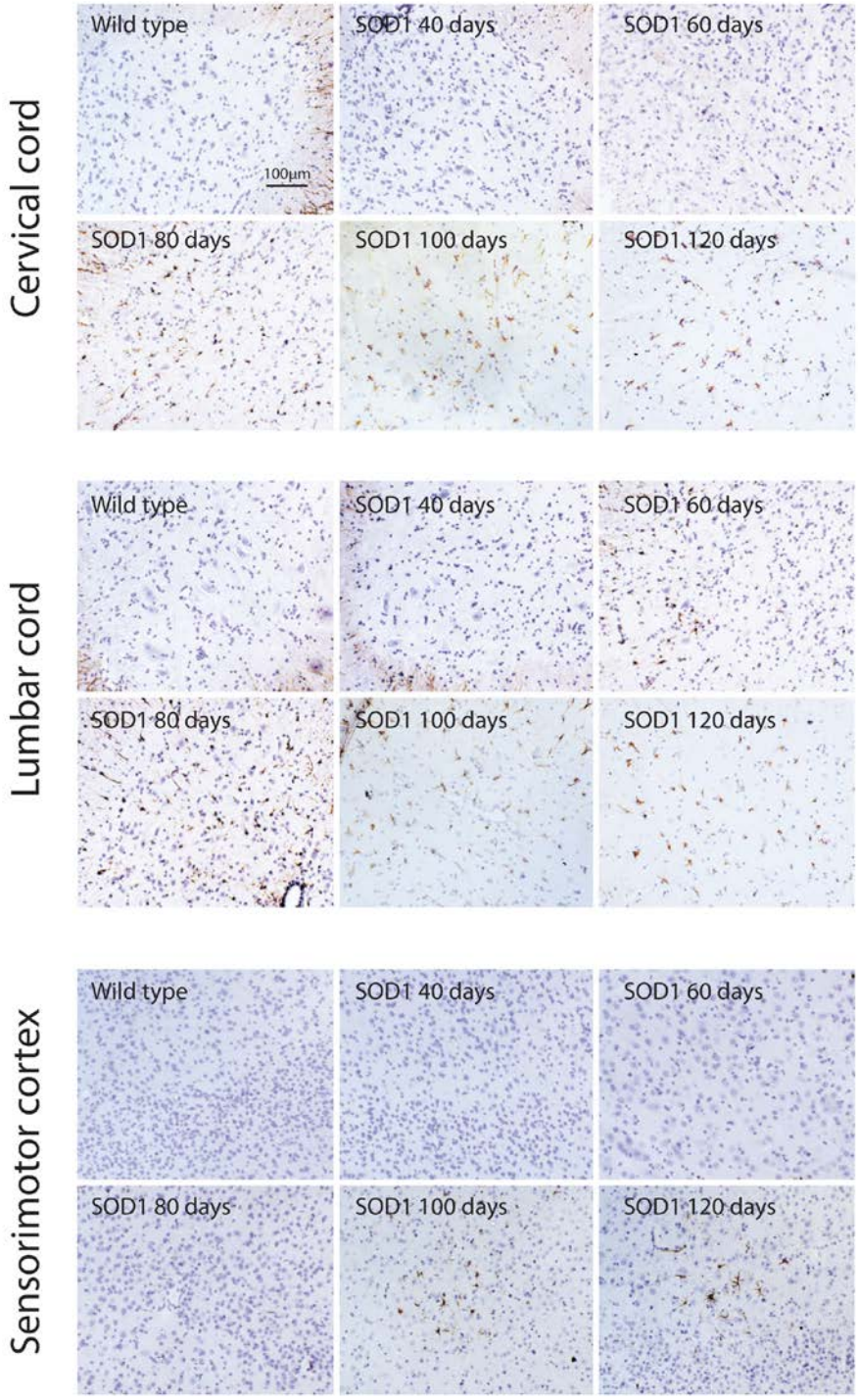


Figure 3.14 - Representative images of GFAP immunohistochemistry in the spinal cord and sensorimotor cortex

Immunoreactivity to GFAP was very low in wild type and 40 day *SOD1*^{G93A} mice in the cervical spinal cord (top row), lumbar spinal cord (middle row) and sensorimotor cortex (bottom row). There was an increase in GFAP staining in the lumbar spinal cord at 60 days, and in the cervical spinal cord at 80 days for *SOD1*^{G93A} mice, which became more prominent as the disease progressed. In the sensorimotor cortex, the general GFAP immunoreactivity was very low in *SOD1*^{G93A} mice at all time points, but at 100 and 120 days, small areas of focal high GFAP immunoreactivity were present.

N=4; scale bar applies to all images

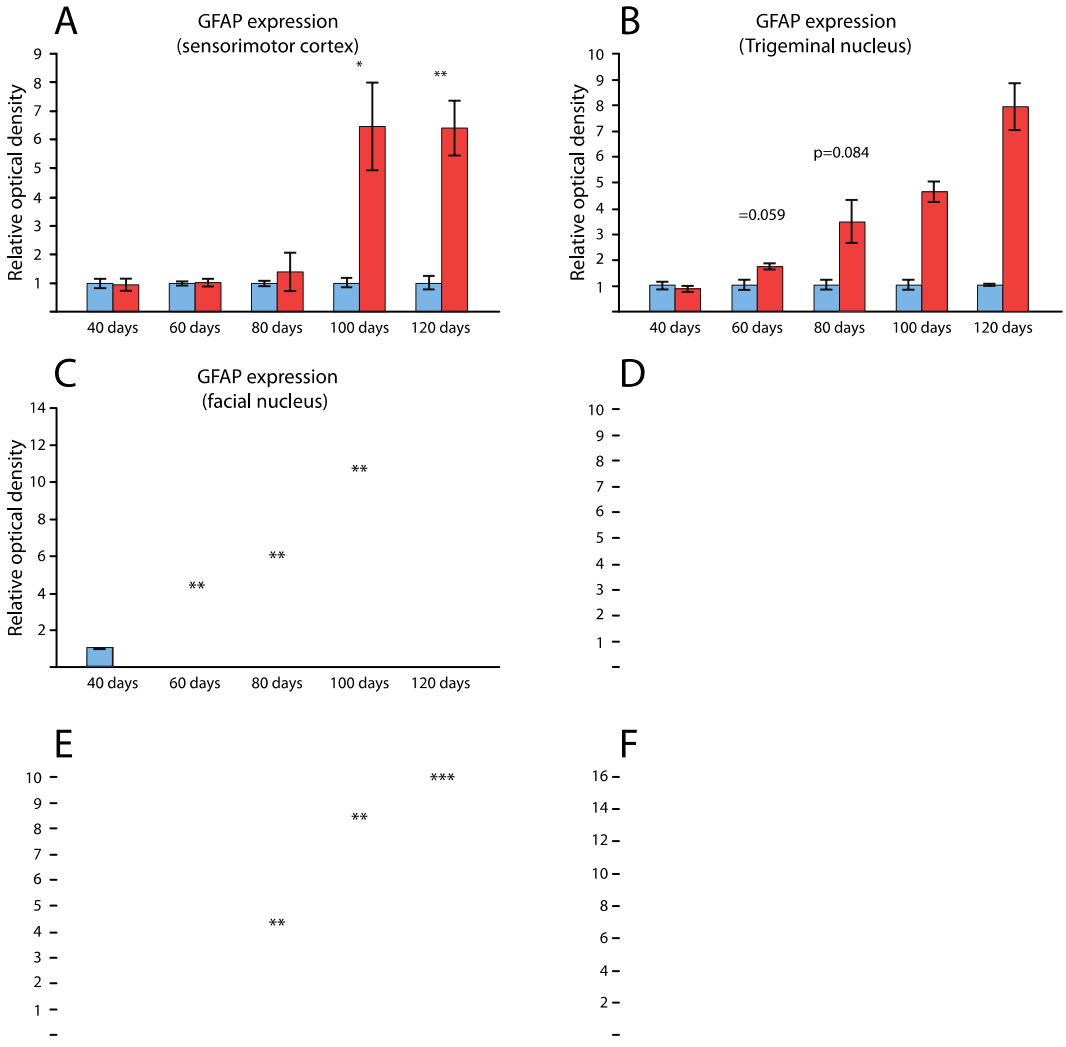


Figure 3.15 – Quantification of optical density of DAB product from GFAP staining, in the spinal cord, cranial nuclei and sensorimotor cortex

The earliest increase in GFAP immunoreactivity in *SOD1*^{G93A} mice was in the lumbar spinal cord (F), trigeminal nucleus (B) and facial nucleus (C) at 60 days, which increased towards 120 days. A slightly later increase in GFAP staining was found in the cervical spinal cord (E) and hypoglossal nucleus (D) at 80 days of age, which, again, increased through to 120 days. The general immunoreactivity for GFAP did not differ between *SOD1*^{G93A} and wild type mice in the sensorimotor cortex, but by placing an ROI over the highest area of GFAP immunoreactivity, a focal increase in GFAP staining was seen at 100 and 120 days ion *SOD1*^{G93A} mice.

* p<0.05; ** p<0.01; *** p<0.001, N = 4 in each group

3.4.3.3 Iba1

Sections of the sensorimotor cortex, cranial nuclei and spinal cord were stained using antibodies against Iba1, a marker of “activated” microglia, to investigate the time course of phenotypic changes in this cell population.

For the cranial nuclei, there was a significantly elevated expression of Iba1 in all three nuclei for *SOD1*^{G93A} compared with wild type mice (main effect of genotype, $p<0.05$; main effect of time point, $p<0.05$; interaction between genotype and time point $p<0.05$). Iba1 immunoreactivity within the trigeminal nucleus (**Figure 3.16**, top row; **Figure 3.18**C) was significantly increased in *SOD1*^{G93A} mice at 100 and 120 days ($p<0.01$). In addition there was higher Iba1 immunoreactivity at 80 days, but this did not reach statistical significance ($p=0.071$). In the facial nucleus (**Figure 3.16**, middle row; **Figure 3.18**D), there was higher Iba1 staining from 80 – 120 days of age ($p<0.05$) in *SOD1*^{G93A} mice compared with wild type controls. There was also significantly more Iba1 immunoreactivity in the hypoglossal nucleus (**Figure 3.16**, bottom row; **Figure 3.18**E) from 80 – 120 days in *SOD1*^{G93A} mice ($p<0.05$).

Changes in Iba1 expression were also found in the spinal cord, with significantly higher immunoreactivity in the cervical and lumbar spinal cord (main effect of genotype, $p<0.01$; main effect of time point $p<0.05$; interaction between genotype and time point, $p<0.05$). The earliest change in Iba1 expression was in the lumbar cord, where there was significantly higher immunoreactivity in SOD1^{G93A} compared with wild type mice at 60 ($p<0.05$), 80 ($p<0.001$), 100 ($p<0.05$) and 120 days of age ($p<0.05$). A slightly delayed microglial response was observed in the cervical region, with significantly more Iba1 immunoreactivity at 80 ($p<0.05$), 100 ($p<0.001$) and 120 days ($p<0.05$).

For analysis of Iba1 expression in the sensorimotor cortex, the superficial (layers I-III) and deep (layers IV-VI) layers were analysed separately. For the deep layers, no significant difference was found between *SOD1*^{G93A} and wild type mice in terms of Iba1 expression

at any point in the disease ($p>0.05$). However, in the superficial layers, there was higher Iba1 immunoreactivity in *SOD1*^{G93A} compared with wild type mice (main effect of genotype, $p<0.05$; main effect of time point, $p<0.05$; interaction between genotype and time point, $p<0.05$), driven by increases in the Iba1 immunoreactivity at 100 ($p<0.01$) and 120 days ($p<0.05$).

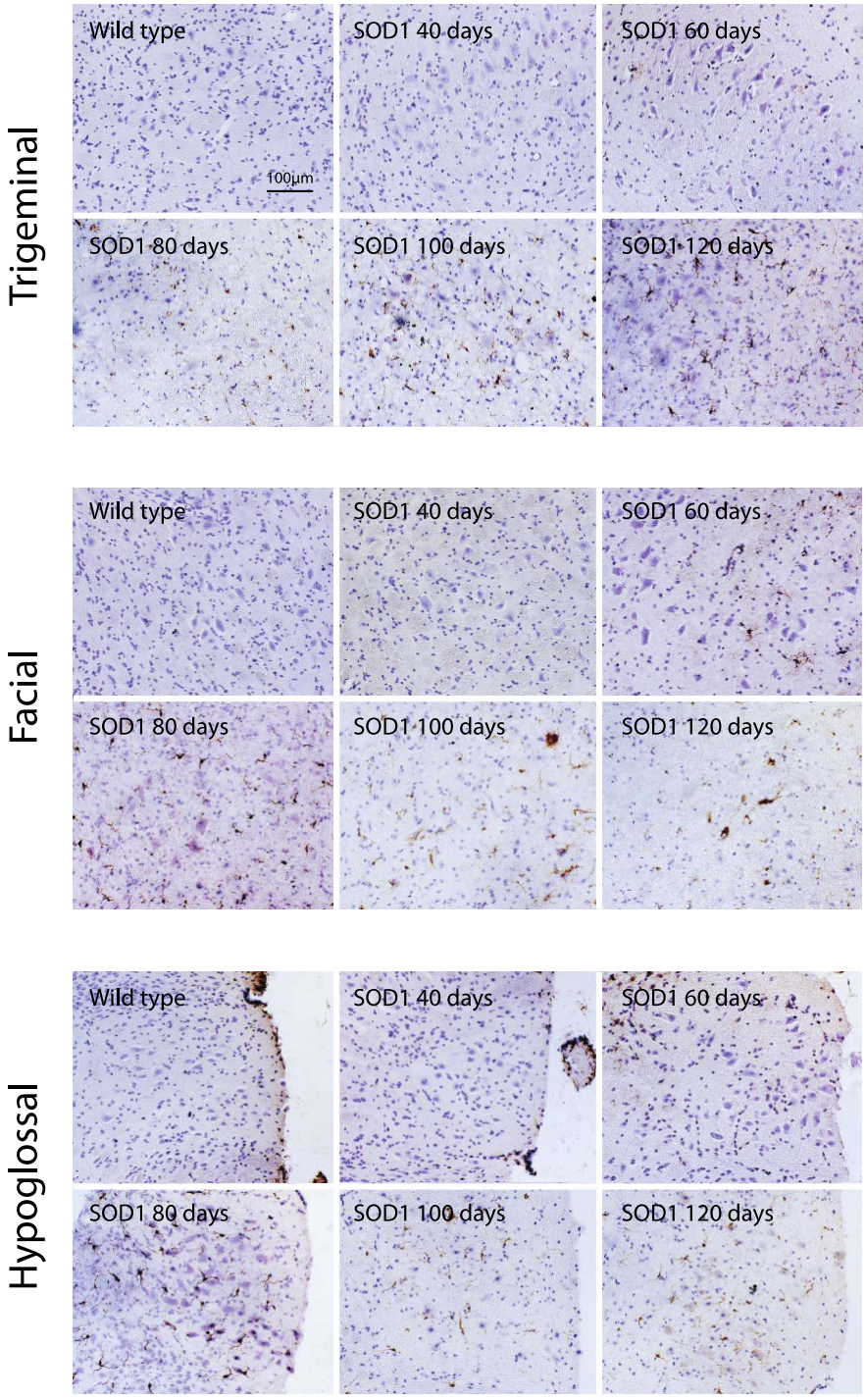


Figure 3.16 - Representative images of Iba1 immunohistochemistry in the trigeminal, facial and hypoglossal nucleus

Immunoreactivity to Iba1 was very low in wild type mice and 40 days *SOD1*^{G93A} mice in the grey matter of the trigeminal (top row), facial (middle row) and hypoglossal nuclei (bottom row). There was an increase in Iba1 staining in the all three cranial motor nuclei at 80 days in *SOD1*^{G93A} mice, which became more prominent as the disease progressed.

N=4; scale bar applies to all images

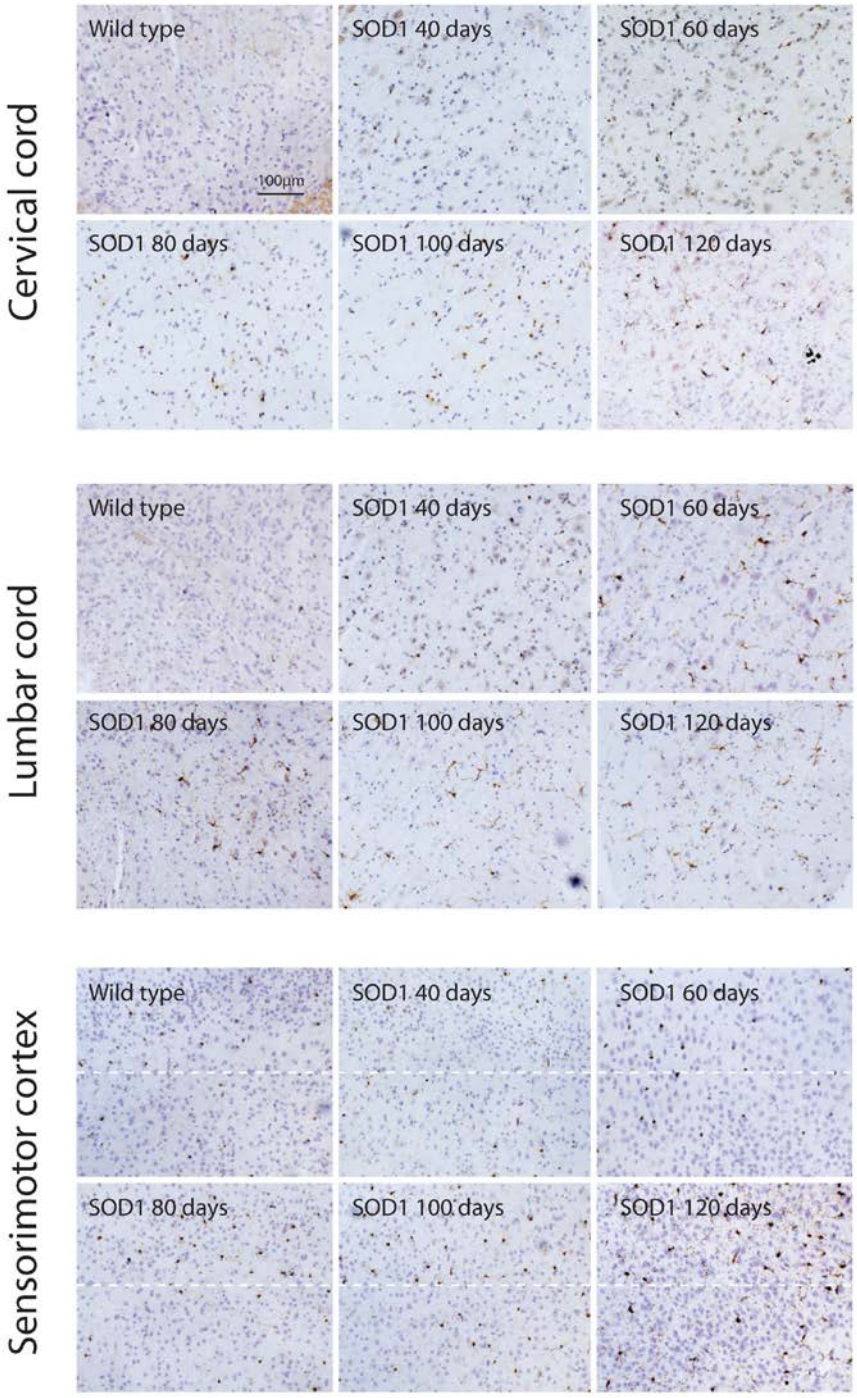


Figure 3.17 - Representative images of Iba1 immunohistochemistry in the spinal cord and sensorimotor cortex

Immunoreactivity to Iba1 was very low in wild type and 40 day *SOD1*^{G93A} mice in the cervical spinal cord (top row), lumbar spinal cord (middle row) and sensorimotor cortex (bottom row). There was an increase in GFAP staining in the lumbar spinal cord at 60 days, and in the cervical spinal cord at 80 days for *SOD1*^{G93A} mice, which became more prominent as the disease progressed. In the sensorimotor cortex, the general GFAP immunoreactivity was comparable for *SOD1*^{G93A} and wild type mice at 40 to 60 days, but at 100 and 120 days there was an increase in Iba1 staining intensity in the superficial part of the sensorimotor cortex (layers I-III – above the dotted line) in *SOD1*^{G93A} compared with wild type mice.

N=4; scale bar applies to all images

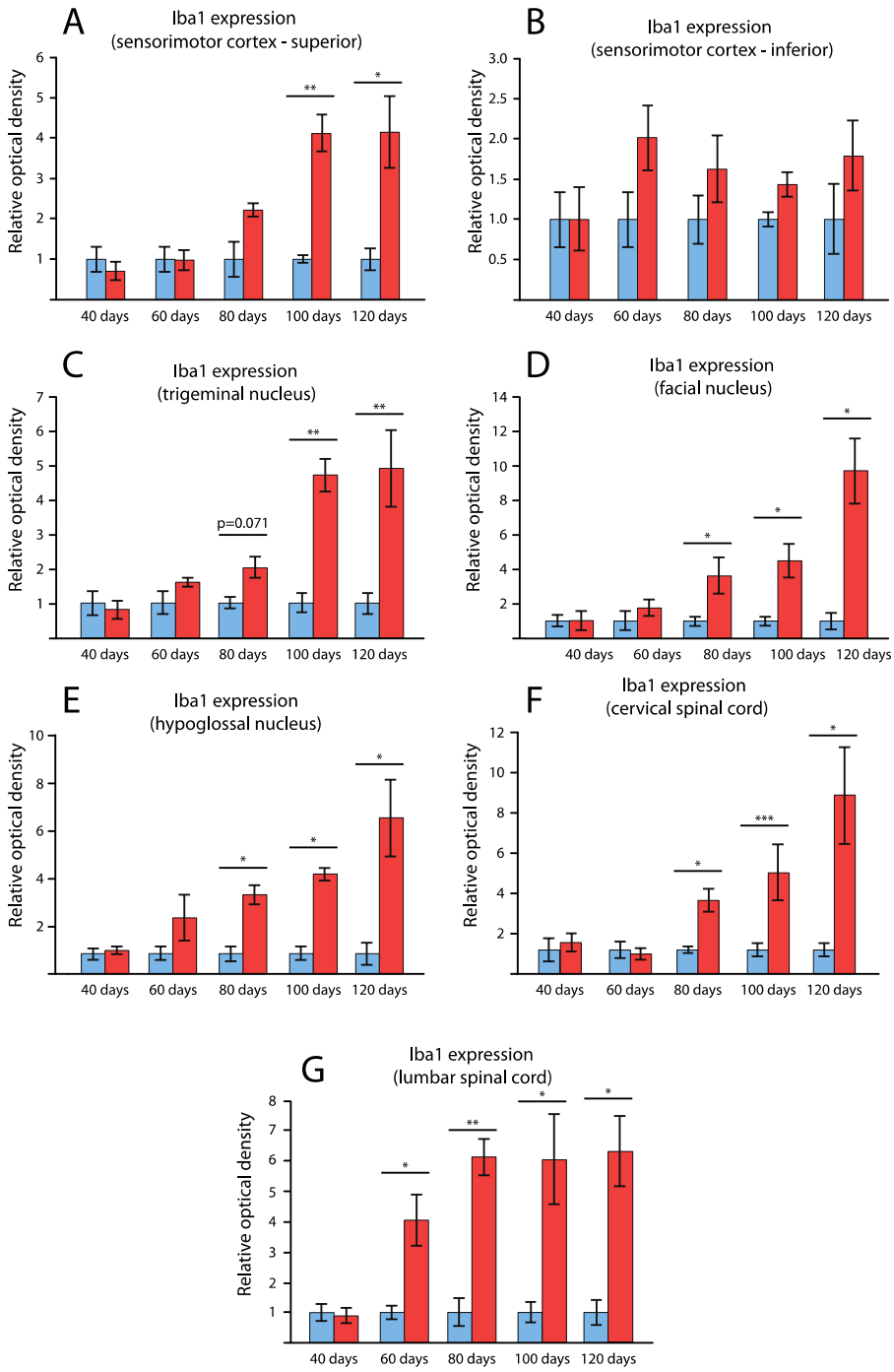


Figure 3.18 - Quantification of optical density of DAB product from Iba1 staining, in the spinal cord, cranial nuclei and sensorimotor cortex

The earliest increase in Iba1 immunoreactivity in *SOD1*^{G93A} mice was in the lumbar spinal cord (G) at 60 days of age, which increased to 120 days of age. In the trigeminal (C), facial (D) and hypoglossal nuclei, and in the cervical spinal cord, there is an increase in Iba1 immunoreactivity at 80 days, which increased towards 120 days. In the sensorimotor cortex, there was no difference between *SOD1*^{G93A} and wild type mice from 40 to 80 days, either in the superficial or deep cortex, but at 100 and 120 days there was an increase in Iba1 immunoreactivity in the superficial layers of cortex (layers I-III), but not the deep layers (IV-VI), for *SOD1*^{G93A} compared with wild type mice.

* p<0.05; ** p<0.01; *** p<0.001, N = 4 in each group

3.4.4 Correlation between T_2 hyperintensity and histological markers

As described in 3.3.8, correlational analysis was carried out to compare the MRI changes (T_2) in the brainstem with quantification of vacuolation, intensity of GFAP staining and intensity of Iba1 staining. Values for r were converted to r', and these used to calculate z scored to compare strength of correlations.

In the trigeminal nucleus, there was a significant correlation of degree of T_2 hyperintensity with vacuolation (r = 0.79), GFAP (r = 0.82) and Iba1 (r = 0.72), but there was no significant difference between the strength of any of the correlations (p>0.05). In the facial nucleus, there was a significant correlation of T_2 hyperintensity with vacuolation (r = 0.84), GFAP (r = 0.85) and Iba1 (r = 0.75), and again there was no significant difference between any of the correlation coefficients (p>0.05). Finally, in the hypoglossal nucleus, there was a significant correlation of T_2 hyperintensity with vacuolation (r = 0.67), GFAP (r = 0.72) and Iba1 (r = 0.72), with no significant difference between strength of any of the correlations (p>0.05). **Figure 3.19** illustrates the relationship between T_2 change and vacuole / glial change in the facial nucleus.

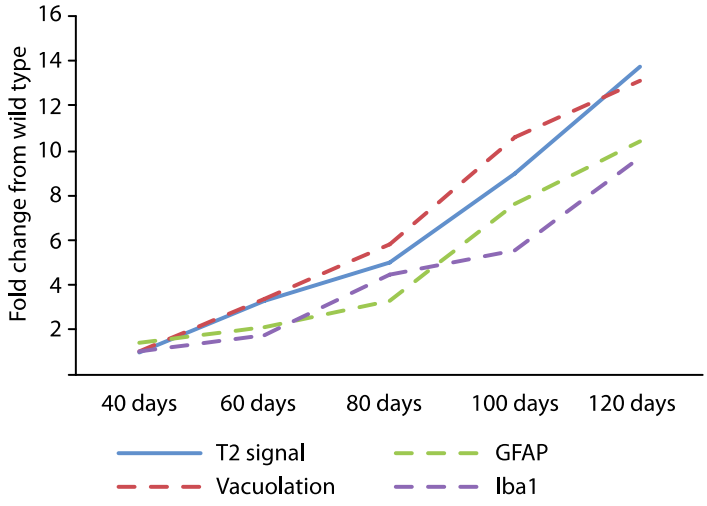


Figure 3.19 - Time course of T_2 signal change plotted along side vacuole and glial change

Change in T_2 signal intensity is mirrored by a comparable change in vacuole formation, as described in Bucher et al. (2007), but also has a similar relationship with astrocyte and microglial changes, as shown by immunohistochemistry for GFAP and Iba1 respectively. The data shown is for the facial nucleus, but is representative of the trigeminal and hypoglossal also.

3.4.5 BBB permeability

SOD1^{G93A} and wild type mice were imaged using a T_1-weighted sequence before and after the administration of Gd-DTPA. The pre-Gd-DTPA image was then subtracted from the post-gadolinium image to show areas of positive intensity associated with vascular permeability. *SOD1*^{G93A} mice were indistinguishable from wild type mice in all areas of the brain, including midbrain/brainstem motor nuclei, at all time-points. Representative images are shown in **Figure 3.20**A.

Paraffin sections taken from *SOD1*^{G93A} and wild type mice from the MRI experiment were stained using antibodies against mouse IgG to measure BBB permeability. No immunoreactivity was noted in any brain region at any time-point in *SOD1*^{G93A} or wild type mice, but was seen extensively in the experimental brain trauma positive control tissue. Photomicrographs of IgG staining are shown in **Figure 3.20**B.

3.4.6 *In vivo* MRI with VCAM-MPIO contrast agent to detect endothelial activation

Super paramagnetic MPIO cause in homogeneities in the magnetic field, leading to hypointense regions on T_2*-weighted MRI. Thus, hypointense regions correspond to VCAM-MPIO binding to the VCAM-1 protein on the activated vascular endothelium. Interestingly, despite VCAM-MPIO highlighting VCAM-1 expression in a number of models of inflammation, no evidence of VCAM-MPIO binding was evident in *SOD1*^{G93A} mice at any time-point ($p>0.05$), even at 120 days when there is clear pathology seen on T_2*-weighted images ($p>0.05$) (**Figure 3.21**). Nor was any increased binding seen when regional analysis was carried out on the brainstem and sensorimotor cortex specifically ($p>0.05$). As a positive control to ensure correct construction of beads, we injected 3 mice in the sensorimotor cortex bilaterally with recombinant human IL-1β to cause inflammation and activate the endothelium (McAteer et al., 2007). Images from these mice 4 hours after injection showed high level of binding, especially in the region of the sensorimotor cortex.

Immunohistochemistry for VCAM-1 was carried out in *SOD1*^{G93A} mice and wild type littermates to confirm the MRI findings (**Figure 3.22**). Only a very low level of VCAM-1 immunoreactivity could be seen in *SOD1*^{G93A} mice or wild type littermates, with no differences in VCAM-1 staining in the sensorimotor cortex, cranial nuclei, or spinal cord, at any point from 40 to 120 days of age. However, there was strong VCAM-1 immunoreactivity in positive control tissue, around the site of cytokine injection.

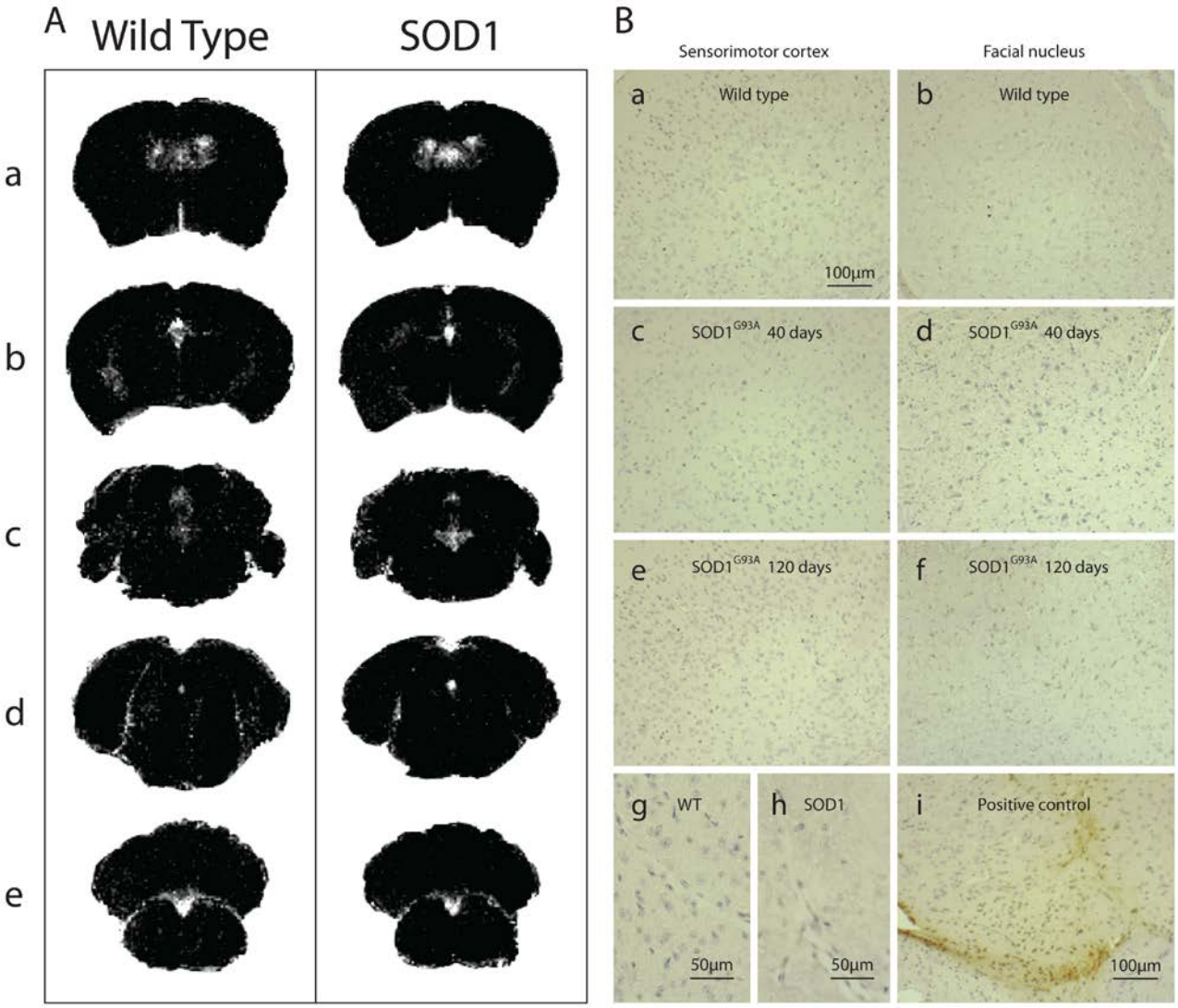

A
Wild Type
SOD1
a
b
c
d
e
B
Sensorimotor cortex
Facial nucleus
a Wild type
b Wild type
100µm
c SOD1G93A 40 days
d SOD1G93A 40 days
e SOD1G93A 120 days
f SOD1G93A 120 days
g WT
h SOD1
i Positive control
50µm
50µm
100µm

Figure 3.20 No BBB breakdown is seen at any time point in *SOD1*^{G93A} mice

Subtraction of Gadolinium T_1 images (A) shows that Gd-DTPA causes signal change in the ventricles in both *SOD1*^{G93A} and wild type mice, but no signal change is seen in the tissue, either in the sensorimotor cortex (panels a and b), or any of the midbrain/brainstem motor nuclei (panels c-e). No IgG staining was noted at any time point (B) in either wild type (panels a and b), 40 day *SOD1*^{G93A} (panels c and d) or 120 day SOD1^{G93A} (panels e and f) tissue. Panels a, c and e show images from the sensorimotor cortex, b, d and f show images from the facial (VII) motor nucleus. Similarly even at high magnification, no staining could be seen around vessels in *SOD1*^{G93A} (panel h) or wild type (panel g) mice. Panel i shows a photomicrograph from positive control tissue (experimental brain trauma) as a comparison.

N = 4 in each group; 100μm scale bar applies unless otherwise stated

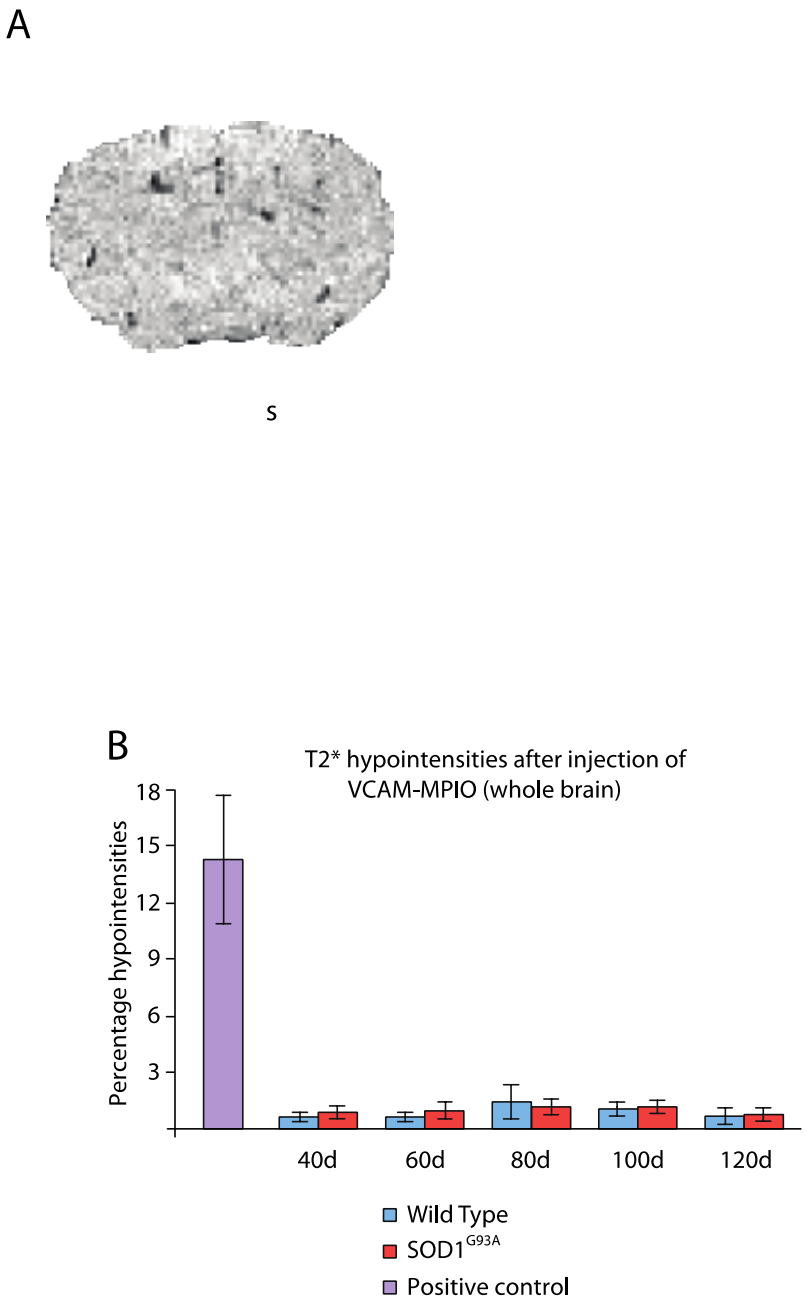


Figure 3.21 – Imaging of VCAM-1 expression in the brains of *SOD1*^{G93A} mice and wild type controls at 120 days, and positive IL-1β-injected controls.

Representative T_2* images of the cortex (A, top right panel) and brainstem nuclei (A, bottom panels) in *SOD1*^{G93A} mice at end stage show no binding of VCAM-MPIO. However, significant binding could be seen in a model of experimental inflammation (A, top left), where VCAM-MPIO binding causes signal dropout. Quantification of T_2* hypointensities shows that there was significant VCAM-MPIO binding in the positive control only, with no significant binding in *SOD1*^{G93A} or wild type mice at any time point. Data presented are for whole brain; analysis was also performed for the sensorimotor cortex and brainstem in isolation, but no regional effects were found either (data not shown).

Positive control N=3; *SOD1*^{G93A} and wild type N=4

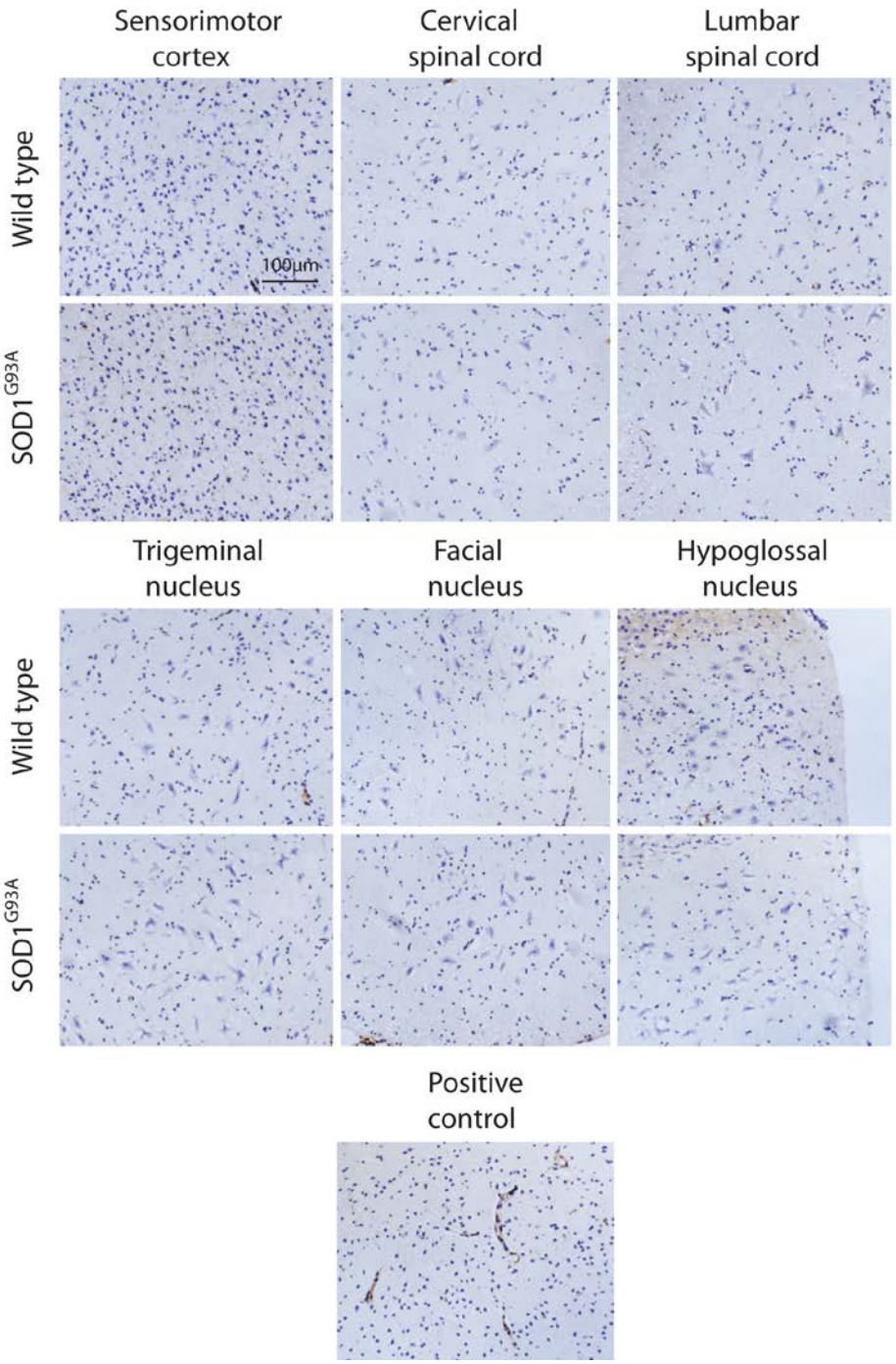


Figure 3.22 – Representative images of VCAM-1 immunohistochemistry in the sensorimotor cortex, spinal cord and cranial nuclei

There was no increase in VCAM-1 immunoreactivity in *SOD1*^{G93A} compared with wild type mice, in the trigeminal, facial or hypoglossal nuclei (middle row), in the cervical or lumbar spinal cord, or in the sensorimotor cortex (top row). However, marked VCAM-1 immunoreactivity was seen around the area of cytokine injection in the positive control tissue (bottom panel).

N = 4; scale bar applies to all images

3.5 Discussion

One of the reasons that *SOD1* mouse models in general, and the G93A mutation in particular, are so popular as pre-clinical models of ALS is that their motor deficits mimic very well the deficits seen in many ALS patients, if in a rather accelerated manner. They also have a very stereotyped disease progression, which makes them particularly attractive as models in which to test disease-modifying agents. Motor ability using the rotarod apparatus and weight were measured throughout the disease process (40, 60, 80, 100, 120 days of age) to see if mice in our colony followed the typical progression seen other institutions, and to investigate which behavioural measure would be the most sensitive to ALS pathology. **Figure 3.5** shows that *SOD1*^{G93A} mice underperformed compared to their wild type littermates at all time points. Their motor behaviour deteriorated as the disease progressed, and their motor score was significantly different from baseline performance (40 days) from 100 days. Weight data followed a similar pattern – *SOD1*^{G93A} and wild type mice were indistinguishable by weight up to a point between 80 and 100 days, when wild type mice continued to gain weight, but *SOD1*^{G93A} mice levelled off before beginning to loose bodyweight. This is consistent with previous reports of motor behaviour and weights in *SOD1* models (Weydt et al., 2003, Fischer et al., 2004, Miana-Mena et al., 2005).

Three measures of motor performance on the rotarod were used here. Most previous studies in this field use final fall as the behavioural measure, but in addition to this, I measured time of first footfall (where mice slip and regain footing) and time to double spin (as sometimes when mice are struggling to keep up, instead of falling off they cling on and rotate around with the rotarod). I calculated the effect size for the decrease from baseline performance in *SOD1*^{G93A} mice, and plotted this over time as a comparison of the sensitivity of these measures for pathology in *SOD1*^{G93A} mice. At all time points the final fall measure had the highest effect size, closely followed by double spin, and first footfall having the lowest effect size between *SOD1*^{G93A} and wild type mice. There was a

low incidence of double spins, so this measure often defaulted to being equivalent to final fall. As such the effect size was very similar for double spin and final fall. Initial footfall is a subjective measure, which contributes to the experimental variation compared to the other measures. This is particularly relevant when considering the frequent use of the rotarod in drug trials. Final fall is a simple and objective measure, so five mice can be run at any given time on the rotarod, and their falls are recorded automatically on the electronic apparatus. Measuring first footfall and double spin puts a higher load on the experimenter; a maximum of two mice can be run at any given time using these more intensive measurements. If these measures provided significantly greater sensitivity for disease progression, they may still be useful despite this drawback. However, given that final fall appears to be the most sensitive test, as well as the simplest measure, the data here indicate that this would be the most attractive behavioural biomarker in any study testing disease-modifying agents.

T_2-weighted MRI demonstrated progressive signal change in the trigeminal, facial and hypoglossal nuclei in *SOD1*^{G93A} mice. This progressive T_2 MRI signal change is consistent with previous studies, demonstrating signal change either post-symptomatically, or just prior to the onset of symptoms (Angenstein et al., 2004, Zang et al., 2004, Niessen et al., 2006). However, the present study found more dramatic changes in motor nucleus VII, beginning at 60 days, 20 days earlier than previously reported, with changes at 40 days that did not reach the statistical significance threshold in this small sample size (p=0.14, effect size r = 0.75). Similarly, there was a trend to increased T_2 signal intensity in the hypoglossal nucleus at 60 days, but this was also not statistically significant (p=0.35, effect size r = 0.58). Due to the anatomical position of the hypoglossal nucleus, it often contains motion artefacts, and artefacts due to averaging with adjacent CSF (partial volume effects), which may account for the lower effect size in this region. The change seen in the facial nucleus occurs much earlier than the other nuclei, and is associated with a greater effect size at all time-points. Therefore, the facial nucleus is either more prone to pathology than the other two nuclei, or the pathological processes

are more noticeable on MRI owing to the size and shape of the nucleus, and the interaction between this and partial volume effects.

The facial nucleus has been noted by numerous studies as a focus of degenerative changes in this model, as has the trigeminal nucleus (Nimchinsky et al., 2000, Zang et al., 2004). However, some studies have not found changes in the hypoglossal nucleus (Zang et al. (2004)), and in histological examination only a trend towards loss of neurons in this nucleus was observed (Nimchinsky et al., 2000). Results in the present study corroborate reports that the hypoglossal nucleus does in fact show a robust pathological change (at least in the *SOD1*^{G93A} model) (Niessen et al., 2006), although to a lesser extent than the facial and trigeminal nuclei, as discussed above.

This data highlights the advantage of using high field MRI in detecting the earliest possible changes, as pathological changes were identified earlier here than in previous reports. Importantly, this was achieved with much shorter acquisition time (3 mins 12 seconds), compared with the 77 mins required to construct T_2 maps (Niessen et al., 2006) and the 42 minutes required to acquire the high resolution T_2 images (Zang et al., 2004). The T_2 scan acquired here had a spatial resolution of 96 x 96μm in 1mm thick slices. It seems that these longer sequences are not necessary to follow pathological changes in the brainstem, so our shorter sequence will allow for higher throughput of mice in therapeutic trials, reducing cost of pre-clinical trials or enabling acquisition of other MRI data sets for additional information on the biology of the disease. The main advantage of T_2 mapping is that it allows absolute quantification of T_2 relaxation, but the ROI-reference relative quantification method used here is effective at uncovering early pathological changes.

Previous studies using T_2 mapping in the brainstem have attributed changes in T_2 relaxation time to the appearance of water filled vacuolation of the neuropil, which increases throughout the disease process in *SOD1*^{G93A} mice (Bucher et al., 2007). If this were a simple effect of increased water load on T_2 relaxation, it would also be accompanied by a complementary change to T_1 relaxation (Brant-Zawadzki et al., 1984).

However, my data do not support this view – it is clear from this data that even at disease end-point (120 days), when there is a ~15-fold increase in T_2 signal intensity, there is no detectable change in T_1 signal intensity (see **Figure 3.9**). Therefore, either other pathological features account for the signal change, or the relationship between water load and effect on T_2 is more complex.

To probe this issue further, a separate cohort of *SOD1*^{G93A} and wild type mice underwent not only T_2-weighted imaging, but also ADC and MTR data acquisition at 120 days, when there is prominent pathological change. A decrease in ADC values was observed in all three motor nuclei, consistent with previous reports (Niessen et al., 2006), but there was also a novel observation of a decrease in MTR signal. Whilst similar changes to T_2-weighted sequences were found on ADC and MTR, in all three motor nuclei the effect size was much larger for T_2 relaxation than MTR and ADC. This is consistent with a previous comparison of T_2 and ADC (Niessen et al., 2006), and suggests that T_2 relaxation would be the leading candidate biomarker of disease progression in *SOD1*^{G93A} mice.

As well as measuring disease progression, imaging modalities may also give us insight into the specific neuropathological changes occurring. However, if we consider T_2 signal intensity to only reflect an increase in free tissue fluid, the ADC result is counterintuitive. A reduction in ADC indicates restricted tissue diffusion, which has been suggested can reflect intracellular oedema in other neuropathologies such as ischaemia and head injury (Huisman, 2003, Pasco et al., 2006). Cytotoxic oedema is typically thought of as simply a shift of extracellular to intracellular water, so one hypothesis that could explain the change in T_2 is that reduction in the water concentration in the neuropil, due to osmosis into the cell, sets up an osmotic gradient, leading to osmosis of water from adjacent areas, leading to an increase in total water.

At the same time, the MTR change indicates a reduction in the transfer of magnetization from the bound proton pool (associated with macromolecules) to free protons (mostly

from water in tissue) (Dousset et al., 1992, Gass et al., 1994). Reductions in MTR have frequently been linked with reductions in the macromolecular pool as a consequence of demyelination (Filippi et al., 1995). However, this cannot explain the source of signal change in this instance, because brainstem demyelination is not reported as being a significant pathological feature in this model, although there are a few reports of subtle changes in myelin content in the corticospinal tract (Niebroj-Dobosz et al., 2007). The changes noted here are in the cranial motor nuclei, areas of grey matter that have relatively low myelin content in wild type. Therefore it is not feasible that a change in myelin in already myelin-deprived region could explain such dramatic signal change (especially given that the sensitivity of MTR is not so high that it can delineate these nuclei in wild type mice, when the myelin content within the nucleus is very different to that outside the nucleus). On the other hand, work from our group has previously shown that such reductions in MTR can be dissociated from demyelination, and rather reflect generalised inflammatory processes (Serres et al., 2009b). These features may be intricately tied together, with the combination of morphological changes acting in tandem to cause signal change in the three MRI sequences used here. For example, vacuolation and structural changes of the neuropil due to glial activation could increase tissue tortuosity, which would affect the diffusion parameters; these structural changes would also change the proportion of free and bound protons, thereby altering MTR, and osmotic changes due to structural alterations in the tissue and disturbed ionic balance could alter the T_2 parameters. More in depth experimental paradigms would allow the influence these factors on T_2, ADC and MTR to be disambiguated, in order to tease apart this relationship.

Whilst a causative relationship remains to be demonstrated, the histological and immunohistochemistry data presented here provides evidence that other features other than changes in tissue water could affect these MRI parameters. Consistent with Bucher et al. (2007), we found vacuole change from around the time of increased T_2 signal, which increased throughout the disease in a way that was comparable to T_2 signal change,

providing some evidence that vacuolation could contribute to the signal. However, in addition to this, there was a similar change in the morphology of astrocytes and microglia, as shown by an increase in expression of GFAP and Iba1 respectively, which also starts from approximately the time of signal change on T_2 MRI, and increases as the disease develops. In fact, if we plot the T_2 data along with the quantification of vacuole change and GFAP and Iba1 expression, we can see a similar relationship between all three of these features with T_2 change (**Figure 3.19**). The correlation coefficient for the relationship with T_2 hyperintensity was comparable for the three measures (vacuolation, GFAP and Iba1), and if anything was higher (although not significantly so) for GFAP than for vacuolation. As mentioned above, correlation does not indicate a causal relationship, and experimental paradigms need to be devised to disambiguate these different pathological features. However, it highlights a flaw with the argument put forward in previous studies, that a temporal relationship between vacuole formation and T_2 signal is indicative of a causal relationship, because the same could be argued for the involvement of astrocytes and microglia.

There are no published reports of the use of Gd-DTPA as a contrast agent in *SOD1* mouse models. I found no evidence of BBB compromise, in any brain region at any time-point. This was confirmed histologically by staining for the blood serum protein IgG. Under normal conditions, IgG is present in extremely low concentrations in the CNS, but where there has been BBB breakdown, this molecule is able to leak through into the parenchyma, and an increase in staining can be detected. No increase in IgG was found in any of the *SOD1*^{G93A} mice, in any region of the CNS, at any time-point. These findings contradict previous reports of BBB breakdown (Garbuzova-Davis et al., 2007b, Zhong et al., 2008, Nicaise et al., 2009a), vascular damage (Garbuzova-Davis et al., 2007a) and tight junction protein down-regulation (Zhong et al., 2008, Miyazaki et al., 2011) in *SOD1* mice, as well as reports of Gd-DTPA leakage in the *SOD1*^{G93A} rat model (Andjus et al., 2009, Bataveljic et al., 2009). It is possible that subtler vascular changes, such as alterations in tight junctions, could be present without significantly increasing permeability

to contrast agents or larger proteins such as IgG. The discrepancy between my findings, and previous reports in the *SOD1*^{G93A} rat model could have a number of explanations. Firstly, there may be a species difference between the effect of mutant SOD1 protein in mice compared to rats. Secondly, differences in exposure to pathogens may alter the pathogenesis of the disease in different animal facilities – there is now a substantial literature illustrating that peripheral inflammation can interact with central pathology (Cunningham et al., 2005, McColl et al., 2007, Serres et al., 2009a, Bay-Richter et al., 2011). However, one thing that must be pointed out from the previous studies (e.g. Andjus et al., 2009) is that the *SOD1* Gd-DTPA images are shown without corresponding wild type images. The data clearly show increased signal around the area of the lateral ventricles. However, our data in **Figure 3.20** also show increased signal around the lateral ventricles in *SOD1*^{G93A} mice, but also in age matched wild type mice. The blood-CSF barrier has different permeability characteristics to the blood-brain barrier (Johanson et al., 2011), so it is our belief that the previous reports of “breakdown” using Gd-DTPA may, in fact, have reflected leakage through the blood-CSF-barrier and/or partial volume effects with ventricular fluid.

Whichever is the case, it is concluded that in the *SOD1*^{G93A} mouse model, housed in mostly pathogen-free conditions, there is no significant breakdown of the BBB, as evidenced by Gd-DTPA-based MRI and IgG immunohistochemistry. This finding has important implications for the disease, as understanding the state of the CNS barriers can have important consequences for drug delivery. Also, any impairment to the barriers may interact with the disease process. It is generally acknowledged that the brain is immune-privileged (Anthony et al., 2012), in that the BBB barrier prevents cells and larger/hydrophilic molecules from systemic circulation from entering the CNS unless there is a specific transport mechanism (Pardridge, 2003, Abbott et al., 2006). We do know, however, that there is some cross-talk between central and systemic inflammation, in both directions (Campbell et al., 2008, Murray et al., 2011a). For example, peripheral inflammation can activate microglia that have been primed as a result of previous central

insults, such as neurodegeneration or MS-like pathology (Cunningham et al., 2005, Serres et al., 2009a, Perry et al., 2010). This is a controlled process, which relies on normal barrier characteristics to function. A breakdown of the barrier, however, results in inflammatory molecules and cells, which are not normally able to enter the CNS (such as IgG, as mentioned above), to cross into the CNS parenchyma, thereby diminishing the privileged state of the CNS. Thus, the observation of apparently normal BBB characteristics, even at late stage disease, in the *SOD1*^{G93A} mouse may be of considerable importance. This is discussed further in the General Discussion, particularly in relation to drug treatments.

Finally, I used a novel VCAM-MPIO contrast agent in the *SOD1*^{G93A} mouse model, the first report of molecularly-targeted MRI in this mouse model. Contrary to my initial hypothesis, no significant VCAM-1 expression was found in the brain at any time point in *SOD1*^{G93A} mice, which was confirmed by immunohistochemistry. This was surprising, as VCAM-1 is typically seen as one of the crucial CAMs involved in leukocyte transport into the CNS, along with ICAM-1 and the selectins (Shimizu et al., 1991, Barten and Ruddle, 1994, Muller, 1995, Verbeek et al., 1995, Wong et al., 1999). A number of previous studies have shown that lymphocyte infiltration is an important feature of the disease (Alexianu et al., 2001), interacting with the resident glia population and influencing disease course (Chiu et al., 2008, Tada et al., 2011). If this is the case, there must be an accompanying up-regulation of CAMs to allow lymphocyte rolling, binding and diapedesis. It is surprising, therefore, that VCAM-1 does not appear to play a role in the pathogenesis of this model. The following chapter will probe these issues further. I will investigate the inflammatory conditions present in different regions of the CNS, and the vascular changes (activation of cellular adhesion molecules and tight junction protein expression) that occur in *SOD1* ALS.

To conclude, the data presented here show that ADC, MTR and T_2 allow *in vivo* monitoring of the disease process in *SOD1*^{G93A} mice, but that T_2 is the most sensitive

biomarker in this case. Additionally, there is no evidence of significant vascular changes in any region of the CNS in *SOD1*^{G93A} mice.

Chapter 4: Exploring the inflammatory environment in the *SOD1*^{G93A} mouse at multiple levels of the neuraxis

4.1 Aims of this chapter

The aim of this chapter is to follow up on the negative VCAM-1 findings presented in Chapter 3, and determine whether this is representative of the state of vascular activation generally, or whether other molecules are upregulated. In addition, given the discrepancy with some findings reported by other groups, I wanted to explore whether the reduced vascular phenotype is associated with a limited release of pro-inflammatory mediators. To address these aims, I used immunohistochemistry at 40, 60, 80, 100 and 120 days to investigate ICAM-1, E-selectin and VAP-1, to see if they are expressed higher than wild type any time point in *SOD1*^{G93A} mice. The tissue used for the immunohistochemistry in this chapter is the same tissue taken from the MRI cohort in Chapter 3. In a separate cohort of mice (5 *SOD1*^{G93A}, 5 wild type at each time point), I used quantitative real-time PCR (qRT-PCR) at 40, 60, 80, 100 and 120 days to investigate the transcriptional regulation of salient pro-inflammatory cytokines and chemokines (IL-1β, TNF-α, IFN-γ, CXCL-10), to compare these to the protein regulation for the adhesion molecules. These cytokines were chosen specifically because IL-1β and TNF-α are the most commonly reported pro-inflammatory cytokines, which are upregulated in neuronal inflammation; IFN-γ similarly has been implicated in a wide array of damaging stimuli (degeneration, viral infection etc.); and finally CXCL-10 has been suggested to be an important chemokine involved in leukocyte homing to sites of injury. Importantly for this thesis, all of these markers have been highlighted by previous studies into ALS, although their involvement is still contentious.

4.2 Introduction

Cytokines and chemokines (chemotactic cytokines) are cell signalling molecules, that are involved in aspects of immunity and development. As such, many of these molecules have been highlighted as having particular roles in degenerative disease.

Interleukin-1β (IL-1β) is a pro-inflammatory cytokine, primarily produced by classically activated (M1) macrophages (Xing et al., 1994), including microglia in the brain (Chao et al., 1992, Lee et al., 1993). This cytokine is produced in a precursor form (pro-IL-1β), and is cleaved to the active protein by caspase-1 (Thornberry et al., 1992). IL-1β is one of the most potent mediators of inflammation (Dinarello, 2009), and has roles in both lymphocyte proliferation (Gery et al., 1972, Gery and Waksman, 1972) and activation of endothelial cells, by upregulating the expression of cellular adhesion molecules (CAMs) on the vasculature, including VCAM-1, ICAM-1 and E-selectin (Wyble et al., 1996, Wang et al., 2005a). The latter is an important process for recruiting leukocyte populations to sites of injury (Carlos and Harlan, 1994, Carlos et al., 1997). IL-1β also has a role in developmental processes such as cellular differentiation (Lasiglie et al., 2011) and in apoptosis, through interactions with caspase-1, (Nesic et al., 2001, Fortunato and Menon, 2003). IL-1β has been implicated in many diseases of the CNS, including stroke (Davies et al., 1999) and degenerative disease (Mogi et al., 1994, Lanzrein et al., 1998).

A number of strands of evidence implicate IL-1β in the pathogenesis of ALS. Research using various *SOD1* strains has shown an upregulation of IL-1β post-symptomatically (Gowing et al., 2009, Fang et al., 2010), but there does not appear to be significantly different expression at earlier, pre-symptomatic time points in *SOD1*^{G93A} mice or rats (Fang et al., 2010, Berger et al., 2011). One study compared cervical and lumbar expression of IL-1β, and found increased expression in both regions from around 100 days (early post-symptomatic), with no substantial difference in relative expression between the two spinal cord regions (other than a small increase in the lumbar cord at 98 days) (Beers et al., 2011). This evidence of involvement of IL-1β in ALS is corroborated

by *in vitro* evidence showing an upregulation of caspase-1 (involved in production of mature IL-1β as described above) and IL-1β in neuroblastoma cells carrying a *SOD1* mutation (Pasinelli et al., 1998). This may, at least in part, be due to the effect of mutant SOD1 protein, as this has been shown to activate microglia, increasing the concentration of caspase-1, and, therefore, mature IL-1β (Meissner et al., 2010). One study, treating *SOD1*^{G37R} mice with macrophage colony stimulating factor (M-CSF), found elevated levels of IL-1β and TNF-α, which exacerbated the disease.

A number of attempts have been made to manipulate IL-1β to ameliorate the disease. Administration of zVAD-fmk, a pan-caspase inhibitor, delayed disease onset and prolonged survival in *SOD1*^{G93A} (Li et al., 2000). Similarly, *SOD1*^{G93A} mice crossed either with mice with a caspase-1 inhibitor under a neuron-specific promoter, or with caspase-1 or IL-1β knockout mice, did not alter disease onset, but prolonged survival (Friedlander et al., 1997, Meissner et al., 2010). These findings suggest that the mechanism of the effect of caspase-1 is mediated through IL-1β function. However, such mice still develop the disease and die, albeit at a slower pace, so IL-1β is clearly not essential for the development of the disease, just a modulating factor.

Not all the evidence is consistent with the studies cited above. Crossing *SOD1*^{G37R} mice onto an IL-1β$^{-/-}$ background had no effect no effect on the disease in one study (Nguyen et al., 2001). Also, mature IL-1β production is regulated by caspase-11 as well as caspase-1, and a second study found that crossing *SOD1*^{G93A} mice with *caspase-11*$^{-/-}$ mice inhibited caspase-1 and caspase-3, and was associated reduced IL-1β production, but crucially this did not alter disease progression (Kang et al., 2003). It is unclear at present what the cause of this discrepancy is, but one factor may be the different *SOD1* mutations and background strains used in the different studies. Nonetheless, it seems safe to conclude that IL-1β is upregulated, at least in some cases, in *SOD1* mice, and that this may have a modulatory, although perhaps not necessary, role in ALS pathogenesis.

TNF-α is another important cytokine involved in inflammatory mechanisms. It is produced primarily by macrophages (Myers et al., 1989), but can also be produced by other immune cells such as T lymphocytes (Wallays and Ceuppens, 1993, Xia et al., 1993). In addition to being produced by macrophages, it can act on macrophages, influencing macrophage phenotype and impacting on differentiation (Riches et al., 1996). TNF-α has pro-inflammatory effects on a number of cell types by binding to one of two receptors: TNF-R1 and TNF-R2. After ligand binding, the receptors form trimers, leading to a conformational change resulting in loss of the inhibitory protein SODD, and binding of the adaptor protein TRADD with the death domain. This can activate three pathways: a pro-inflammatory pathway, caused by activation of NF-κB; the MAPK pathway, involved in cell proliferation and differentiation; and a death pathway involving the caspase family and eventual apoptosis.

A number of observations suggest that TNF-α may play an important role in ALS. Firstly, TNF-α and its receptor are upregulated in the CSF and serum of ALS patients (Poloni et al., 2000, Moreau et al., 2005, Babu et al., 2008, Cereda et al., 2008), and TNF-α has also been found to be expressed at a higher level in ALS, compared with control subject peripheral blood mononuclear cells exposed to aggregated SOD1 protein (Liu et al., 2012). Work in the *SOD1*^{G93A} mouse model has shown an involvement of TNF-α from late pre-symptomatic time points (~75 days onwards), which appears to be driven by microglial production, as well as upregulation of the TNF-receptor (TNFR) (Hensley et al., 2002, Yoshihara et al., 2002). Beers et al. (2011), on the other hand, only found a difference in TNF-α expression between *SOD1* and control mice post-symptom onset, with elevated expression in both the lumbar and cervical cord from around 100 days of age, increasing with the development of the disease, and mostly similar expression in the cervical and lumbar regions at all time points. Induction of pro-inflammatory cytokines, including TNF-α, has also been shown pre-symptomatically in *SOD1*^{G37R} mice and slowly progressing *SOD1*^{G93A} strains (Elliott, 2001, Nguyen et al., 2001), providing evidence that TNF-α may be an important cytokine in ALS pathogenesis.

TNF-α binding triggers a number of converging intracellular pathways, one of which involves 5-lipooxygenase (5-LOX). This enzyme oxidizes arachidonate, in the first of a series of reactions ending in production of leukotrienes, causing upregulation of pro-inflammatory transcripts (Funk, 2001, Haeggstrom and Wetterholm, 2002). Consistent with the findings above, of increased TNF-α expression in the spinal cord, increased levels of 5-LOX were found at 120 days in *SOD1*^{G93A} mice, and inhibition of 5-LOX was found to ameliorate the TNF-induced activation of microglia, and extend survival (West et al., 2004). Using a related but different approach, another study (Liu et al., 2012) found that administration of resolvin D_1 , which is a metabolite of ω-3-polyunsaturated fatty acids (docosahexaenoic acid, eicosapentaenoic acid) that has anti-inflammatory properties (Titos et al., 2011), ameliorated the increase in TNF-α expression in macrophage cell cultures from ALS patients activated with aggregated SOD1 protein. Thalidomide has also been used as an immunosuppressant, and despite the controversy over its use, still has therapeutic value due to varied effects on cytokine pathways, including inhibition of TNF-α, IL-6 and IL-12 (Moreira et al., 1993, Moller et al., 1997, Corral et al., 1999, Chaulet et al., 2011). Thalidomide and its analogue, lenalomide, appeared promising as a treatment of ALS in preclinical trials in *SOD1*^{G93A} mice. These compounds reduced TNF-α expression in the spinal cord, reduced motor neuron loss, and increased survival when administered either 2 months prior to the onset of symptoms (Kiaei et al., 2006), or after symptom onset (Neymotin et al., 2009). However, thalidomide was found to be unsuccessful in phase II clinical trials (Stommel et al., 2009).

Interferons are a class of cytokines that “interfere” with viral replication and, therefore, have a role in anti-viral host defence. There are two main types of interferon, and Interferon-γ (IFN-γ) is the only member of class II interferons (Pestka et al., 1987). Like many other cytokines, IFN-γ can be produced by many different cell types, but is most associated with natural killer cells (Martin-Fontecha et al., 2004), lymphocytes (Yoshimoto et al., 1998) and, perhaps more controversially, macrophages and dendritic cells (Frucht et al., 2001). IFN-γ exerts its action by binding to the IFN-γ receptor, which

is a heterodimer comprising IFNGR1 and IFNGR2 units, and which signals through members of the Janus activated kinase (JAK) and signal transducer and activator of transcription (STAT) family to upregulate expression of specific genes (Platanias, 2005).

Literature on the involvement of IFN-γ in ALS is very sparse, but two conflicting human studies exist: one study found no elevation of IFN-γ in CSF of ALS patients (Holmoy et al., 2006), but a subsequent report found IFN-γ levels to be elevated in the CSF of ALS patients (Babu et al., 2008). In accordance with the first report, a study investigating protein expression of a number of cytokines by Western blot found no evidence of IFN-γ upregulation in *SOD1*^{G93A} mice (Elliott, 2001). Similarly, a further study in *SOD1* mice found only a marginal elevation at 120 days compared with wild type, and no elevation compared with wild type *SOD1* overexpressing mice (Hensley et al., 2002). Evidence from cell culture shows that co-culture of neuroblastoma and glioblastoma cells carrying mutations in *SOD1* increases IFN-γ release from astrocytes (Ferri et al., 2004). However, it is unclear whether astrocytes would produce IFN-γ *in vivo* in this context. Also, no evidence was found for upregulation of IFN-γ in SOD1 microglia, either at rest or after activation, in a cell culture model (Sargsyan et al., 2009).

CXCL-10 is also known as IFN-γ-induced protein-10 (IP-10), and, in keeping with its name, it is typically thought to be induced by IFN-γ (Ohmori and Hamilton, 1993). However, given that CXCL-10 expression is NF-κB-dependent (Hiroi and Ohmori, 2003, Williams et al., 2009), it seems likely that it is also induced by other pro-inflammatory mediators such as IL-1β and TNF-α, which is supported by findings in cell culture (Yeruva et al., 2008). As well as having an important role in chemoattraction for various cell types, including neutrophils and T cells (Michalec et al., 2002, Klein, 2004), CXCL-10 has also been shown to have neurotoxic properties, possibly mediated though apoptotic pathways (Sui et al., 2004, Sui et al., 2006).

CXCL-10 has been shown to be upregulated in the CSF of ALS patients compared with other non-inflammatory neurological disease control patients, although interestingly

higher levels of CXCL-10 expression seemed to be associated with better prognosis (Tateishi et al., 2010b). Thus, it is possible that this increase in CXCL-10 is due to a compensatory, neuroprotective role rather than a neurotoxic one. However, another study failed to find any change in CXCL-10 levels in CSF or serum of ALS patients (Kuhle et al., 2009). Preclinical work has shown that *SOD1*^{G93A} mice have CXCL-10-positive clusters in the spinal cord, but not the sensorimotor cortex at 120 days (Israelsson et al., 2010). Also, using an in-depth, transcriptional analysis another study showed the importance in the co-stimulatory pathway, including CXCL-10, in the brain, spinal cord and peripheral nerves from around symptom onset in *SOD1*^{G93A} mice (Lincecum et al., 2010). However, it is unclear from these data what the relative contribution is of cells from the brainstem and sensorimotor cortex in terms of CXCL-10 production. Therefore, despite its apparent involvement in ALS, little is known about the spatiotemporal distribution of CXCL-10 expression.

The main issue emerging from the data concerning the role of cytokines in ALS, is that they are still surprisingly limited and lacking in regional, and temporal, detail. Whilst there is one report of a comparison of different CNS regions, with cervical and lumbar cord analysed (Beers et al., 2011), almost all other studies focus solely on the lumbar cord. Similarly, most studies use very few time points, or use multiple time points only after the onset of symptoms, so our understanding of how these cytokines are expressed throughout the disease, in different parts of the spinal cord is very basic.

The physiological consequences of cytokine release in the CNS are varied, but one important effect is activation of endothelial cells. Cytokines, including IL-1β, TNF-α and IFN-γ, bind to their respective receptors on endothelial cells, and, through a series of signalling mechanisms, result in the upregulation of CAMs. These CAMs are central to leukocyte adhesion and diapedesis into the CNS. IL-1β and TNF-α have both been shown to increase protein expression of VCAM-1, ICAM-1 and E-selectin, three of the most intensively-studied CAMs with regards to leukocyte trafficking (Springer, 1990, Wyble et

al., 1996, Zhou et al., 2005, Dong et al., 2011). In addition, IFN-γ increases the expression of ICAM-1 on endothelial cells, although it appears to have less of an effect on VCAM-1 and E-selectin expression than the other cytokines (Thornhill and Haskard, 1990). Vascular adhesion protein-1 (VAP-1) is an interesting adhesion molecule, with both adhesion and enzymatic functions (Salmi and Jalkanen, 2001). Like many other CAMs, VAP-1 has an important role in leukocyte trafficking, and has been noted to be up-regulated in many inflamed tissues, including skin (Arvilommi et al., 1996), liver (McNab et al., 1996) and synovial vessels (Salmi et al., 1997). The VAP-1 protein is also induced on tumour endothelium outside of the CNS (Yoong et al., 1998), and our group has recently demonstrated that it is upregulated on the CNS endothelium in the vicinity of brain tumours. However, very little is known about the regulation of VAP-1 in the CNS, and indeed the involvement of VAP-1 in diseases of the CNS.

As discussed in Chapter 3, there are no data in the literature concerning either VCAM-1 levels, or the involvement of VAP-1 in ALS. There is also a lack of data regarding membrane-bound E-selectin levels, although a human study has suggested that levels of soluble selectin proteins are increased in ALS patients (Ikeda et al., 2000). However, this finding was not replicated by a subsequent study (Rentzos et al., 2005). Using *SOD1* mouse models, other studies have shown increased expression of ICAM-1 and melanoma CAM (MelCAM) in the disease (Alexianu et al., 2001, Garbuzova-Davis et al., 2007b, Zhong et al., 2008). However, again, the time course of ICAM-1 regulation is unclear: one study identified ICAM-1 up-regulation as an early disease feature, around 40 days of age in the *SOD1*^{G93A} mouse (Alexianu et al., 2001), and suggested that this may be driven by expression on microglia rather than endothelial cells; in contrast, a more recent study suggested that ICAM-1 upregulation occurs late in the disease, after the onset of symptoms (Zhong et al., 2008).

In this chapter I aim to shed light on some of these discrepancies in the literature, and provide a more complete picture of cytokine and CAM expression in different regions of the CNS, throughout the lifespan of *SOD1*^{G93A} mice.

4.3 Methods

4.3.1 Experimental groups

For immunohistochemistry, the same tissue was used as for the MRI in Chapter 3 (4 *SOD1*^{G93A} and 4 wild type mice per time point), with analysis carried out at 40, 60, 80, 100 and 120 days. For qRT-PCR, a separate cohort of mice was used, with 5 *SOD1*^{G93A} and 5 wild type mice at each time point, at 40, 60, 80, 100 and 120 days.

4.3.2 Behavioural testing

All wild type and *SOD1* mice were tested using the rotarod apparatus as described in 2.4.3. The data for the two groups of mice (those from Chapter 3 and those used for qRT-PCR from this chapter), have been pooled for increased sample size, and have been discussed in 3.4.1.

4.3.3 Quantitative real-time PCR (qRT-PCR)

The specific protocol for quantitative real-time PCR (qRT-PCR) is provided in 2.6. Briefly, brains were dissected to retrieve the sensorimotor cortex, brainstem, cervical spinal cord and lumbar spinal cord. RNA was extracted from the tissue using the RNeasy mini kit (Qiagen), and then converted to cDNA using Superscript III (Invitrogen).

For IL-1β and TNF-α, a primer probe mix from Primer Design was used. For IFN-γ and CXCL-10, primers were designed using the assay design centre from Roche diagnostics, with appropriate probes from the Roche Universal Probe Library. The mouse GAPDH control gene probe/primer mix from Primer Design was used for normalization of input cDNA concentration. For all probes and primers, the Roche mastermix system was used, using an LC480 PCR machine. Primers and probes for the relevant genes are given in 2.6.3. Cycle numbers for PCR for each sample were normalized to GAPDH expression in Microsoft Excel.

4.3.4 Immunohistochemistry

Tissue was prepared for immunohistochemistry as described in 2.5.3 and 3.3.5. The basic immunohistochemistry protocol is given in 2.5.5, as are the antibody details. I stained for ICAM-1, VAP-1 and E-selectin. Analysis was performed as described in 3.3.7.

4.3.5 Positive control tissue

Mice were injected into the left striatum with IL-1β to create positive control tissue for inflammatory immunohistochemistry. Details of this are given in 3.3.6.

4.3.6 Statistical analysis

All statistical analysis was carried out using SPSS. For qRT-PCR analysis, non-parametric analysis was used, because of the inherent non-normally distributed nature of the data. Kruskall Wallis was used for an ANOVA-type analysis, and paired comparisons using Mann-whitney U test. For analysis of the immunohistochemistry images, parametric analysis was performed, using a two-way ANOVA, and paired comparisons using Hulm-Bonferroni-corrected t-tests. Data is presented as mean and standard error of the mean (including error bars).

4.4 Results

4.4.1 qRT-PCR for IL-1β

In the sensorimotor cortex, no significant difference was found between the amount of IL-1β transcript in *SOD1*^{G93A} and wild type littermates at any time point ($p>0.05$) (see **Figure 4.1**A).

However, in the brainstem, expression of IL-1β was significantly higher in *SOD1*^{G93A} than control mice ($p<0.05$); using pairwise *post-hoc* comparisons, at 100 days, the level of IL-1β expression was approximately 75% higher than for wild type, although this did not quite reach significance ($p=0.056$), whilst at 120 days IL-1β expression was approximately 367% higher in *SOD1*^{G93A} than wild type control mice ($p<0.01$) (see **Figure 4.1**B).

An increase in the expression of IL-1β was found in the cervical spinal cord in *SOD1*^{G93A} mice compared with wild type littermate controls ($p<0.01$); pairwise *post-hoc* comparisons revealed that at 100 days of age, the expression of IL-1β was 385% higher in *SOD1*^{G93A} compared with wild type mice ($p<0.01$), with an even more pronounced 1079% increase in IL-1β expression at 120 days ($p<0.01$) (see **Figure 4.1**C).

Increased expression of IL-1β was also evident in the lumbar region of the spinal cord in *SOD1*^{G93A} mice compared with wild type mice ($p<0.01$); IL-1β expression was 122% higher in *SOD1*^{G93A} cervical spinal cord at 100 days ($p<0.05$) and 563% greater in *SOD1*^{G93A} mice compared with wild type mice at 120 days ($p<0.01$), after the onset of motor symptoms (see **Figure 4.1**D).

No pre-symptomatic increases in the expression of IL-1β were found in any of the regions of the CNS ($p>0.05$).

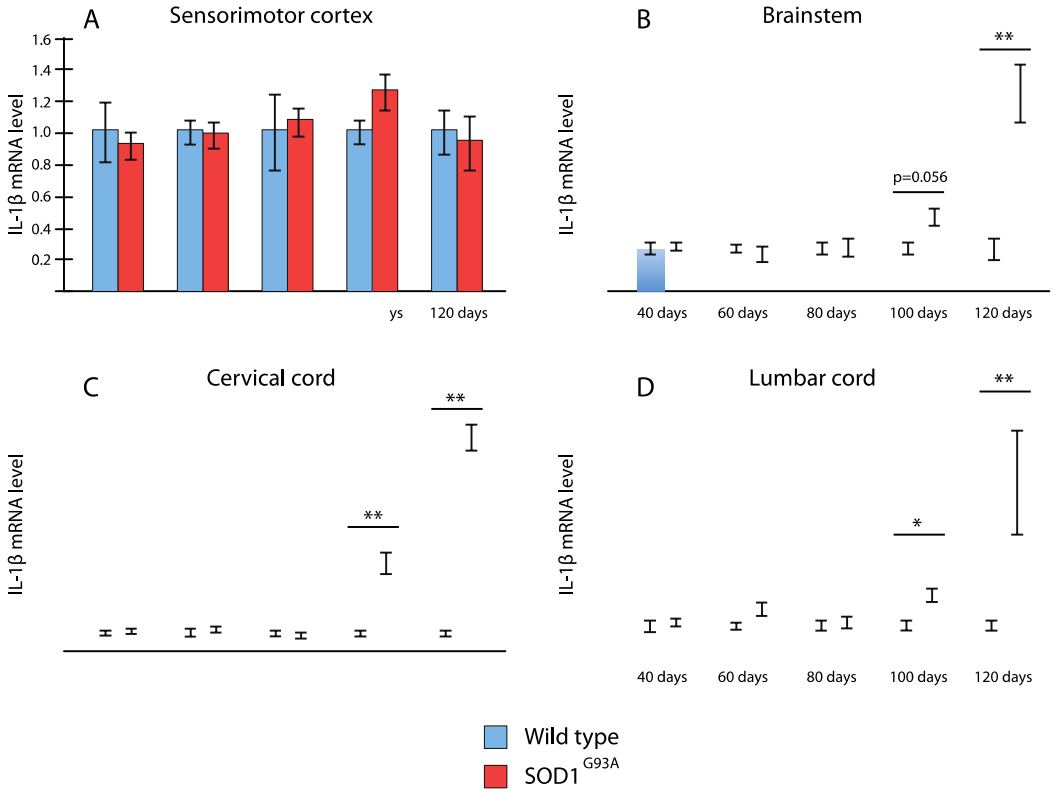


Figure 4.1 – IL-1β expression in the sensorimotor cortex, brainstem, cervical spinal cord and lumbar spinal cord in *SOD1*^{G93A} and wild type control mice

IL-1β expression in the sensorimotor cortex was not significantly different between *SOD1*^{G93A} and wild type control mice (A). However, IL-1β expression was higher for *SOD1*^{G93A} than for wild type in the brainstem (B) cervical spinal cord (C) and lumbar spinal cord (D) post-symptomatically, at both 100 and 120 days. Data is mean ± standard error of mean.

N = 5 mice in each group

* $p<0.05$, ** $p<0.01$

4.4.2 qRT-PCR of TNF-α

No significant difference was found in TNF-α expression in the sensorimotor cortex between *SOD1*^{G93A} mice and wild type littermate controls at any time point during the disease process ($p>0.05$) (see **Figure 4.2**A).

However, a significant increase in the expression level of TNF-α was found in *SOD1*^{G93A} compared with wild type control mice in the brainstem region ($p<0.05$). Pairwise *post-hoc* comparisons revealed that the only one time point showed a significant increase in *SOD1*^{G93A} compared to wild type (120 days, $p<0.01$), where a 465% increase in TNF-α expression was found (**Figure 4.2**B).

A more pronounced effect was found in the spinal cord. Within the cervical spinal cord region, a significant increase in TNF-α expression was seen in *SOD1*^{G93A} mice compared with wild type littermate controls ($p<0.01$). No significant difference was found at 40 or 60 days ($p>0.05$), but at 80 days TNF-α expression was 79% higher in the cervical cord of *SOD1*^{G93A} mice than wild type controls ($p<0.05$). This increase in TNF-α continued as the disease progressed, with a 274% increase at 100 days ($p<0.01$) and a 1370% increase at 120 days ($p<0.01$) (see **Figure 4.2**C).

In the lumbar spinal cord, a significant increase was also found in TNF-α expression in *SOD1*^{G93A} mice compared with controls ($p<0.01$). Pairwise *post-hoc* tests showed no significant differences between genotypes at 40 or 60 days of age ($p>0.05$). However, TNF-α expression was 71% higher in the lumbar spinal cord for *SOD1*^{G93A} mice compared with controls at 80 days ($p<0.05$), and again, continued to increase as the disease progressed, showing a 175% increase at 100 days ($p<0.01$), and a 1176% increase over wild type mice at 120 days ($p<0.01$) (see **Figure 4.2**D).

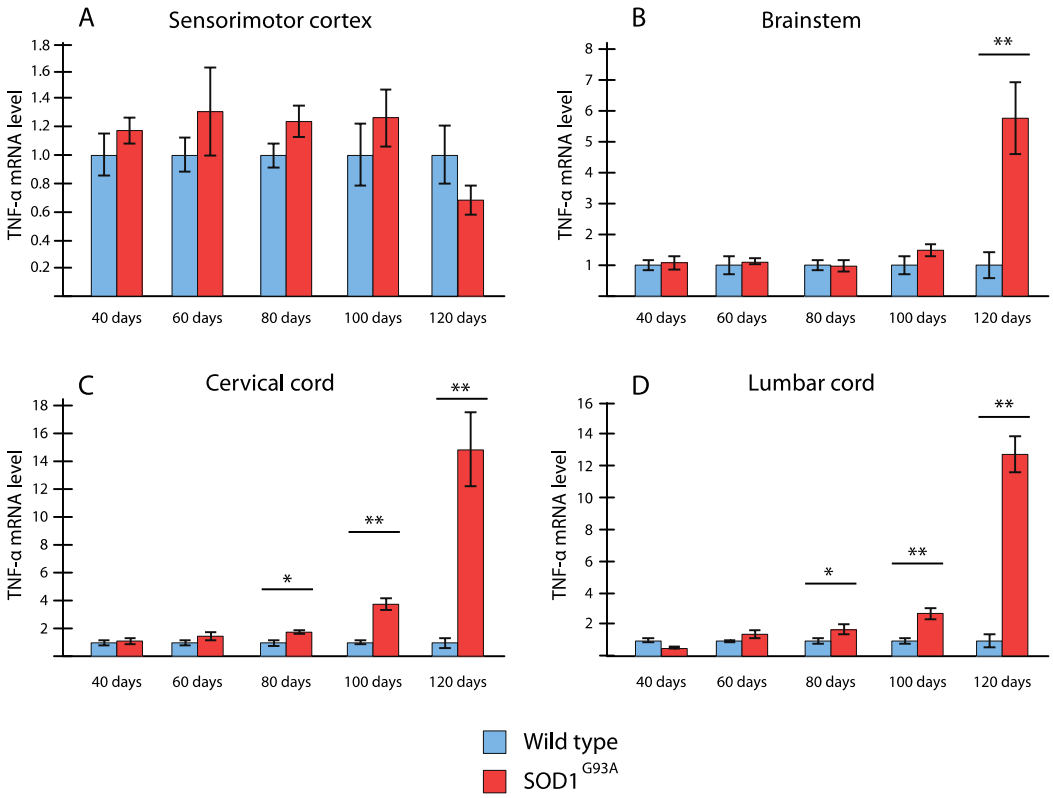


Figure 4.2 – TNF-α expression in the sensorimotor cortex, brainstem, cervical spinal cord and lumbar spinal cord in *SOD1*^{G93A} and wild type control mice

TNF-α expression in the sensorimotor cortex was not significantly different between *SOD1*^{G93A} and wild type control mice (A). However, TNF-α expression was higher for *SOD1*^{G93A} than for wild type in the brainstem (B) at 120 days, and both the cervical spinal cord (C) and lumbar spinal cord (D) from 80 – 120 days. Data is mean ± standard error of mean.

N = 5 mice in each group

* $p<0.05$, ** $p<0.01$

4.4.3 qRT-PCR for IFN-γ

No significant difference was found in the expression level of IFN-γ between *SOD1*^{G93A} mice, in the sensorimotor cortex, brainstem, cervical spinal cord or lumbar spinal cord, at any time point of the disease ($p>0.05$) (see **Figure 4.3**). In the cervical cord, there was a trend to higher expression of IFN-γ in *SOD1*^{G93A} compared with wild type mice throughout the disease, but this was not significant at any time point ($p>0.05$).

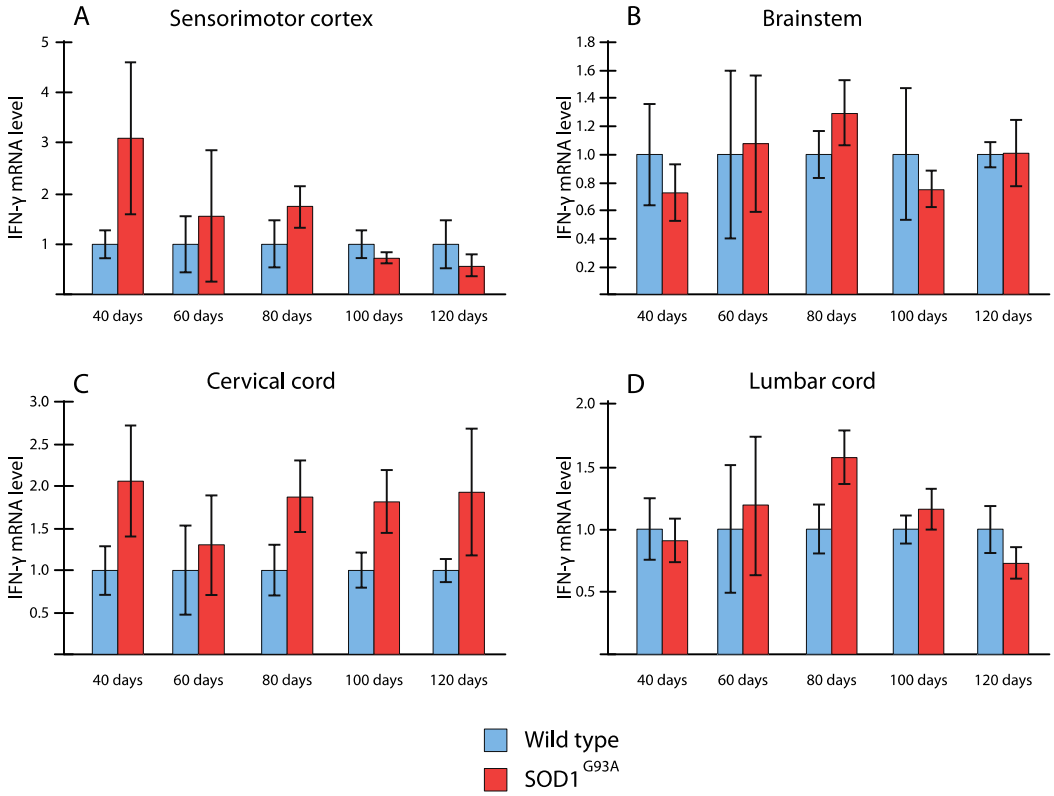


Figure 4.3 – IFN-γ expression in the sensorimotor cortex, brainstem, cervical spinal cord and lumbar spinal cord in *SOD1*^{G93A} and wild type control mice

The level of expression of IFN-γ did not differ significantly between *SOD1*^{G93A} and wild type control mice at any time point, in the sensorimotor cortex (A), brainstem (B), cervical spinal cord (C) or lumbar spinal cord (D). Data is mean ± standard error of mean.

N = 5 mice in each group

4.4.4 qRT-PCRT for CXCL-10

No significant difference was found in the expression of CXCL-10 in the sensorimotor cortex between *SOD1*^{G93A} and wild type littermates at any point in the disease process ($p>0.05$). There was a higher mean expression at 60 days in *SOD1*^{G93A} mice, but this was driven by two outliers, and did not reach significance (see **Figure 4.4**A).

In the brainstem, however, an increase in CXCL-10 expression was seen in *SOD1*^{G93A} compared with wild type mice ($p<0.01$). CXCL-10 expression appeared to be higher in *SOD1*^{G93A} than wild type mice at 60 days, although this was not significant ($p>0.05$), whilst significantly elevated expression was found at 100 and 120 days ($p<0.01$) (see **Figure 4.4**B).

Similarly, CXCL-10 expression in the cervical region of the spinal cord was significantly higher in *SOD1*^{G93A} than wild type mice ($p<0.01$), with significantly elevated mRNA levels at 60 days ($p<0.05$), 100 days ($p<0.01$) and 120 days ($p<0.05$), shown using pairwise *post-hoc* tests, and a trend to higher CXCL-10 in *SOD1*^{G93A} at 80 days compared with wild type mice ($p=0.095$), (see **Figure 4.4**C).

Expression of CXCL-10 was also increased in the lumbar spinal cord of *SOD1*^{G93A} mice compared with wild type littermates ($p<0.01$), with significant expression at 60 days ($p<0.05$), 80 days ($p<0.05$), 100 days ($p<0.05$) and 120 days ($p<0.05$) of age (see **Figure 4.4**D).

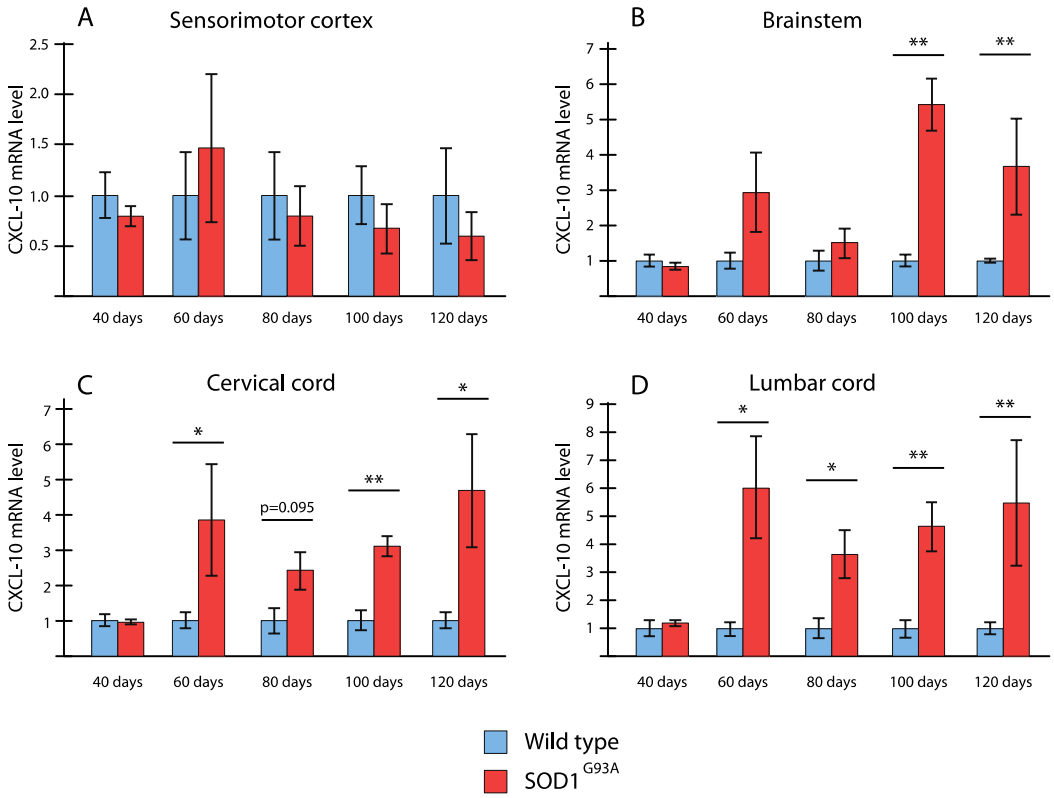


Figure 4.4 – CXCL-10 expression in the sensorimotor cortex, brainstem, cervical spinal cord and lumbar spinal cord in *SOD1^{G93A}* and wild type control mice

CXCL-10 expression in the sensorimotor cortex was not significantly different between *SOD1^{G93A}* and wild type control mice at any time point (A). However, CXCL-10 expression was higher for *SOD1^{G93A}* than for wild type in the brainstem (B) at 100 and 120 days, and both the cervical spinal cord (C) and lumbar spinal cord (D) from 60 – 120 days. Data is mean ± standard error of mean.

N = 5 mice in each group

* p<0.05, ** p<0.01

4.4.5 ICAM-1 immunohistochemistry

Significant upregulation of ICAM-1 was seen in all three cranial motor nuclei of *SOD1*^{G93A} mice ($p<0.05$). In the trigeminal nucleus (**Figure 4.5**, top row; **Figure 4.7**B), a bimodal pattern of ICAM-1 expression was evident, with significant expression at 60 days, and then again at 100 and 120 days ($p<0.05$). The same was true of the facial nucleus (**Figure 4.5**, middle row; **Figure 4.7**C), with significant ICAM-1 expression at 60 days ($p<0.05$), and also later at 100 ($p<0.05$) and 120 days ($p<0.01$). Similarly in the hypoglossal nucleus (**Figure 4.5**, bottom row; **Figure 4.7**D), a pre-symptomatic upregulation of ICAM-1 was seen at 60 days, which approached significance ($p=0.060$), with a significant upregulation post-symptomatically at 120 days ($p<0.05$).

A similar bi-modal expression pattern was also observed in the spinal cord. For the cervical spinal cord (**Figure 4.6**, top row; **Figure 4.7**E), significantly higher ICAM-1 expression was evident in *SOD1*^{G93A} mice compared with wild type at 60 days ($p<0.05$), with even higher expression at 120 days ($p<0.01$). In the lumbar region (**Figure 4.6** middle row, **Figure 4.7**F), higher expression was also seen in *SOD1*^{G93A} mice compared with wild type mice at 60 days ($p<0.05$), and an earlier and more protracted upregulation post-symptomatically compared with the cervical cord, which was significant at both 100 and 120 days ($p<0.01$).

In contrast, ICAM-1 expression did not differ between *SOD1*^{G93A} and wild type mice in the sensorimotor cortex **Figure 4.6** bottom row, **Figure 4.7**A), at any point of the disease studied here ($p>0.05$).

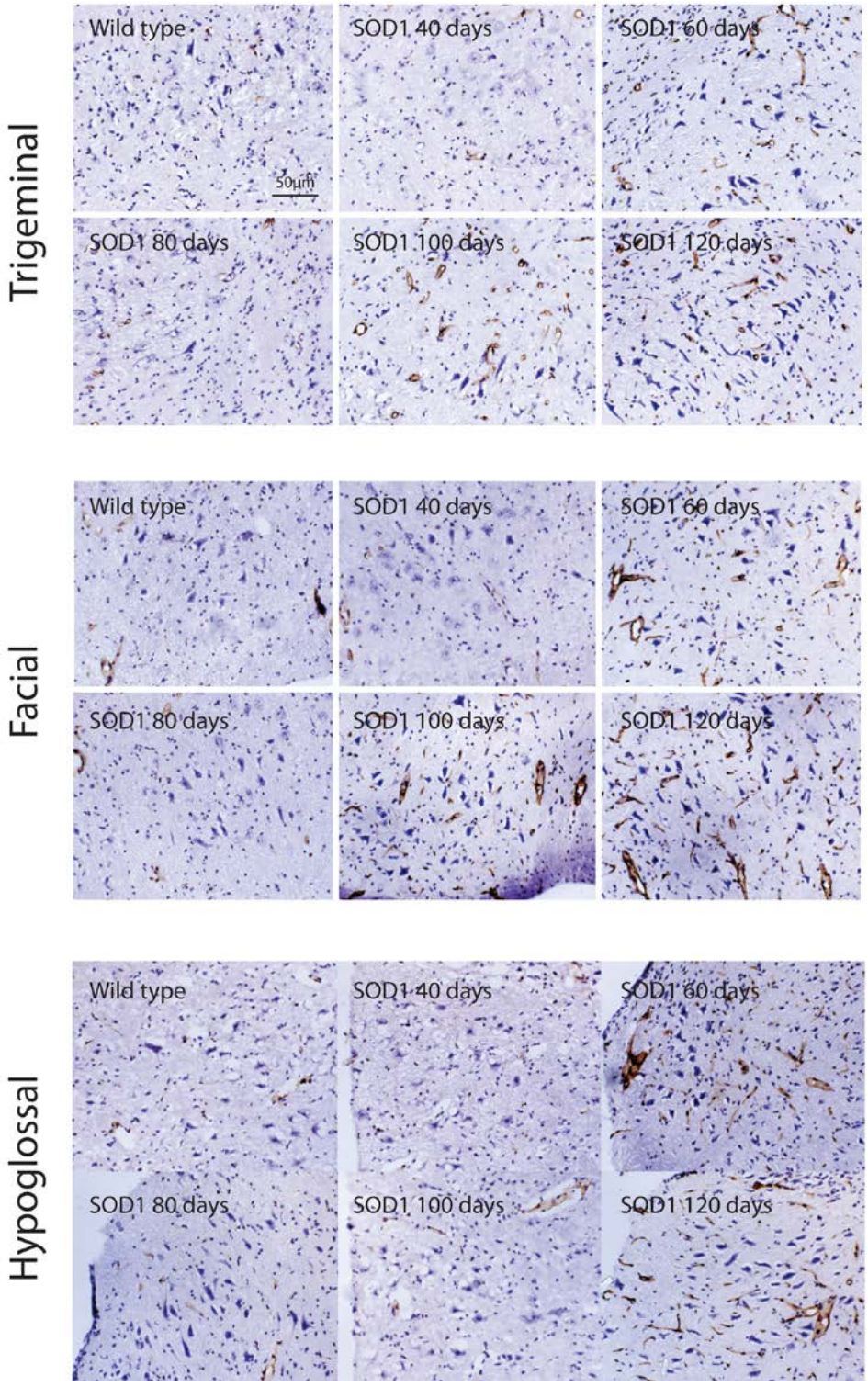


Figure 4.5 – Representative images of ICAM-1 immunohistochemistry in the trigeminal, facial and hypoglossal nuclei in *SOD1*^{G93A} and wild type mice

In the trigeminal (top row) and facial (middle row) nuclei, higher ICAM-1 expression was seen in *SOD1*^{G93A} compared with wild type controls at 60, 100 and 120 days of age. In the hypoglossal nucleus, production of ICAM-1 was also higher in *SOD1*^{G93A} mice at 60 and 120 days, but no significant difference compared with wild type littermate controls at 100 days.

N = 4 mice per group. Scale bar is representative of all images.

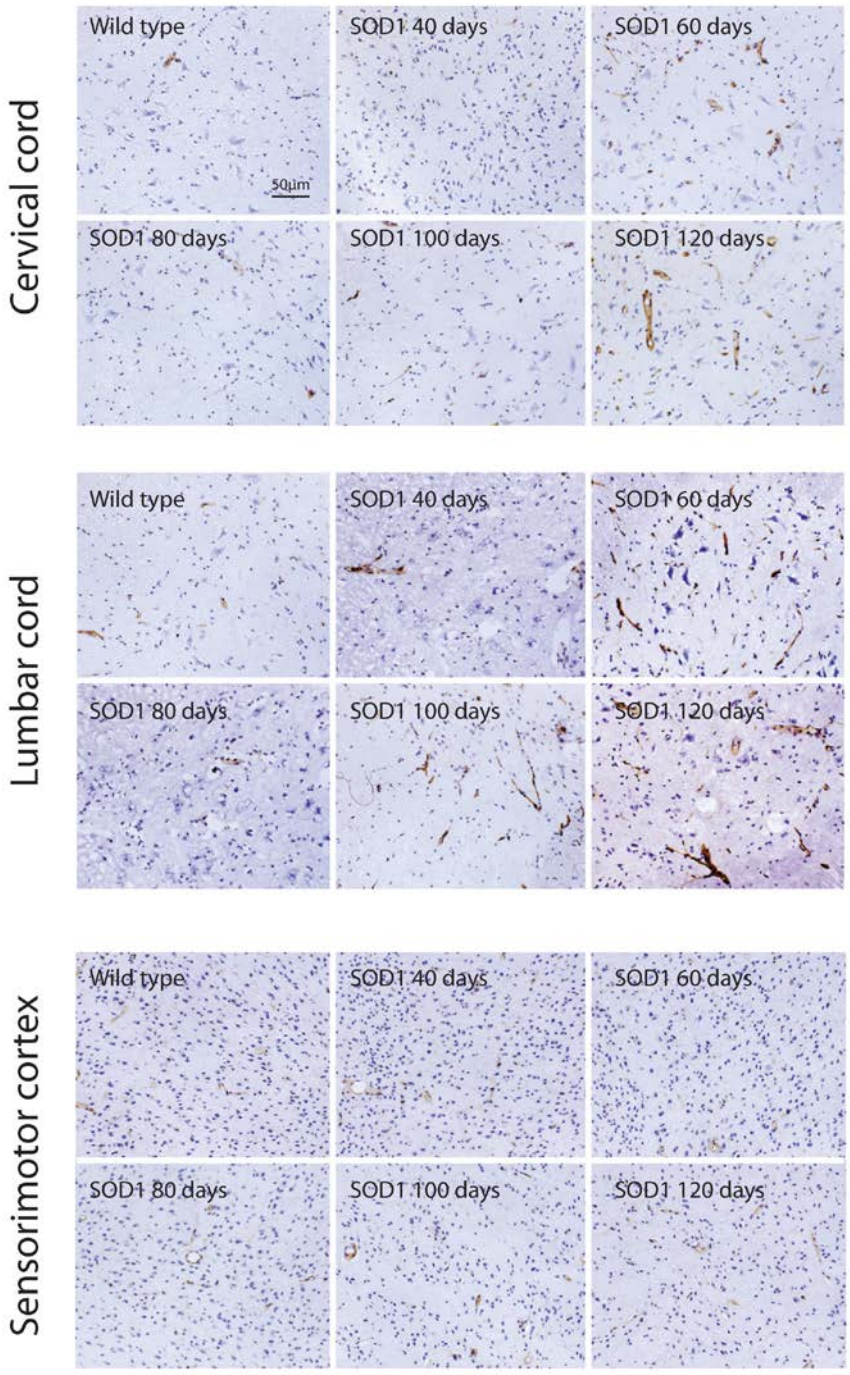


Figure 4.6 – Representative images of ICAM-1 immunohistochemistry in the cervical and lumbar spinal cord and sensorimotor cortex in *SOD1*^{G93A} and wild type mice

Higher expression of ICAM-1 was evident in *SOD1*^{G93A} mice compared with wild type controls at 60 and 120 days in the cervical spinal cord (top row) and at 60, 100 and 120 days in the lumbar region (middle row). However, no difference was found in the staining pattern for ICAM-1 in the sensorimotor cortex at any time point.

N = 4 mice per group. Scale bar is representative of all images.

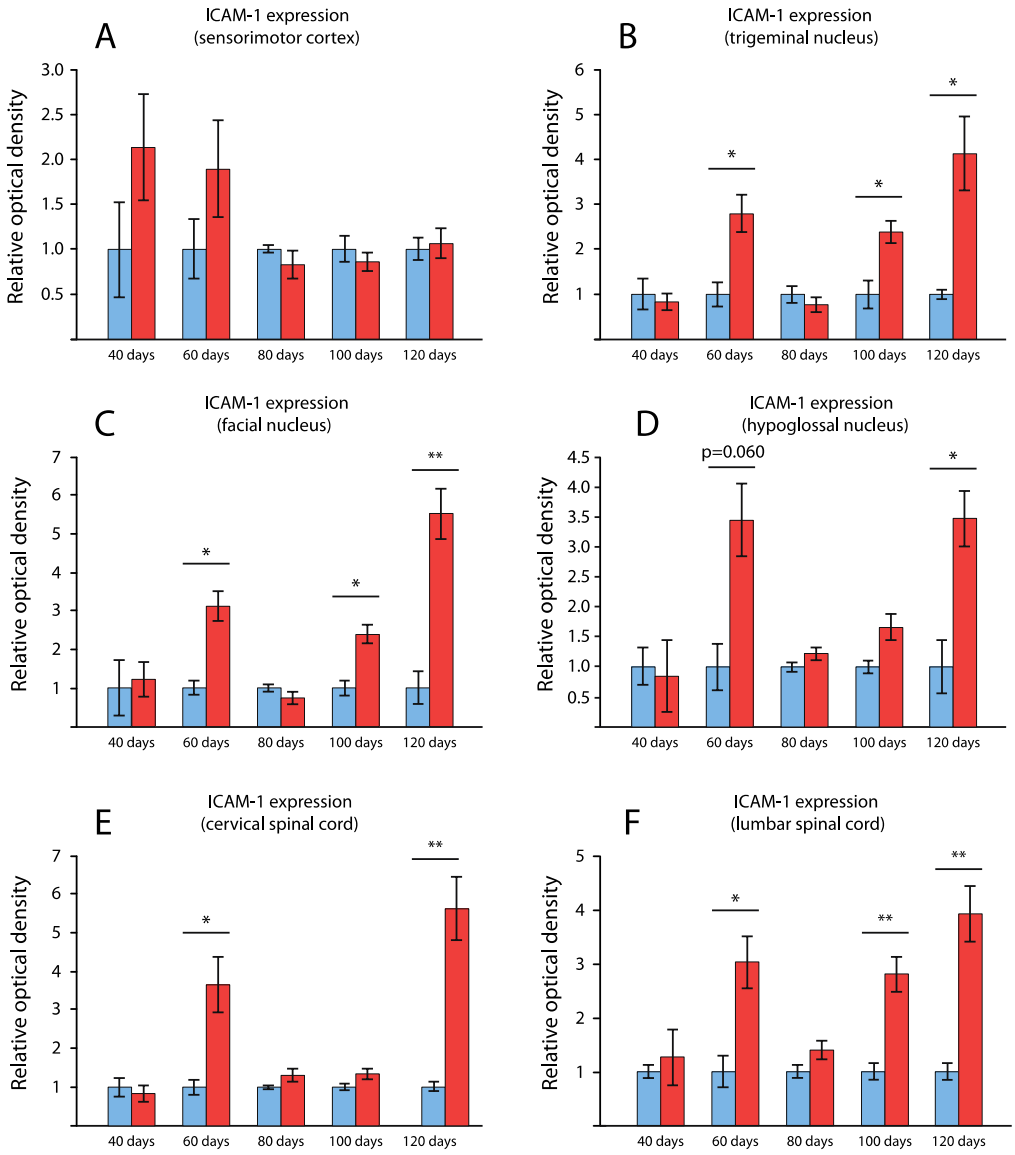


Figure 4.7 – Quantification of ICAM-1 optical density in the sensorimotor cortex, brainstem and spinal cord of *SOD1*^{G93A} and wild type mice

No differences in ICAM-1 optical density could be found at any time point in the sensorimotor cortex (A) between *SOD1*^{G93A} and wild type mice. However, in the trigeminal (B) and facial nuclei (C) and in the lumbar spinal cord, significantly higher ICAM-1 staining was seen at 60, 100 and 120 days of age in *SOD1*^{G93A} mice. ICAM-1 staining in *SOD1*^{G93A} mice was also significantly higher in the cervical cord at 60 and 120 days, and the hypoglossal nucleus at 120 days. There was a trend to higher ICAM-1 production in the hypoglossal nucleus at 60 days, but this did not quite reach significance.

N = 4 mice per group.

* p<0.05, ** p<0.01, *** p<0.001

4.4.6 E-selectin immunohistochemistry

Immunohistochemistry was also performed for E-selectin. However, unlike ICAM-1, no significant E-selectin immunoreactivity could be seen in either *SOD1*^{G93A} or wild type mice, in any of the regions studied (**Figure 4.8**A-L). As a positive control, extensive E-selectin staining was found in the striatum of IL-1β-injected mice (**Figure 4.8**M).

4.4.7 VAP-1 immunohistochemistry

Similar to the findings reported above for E-selectin, no differences in VAP-1 immunoreactivity were observed at any time point in *SOD1*^{G93A} or wild type littermates, in any CNS region (**Figure 4.9**A-L). Again, significant VAP-1 immunoreactivity was found in the positive control tissue (**Figure 4.9**M).

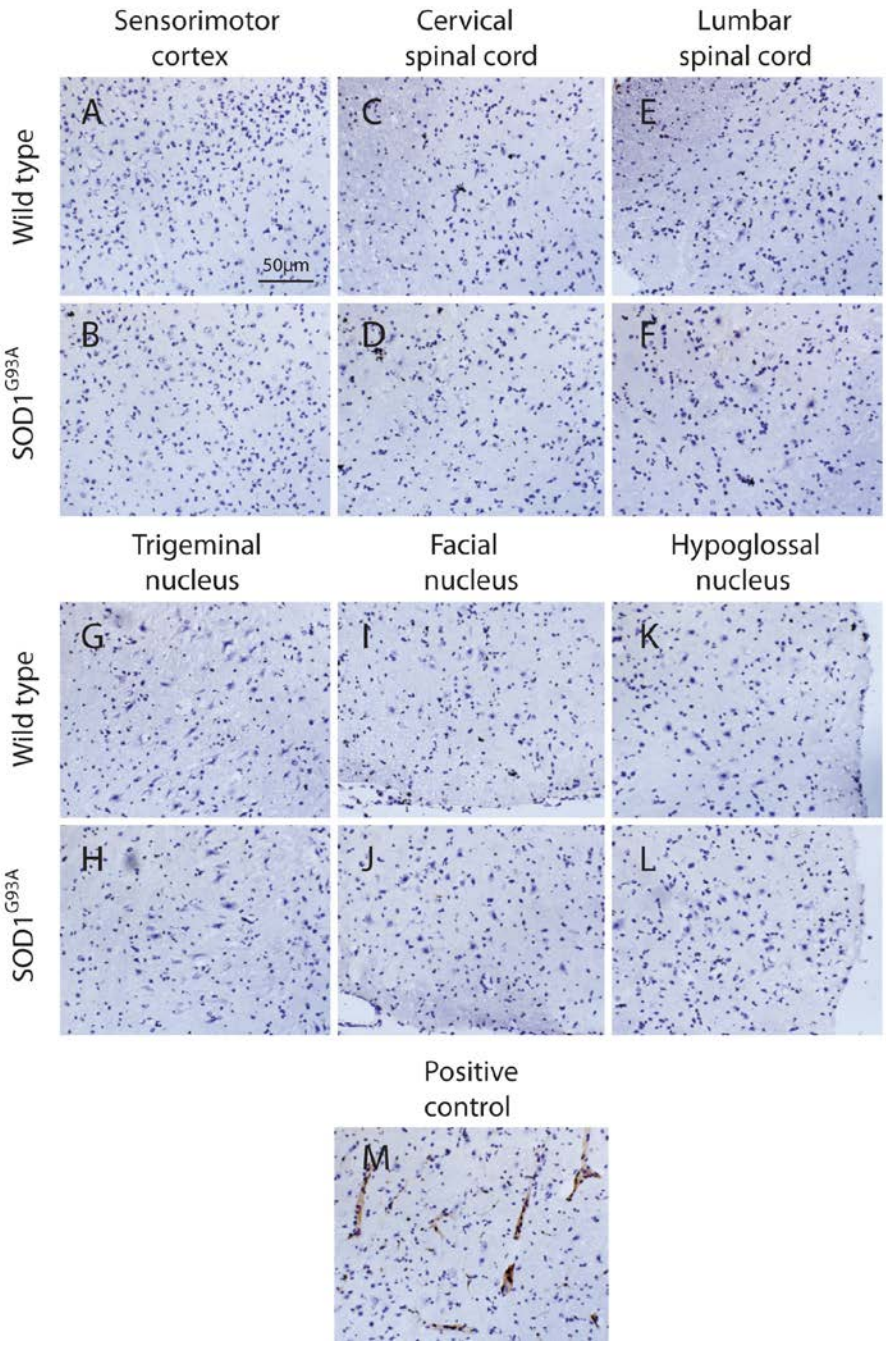


Figure 4.8 – Representative images of E-selectin immunoreactivity in *SOD1*^{G93A} and wild type mice

No E-selectin immunoreactivity was noted in the sensorimotor cortex (A,B), spinal cord (C-F) or brainstem (G-L), at any time point, either in *SOD1*^{G93A} or wild type mice. However, cytokine-injected positive control tissue showed significant E-selectin immunoreactivity around the site of injection (M). Images presented here are at disease end point (120 days), but are representative of all other time points.

N=4 for *SOD1*^{G93A} and wild type mice. Scale bar is representative of all images.

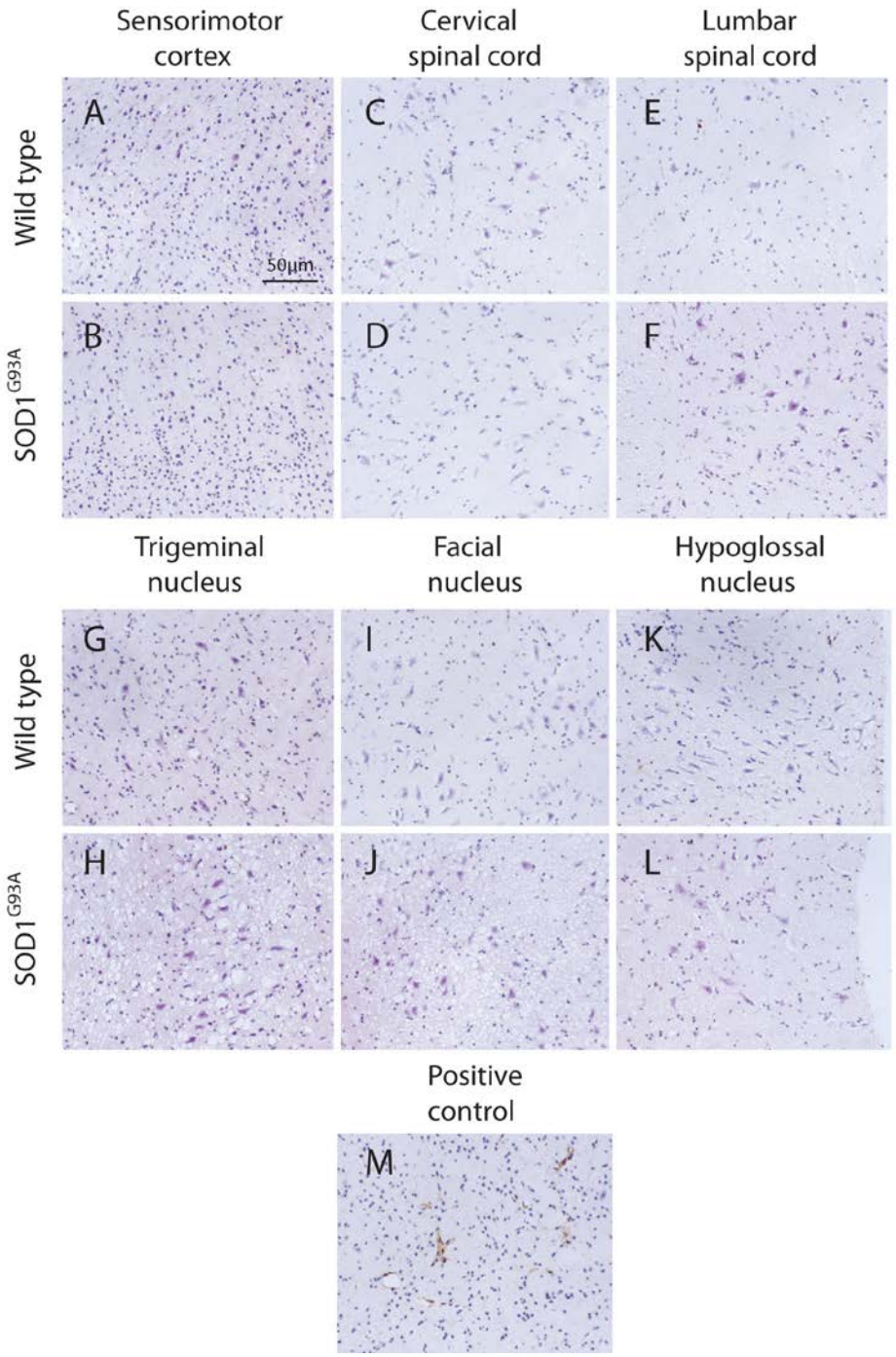


Figure 4.9 - Representative images VAP-1 immunoreactivity in *SOD1*^{G93A} and wild type mice

VAP-1 staining was absent from the sensorimotor cortex (A,B), spinal cord (C-F) and brainstem (G-L) of both *SOD1*^{G93A} and wild type mice at all time points. However, significant VAP-1 immunoreactivity was seen in the positive control tissue around the area of cytokine injection (M). Images presented here are at disease end point (120 days), but are representative of all other time points.

N=4 for *SOD1*^{G93A} and wild type mice. Scale bar is representative of all images.

4.5 Discussion

The data presented in this chapter illustrate that a number of cytokines are upregulated in *SOD1*^{G93A} mice compared with wild type littermates. IL-1β was only up-regulated after the onset of symptoms (100 and 120 days), which is consistent with previous findings in the literature showing post-symptomatic IL-1β upregulation in spinal cords of *SOD1* rodent models (Gowing et al., 2009, Fang et al., 2010), with no change pre-symptomatically (Fang et al., 2010, Berger et al., 2011). The timing of the increased IL-1β expression did not differ between cervical and lumbar regions, consistent with previous findings (Beers et al., 2011), although the increase in expression was approximately twice as high in the cervical compared with the lumbar cord in *SOD1*^{G93A} mice here, contrary to expectations. From previous reports, data were lacking regarding IL-1β expression in other regions of the CNS, other than the spinal cord (and muscle or skin), but the data presented here show an increase in IL-β expression in the brainstem of *SOD1*^{G93A} mice that is comparable to spinal changes, again, only present after the onset of symptoms (100 and 120 days). However, no changes were found in IL-1β expression at any time point in the sensorimotor cortex.

TNF-α appears to be upregulated slightly earlier in the disease than IL-1β, as TNF-α mRNA levels were significantly higher in *SOD1*^{G93A} mice from 80 days onwards in both cervical and lumbar spinal cord segments. However, it is not clear whether mRNA expression twice that of wild type would be biologically relevant in neurodegenerative disease, especially given that changes in mRNA levels are not necessarily associated with linear changes in protein expression (Gygi et al., 1999). Protein data would be useful in ascertaining how relevant these more subtle changes are. A much higher expression of TNF-α was found, though, at 100 and 120 days in the cervical and lumbar spinal cord. These data are consistent with previous findings of upregulation of TNF-α in the spinal cord from around 75 days in the *SOD1*^{G93A} mouse (Hensley et al., 2002, Yoshihara et al., 2002), and pre-symptomatic upregulation of TNF-α in the spinal cord of other *SOD1*

models (Elliott, 2001, Nguyen et al., 2001). Considerable upregulation has also been reported after the onset of symptoms (Beers et al., 2011). Again, comparison of expression levels in different parts of the spinal cord had previously shown a similar extent of TNF-α expression in the lumbar and cervical spinal cord regions of *SOD1*^{G93A} mice (Beers et al., 2011), which is corroborated by the findings in this chapter. This is the first report, however, of TNF-α expression in regions of the CNS other than the spinal cord. The data show an involvement of TNF-α expression in *SOD1*^{G93A} brainstem tissue, but only at the very end of the disease (120 days) in contrast to the earlier upregulation in spinal cord. As was the case for IL-1β, no increase in TNF-α expression was found in the sensorimotor cortex in *SOD1*^{G93A} mice compared with control mice, at any point in the progression of the disease.

Consistent with the available evidence from the *SOD1* literature (Elliott, 2001, Hensley et al., 2002), no evidence was found for increased expression of IFN-γ in *SOD1*^{G93A} mice, in any of the CNS regions studied. However, there was a general trend to higher IFN-γ expression in the cervical spinal cord, and it is possible that there are subtle changes in this region that did not reach statistical significance due to the low sample size. It is important to consider whether a subtle change such as this would have any biological relevance, however. Either way, the data here suggests that there is no substantial change in IFN-γ expression in *SOD1*^{G93A} mice.

The lack of IFN-γ expression may have led us to predict that there would be no involvement of CXCL-10, as this chemokine is mostly thought to be upregulated by IFN-γ (Ohmori and Hamilton, 1993). However, other evidence suggests that CXCL-10 may be induced by other cytokines such as IL-1β and TNF-α (Yeruva et al., 2008). In accordance with this, despite no change in IFN-γ expression, CXCL-10 was indeed upregulated in *SOD1*^{G93A} mice and, surprisingly, was evident through more of the disease time course than any of the other cytokines studied here. As for IL-1β and TNF-α, the most pronounced effect was found in the spinal cord, with upregulation of CXCL-10 seen in the

lumbar and cervical regions from 60 days, and remaining upregulated throughout the disease. Moreover, a similar magnitude of change was seen in the two spinal cord regions. An increase in mRNA was also seen in the brainstem, which was significantly elevated post-symptomatically (100 and 120 days), but was also three times (though not statistically significantly) higher than wild type expression at 60 days. Two main conclusions can be made from this finding: firstly, CXCL-10 is expressed at high levels throughout much of the disease course in *SOD1*^{G93A} mice, suggesting that it may be an important chemokine in ALS pathogenesis; secondly, the data suggest that CXCL-10 is not, in fact, only induced by IFN-γ, as the increase in CXCL-10 expression was found in a molecular environment with no significant IFN-γ expression. With regards to the second conclusion, it is unclear from these data what is the inducing factor for CXCL-10. Whilst previous studies have tentatively suggested a role for IL-1β and TNF-α (Yeruva et al., 2008), the changes in CXCL-10 noted here precede any significant alteration in IL-1β and TNF-α mRNA levels, making these unlikely candidates in this case. However, one possibility is that this is a sensitivity issue – it may be that a dramatic increase in CXCL-10 can be caused by very subtle changes in IL-1β or TNF-α signalling, which were not picked up with the methods and sample size used in this study. Alternatively, CXCL-10 expression is induced by a chemical mediator not investigated in this chapter.

A few general comments should be made at this point based on the qRT-PCR findings. Firstly, the role of inflammation and other aspects of pathology in the sensorimotor cortex is still controversial, particularly in *SOD1* mice, with conflicting results in different studies (Zang and Cheema, 2002, Leichsenring et al., 2006, Petrik et al., 2007, Kassa et al., 2009). The data presented here contribute to this debate showing that, at least in terms of cytokine production, the sensorimotor cortex is not implicated to the same extent as other motor regions (brainstem and spinal cord) in *SOD1* ALS pathology (unless, as discussed next for the spinal cord) a focal inflammatory effect is “diluted” by unaffected tissue).

The second point to make, when considering relative cytokine upregulation between different CNS regions, is that we must bear in mind that qRT-PCR data is only as good as the dissection of the tissue used to obtain the RNA. The largest effect for all cytokines studied was in the spinal cord (lumbar and cervical), but in this instance the relevant inflammatory tissue comprises a large portion of the tissue dissected (perhaps 50% if we assume that cytokine production is restricted to the ventral rather than dorsal portion). With the brainstem, however, where a smaller effect was seen, the relevant motor areas will only comprise a very small portion of the tissue; in addition to the trigeminal, facial and hypoglossal nuclei, which are implicated in *SOD1* pathology, the RNA will also be representative of other cranial nuclei, where pathology will not necessarily be expected, as well as the many other areas of grey and white matter pathways that pass through this region. Therefore, it may not be that the brainstem is affected less than the spinal cord, just that the effect is diluted by the RNA contribution from uninvolved regions.

Regarding expression of CAMs in *SOD1*^{G93A} tissue, the main finding is that there is a surprising lack of endothelial activation in this model. Of the 4 CAMs studied, only ICAM-1 appears to show any involvement in the disease process. ICAM-1 shows an interesting pattern, with two periods of upregulation in the spinal cord, trigeminal nucleus, facial nucleus and hypoglossal nucleus: a brief upregulation at 60 days, pre-symptomatically, and more robust upregulation at 100 and/or 120 days of age. Therefore, this confirms both previous studies, showing an upregulation early (Alexianu et al., 2001) and late (Zhong et al., 2008) in *SOD1*^{G93A} mice. However, no involvement of VCAM-1, E-selectin or VAP-1 was apparent here.

The above findings bring up some interesting issues when related to the cytokine findings. With regards to ICAM-1 upregulation, the post-symptomatic changes are consistent with the cytokine profile, as they correspond temporally to increased IL-1β and TNF-α, both of which are known to increase expression of ICAM-1 on endothelial cells (Wyble et al., 1996). However, the increase in ICAM-1 at 60 days does not correspond to an increase

in any of the cytokines studied here, which begs the question, which chemical messenger is responsible for increasing ICAM-1 production? Given that there is an increase in the chemokine CXCL-10 at 60 days, it appears that inflammatory signalling is occurring, just not involving the cytokines selected for this study. To target this, the most effective way would be to take tissue from *SOD1*^{G93A} and wild type controls and 60 days, and perform a microarray to investigate a larger number of inflammatory transcripts, rather than select specific targets based on past literature, as was done here.

The other interesting finding here is the lack of endothelial response of the other CAMs, specifically VCAM-1 (discussed in the previous chapter), E-selectin and VAP-1. Whilst VAP-1 would not necessarily be expected to change in *SOD1*^{G93A} mice, there are many reports showing how endogenous and exogenous IL-1β and TNF-α cause an increase in VCAM-1 and E-selectin production in endothelial cells (Springer, 1990, Wyble et al., 1996, Zhou et al., 2005, Dong et al., 2011). Therefore, at the end of the disease (100-120 days), when there is a high level of both IL-1β and TNF-α production in the spinal cord and brainstem, some other feature of the disease process, or a general effect of the overexpression of the *SOD1*^{G93A} mutation must interfere with this process, frustrating the action of cytokines on endothelial cells. I propose that it is more likely to be the latter, and owing to its relevance to *SOD1*^{G93A} models generally, this is discussed further in the general discussion.

To conclude, we report significant post-symptomatic expression of the classical cytokines IL-1β and TNF-α in *SOD1*^{G93A} mice, with an earlier, pre-symptomatic, involvement of the chemokine CXCL-10, which was not induced by IFN-γ. Cytokine and chemokine expression was found in the spinal cord, consistent with previous reports, and I show for the first time significant expression in the brainstem, but not the sensorimotor cortex, of *SOD1*^{G93A} mice. Overall there was a surprising lack of CAM production in endothelial cells, other than a significant upregulation of ICAM-1, both pre- and post-symptomatically, in the spinal cord and cranial motor nuclei.

Chapter 5: Liposomally-packaged steroids as a treatment of neuroinflammation associated with *SOD1* ALS

5.1 Aims of this chapter

The focus of this chapter is investigating the potential of CNS-targeted steroids as a therapeutic agent in *SOD1* ALS. Results from previous chapters in this thesis, as well as previous published studies, implicate neuroinflammatory processes strongly in the natural history of ALS. Work in preclinical models has shown the therapeutic potential of immuno-modulatory strategies (e.g. corticosteroids), but this has not translated to human ALS patients to date. However, one possibility for the lack of therapeutic effect of corticosteroids is poor BBB penetrance; therefore it is possible that with improved drug delivery to the CNS, corticosteroids could prove efficacious in treating ALS. To test this hypothesis, *SOD1*^{G93A} mice were treated once a week for 9 weeks, starting from 60 days of age, either with the liposomally-packaged methylprednisolone (2B3), free methylprednisolone, or saline, and compared with a saline-treated wild type control. Once a week, prior to injections, mice were weighed and their motor behaviour was tested using the rotarod apparatus. The last injection was at 116 days, and three days later mice were scanned with MRI using a short T_2 sequence to measure brainstem pathology. Tissue was taken for histology and immunohistochemistry; the number of motor neurons in the lumbar spinal cord and three brainstem nuclei (V, VII, and XII), vacuolation in the brainstem nuclei, and astrocyte (GFAP) and microglia (Iba-1) activation in the spinal cord and brainstem nuclei were all quantified.

5.2 Introduction

Steroids are a class of organic compounds linked by a basic underlying molecular structure: they comprise three fused cyclohexane rings (rings A, B, and C) and one fused

cyclopentane ring (ring D). This basic skeleton can be modified by functional groups in a variety of ways, yielding the wide array of steroids that are naturally produced in the body, as well as synthetic steroids that mimic the effect of natural compounds, to treat a large number of diseases. Steroids are produced under normal conditions by a number of different glands (e.g. gonads, adrenal gland), are up- or down-regulated by conditions such as stress (Dickerson and Kemeny, 2004), and they vary during development (Dickerman et al., 1984). Steroids act as hormones, in that they are released into the bloodstream and are capable of acting on most cells in the body.

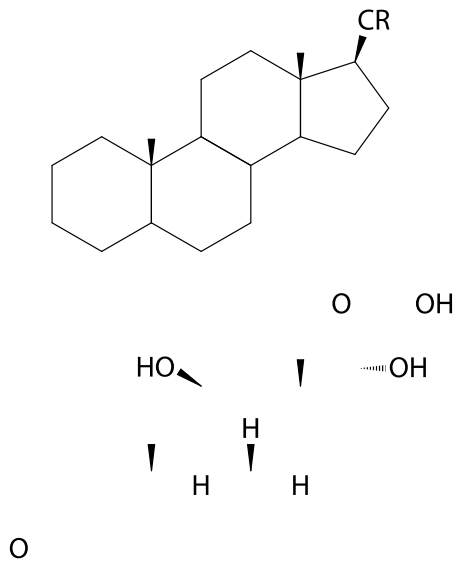


Figure 5.1 – Steroid structure

The steroid nucleus, gonane, consists of three fused cyclohexane rings and one fused cyclopentane ring, which is usually methylated at carbons 10, 13 and 17 to give the basic steroid core (top figure). The structure of methylprednisolone is given below, with the characteristic ketone on carbon 3, found in other glucocorticoids, and differs from prednisolone by the presence of a methyl group at carbon 6 (highlighted by dashed box).

Steroids can be classified in a number of ways based on structure or function, but one classification distinguishes glucocorticoids, mineralocorticoids[3] and sex steroids, which are based on the structures of cortisol, aldosterone and testosterone, respectively. In a broad sense, sex steroids are involved in sexual differentiation and support the development of the reproductive system (Murakami, 1987), and mineralocorticoids have an important physiological role in salt balance, hence are important for renal function (Swingle et al., 1959). Glucocorticoids on the other hand have a role in aspects of

[3] On a point of definition, glucocorticoids and mineralocorticoids are both types of corticosteroids, as their structure is based on naturally produced steroids synthesized in the adrenal cortex. However, occasionally the word ‘corticosteroid’ is used synonymously with ‘glucocorticoid’, which is avoided here for clarity.

metabolism and immune mediation, and are used clinically in conditions that are characterized by an aberrant inflammatory response. For example, inhalation of glucocorticoids such as budesonide is the staple treatment for asthma (Juniper et al., 1990), and chronic eczema can be treated with hydrocortisone (cortisol) (Korting et al., 1995). In addition, for patients with the classical auto-immune disease of the CNS, multiple sclerosis, acute relapses have been treated with corticosteroids, including methylprednisolone, which lessens the effect of the relapse and decreases the time to recovery (Milligan et al., 1987).

Steroids bind to a number of receptors, but the most intensively studied is the nuclear receptor 3 (NR3) family. Steroid receptors may be found in the plasma membrane, the cytoplasm, or the nucleus, and come in two main types: Type I receptors, which are extranuclear (usually cytoplasmic), and bound to heat shock proteins at baseline; and type II receptors, which are nuclear in origin, and are not associated with heat shock proteins. On binding, both types of receptor act as transcription factors, altering the transcriptional (and, by extension, protein) profile of the cell, acting over hours or even days. Glucocorticoids are produced naturally by the adrenal cortex, and enter the blood stream to act throughout the body. They are able to cross the plasma membrane, and bind to the glucocorticoid receptor, NR3C1, in the cytosol, which causes translocation of the bound receptor to the nucleus, and dissociation from the heath shock protein, for example hsp90 (Davies et al., 2002). Once in the nucleus, the steroid-receptor complex, no longer bound to the heat shock protein, acts as a transcription factor, up-regulating anti-inflammatory genes directly by binding to DNA response elements (Beato, 1989), or down-regulating pro-inflammatory genes by binding to pro-inflammatory transcription factors such as NF-κB (Ray and Prefontaine, 1994), thereby frustrating their action.

There is some evidence that corticosteroids can modify the disease in *SOD1* mice. One study found that restraint stress led to earlier disease onset and more rapid disease progression in *SOD1* mice, and found that disease duration correlated negatively with

serum corticosterone levels, i.e. higher corticosterone levels associated with more rapid progression (Fidler et al., 2011). However, this study notably did not control for confounding variables such as diet and level of exercise; non-restrained mice were allowed to feed and exercise *ad libitum*. Both of these variables are likely to alter cellular signalling mechanisms, making the data difficult to interpret. In ALS patients there is limited evidence for a role of steroids in the disease. The cortisol awakening response (CAR) was blunted in one report, resulting in lower levels of cortisol, with a positive correlation between CAR and motor behaviour, i.e. lower CAR associated with poorer motor behaviour (Roozendaal et al., 2012).

A number of studies provide evidence that synthetic and non-synthetic steroids, including glucocorticoids, can be administered to therapeutic value in ALS. Numerous reports have indicated that cholest-4-en-3-one (Olesoxime), a cholesterol derivative, delayed disease onset, extended survival, reduced gliosis, protected against loss of NMJs and protected spinal motor neurons in *SOD1* mice (Bordet et al., 2007, Sunyach et al., 2012). Glucocorticoids are synthesised from cholesterol, so this may have some relevance for steroids as a therapeutic target. Both corticosterone and 21-aminosteroids were also found to be effective in the Wobbler mouse, extending survival and altering the inflammatory environment in the CNS (Gonzalez Deniselle et al., 1996, Deniselle et al., 1999, Gonzalez Deniselle et al., 1999a, Gonzalez Deniselle et al., 1999b, Gonzalez Deniselle et al., 2001). Therefore steroids may offer some therapeutic potential in ALS. However, a study investigating the therapeutic potential of prednisolone and azathioprine in ALS patients found no difference between treatment groups (Werdelin et al., 1990).

There may be a number of reasons for the apparent lack of therapeutic effect conferred by steroids, but one caveat common to the studies cited above is that, whilst steroids are able to cross into the CNS, the permeability of the BBB to individual steroids can differ significantly. BBB permeability for the sex hormones testosterone, progesterone and estradiol is much higher than for the glucocorticoids cortisol and corticosterone or the

mineralocorticoid aldosterone (Pardridge and Mietus, 1979). This is particularly pertinent in the *SOD1*^{G93A} mouse model, as the data presented in this thesis in Chapters 3 and 4 show that the BBB remains intact both in the brain and the spinal cord, even at disease end point. Consequently, drugs will not be able to pass as freely into the CNS as they would across a disrupted barrier. Therefore, increasing the delivery of steroid compounds into the CNS may be a way to maximize the therapeutic action, and to reduce side-effects owing to peripheral effects of the drug.

One efficient way of targeting the brain for specific drugs is to capitalize on endogenous transport mechanisms. One such mechanism is the transport of glutathione (GSH) from the blood into the brain. GSH is a tripeptide, consisting of L-glutamic acid, L-cysteine and glycine, whose diverse roles in the brain include antioxidant activity (Meister and Anderson, 1983) and possible neurotransmission/modulation (Janaky et al., 1993, Shaw et al., 1996). In this chapter, we use the glucocorticoid methylprednisolone (see **Figure 5.1** for chemical structure), packaged in a PEGylated liposome with the addition of GSH on the tips of the PEG groups (2B3-201). Methylprednisolone was used here because this is one of the most commonly used steroids in the clinic for a wide variety of inflammatory conditions. This packaging system has a number of advantages: the liposome surrounds the drug compound, which should reduce side effects owing to peak drug concentration (Szebeni, 1998, Harris and Chess, 2003); the PEG groups shields the liposome, increasing the time in circulation before clearance, and reduces unwanted side effects associated with liposome administration, such as activation of complement, and the ensuing inflammatory reaction (Harris and Chess, 2003); and importantly, the GSH on the PEG groups allows binding to endogenous GSH transporter mechanisms at the BBB, thereby increasing delivery to the CNS.

Work has recently been published using this packaged drug (2B3-201) in experimental autoimmune encephalomyelitis (EAE), a common rodent model of multiple sclerosis (Gaillard et al., 2012). It was found that methylprednisolone packaged in liposomes with

both PEG groups and glutathione reduced clinical signs more than either free methylprednisolone or methylprednisolone in a PEGylated-only liposome (i.e. without the glutathione). Therefore, this treatment has potential for inflammatory conditions of the CNS.

I administered 2B3-201 i.v. to *SOD1*^{G93A} mice, and compared with free methylprednisolone (MP) or saline. Wild type mice were injected with saline once a week as a further control. I assessed mice for motor behaviour (rotarod), and measured aspects of pathology, including vacuolation and neuronal number, in the spinal cord and cranial motor nuclei. Astrocyte and microglia activation were also measured to ascertain the inflammatory environment of the CNS. T_2 MRI was also used as an *in vivo* biomarker ALS pathology.

5.3 Materials and Methods

5.3.1 Drug administration

Four groups of mice were used in this study: wild type given i.v. saline (wild type saline) (N=10); *SOD1*^{G93A} mice given i.v. saline (*SOD1* saline) (N=8); *SOD1*^{G93A} mice given i.v. free methylprednisolone (*SOD1* MP) (N=9); *SOD1*^{G93A} mice given i.v. packaged methylprednisolone (*SOD1* 2B3-201) (N=10). 2B3-201 consists of a PEGylated spherical lipid bilayer, with glutathione groups attached, and filled with MP. Injections were given once a week for 9 weeks (60-116 days). Experimental groups and dosing regimes were designed in collaboration with toBBB, from whom the drugs were obtained. For i.v. injections mice injected as described in 3.3.4.

5.3.2 Behavioural testing

Rotarod testing (accelerating paradigm) was carried out once a week from 60 to 116 days, as described in 2.4.3. Time taken to final fall was measured 3 times for each animal, with the longest time used for analysis. Mice were also weighed once a week.

5.3.3 MRI experimental protocol

T_2 MRI was carried out as described in 3.3.4.1, and analysed as described in 3.3.4.6.

5.3.4 Histology and immunohistochemistry

Tissue was prepared as described in 2.5.3. In brief, mice were perfused initially with saline until full exsanguination, followed by perfusion with PLP. Tissue was dissected out and post-fixed in PLP. Unlike the previous two chapters, the brain was taken whole, as were the cervical and lumbar spinal cord. Tissue was cryo-protected with 30% sucrose, and then frozen. 10μm sections were cut using a cryostat. Immunohistochemistry was performed for GFAP and Iba1 - the basic immunohistochemistry protocol and antibody

details are given in 2.5.5. The standard H&E protocol was carried out, as described in 2.5.6.

For quantification of vacuolation, midbrain and brainstem sections were stained with H&E. Photographs were taken of the 2 largest brainstem nuclei cross-sections (spaced 150μm apart), left and right (4 regions in total). Using the thresholding function of ImageJ, the picture was binarized as described in 3.3.7. An ROI was then drawn around the area of tissue affected by the vacuoles, and a number of measures made: i) the area affected by vacuolation; ii) the average amount of vacuolation (i.e. within the ROI, the average intensity value, with 266 being complete vacuolation, and 0 being no vacuolation); the total amount of vacuolation in the tissue, calculated from the product of the first two measures. For wild type, area was designated a value of 0, because there was no vacuolation to be seen in wild type sections. Average vacuolation of the wild types was measured in the same way as the *SOD1* tissue, except that an arbitrary ROI was used, placed around the boundary of the nucleus, with the size consistent with the ROI for *SOD1*.

For spinal cord motor neuron counts, the total number of neurons and total number of morphologically normal neurons were counted in the ventral horn of 2 spinal cord cross-sections, left and right hemisphere (total of 4 regions), and then the average was taken. For brainstem motor neuron counts, the number of neurons and number of healthy neurons were counted in the cross section of the nucleus, for 2 cross sections, left and right hemisphere (total of 4 regions). For each nucleus, the two largest (i.e. most central) cross sections were taken for consistency, spaced 150μm apart. Morphologically normal neurons display a regular staining pattern with H&E, whereas abnormal neurons have significant amount of intracellular vacuolation and often have a withered, pyknotic appearance. An example of a morphologically normal, and morphologically abnormal neuron by this definition are shown in **Figure 5.2**.

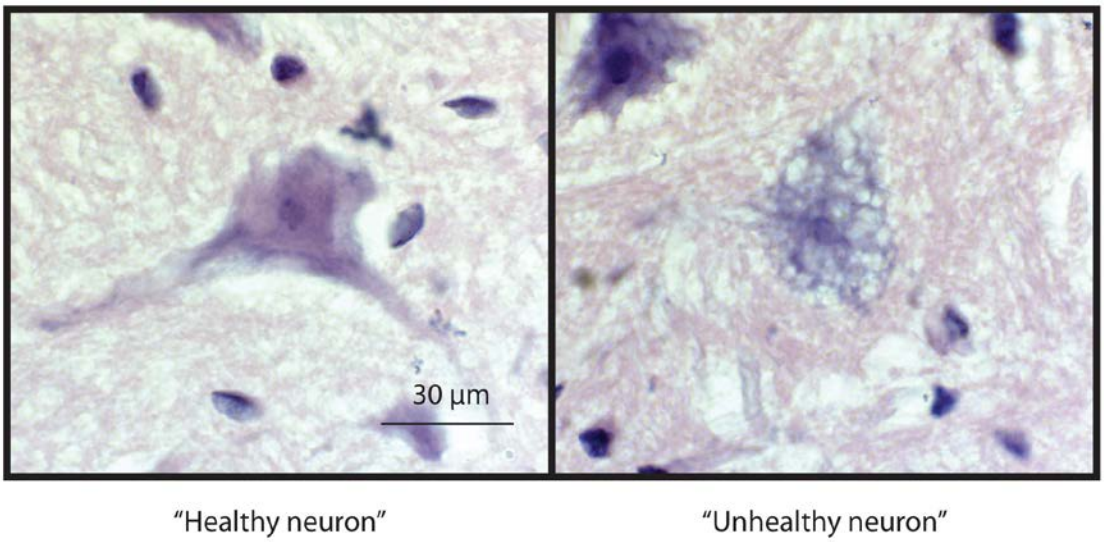


Figure 5.2 – Example of a neuron defined as morphologically normal and an abnormal neuron with significant vacuolation

The left panel displays morphologically normal neurons, which have a regular H&E staining pattern, with no sign of vacuolation. On the right is a morphologically abnormal neuron with much vacuolation throughout the cytosol.

For quantification of both GFAP and Iba1 immunostaining, the two largest cross sections of the brainstem nuclei in both hemispheres (total 4 regions), or the left and right ventral horns in 2 cross sections (total 4 regions) were photographed from the microscope, at 20x magnification, using Leica Firecam software. Average intensity was calculated for each region as described in 3.3.7, and the four regions for the spinal cord or brainstem nuclei were then averaged. In addition to staining intensity, the number of astrocytes stained with GFAP, and the number of microglia stained with Iba1 were counted in the same regions of the brainstem and spinal cord, and averaged over each.

5.3.5 Positive control tissue

Mice were injected into the left striatum with IL-1β to create positive control tissue for inflammatory immunohistochemistry. Details of this are given in 3.3.6.

5.3.6 Statistical analysis

For behavioural data, 2-way ANOVAs (treatment and time) and Hulm-Bonferroni t-tests were carried out at each time point between each of the treatment groups. Area under the

curve (AUC) analysis was also performed, with t-tests to compare group means. For MRI and IHC / histology data, nonparametric testing was used because the data was not normally distributed, and this could not be corrected by simple normalization methods. Kruskall-Wallis analysis was used to investigate differences between treatment groups in the three brainstem motor nuclei, and individual comparisons were made using Mann-Whitney U tests. Power analysis was also carried out on the behavioural data for sample size estimation. An online power analysis calculator was used for power analysis (http://www.surveysystem.com/sscalc.htm), and SPSS was used for the remaining parametric and non-parametric statistics. Data are presented as median ± standard error. For graphical data presentation, box and whisker plots were used, displaying the median (strong central band), interquartile range (box) and range (whiskers).

5.4 Results

5.4.1 Behaviour and weights

All groups of mice showed an increase in weight over time, but unlike the previous weight data presented in Chapter 3 there was no significant difference between any of the groups at any time point (**Figure 5.3**A) ($p>0.05$). In spite of there being no significant differences between the groups, some degree of variation was evident in baseline weights between the groups. To overcome this, the data were also analysed after normalizing the data points to the baseline weight (**Figure 5.3**B). However, no significant differences were found between any of the groups using the normalized weight data. Taking the entire time course, AUC analysis confirmed this, with no significant difference in area at any time point (**Figure 5.3**D, left) ($p>0.05$).

For rotarod score, wild type mice were significant higher than all treated groups at all time points ($p<0.05$). A decline in motor performance was seen across the disease in all *SOD1* mice, reaching significance from baseline ($p<0.05$) between 80 and 95 days (*SOD1* saline, 95 days; *SOD1* free MPS, 81 days; *SOD1* 2B3-201, 88 days). No significant difference was found between *SOD1* treatment groups at any time point ($p>0.05$), although AUC analysis revealed a significant difference between WT and all *SOD1* treatment groups ($p<0.05$). Although not significant, there was a trend towards greater AUC for *SOD1* 2B3-201 compared with *SOD1* free MP ($p=0.17$), suggestive of slightly preserved motor performance in 2B3-201-treated animals compared with free MP. Post-hoc power analysis revealed that a sample size of N=52 would be required to show a statistical difference between *SOD1* saline and *SOD1* 2B3-201, and a sample size of N=12 to show a statistical difference between *SOD1* MPS and *SOD1* 2B3-201 ($\alpha=0.05$; $\beta=0.5$).

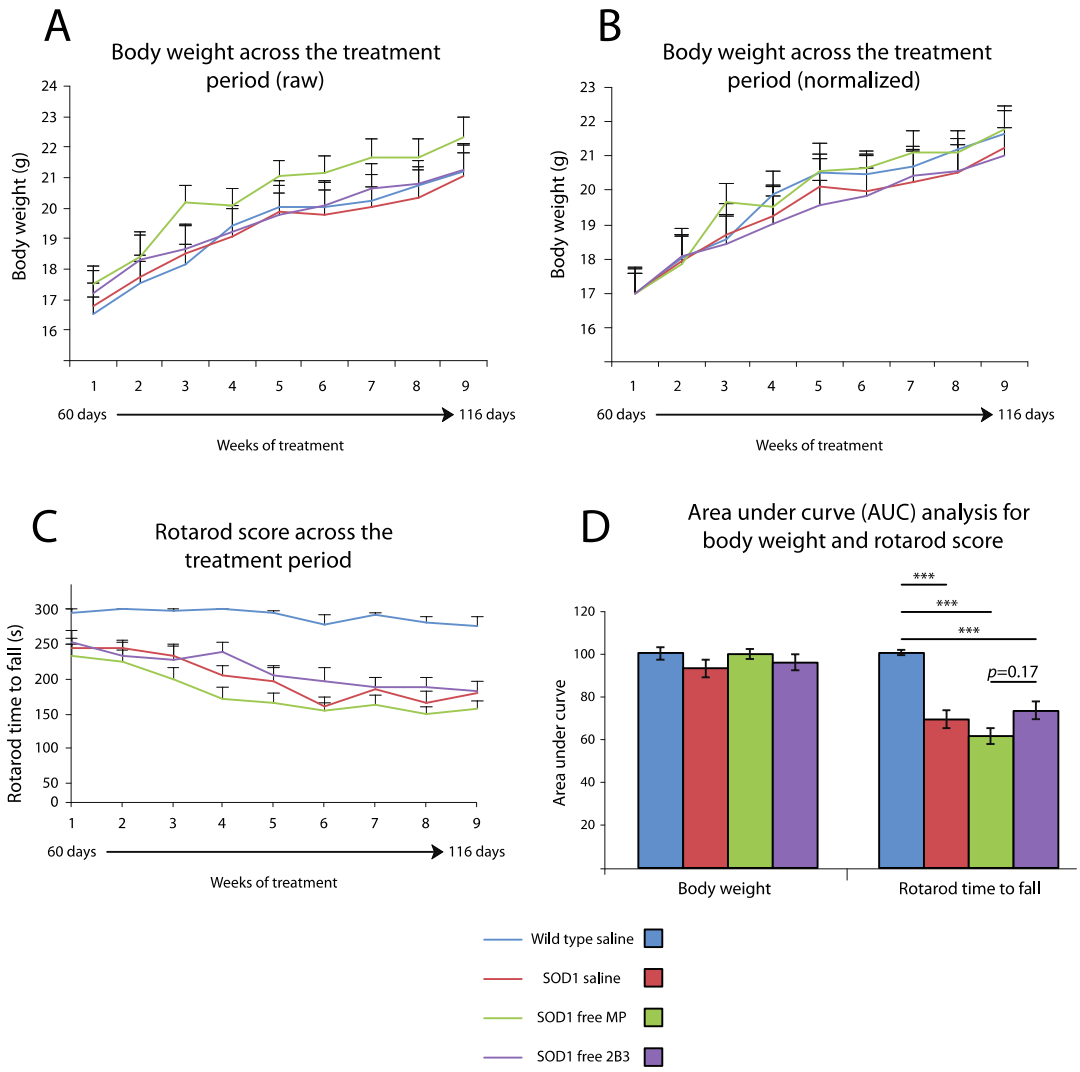


Figure 5.3 – Behaviour and weight data for the 2B3-201 study

Weight data (unadjusted – A; normalized at 60 days – B) shows a gradual increase in weight in all groups, with no significant difference between genotypes or treatment groups at any time point. Rotarod scores (C) were higher at all time points for WT compared with all *SOD1* treatment groups, and all SOD1 groups showed a typical decline over time, with no significant difference between any of the treatment groups. Area under the curve analysis was carried out for weight and rotarod scores (D). There was no significant different between groups for weight data or rotarod score, although there was a trend to higher motor performance for 2B3-201 treated *SOD1* compared with free MP treated *SOD1* mice. Data is median ± standard error.

Wild type saline N=10; *SOD1* saline N=8; *SOD1* MP N=9; *SOD1* 2B3-201 N=10.

* p<0.05; ** p<0.01; *** p<0.001

5.4.2 T_2 MRI

As shown in Chapter 3, no significant increase in signal intensity was seen in the cranial motor nuclei compared with surrounding grey matter in WT mice treated with saline, either in the trigeminal nucleus (-1.3 ± 3.3%), facial nucleus (-0.0 ± 2.9%), or hypoglossal nucleus (7.1 ± 3.7%) (**Figure 5.4**, top row and **Figure 5.5**).

In the trigeminal nucleus (**Figure 5.4**A, **Figure 5.5**A), *SOD1* saline had an increase in T_2 signal intensity compared with the surrounding tissue (25.7 ± 4.2%), and this increase was significantly greater than WT saline ($p<0.001$). A similar increase in signal intensity was seen for *SOD1* MP (24.4 ± 3.2%), and again was significantly higher than WT saline ($p<0.001$), but not significantly different from *SOD1* saline ($p>0.05$). SOD1 mice treated with 2B3-201 showed a smaller increase in signal intensity (18.7 ± 5.1%) than either of the other *SOD1* groups. This increase was significantly higher than the WT saline group ($p>0.05$), but significantly lower than both *SOD1* saline ($p<0.05$) and *SOD1* free MP ($p<0.01$).

In the facial nucleus (**Figure 5.4**B **Figure 5.5**B), *SOD1* saline showed an increase in T_2 signal intensity compared with surrounding brainstem tissue (37.3 ± 5.3%), and this increase was significantly greater than WT saline ($p<0.001$). A comparable signal change was seen in *SOD1* MP (32.5 ± 2.7%), which was significantly higher than WT saline ($p<0.001$) but not *SOD1* saline ($p>0.05$). Compared to the other *SOD1* groups, the signal increase seen in *SOD1* mice treated with 2B3-201 was attenuated (24.8 ± 4.9%), and although still significantly higher than WT saline ($p<0.001$), was significantly lower than both *SOD1* saline ($p<0.01$) and *SOD1* free MP ($p<0.01$).

In the hypoglossal nucleus (**Figure 5.4**C, **Figure 5.5**C), *SOD1* saline showed an increase in T_2 signal intensity compared with the surrounding brainstem tissue (26.8 ± 5.5%), and this increase was significantly greater than for WT saline ($p<0.001$). *SOD1* mice treated with free MP showed a similar signal change (27.8 ± 6.5%), which was significantly greater

than WT mice given saline ($p<0.001$), but not significantly different from *SOD1* saline mice ($p>0.05$). *SOD1* mice treated with 2B3-201 showed a slightly lower signal change compared with the other *SOD1* groups (20.9 ± 4.5%). This increase in signal intensity was significantly higher than for WT saline mice ($p<0.001$), and showed a trend to lower signal intensity than *SOD1* saline ($p=0.062$) and *SOD1* MP mice ($p=0.091$).

5.4.3 Histological confirmation of vacuolation

Vacuolation was quantified as described in Chapter 3, using histological sections from the trigeminal, facial and hypoglossal nuclei, stained with H&E. Representative micrographs of these nuclei are shown in **Figure 5.6**.

WT tissue shows the typical H&E staining pattern, with a large number of heavily haematoxylin-stained motor neurons, and eosinophilic connective tissue, showing high tissue integrity (i.e. no vacuoles present). Because there was no vacuolation to speak of, for the quantification (**Figure 5.7**) the area of vacuolation was set at 0 for wild type mice in all regions. The average amount of vacuolation (quantified from image J) was therefore very low in the trigeminal (1.97 ± 0.32 arbitrary units), facial (11.20 ± 0.89 units) and hypoglossal (7.00 ± 0.65 units) nuclei, as was total vacuolation (trigeminal, 7.28 ± 1.18 units; facial 48.50 ± 3.87 units; hypoglossal 12.68 ± 1.31 units).

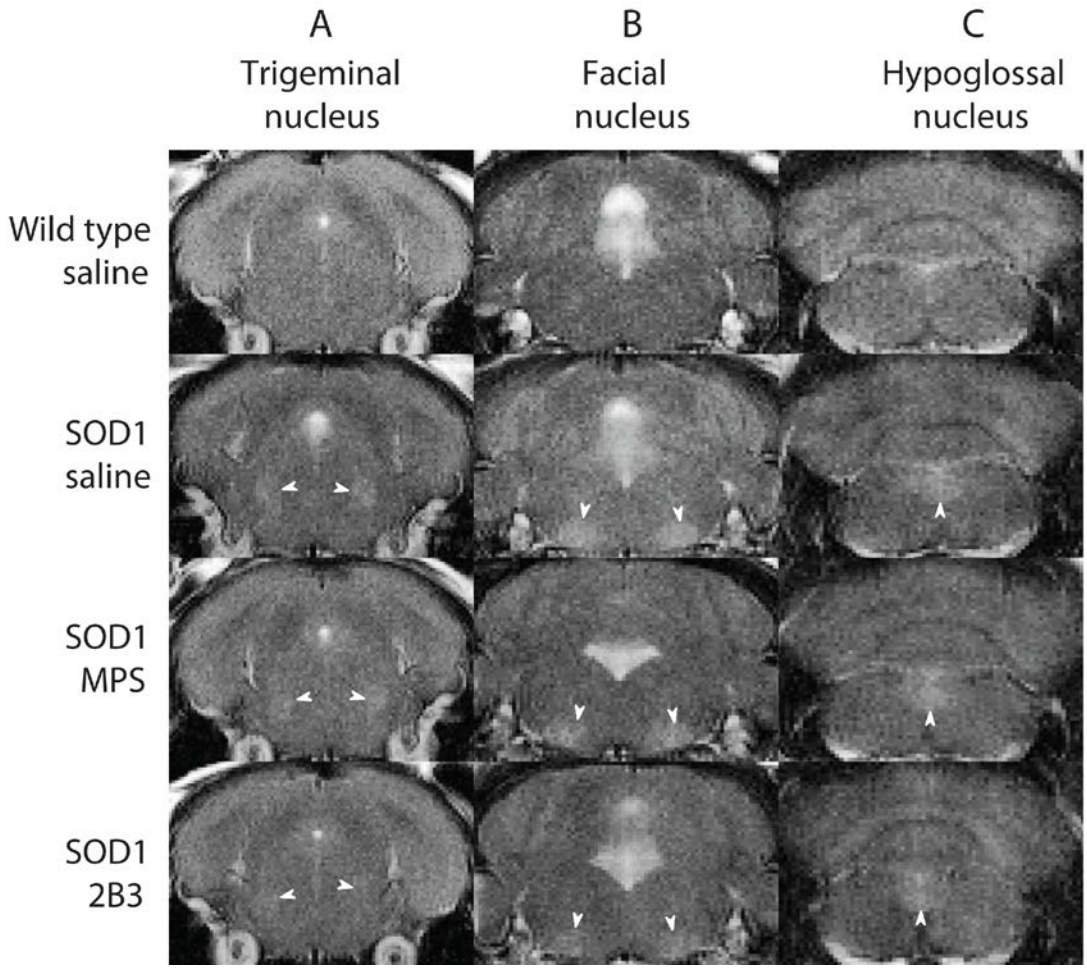


Figure 5.4 – Representative T_2 MR images of the cranial motor nuclei in the 2B3-201 study

No difference can be seen in signal intensity in the cranial motor nuclei compared with surrounding brainstem in WT mice. An increase in signal can be seen in the trigeminal (V), facial (VII) and hypoglossal (XII) nuclei in *SOD1* saline mice. A comparable signal increase in seen for *SOD1* mice treated with free MP, but in comparison to saline and free MP treated *SOD1* mice, those treated with 2B3-201 show a markedly reduced signal intensity in these three motor nuclei.

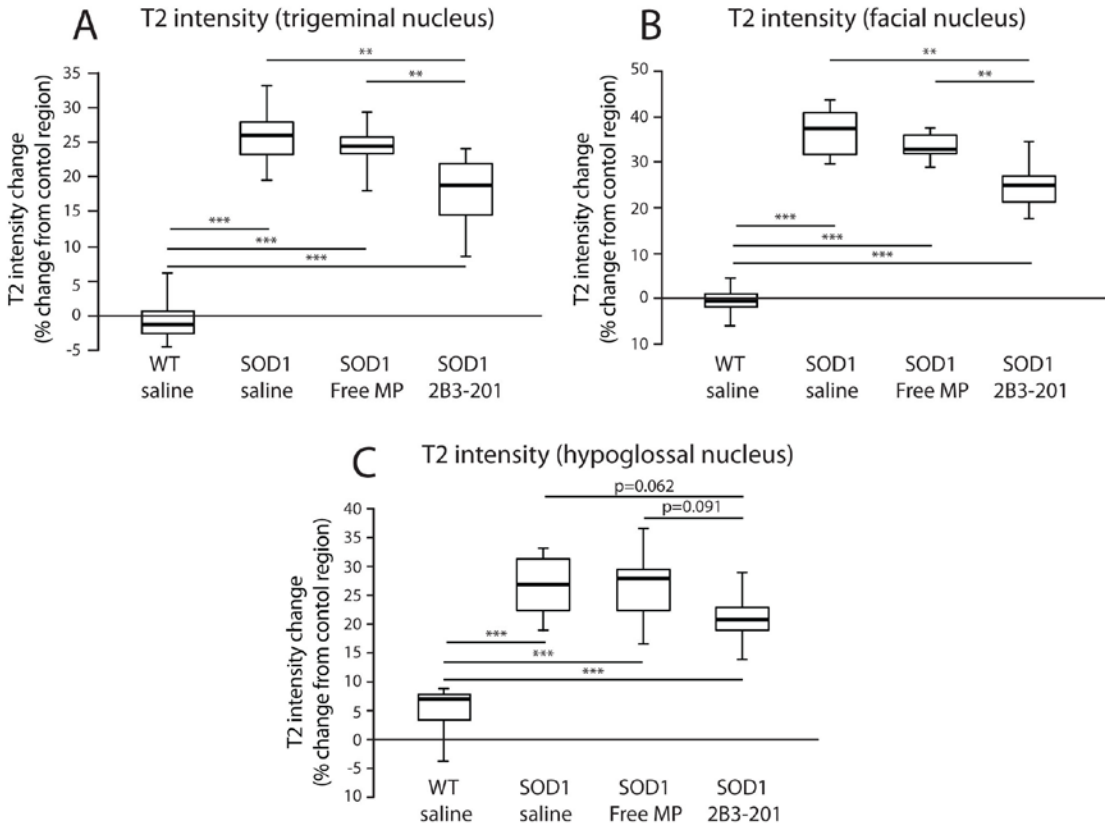


Figure 5.5 – Quantification of T_2 intensity in the midbrain/brainstem motor nuclei in the 2B3-201 study

T_2 signal intensity was measured in the trigeminal (V), facial (VII) and hypoglossal (XII) nuclei, and expressed as a ratio with surrounding brainstem tissue. In all nuclei, the three *SOD1* treatment groups showed significant signal change compared to WT control mice. In the trigeminal (A) and facial nucleus (B), *SOD1* 2B3-201 mice showed a significantly lower signal increase compared with both the *SOD1* MP and *SOD1* saline treated mice. In the hypoglossal nucleus (C) the same pattern was observed, but did not reach statistical significance. Because of the non-parametric analysis performed here, data are presented in a box and whisker plot, with the median (strong central band), interquartile range (box) and range (whiskers).

WT saline N=10; *SOD1* saline N=8; *SOD1* MP N=9; *SOD1* 2B3-201 N=10.

* p<0.05; ** p<0.01; *** p<0.001

In the trigeminal nucleus (**Figure 5.6**A-D**, Figure 5.7**A-C), *SOD1* mice treated with saline showed profound vacuolation (area of 47.16 ± 1.34 units), and had significantly more average (28.58 ± 3.30 units) and total vacuolation (140.80 ± 16.12 units) than wild type mice ($p<0.001$). *SOD1* mice treated with free MP showed a similar level of vacuolation; the area (49.08 units ±1.64), average vacuolation (30.58 ± 2.40 units), and total vacuolation (139.45 ± 13.74 units) were all significantly different from wild type saline mice ($p<0.001$), but none of the measures were significantly different from *SOD1* saline ($p>0.05$). Similarly, the 2B3-201 *SOD1* group showed a significantly different area (45.03 ± 1.53 units), average vacuolation (18.25 ± 2.03 units) and total vacuolation (84.40 ± 10.76 units) than wild type mice ($p<0.05$). However, these mice exhibited lower average and total vacuolation than both *SOD1* saline (average $p=0.076$, total $p<0.05$) and *SOD1* MP mice (average $p<0.05$, total $p<0.05$), although the area affected by vacuolation was not different between the other SOD1 treatment groups ($p>0.05$).

In the facial nucleus (**Figure 5.6**E-H**, Figure 5.7**D-F), the *SOD1* saline group showed substantial average (53.04 ± 2.55 units) and total (283.92 ± 19.69 units) vacuolation, with an area of vacuolation of 52.71 ± 1.80 units, all of which were significantly greater than wild type saline mice ($p<0.001$). Similarly the average vacuolation (50.70 ± 3.34 units) and total vacuolation (266.6 ± 23.26 units) in *SOD1* MP was significantly greater than wild type mice given saline ($p<0.001$), but not significantly different from the *SOD1* saline group ($p>0.05$). The area of vacuolation in *SOD1* MP mice in the facial nucleus was 51.21 ± 1.44 units, which was not significantly different from the *SOD1* saline group ($p>0.05$). Similarly, the area of vacuolation in *SOD1* 2B3-201 mice, was 50.15 ± 1.81 units, again not significantly different from either of the other *SOD1* groups. However, average vacuolation (41.65 ± 2.45 units) and total vacuolation (225.31 ± 16.26 units) were significantly lower in the *SOD1* 2B3-201 group compared with *SOD1* saline mice (average $p<0.01$, total $p<0.05$), but not significantly different from MP-treated *SOD1* mice ($p>0.05$).

In the hypoglossal nucleus (**Figure 5.6**I-L**, Figure 5.7**G-I), again, substantial vacuolation was evident in *SOD1* mice treated with saline, with an area of 21.39 ± 0.63 units, average vacuolation of 52.78 ± 4.79 units and total vacuolation of 113.81 ± 13.05 units, which were significantly greater than wild type saline mice ($p<0.001$). *SOD1* mice given MP had a similar area (23.84 ± 1.27 units), average vacuolation (43.89 ± 5.53 units) and total vacuolation (106.35 ± 16.41 units), and these were significantly different from wild type saline ($p<0.001$), but not significantly different to *SOD1* saline mice ($p>0.05$). Just as for the other two nuclei, the hypoglossal nucleus in *SOD1* mice treated with 2B3-201 showed a significantly lower average (36.72 ± 2.41 units) and total vacuolation (73.56 ± 7.22 units), and these were both significantly lower than *SOD1* saline ($p<0.05$) but not *SOD1* mice treated with free MP ($p>0.05$). The area of vacuolation however, was not significantly different from the other two *SOD1* treatment groups ($p>0.05$).

5.4.4 Motor neuron counts

Motor neurons were counted in the three motor nuclei, to give the total number of motor neurons and the number of morphologically normal motor neurons, i.e. vacuole-free, and these data were used to calculate the percentage of morphologically normal neurons.

In the trigeminal nucleus (**Figure 5.6**A-D**, Figure 5.8**A-C), wild type mice had 287.0 ±13.3 neurons, of which 241.5 ± 13.5 neurons were normal in appearance, giving 91.0 ± 1.7% of morphologically normal neurons. The total number of neurons were lower in all three *SOD1* treatment groups compared with wild type mice ($p<0.001$): *SOD1* saline had 200.5 ± 11.9 neurons, *SOD1* MP 186.0 ± 9.0 neurons, and *SOD1* 2B3-201 178.0 ± 13.7 neurons. No difference was found between *SOD1* treatment groups with regards total neurons ($p>0.05$). The number of morphologically normal neurons was also significantly lower in all three *SOD1* treatment groups compared with wild type ($p<0.001$): *SOD1* saline had 128.0 ± 14.4 neurons, *SOD1* MP 123 ± 13.2 neurons, and *SOD1* 2B3-201 141.0 ± 12.5 neurons. Again, no statistical difference was found between *SOD1* treatment groups ($p<0.05$). Similarly, the proportion of morphologically normal to abnormal appearing

neurons was much lower in all *SOD1* treatment groups compared with wild type mice ($p<0.001$): 67.5 ± 4.6% of neurons were morphologically normal in *SOD1* saline, 70.3 ± 5.9% for *SOD1* MP and a higher proportion of 80.0 ± 2.4% for *SOD1* 2B3-201. In this case, the proportion of morphologically normal neurons was significantly higher in *SOD1* 2B3-201 compared with *SOD1* saline ($p<0.05$), and there was a trend to a higher proportion in *SOD1* 2B3-201 compared with free MP ($p=0.13$), but no difference was found between *SOD1* saline and *SOD1* MP ($p>0.05$).

In the facial nucleus (**Figure 5.6**E-H**, Figure 5.8**D-F) wild type mice had 612.0 ± 10.8 neurons in total, 563 ± 11.2 neurons of which were normal in appearance, giving 92.9 ± 1.1% morphologically normal neurons. The total number of neurons was significantly lower in all *SOD1* groups compared with wild type mice ($p<0.001$): *SOD1* saline had 417.5 ± 14.3 neurons, *SOD1* MP 427.0 ± 19.2 neurons, and *SOD1* 2B3-201 488.0 ± 20.5 neurons, with *SOD1* 2B3-201 having significantly more neurons than either *SOD1* saline or *SOD1* MP ($p<0.05$). No significant difference was found between *SOD1* saline and MP in terms of total neurons. The number of morphologically normal neurons was also significantly lower in all *SOD1* treatment groups compared with wild type mice ($p<0.001$): there were 244.5 ± 25.0 neurons in *SOD1* saline, 262.5 ± 41.9 in *SOD1* MP, and 382.0 ± 31.8 neurons in *SOD1* 2B3-201. *SOD1* mice treated with 2B3-201 had significantly more morphologically normal neurons than either *SOD1* treated with saline ($p<0.05$) or free MP ($p<0.05$), but no difference was seen between *SOD1* saline and *SOD1* MP ($p>0.05$). Again, the percentage of morphologically normal neurons was much lower in all three *SOD1* groups compared with wild type saline control ($p<0.001$): 56.4 ± 5.6% of neurons were morphologically normal in *SOD1* saline, 60.7 ± 7.9% in *SOD1* MP, and 77.7 ± 6.5% in *SOD1* 2B3-201 mice. *SOD1* 2B3-201 had a significantly higher proportion of morphologically normal appearing neurons compared with *SOD1* saline and *SOD1* MP ($p<0.05$), but there was no difference between *SOD1* saline and *SOD1* MP mice ($p>0.05$).

In the hypoglossal nucleus (**Figure 5.7**I-L**, Figure 5.8**G-I) wild type mice had 240.0 ± 8.0 total neurons, 229.5 ± 7.6 morphologically normal neurons, and thus 93.6 ± 0.8% morphologically normal neurons from the total neuron pool. All three *SOD1* treatment groups had fewer total neurons compared with wild type mice ($p<0.001$): *SOD1* saline had 203.0 ± 13.9 total neurons, *SOD1* MP had 193.5 ± 8.8 neurons, and *SOD1* 2B3-201 had 207.0 ± 10.1 neurons. No significant differences were found between *SOD1* treatment groups ($p>0.05$). The number of morphologically normal neurons was significantly lower in all *SOD1* treatment groups compared with wild type ($p<0.05$): 105.0 ± 16.1 morphologically normal neurons in *SOD1* saline, 117.0 ± 15.0 in *SOD1* MP, and 162.0 ± 17.1 for *SOD1* 2B3-201. The number of morphologically normal neurons was significantly higher for *SOD1* 2B3-201 compared with both *SOD1* saline and *SOD1* MP ($p<0.05$), but there was no difference between *SOD1* saline and *SOD1* MP ($p>0.05$). The percentage of morphologically normal neurons in the total neuron pool was also significantly lower for all *SOD1* treatment groups compared with wild type control ($p<0.001$): there was 54.9 ± 6.1% in *SOD1* saline, 60.1 ± 8.6% in *SOD1* MP, and 83.0 ± 1.9% for *SOD1* 2B3-201. A significantly higher percentage of healthy neurons was found in the *SOD1* 2B3-201 group compared with both other *SOD1* treatment groups ($p<0.01$), but no significant difference between *SOD1* saline and *SOD1* MP.

Within the ventral horn of the spinal cord (**Figure 5.6**M-P**, Figure 5.8**J-L), wild type mice had a total of 81.0 ± 3.7 neurons, of which 76.5 ± 3.8 were morphologically normal, giving 95.0 ± 3.4% morphologically normal neurons. All *SOD1* treatment groups had significantly lower total neurons compared with wild type control mice ($p<0.001$): 60.0 ± 5.1 neurons in the *SOD1* saline group, 54.0 ± 3.3 in *SOD1* MP, and 61.5 ± 2.6 in *SOD1* 2B3-201. Significantly fewer morphologically normal neurons were found in the three *SOD1* treatment groups compared with wild type mice ($p<0.001$): 39.0 ± 8.9 neurons in *SOD1* saline, 33.5 ± 6.3 neurons in *SOD1* MP, and 43.0 ± 5.1 neurons in *SOD1* 2B3-201. Correspondingly, a smaller percentage of morphologically normal neurons was evident in the three *SOD1* treatment groups compared with wild type mice ($p<0.001$): 72.0 ± 10.7%

in *SOD1* saline, 62.3 ± 8.9% in *SOD1* MP, and 75.7 ± 7.2% in *SOD1* 2B3-201. However, unlike the three cranial motor nuclei above, no significant difference was found between any of the *SOD1* treatment groups, either for total neurons, number of morphologically normal neurons, or percentage morphologically normal neurons ($p>0.05$).

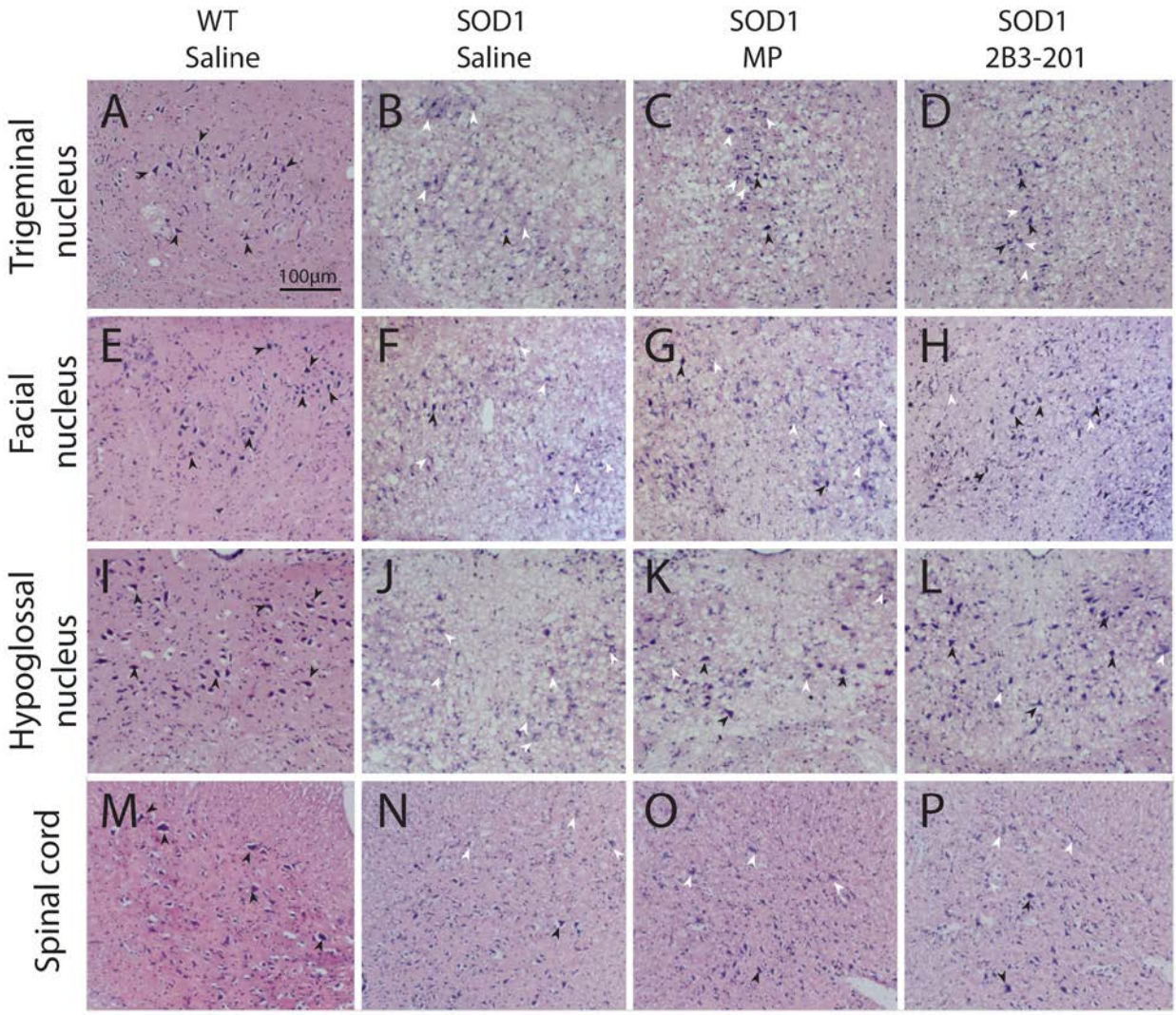


Figure 5.6 – Light micrographs of sections of trigeminal, facial and hypoglossal nuclei, and ventral spinal cord from the 2B3-201 study, stained with H&E

Wild type tissue shows staining of large, morphologically normal motor neurons (black arrows) in the cranial motor nuclei (A, E, I) and spinal cord (M), with no structural abnormalities. In contrast, *SOD1* saline (B, F, J, N) and *SOD1* MPS (C, G, K, O) show a reduction in large motor neurons, with more morphologically abnormal neurons (white arrows), in the cranial motor nuclei. There is also substantial vacuolation, and a loss of large motor neurons in the ventral spinal cord. *SOD1* mice treated with 2B3-201 (D, H, L, P) have an increase in the number of morphologically normal neurons, and reduced vacuolation, in the cranial motor nuclei compared with *SOD1* saline and free MP, but pathology in the spinal cord is not altered.

SOD1 saline and *SOD1* 2B3-201 N=10, *SOD1* saline N=8, and *SOD1* MP N=9. Scale bar applies to all images.

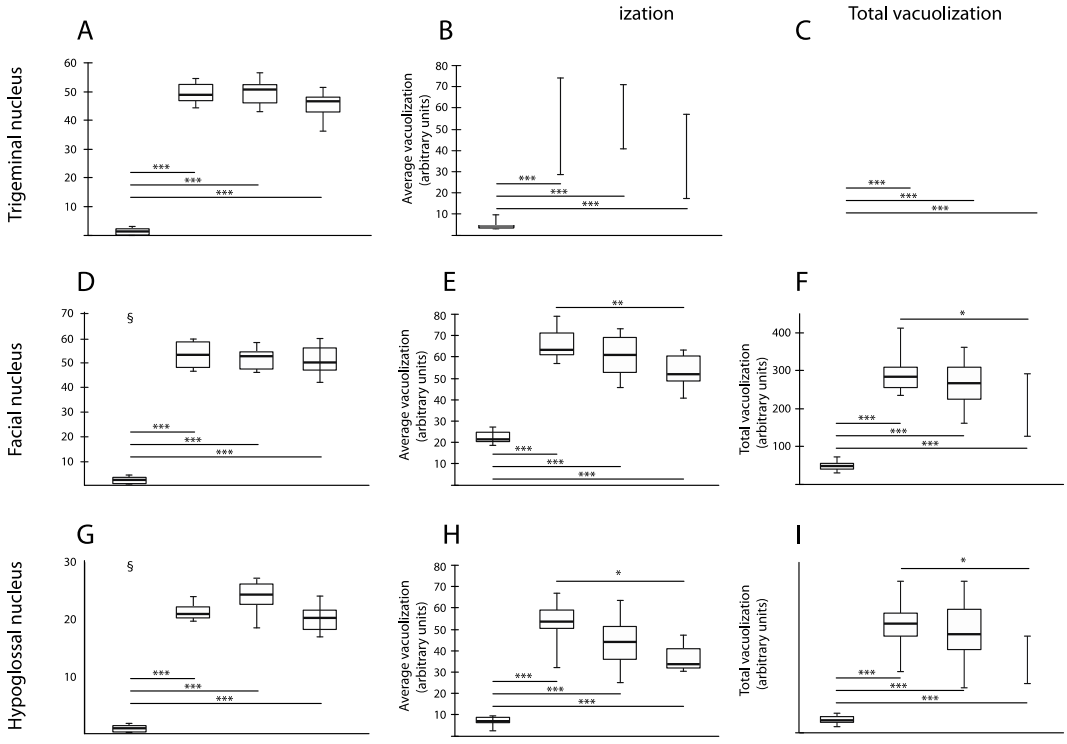


Figure 5.7 – Quantification of vacuolation in the trigeminal, facial and hypoglossal nuclei from the 2B3-201 study

Vacuolation (A, D, G) was present in all *SOD1* groups and absent in wild type mice, but was not significantly different between *SOD1* treatment groups. However, the average (B, D, G) and total amount of vacuolation (C, F, I) were significantly lower in *SOD1* mice treated with 2B3-201 compared with both saline and free MP in the trigeminal nucleus, and was also significantly lower than saline in the facial and hypoglossal nuclei. Both average and total vacuolation were also higher in all *SOD1* groups compared with wild type mice. Because of the non-parametric analysis performed here, data are presented in a box and whisker plot, with the median (strong central band), interquartile range (box) and range (whiskers).

§ For area of vacuolation, WT values are set to 0, because no vacuolation is present.

SOD1 saline and *SOD1* 2B3-201 N=10, *SOD1* saline N=8, and *SOD1* MP N=9.

* p<0.05; ** p<0.01; *** p<0.001

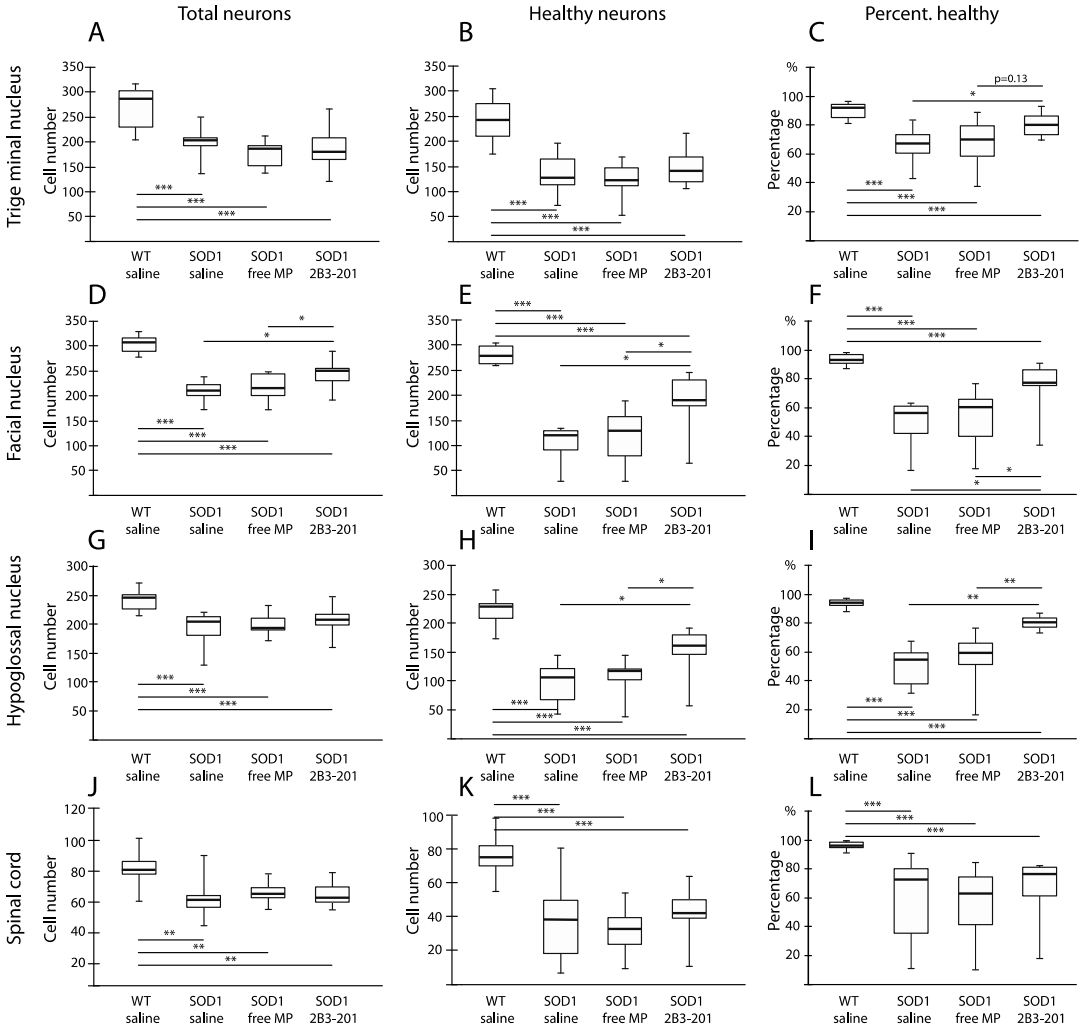


Figure 5.8 – motor neuron counts in the trigeminal, facial and hypoglossal nuclei, and the lumbar spinal cord (ventral horn) from the 2B3-201 study

The total number of neurons (A, D, G, J), number of morphologically normal neurons (B, E, H, K) and the proportion of morphologically normal neurons (C, F, I, L) are reduced in all *SOD1* groups compared with wild type mice. The total number of neurons is significantly higher in *SOD1* mice treated with 2B3-201 compared with both saline and free MP in the facial nucleus, but in no other regions. However, The number of morphologically normal neurons is higher in *SOD1* mice treated with 2B3-201 compared with both saline and free MP in the facial and hypoglossal nuclei, and the proportion of morphologically normal neurons is increased in *SOD1* 2B3-201 compared with saline and free MP in all three cranial nuclei. No improvement was seen in the spinal cord. Because of the non-parametric analysis performed here, data are presented in a box and whisker plot, with the median (strong central band), interquartile range (box) and range (whiskers).

SOD1 saline and *SOD1* 2B3-201 N=10, *SOD1* saline N=8, and *SOD1* MP N=9.

* p<0.05; ** p<0.01; *** p<0.001

5.4.5 GFAP staining

Brainstem and spinal cord sections were stained using an antibody against GFAP, and then the intensity of stain was quantified as discussed in the Methods above. In addition, the number of GFAP positive astrocytes were counted in the grey matter of the cranial motor nuclei and ventral horn of the spinal cord. Unlike the white matter, where there is a large population of GFAP-positive astrocytes, not many can be seen typically in the grey matter of wild type mice.

In the trigeminal nucleus (

Figure 5.9A-D**, Figure 5.10**A-B), the wild type GFAP staining intensity was 1.4 ± 0.1 units, with 2.6 ± 0.6 astrocytes per ROI. GFAP staining intensity was much higher in all *SOD1* treatment groups compared with wild type mice ($p<0.001$): 11.9 ± 1.6 units for *SOD1* saline, 14.3 ± 1.6 units for *SOD1* MP, and 8.4 ± 1.0 units for *SOD1* 2B3-201. GFAP signal intensity was also significantly lower in *SOD1* 2B3-201 compared with both *SOD1* saline ($p<0.05$) and *SOD1* MP ($p<0.01$), but there was no significant difference between *SOD1* saline and *SOD1* MP mice ($p>0.05$). The number of reactive astrocytes was also significantly higher in the three *SOD1* treatment groups compared with wild type mice ($p<0.001$): 82.9 ± 8.2 for *SOD1* saline, 102.8 ± 4.6 for *SOD1* MP, and 48.9 ± 6.5 for *SOD1* 2B3-201. Again, *SOD1* 2B3-201 had significantly fewer astrocytes compared with both *SOD1* saline ($p<0.01$) and *SOD1* MP mice ($p<0.001$), but no significant difference was found between *SOD1* saline and *SOD1* MP ($p>0.05$).

In the facial nucleus (

Figure 5.9E-H**, Figure 5.10**C-D), the wild type saline GFAP staining intensity was 1.5 ± 0.2 units, and 2.6 ± 1.0 GFAP-positive astrocytes were counted per ROI. The GFAP staining intensity was significantly higher in all three *SOD1* groups compared with wild type mice ($p<0.001$): 17.0 ± 1.6 units in *SOD1* saline, 17.3 ± 2.1 units in *SOD1* MP, and 10.0 ± 1.1 units in *SOD1* 2B3-201. The staining intensity in the *SOD1* 2B3-201 group was

significantly lower than both *SOD1* saline and *SOD1* MP ($p<0.01$), but no significant difference was found between *SOD1* saline and *SOD1* MP mice ($p>0.05$). The number of reactive astrocytes seen in the facial nucleus was significantly higher in *SOD1* 2B3-201 than wild type mice ($p<0.001$): 111.0 ± 6.0 in *SOD1* saline, 105.6 ± 6.7 in *SOD1* MP and 58.1 ± 6.3 for *SOD1* 2B3-201. Significantly fewer astrocytes were counted in *SOD1* mice treated with 2B3-201 compared with either saline or free MP ($p<0.001$), but no significant difference was found between *SOD1* saline and *SOD1* MP ($p>0.05$).

In the hypoglossal nucleus (

Figure 5.9I-L**, Figure 5.10**E-F), GFAP staining intensity for wild type mice was 2.0 ± 0.3 units, with an average of 2.3 ± 1.4 astrocytes per ROI. Staining intensity was significantly higher in the three *SOD1* treatment groups compared with wild type mice ($p<0.001$): 18.6 ± 1.1 units in *SOD1* saline, 21.6 ± 1.5 units in *SOD1* MP, and 7.6 ± 1.0 units in *SOD1* 2B3-201. The *SOD1* groups treated with 2B3-201 had significantly lower GFAP immunoreactivity in the hypoglossal nucleus than *SOD1* saline or *SOD1* MP ($p<0.001$), but no significant difference was found between *SOD1* saline and *SOD1* MP mice ($p>0.05$). Significantly more reactive astrocytes were evident in the three *SOD1* groups compared with wild type ($p<0.001$): 82.7 ± 8.7 for *SOD1* saline, 73.3 ± 3.2 for *SOD1* MP, and 36.3 ± 8.0 for *SOD1* 2B3-201. The number of astrocytes in the hypoglossal nucleus was significantly lower for *SOD1* 2B3-201 compared to both *SOD1* saline and MP ($p<0.05$), but no significant difference was evident between *SOD1* saline and *SOD1* MP mice ($p>0.05$).

In the ventral horn of the spinal cord (

Figure 5.9M-P**, Figure 5.10**G-H), wild type GFAP staining intensity was 1.1 ± 1.1 units, and 31.3 ± 1.1 reactive astrocytes were detected per ROI. Significantly higher GFAP immunoreactivity was seen in all three *SOD1* groups compared with wild type ($p<0.001$): 11.8 ± 1.4 units in *SOD1* saline, 15.2 ± 1.9 units in *SOD1* MP, 17.9 ± 2.2 units *SOD1* 2B3-201. Significantly more reactive astrocytes were found in the three *SOD1* treatment

groups compared with wild type ($p<0.001$): 43.8 ± 4.4 in *SOD1* saline, 30.8 ± 5.8 in *SOD1* MP, and 39.5 ± 6.9 in SOD1 2B3-201. However, unlike for the cranial motor nuclei, no significant differences were found between *SOD1* treatment groups with regards to either GFAP staining intensity or number of astrocytes.

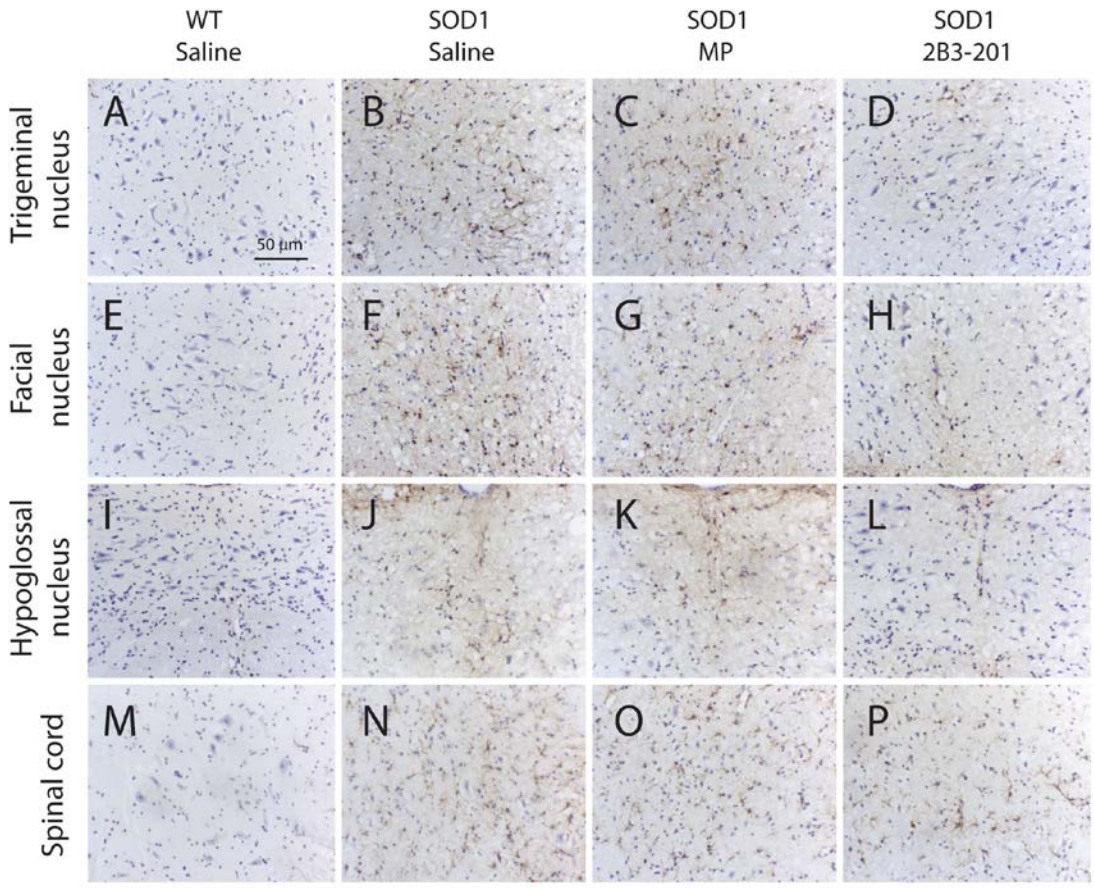


Figure 5.9 – Photomicrographs of GFAP staining in the cranial motor nuclei and spinal cord of mice in the 2B3-201 study

Unlike the white matter, there is very little GFAP staining in the grey matter in wild type mice, either in the cranial motor nuclei (A, E, I), or the ventral grey matter of the spinal cord (M). *SOD1* injected with saline, however, show marked GFAP up-regulation in the trigeminal (B), facial (F) and hypoglossal (J) nuclei, as well as the ventral spinal cord (N). A similar staining pattern is observed in *SOD1* mice treated with free MP (C, G, K, O). GFAP staining in *SOD1* 2B3-201 mice, however, is significantly reduced, both in the trigeminal (D), facial (H) and hypoglossal (L) nuclei, but not in the ventral spinal cord (P). Because of the non-parametric analysis performed here, data are presented in a box and whisker plot, with the median (strong central band), interquartile range (box) and range (whiskers).

SOD1 saline and *SOD1* 2B3-201 N=10, *SOD1* saline N=8, and *SOD1* MP N=9. Scale bar applies to all images.

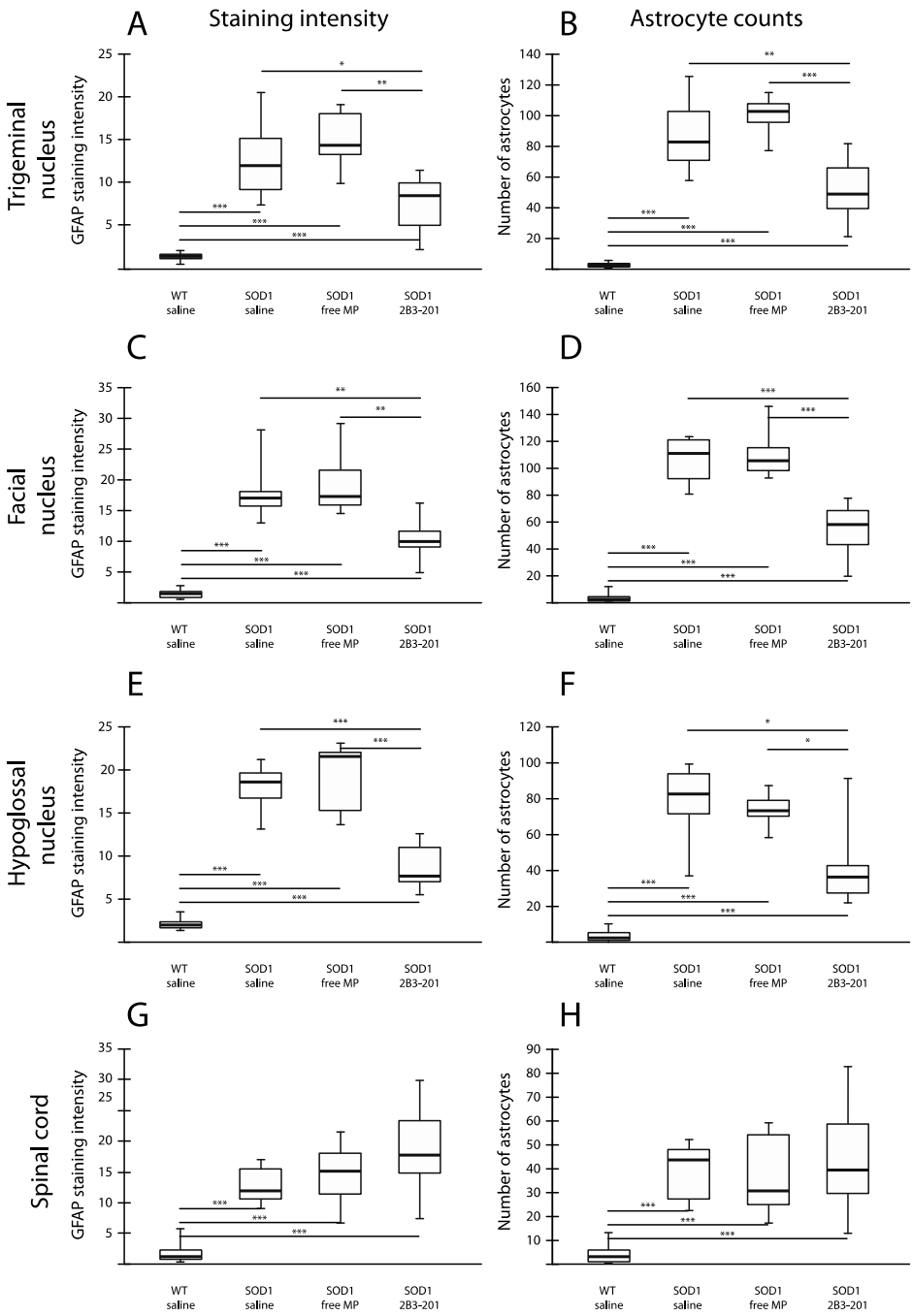


Figure 5.10 – Quantification of GFAP staining intensity and astrocyte counts in the cranial motor nuclei and spinal cord of mice from the 2B3-201 study

All SOD1 mice had stronger GFAP staining (A, C, E, G) and more astrocytes (B, D, F, H) in the three motor nuclei and spinal cord compared with wild type mice. GFAP staining was significantly reduced, and was associated with fewer reactive astrocytes, in *SOD1* mice treated with 2B3-201 compared with both saline and free MP in the trigeminal, facial and hypoglossal nucleus, but not in the spinal cord. Because of the non-parametric analysis performed here, data are presented in a box and whisker plot, with the median (strong central band), interquartile range (box) and range (whiskers).

SOD1 saline and *SOD1* 2B3-201 N=10, *SOD1* saline N=8, and *SOD1* MP N=9.

* p<0.05; ** p<0.01; *** p<0.001

5.4.6 Iba1 staining

Sections of the cranial motor nuclei and spinal cord were stained using an antibody against Iba1, and the intensity of stain was quantified in the same manner as for GFAP. In addition, the number of Iba1-positive microglia were counted in the grey matter of the cranial motor nuclei and ventral horn of the spinal cord. Iba1 is mainly expressed in activated microglia, with only very low levels of constitutive expression in wild type microglia.

In the trigeminal nucleus (**Figure 5.11**A-D**, Figure 5.12**A-B), wild type Iba1 staining intensity was 2.8 ± 0.3 units, with an average of 11.1 ± 1.9 Iba1-positive microglia per ROI. Iba-1 staining was significantly higher in all three *SOD1* treatment groups compared with wild type mice ($p<0.001$): 11.2 ± 0.8 units in *SOD1* saline, 11.3 ± 1.0 units in *SOD1* MP, and 12.3 ± 0.9 units in *SOD1* 2B3-201. Similarly, the average number of Iba1-positive microglia per cross-section was significantly higher in the three *SOD1* treatment groups compared with wild type control mice ($p<0.001$): 53.1 ± 4.0 in *SOD1* saline, 45.9 ± 2.8 in *SOD1* MP, and 49.8 ± 4.0 in *SOD1* 2B3-201. However, no significant differences were seen between any of the *SOD1* treatment groups, either for Iba1 staining intensity or number of Iba1-positive microglia ($p>0.05$).

In the facial nucleus (**Figure 5.11**E-H**, Figure 5.12**C-D) wild type Iba1 staining intensity was 1.8 ± 0.3 units, and on average 10.6 ± 1.3 Iba1-positive microglia were evident per ROI. Iba1 staining intensity was significantly higher for all *SOD1* mice compared with wild type ($p<0.001$); 11.8 ± 1.7 units in *SOD1* saline, 12.1 ± 0.7 units in *SOD1* MP, and 11.2 ± 1.1 units in *SOD1* 2B3-201. Significantly more Iba1-positive microglia were seen in the three *SOD1* groups compared with wild type mice ($p<0.001$): 38.9 ± 3.7 in *SOD1* saline, 40.0 ± 3.2 in *SOD1* MP, and 46.4 ± 3.3 in *SOD1* 2B3-201. As above, no significant differences in Iba1 staining intensity or number of microglia were seen in the facial nucleus between *SOD1* treatment groups ($p>0.05$).

In the hypoglossal nucleus (**Figure 5.11**I-L**, Figure 5.12**E-F) staining intensity for Iba1 in wild type mice was 1.7 ± 0.2 units, with an average of 9.0 ± 1.8 Iba1-positive microglia per ROI. Iba1 staining intensity was significantly higher in all three *SOD1* treatment groups compared with wild type mice ($p<0.001$): 12.2 ± 0.8 units in *SOD1* saline, 12.5 ± 0.9 units in *SOD1* MP, and 10.1 ± 1.2 units in *SOD1* 2B3-201. The number of Iba1-postive microglia per cross-section was also significantly higher in all *SOD1* mice compared with wild type control mice ($p<0.001$): 33.0 ± 4.6 in *SOD1* saline, 34.2 ± 3.4 in *SOD1* MP, and 32.0 ± 4.4 in *SOD1* 2B3-201. No significant difference was found in Iba1 staining intensity or microglia number in the hypoglossal nucleus between any of the *SOD1* treatment groups ($p>0.05$).

Finally, in the ventral horn of the spinal cord (**Figure 5.11**M-P**, Figure 5.12**G-H), Iba1 staining intensity for wild type mice was 0.9 ± 0.2 units, with an average of 12.4 ± 0.8 Iba1-positive microglia per ROI. Iba1 staining intensity was significantly higher in all three *SOD1* treatment groups compared with wild type controls ($p<0.001$): 9.3 ± 0.9 units in *SOD1* saline, 10.2 ± 0.8 units in *SOD1* MP, and 9.6 ± 0.6 units in *SOD1* 2B3-201. Significantly more Iba1-positive microglia were seen in the three *SOD1* treatment groups compared with wild type mice ($p<0.001$): 31.6 ± 4.6 in *SOD1* saline, 40.2 ± 2.8 in *SOD1* MP, and 38.9 ± 2.9 in *SOD1* 2B3-201. However, as for all of the other CNS regions above, no significant differences were found, either in Iba1 staining intensity or Iba1-positive microglia numbers, between *SOD1* treatment groups ($p>0.05$).

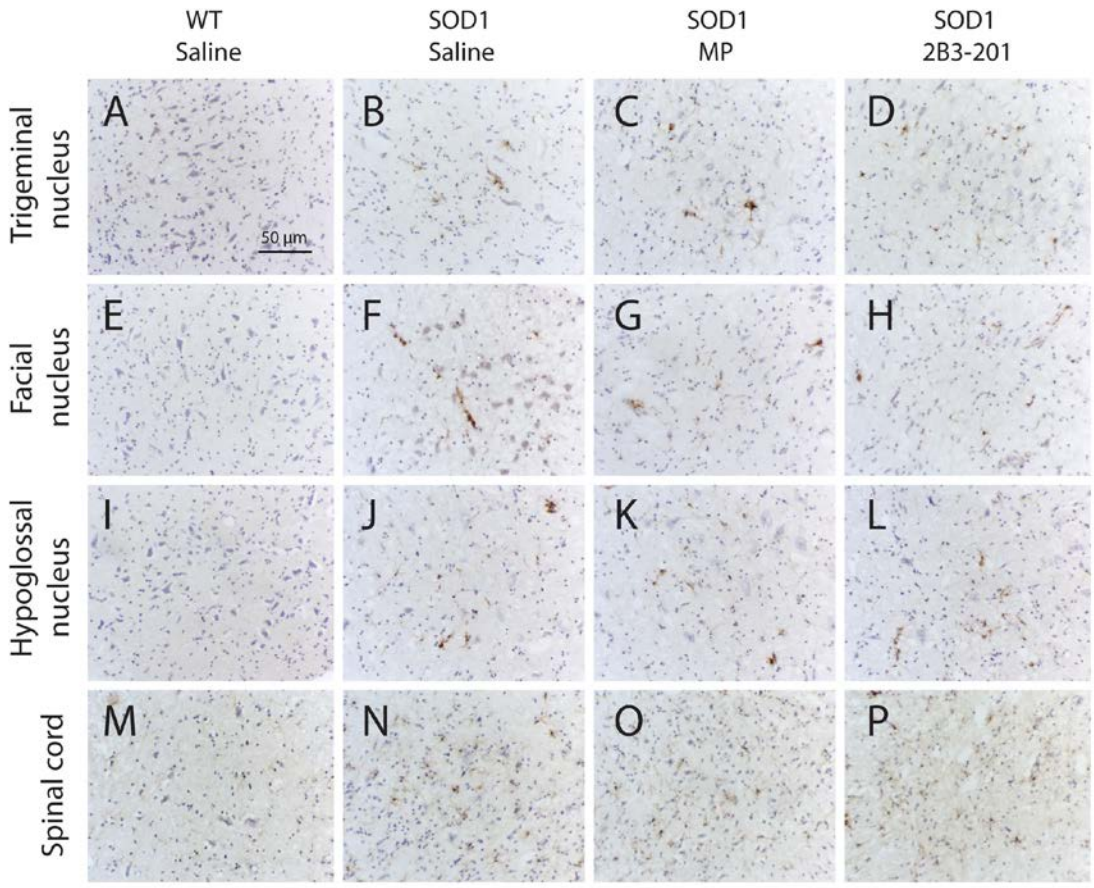


Figure 5.11 - Photomicrographs of Iba1 staining in the cranial motor nuclei and spinal cord of mice in the 2B3-201 study

Wild type Iba1 immunoreactivity was very low, in the trigeminal (A) facial (E) and hypoglossal nuclei (I), and in the spinal cord (M). *SOD1* mice treated with saline (B, F, J, N), free MP (C, G, K, O) and 2B3-201 (D, H, L, P) showed much stronger staining for Iba1, both in the three brainstem nuclei and the spinal cord. However, no difference was found in Iba1 immunoreactivity between *SOD1* treatment groups.

SOD1 saline and *SOD1* 2B3-201 N=10, *SOD1* saline N=8, and *SOD1* MP N=9. Scale bar applies to all images.

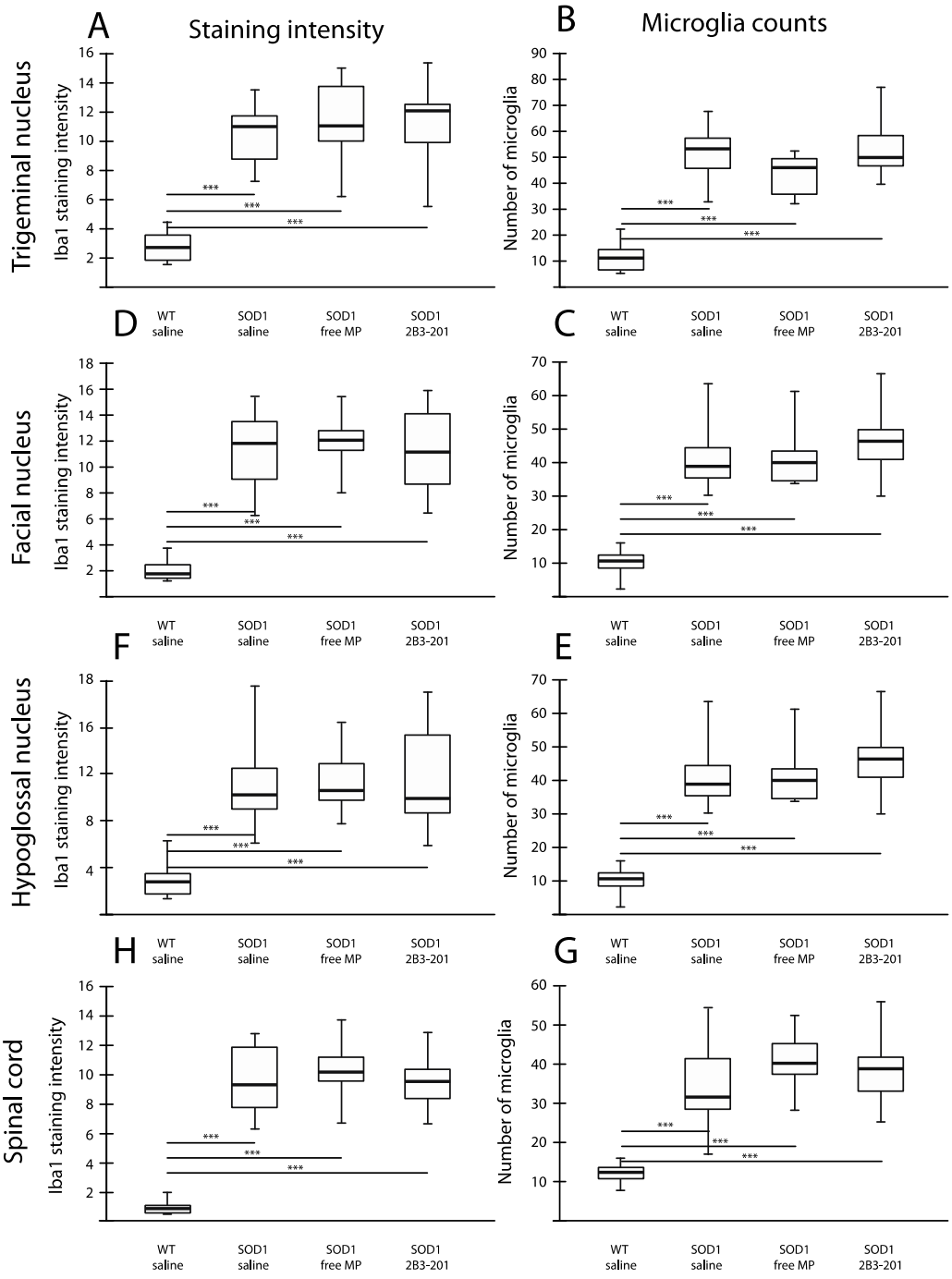


Figure 5.12 - Quantification of Iba1 staining intensity and microglia counts in the cranial motor nuclei and spinal cord of mice from the 2B3-201 study

All *SOD1* mice had stronger Iba1 staining (A, C, E, G) and more microglia (B, D, F, H) in the three motor nuclei and spinal cord compared with wild type mice. However, Iba1 staining intensity and microglia number did not differ between *SOD1* treatment groups in any region. Because of the non-parametric analysis performed here, data are presented in a box and whisker plot, with the median (strong central band), interquartile range (box) and range (whiskers).

SOD1 saline and *SOD1* 2B3-201 N=10, *SOD1* saline N=8, and *SOD1* MP N=9.

* p<0.05; ** p<0.01; *** p<0.001

5.5 Discussion

The results from this chapter show that methylprednisolone packaged in a PEGylated, and glutathione-modified liposome (2B3-201), reduces apparent astrocytosis and increases neuronal health in *SOD1*^{G93A} mice, whereas free methylprednisolone (MP) was ineffective. These findings suggest that previous unsuccessful attempts to use glucocorticoids therapeutically in ALS patients may be due to poor entry into the CNS (Werdelin et al., 1990).

I used the short T_2 sequence used in Chapter 3 to allow high-throughput scanning, thereby using MRI as a cost-effective biomarker to measure the therapeutic value of the packaged steroid. The typical pattern of T_2 signal change was observed, as shown in Chapter 3 of this thesis as well as in previous publications from other groups (Zang et al., 2004, Bucher et al., 2007), with high signal intensity in the trigeminal, facial and hypoglossal nuclei of saline-treated *SOD1*^{G93A} mice. A comparable level of signal change was found in *SOD1*^{G93A} mice treated with free MP, suggesting a similar level of pathology (i.e. no therapeutic effect), but a marked (30%) reduction in signal change was seen for *SOD1*^{G93A} mice treated with 2B3-201, indicating amelioration to the underlying pathology.

These findings were subsequently confirmed histologically, with significantly reduced vacuolation in the trigeminal, facial and hypoglossal nuclei in *SOD1*^{G93A} mice treated with 2B3-201 compared with both saline-treated and free MP-treated mice. This amelioration of pathology extended to preservation of the total neuron number in the facial nucleus, and number of morphologically normal neurons in all three cranial motor nuclei. However, the therapeutic effect of 2B3-201 appeared to be limited to the cranial motor areas – within the ventral horn of the spinal cord, substantial motor neuron loss was not seen in *SOD1*^{G93A} mice treated with saline, free MP or 2B3-201, and thus no amelioration was found for 2B3-201 in the spinal cord.

A caveat to this approach, however, is in the interpretation of increased morphologically normal neurons based on H&E. The definition used for normal and abnormal in this instance was based on the presence or absence of intracellular vacuoles. The assumption here is that a neuron like the one shown in the right panel of **Figure 5.2**, for example, would have a poorer general cellular health than a normal appearing neuron, and will probably progress to death in the near future. It is also possible that, given the high degree of vacuolation, the neuron could have problems with basic cellular processes, such as maintaining a stable resting membrane potential. Consequently, these vacuolated cells may also have functional deficits that have consequences for muscle action. However, this concept is just a hypothesis, and to confirm this, electrophysiological recordings could be carried out to test whether there are indeed functional savings for mice treated with 2B3-201, as well as the pathological savings detected here. An important extension to this caveat is that an apparently morphologically normal cell, does not necessarily functionally normally, so the degree of morphological amelioration seen here may not result in the same degree of functional amelioration.

Any benefit of 2B3-201 may be through its anti-inflammatory effect on resident glial cells. Glucocorticoids up-regulate anti-inflammatory genes in cells by steroid-receptor complexes binding to gene response elements on pertinent genes (Beato, 1989), and can also interfere with regulation of pro-inflammatory genes by inhibiting transcription factors such as NF-κB (Ray and Prefontaine, 1994). Using immunohistochemistry, I showed that, as has been frequently shown in *SOD1* models of ALS (Hall et al., 1998, Alexianu et al., 2001, Feeney et al., 2001), there is marked activation of astrocytes, both in the cranial motor nuclei and ventral horn of the spinal cord. Consistent with the histological findings above, of vacuolation and neuronal degeneration, no effect of free MP administration on astrocyte activation was evident. However, administration of 2B3-201 to *SOD1*^{G93A} mice significantly down-regulated GFAP in the trigeminal, facial and hypoglossal nuclei, but not in the ventral horn of the spinal cord. The same cannot be said of microglia; whilst up-regulation of Iba1 was evident on microglia in the cranial motor nuclei and ventral horn of

the spinal cord in *SOD1*^{G93A} mice compared to controls, as reported many times previously (Hall et al., 1998, Alexianu et al., 2001, Zhao et al., 2010), no effect of administration of either free MP or 2B3-201 was found in any of the regions studied.

This astrocyte-specific anti-inflammatory effect of 2B3-201 raises the possibility that the effect of the drug may be mediated through astrocyte function. Studies from other neuro-inflammatory models, such as EAE, have indicated that reactive, GFAP-positive astrocytes can have impaired glutamate metabolism, with decreased action of glutamate dehydrogenase and glutamine synthase, which results in higher glutamate concentration and potential excitotoxicity (Hardin-Pouzet et al., 1997). This effect is important, as glutamate excitotoxicity is a common theme in research into ALS pathogenesis (Van Den Bosch et al., 2006). In this framework, then, it is possible that a down-regulation of NF-κB-regulated genes could reduce the reactive nature of astrocytes, thereby restoring normal glutamate transportation and metabolism. This idea is, however, conjecture at present, as we have only shown a correlation between reduction in astrocyte activation and reduction in pathological change. Ideally I would follow up this strand of research with a microdialysis experiment to confirm that there is a reduction in glutamate concentration in mice treated with 2B3-201, and use immunohistochemistry to investigate whether there is an alteration in the glutamate transporter, GLT-1, between treatment groups.

On a related note, there is a need for caution when using the term “activation” of astrocytes or microglia, based on single markers such as GFAP or Iba1. In a broad sense, these are both good markers to indicate a change in phenotype of their respective cell types, but it is becoming increasingly apparent that both astrocytes (Pekny and Nilsson, 2005) and microglia (Henkel et al., 2009) have numerous continua of activation leading to a huge variety of possible phenotypes, so relying entirely on a single marker can be dangerous. Whilst it is clear, from the findings presented here, that astrocytes are altered in some way with 2B3-201 treatment, and it seems that microglia are not, it will be important to use some additional markers to confirm that there really is no change in the microglial

phenotype. If there is a specific effect on astrocytes, though, it will be interesting to determine the source of this specificity, as pathways such as those involved in NF-κB activation are important regulators of transcription in both astrocytes and microglia (Mattson and Camandola, 2001). It is not clear, therefore, why 2B3-201 would effect one cell type, and not the other.

Contrary to the pathological findings discussed in the sections above, whilst all *SOD1*^{G93A} groups significantly underperformed compared with wild type mice on the rotarod, and showed a steady decrease in motor performance throughout the disease, no significant difference was found between any of the *SOD1*^{G93A} treatment groups at any time of testing. A trend to increased motor behaviour was evident in *SOD1*^{G93A} mice treated with 2B3-201, and a trend towards decreased motor behaviour in *SOD1*^{G93A} mice treated with free MP compared with saline-treated *SOD1*^{G93A} mice through much of the testing schedule, but neither reached statistical significance. Because of the differential effect of packaged versus unpackaged MP, there was a trend to increased area under the curve (i.e. preserved motor performance) for *SOD1*^{G93A} mice treated with 2B3-201 compared with free MP, but not for *SOD1*^{G93A} given 2B3-201 compared with saline.

The other issue to highlight with regards to using the rotarod as a measure of motor performance, is that rotarod score will not reflect all of the various motor neuron populations relevant for ALS (i.e. spinal, cranial and cortical). Rotarod performance fundamentally requires balance and motor skills of the fore- and hind-limbs, and as a consequence will primarily reflect physiology of lumbar motor neurons (for hind limbs), cervical motor neurons (for fore limbs) and cerebellar neurons (for balance), the latter of which is not studied here as this region has not typically been implicated in ALS pathology**.** Therefore, the significant improvement in neuronal health seen in the cranial nuclei would not be reflected in the rotarod score. Behavioural tests specific to these nuclei would be difficult to devise, given the areas that they innervate: the trigeminal nerve innervates many of the muscles of the face and jaw, particularly more superficial muscles; the facial

nerve also innervates many muscles of the face and head, especially jaw muscles important for mastication; the hypoglossal nucleus innervates the tongue and associated muscles, and some muscles in the neck. The most pertinent behavioural tests would be those based on eating and drinking behaviour (Lever et al., 2009), but any test of this type would be confounded by affect and appetite, which may make them impractical for a study of this kind. One possibility, which could be considered in the future, is to use EMG recordings of superficial face or neck muscles to measure motor evoked potentials of muscles innervated by these three nuclei.

Consistent with the motor behaviour measurements, no difference in weight was noted at any time point between any of the groups, including between wild type and *SOD1*^{G93A} mice treated with saline, a result that is surprising given previous reports showing a decrease in weight from controls from around 100 days (Weydt et al., 2003), and the weight data reported in Chapter 3. The source of the inconsistency between the weights in this chapter and our/others' previous findings is unknown. The main difference between this paradigm, and that used in Chapter 3, is that mice were tested behaviourally every week from 60 days of age instead of just before sacrifice, so it could be that the drop in weight was prevented by maintenance of muscle mass from the more intense training regime. However, mice were also tested every week by Weydt et al. (2003), so even if this does partially explain the difference between the weight scores from this chapter and those reported in Chapter 3, it cannot be the only influence. Another possible variable is that the diet of the mice was changed mid-way through the experiment, which was outside the experimenters' control, and was only discovered subsequent to completing the experiment. Whilst this would not be expected to have such a dramatic effect, it of course must be taken into consideration when interpreting the weight data. One possibility that must be considered is that occasionally these mice can lose copies of the transgene, which can change the resultant phenotype. In this case, this is not a likely cause of the discrepancy, as all pathological aspects of the disease (brainstem MRI intensities, immunohistochemistry and histology) were consistent between the two chapters.

There are no published reports of glucocorticoid treatment in *SOD1* mouse models of ALS, which is surprising given the interest many groups have in the influence of neuroinflammation in the disease process in these mice (and rats). However, these results are consistent with reports in the Wobbler mouse, showing that corticosterone and 21-aminosteroids can have therapeutic effect in models of motor neuron degeneration (Gonzalez Deniselle et al., 1996, Deniselle et al., 1999, Gonzalez Deniselle et al., 1999a, Gonzalez Deniselle et al., 1999b, Gonzalez Deniselle et al., 2001). However, the studies cited above reported a therapeutic effect for free steroids, whereas the data presented in this chapter only found an effect for packaged steroids. There are, of course, many reasons why this difference might exist, but one attractive idea would be that there are differences in BBB penetrance. Sadly these data are not available, but it would be interesting to compare PK data of drug entry to the CNS, to test the hypothesis that MP is not able to cross into the CNS to the same extent as corticosterone or 21-aminosteroids.

Care must be taken when interpreting these results, however. It has been pointed out time and time again, that treatments highlighted as having great potential *SOD1* models often turn out to fail in the clinic. Therefore, the results from this chapter, whilst exciting in many ways, must be taken with caution. However, it highlights an important principle, which is that some drugs, when apparently having little/no effect when injected unpackaged, may have significant effects on the pathophysiology when targeted to the CNS, where they are actually needed. This may go some way to explain why a closely-related molecule to methylprednisolone – prednisolone – was not effective in ALS patients, nor was the immunosuppressant azathioprine (Werdelin et al., 1990). Perhaps researchers need to reconsider many drug treatments that have been unsuccessful, either in preclinical models, or in human patients, and investigate whether packaging these drugs, and targeting to the CNS offers more of a therapeutic effect than administering the drugs in an unpackaged form. This idea is discussed further in the General Discussion.

Chapter 6: General discussion

6.1 Principal findings

The principal findings from this thesis are as follows:

1. T_2 MRI of the cranial motor nuclei remains the best available MRI biomarker in *SOD1*^{G93A} mice, which is most likely due to changes in tissue structure/integrity rather than a simple accumulation of fluid.
2. Little-to-no vascular changes (activation or permeability) were observed throughout the disease in *SOD1*^{G93A} mice, despite the presence of other inflammatory mechanisms, suggesting this is not a necessary feature of *SOD1*^{G93A} pathophysiology.
3. Specific delivery of methylprednisolone into the CNS, using a PEGylated, glutathione-modified liposome delivery system, improves brainstem indices of neuronal degeneration and astrocytosis in *SOD1*^{G93A} mice, but unpackaged methylprednisolone does not.

6.2 T_2 MRI as a cost-effective biomarker in pre-clinical trials

In Chapter 3, I explored the use of MRI as a biomarker for brainstem pathological changes in the *SOD1*^{G93A} mouse model. I was able to show, consistent with previous findings (Niessen et al., 2006, Bucher et al., 2007), that there are early and progressive changes in the trigeminal, facial and hypoglossal nuclei in *SOD1*^{G93A} mice using T_2 MRI, which had greater sensitivity for *SOD1*^{G93A} pathology than either diffusion-weighted imaging (consistent with the findings of Niessen et al. (2006)) or magnetization transfer imaging. However, the novelty of the sequence used here is that it is substantially shorter than sequences used in previous studies (which were of the order of 10's of minutes, up to

>1h), but still had very good spatial resolution despite the limited acquisition time (96 x 96μm). The sequence also did not compromise sensitivity for pathological processes, as the changes shown in this thesis (Chapter 3) occurred at earlier time points than those found in previous reports; *SOD1*^{G93A} mice had significantly higher signal intensity from 60 days (in the facial nucleus) compared with wild type mice. The application of fast sequences has considerable relevance for pre-clinical trials, as MRI, whilst having much potential for following disease progression, is currently a relatively expensive disease biomarker. The sequence used here, which is relatively standard in clinical MRI, would allow high-throughput scanning, and thereby significantly reduce the costs associated with pre-clinical trials.

The other advantage of using short acquisitions is that multiple sequences can be used in the same imaging session, allowing us to draw stronger conclusions about the underlying pathology by imaging multiple aspects of the disease process. I demonstrated that the T_2 change observed in the cranial nuclei of *SOD1*^{G93A} mice is unlikely to be due simply to increased water load in the tissue, as this would affect T_1 relaxation in a similar manner, which it did not. Instead, I propose that more complex structural changes alter the diffusion properties of the tissue, including vacuolation and morphological change associated with glial activation. These changes could affect T_2 relaxation, and additionally affect the parameters in diffusion-weighted and magnetization transfer images.

T_2 MRI was later used in Chapter 5 as a high-throughput biomarker to investigate the therapeutic effect of packaged methylprednisolone to treat ALS pathology in *SOD1*^{G93A} mice. I demonstrated that T_2 MRI is capable of detecting a therapeutic effect, as the packaged drug ameliorated the increase in T_2 signal intensity associated with *SOD1*^{G93A} pathology, which was confirmed by histological and immunohistochemical analysis. This change in the MR properties of the tissue occurred despite the lack of a statistically significant difference in motor behaviour (rotarod) or weight between the groups. Whilst the lack of behavioural amelioration is probably explained by the lack of sensitivity of

rotarod score to brainstem changes (which is discussed in more detail in 5.5), it highlights a general principal that MRI is highly sensitive to differences in pathology due to drug treatment, which the more variable behavioural measures are not. The specific relevance of packaged versus free methylprednisolone in ALS treatment in discussed in section **6.5** below.

6.3 No change in BBB permeability

In Chapter 3 I demonstrated that markedly increased BBB permeability may not be a necessary feature of disease in *SOD1*^{G93A} mice; injection of Gd-DTPA, a tracer typically used to detect BBB permeability using MRI, did not cause signal change within the CNS in *SOD1*^{G93A} mice at any stage of the disease, even at disease endpoint (120 days). These findings were confirmed with immunohistochemistry for IgG. This result was surprising, as a number of groups have previously shown permeability changes in *SOD1*^{G93A} mice (Garbuzova-Davis et al., 2007a, Garbuzova-Davis et al., 2007b, Zhong et al., 2008) and rats (Andjus et al., 2009, Bataveljic et al., 2009, Nicaise et al., 2009a).

One of the reasons for this discrepancy could be an inherent limitation of one of the techniques used. Garbuzova-Davis et al. (2007b) and Nicaise et al. (2009a) presented data suggestive of BBB breakdown in the brain and spinal cord using Evans blue, a fluorescent injectable tracer. Evans blue is known to bind to large blood-born proteins (predominantly albumin), both *in vivo* and *in vitro* (Allen and Orahovats, 1948, Steinwall and Klatzo, 1966) so is often used as a measure of tissue permeability to large proteins (Saria and Lundberg, 1983). One caveat to the interpretation of Evans blue, is that this low molecular weight dye (961 Da) can dissociate from the larger albumin molecule (67 kDa) and then cross a barrier only permeable to much smaller molecules. A related complication is that unbound Evans blue can bind to other cellular components, including neurons and glia within the CNS (Clasen et al., 1970, Persson et al., 1976). Therefore, in the unbound form, the dye could bind to cells crossing into the CNS (e.g. macrophages), and would then reflect active leukocyte recruitment rather than passive protein diffusion

due to BBB breakdown. Indeed, the fluorescence pattern observed in Garbuzova-Davis et al. (2007b) is notably granular, suggesting that the dye may be sequestered by, or bound to, other cell types. Staining of endogenous blood proteins, such as IgG or albumin, may be easier to interpret; measuring endogenous proteins reflects permeability to molecules of a known size that are not found in healthy conditions in the CNS, and do not have the complication of variation in binding characteristics.

The approach of staining endogenous molecules was used by Zhong et al. (2008), who reported increased IgG penetrance of the CNS, and increased haemosiderin deposits in *SOD1* mouse models, with the latter attributed to microhaemorrhages. These methods, however, are not without their drawbacks. IgG is inherently an immune molecule, so an increase in IgG staining within the CNS, in a model with a strong inflammatory component, should be interpreted with caution. Increased haemosiderin deposition is often taken as a marker of microhaemorrhages, as haemoglobin molecules from infiltrating erythrocytes are broken down to porphyrin, iron and globin, and the iron is subsequently taken up into iron stores (ferritin and haemosiderin). However, many factors can increase iron storage in organs, not least of which are inflammatory signals. For example, IL-1β and IL-6 increase liver production of hepcidin (Lee et al., 2005), which in turn inhibits iron release from macrophage stores (Weinstein et al., 2002). In light of this, it is unsurprising that increased brain iron load has been noted in many degenerative conditions such as Alzheimer's disease (Smith et al., 1997). Presence of haemosiderin would be stronger evidence of microhaemorrages if accompanied by an assay for some other product of haem catabolism, such as biliverdin. However, despite the caveats discussed here, taken together the evidence is strongly suggestive of BBB breakdown in *SOD1* ALS.

Unpublished findings from our laboratory illustrate the potential importance of systemic inflammation in the natural history of the disease in *SOD1*^{G93A} mice, which may go some way to explaining the discrepancy between the lack of permeability change reported in this thesis, and the previously published studies in this area. Our mouse colony was

historically housed in a ‘dirty’ facility, which had high exposure to a variety of pathogens; in this environment the mice had symptom onset at around 90 days, dying at around 120 days. In 2009, the colony was moved to a new ‘clean’ facility, with individually ventilated cages, and very rigorous cleanliness requirements. In this immunologically protected environment, symptom onset shifted to 95-100 days, and survival was increased to 140 days before they reached a state where the license require they be culled (**Figure 6.1**). This marked effect could also be due to other stressors, but it is clear that an environmental factor, most likely immune status, is interacting with the model, and reducing disease severity and progression.

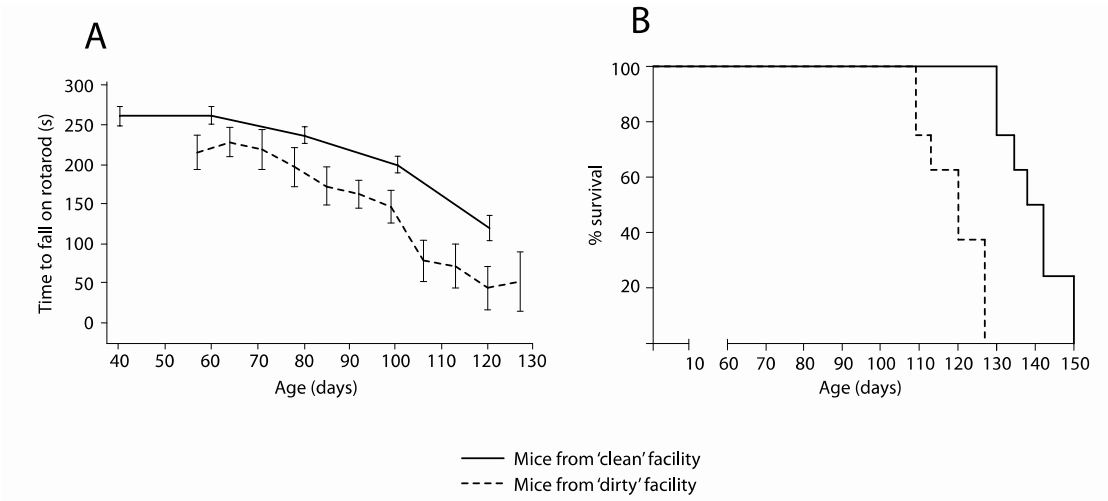


Figure 6.1 – Motor behaviour and survival data of *SOD1*^{G93A} mice housed in a ‘dirty’ and a ‘clean’ facility

SOD1^{G93A} mice housed in a pathogen-containing environment have preserved motor performance (A, full line) compared with the same mice housed in a pathogen-reduced environment (dashed line). Similarly, average survival in the pathogen-containing environment was around 120 days (B, dashed line) whereas this was extended to 140 days when housed in the pathogen-free environment (B full line).

This is an important feature to take into consideration, because there is a large body of research showing that systemic inflammation can exacerbate central inflammation (Palin et al., 2008, Serres et al., 2009a, Murray et al., 2011a, Anthony et al., 2012), possibly due to mechanisms such as microglial priming (Perry et al., 2007). For example, in a prion disease model, intravenous administration of the bacterial cell wall product, lipopolysaccharide (LPS), induced hyperthermia, reduced exploratory activity, and activated microglia, with the latter due to central inflammatory signalling rather than circulating cytokines (Murray et al., 2011a). Similarly, in the ALS literature, the disease process in *SOD1*^{G93A} mice was accelerated by systemic LPS administration (Nguyen et al., 2004). However, because of the limited number of studies addressing BBB mechanisms in ALS, there are no data at present to show how the interaction between central and peripheral inflammation can affect the properties of the BBB. It may be that BBB breakdown is not a consequence of mutant SOD1 expression *per se*, but arises owing to the interaction of *SOD1*-related pathology with peripheral inflammatory mechanisms induced by pathogen exposure. At the very least, the work presented in this thesis shows that BBB breakdown is not necessarily required for disease progression in *SOD1*^{G93A} mice.

Understanding how, and when, the permeability of the BBB changes in disease has important clinical and therapeutic consequences. Firstly, BBB breakdown allows blood-born molecules that are normally excluded from the CNS to cross into the brain parenchyma, which could significantly exacerbate the disease. This may suggest the use of antibiotics, or similar immune-mediated therapies in ALS patients in order to delay disease progression. Secondly, in many ways, BBB breakdown may be beneficial in neurological disorders, as it allows movement of drugs into areas of pathology that are normally too large or hydrophobic to cross the BBB. Drug delivery across an intact barrier is more of a challenge, and requires knowledge of transport mechanisms present on the vessels, which is discussed further in 6.5 below.

6.4 Activation of the endothelium

In Chapters 3 and 4, I explored the activation status of the vascular endothelium using immunohistochemistry for VCAM-1, ICAM-1, E-selectin, and VAP-1. Given the general inflammatory environment in *SOD1*^{G93A} mice, there was a surprising lack of adhesion molecule expression in any of the regions studied, even at disease end stage. In fact, of the four markers studied, only ICAM-1 showed any increase in expression in the disease process, with no change seen for the other three markers. The immunohistochemistry data presented in chapter 3 show significant morphological changes to astrocytes and microglia from 60 days onwards, which presumably undergo functional changes, altering their expression of pro- and anti-inflammatory cytokines. Also, the qRT-PCR data presented in Chapter 4 indicate an early involvement of chemokines (CXCL-10), and substantial post-symptomatic expression of potent pro-inflammatory cytokines (IL-1β, TNF-α). Based on previous experimental findings, from the cytokine expression alone, we would expect a significant up-regulation of VCAM-1, ICAM-1 and E-selectin on the endothelium (Springer, 1990, Wyble et al., 1996, Zhou et al., 2005, Dong et al., 2011).

Two possible explanations may account for the discrepancy between adhesion molecule and cytokine expression. The first is that most of the data relating to the control of adhesion molecule expression by cytokines comes from *in vitro* studies. This is an over-simplified environment where, for example, the influence of IL-1β and TNF-α on endothelial cells can be investigated in isolation. However, in true, physiological conditions, there are likely to be a number of chemical messengers, some pro- and others anti-inflammatory, which act in concert to activate multiple cellular signalling cascades, combining to determine the resultant phenotype of the endothelial cell. In fact, it is clear even in cell culture that two cytokines can have an effect on adhesion molecule expression in combination that neither is capable of when acting individually (Rival et al., 1996). Therefore, it is possible that, had we a fuller picture of cytokine activity, for example using whole transcriptome analysis, the relative combination of pro- and anti- inflammatory

cytokines released at different times in the disease process may account for the lack of VCAM-1, E-selectin and VAP-1 expression.

The other possibility is that there is some inherent feature of the *SOD1*^{G93A} mouse model that interrupts the normal signalling pathways involved in the activation of endothelial cells by cytokines. It is becoming increasingly clear, that at least one important intracellular signalling mechanism that is involved in adhesion molecule up-regulation after cytokine binding is the production of reactive oxygen species (ROS). Interestingly, *SOD1*$^{-/-}$ mice have an increased production of VCAM-1 after ischemic retinopathy compared with wild type mice (Dong et al., 2011), showing that lack of functional SOD1 activity confers vulnerability in terms of endothelial activation to noxious stimuli. This is not just restricted to SOD1, however, as lack of other enzymes with antioxidant activity, such as glutathione peroxidase-1, increases the endothelial expression of VCAM-1 and ICAM-1 (Lubos et al., 2011). Conversely, supplementation with SOD1 protein or other antioxidant compounds attenuates the increase in adhesion molecule expression (ICAM-1 and VCAM-1) caused by treatment of endothelial cells with cytokines, including IL-1β and TNF-α (Kawai et al., 1995, Zhou et al., 2005, Taoufiq et al., 2006), and reduces ICAM-1 expression due to radiation-induced intestinal inflammation (Molla et al., 2005). These observations provide evidence that cytokine signalling involves ROS as second messengers, and that attempts to scavenge ROS by antioxidant treatment can interfere with this pathway. Interestingly, hearts of transgenic mice overexpressing wild type human (i.e. non-mutated) *SOD1* (*SOD1*^{hWT}) show reduced inflammation, including a reduction in ICAM-1 and VCAM-1 expression, due to ischemia-reperfusion injury after transplantation into wild type mice. This result provides further proof that overexpression of SOD1 protein is protective against adhesion molecule expression during inflammation (Tanaka et al., 2004). *SOD1*^{G93A} mice retain functional SOD1 activity (Gurney et al., 1994), so in addition to having inflammatory changes due to the presence of a disease mutation, they also have the effect of overexpression of a potent anti-oxidant enzyme, which could interfere in the normal signalling mechanisms between cytokine binding and adhesion molecule expression. This

hypothesis may partly explain the dampened adhesion molecule response noted in this thesis.

Despite the literature discussed above illustrating the ability of SOD1 protein to interfere with inflammatory pathways, *SOD1* models in general, and the G93A model in particular, have an up-regulation of certain ROS, which has been postulated to cause neuronal damage (Kruman et al., 1999, Zhou et al., 2005). These two strands of evidence seem at odds with each other. However, it may just be that certain species of ROS are produced, perhaps because of some gain-of-function mechanism to the SOD1 protein, that contribute to disease progression, but other species are kept at bay due to the *SOD1* overexpression and retained dismutase activity. For example, one study suggests that the hydroxyl radical is increased, whilst the superoxide anion is diminished by SOD1 overexpression (Liu et al., 1999), so it may be that radicals such as superoxide are involved in the signal transduction, whereas others such as hydroxyl radicals are involved in membrane damage in *SOD1*^{G93A} mice.

6.5 Integration of inflammatory changes in *SOD1*^{G93A}

Individual components of the inflammatory response have been discussed in the relevant chapters (Chapters 3 and 4) and in the previous sections above. However, at this point, it is worth taking a step back to consider the relative timing of different components of the inflammatory response, and how they relate to one another. The CNS regions form two main patterns of responses, broadly a ‘spinal’ response and a ‘brainstem’ response, which are graphically illustrated in **Figure 6.2**. The spinal pattern is most representative of the lumbar region, as the cervical cord sometimes follows the spinal pattern, and otherwise follows the brainstem pattern, as is discussed below. Sensorimotor cortex is not discussed here, as only very negligible changes were seen in this region. However, despite very little changes occurring with regards to cytokines and CAMs, there was a significant change in the morphology of astrocytes and microglia in this region, suggesting some involvement

of the sensorimotor cortex in pathology. This was clearly dampened, though, compared with the other regions of the CNS studied here.

For the brainstem pattern (**Figure 6.2**-A), astrocyte activation (GFAP) occurred parallel to vacuolation, which was significantly increased from wild type at 60 days, and continued to increase throughout the disease. Microglia activation (Iba1) showed a similar pattern, but was slightly delayed, as it was significantly increased compared to controls from 80 days onwards. ICAM-1 was the only adhesion molecule to be expressed significantly, showing an early response at 60 days, possibly with a reduction at 80 days (although this may just be a statistical artefact owing to the small numbers used) and increased again after onset of symptoms (100 and 120 days). No significant upregulation of VCAM-1, E-selectin or VAP-1 was found at any time point. Both of the primary pro-inflammatory cytokines, IL-1β and TNF-α, were expressed at high levels post-symptomatically, with the TNF-α response (significant at 120 days) slightly delayed compared to IL-1β (significant from 100 days). Expression of the chemokine CXCL-10 appeared to be elevated compared to wild type at 60 days, although this was not statistically significant, and was significantly elevated after symptom onset (100 – 120 days).

The spinal cord pattern was broadly similar to that of the brainstem, but there were some notable differences. Unlike the brainstem, the GFAP and Iba1 pattern in spinal cord were concurrent, as the microglial response occurred earlier (both astrocytes and microglia activated from 60 days onwards). Activation of the endothelium with adhesion molecules was the same as reported for the brainstem, with ICAM-1 expressed significantly at 60 and 100-120 days, and no significant expression of VCAM-1, E-selectin or VAP-1. The time course of IL-1β was the same as for the brainstem region (high expression from 100 days), but TNF-α showed a much earlier response, with expression before IL-1β, from 80 days onwards. CXCL-10 expression was broadly the same as for the brainstem region, but it was more pronounced, with significantly increased expression from 60 days onwards. The response for the cervical spinal cord was broadly in between that of the

lumbar cord and brainstem region, and mostly followed the spinal cord pattern, except for activated microglia (Iba1), where it followed the brainstem pattern.

The ultimate relevance of adhesion molecule expression, of course, is that it facilitates entry of leukocyte populations into the CNS. A number of studies have shown that T cell entry occurs during the disease, both in humans and animal models of ALS (Engelhardt et al., 1993, Alexianu et al., 2001), but B cells do not seem to be an important infiltrating population (Engelhardt et al., 1993, Naor et al., 2009). In the *SOD1*^{G93A} mouse model, for example, CD4+ T cells enter from around 70 days (pre-symptomatic), and CD8+ cells only at later, post-symptomatic time points (Beers et al., 2008). I originally hoped to quantify infiltration of T cell populations, and to determine how this related to adhesion molecule expression, but was not able to achieve antibody reactivity with the tissue preparation used here. Therefore, one of the main unresolved questions is whether the lack of adhesion molecule expression reported in this thesis was accompanied by a reduction in lymphocyte infiltration compared with previous studies, or whether the infiltration relied on molecules other than the ones studied here (i.e. VCAM-1, E-selectin, VAP-1). Also, as pointed out in the introduction, the involvement of T cells in the disease is currently contentious, as some reports suggest an early protective role (Beers et al., 2008, Chiu et al., 2008), whilst others suggest an early detrimental role in *SOD1* ALS (Tada et al., 2011). Therefore, the presence or absence of lymphocytes in the CNS of *SOD1* mice (or indeed patients) tells us little about the functional consequences until we understand the role of the lymphocyte better in the disease process.

Expression of CAMs on the vascular endothelium is also important for other leukocyte populations, including macrophages and neutrophils (Bochner et al., 1991, Sakai et al., 1997). Neutrophils appear to play little role in *SOD1*^{G93A} pathology, and I was unable to find any significant neutrophil entry into the CNS in the *SOD1*^{G93A} tissue used for this thesis (data not shown). However, it is possible that significant macrophage entry is occurring in the disease. Indeed, we cannot distinguish between microglia and infiltrating

macrophages based on Iba1 immunohistochemistry, which impacts on the interpretation of the microglia immunohistochemistry presented in chapter 3. These distinct leukocyte populations could be disambiguated using USPIO cell tracking using MRI (Dousset et al., 2006).

6.6 Perspectives on therapeutic interventions

The overview of therapeutic interventions provided in the introduction provides a mixed, and often confused picture of possible strategies in ALS treatment, in a large part due to differences between clinical and pre-clinical trials. This is one of the main factors leading to a growing antipathy towards *SOD1* transgenic models. However, I would argue this is unfounded for various reasons.

Firstly, treatment studies in *SOD1* models typically start in the early pre-symptomatic phase, continuing to end-stage, whereas in patient groups, the vast majority of ALS cases will only present to the clinic substantially after the onset of clinical signs. This is not necessarily a problem with the pre-clinical trials, as increased understanding of the genetics of ALS will allow clinicians to diagnose cases of ALS in the pre-symptomatic phase, and starting treatments early in disease models allows for a larger effect size to increase the chance of correctly identifying a positive hit. Nonetheless, this needs to be factored in when considering treatments for patients in the post-symptomatic phase.

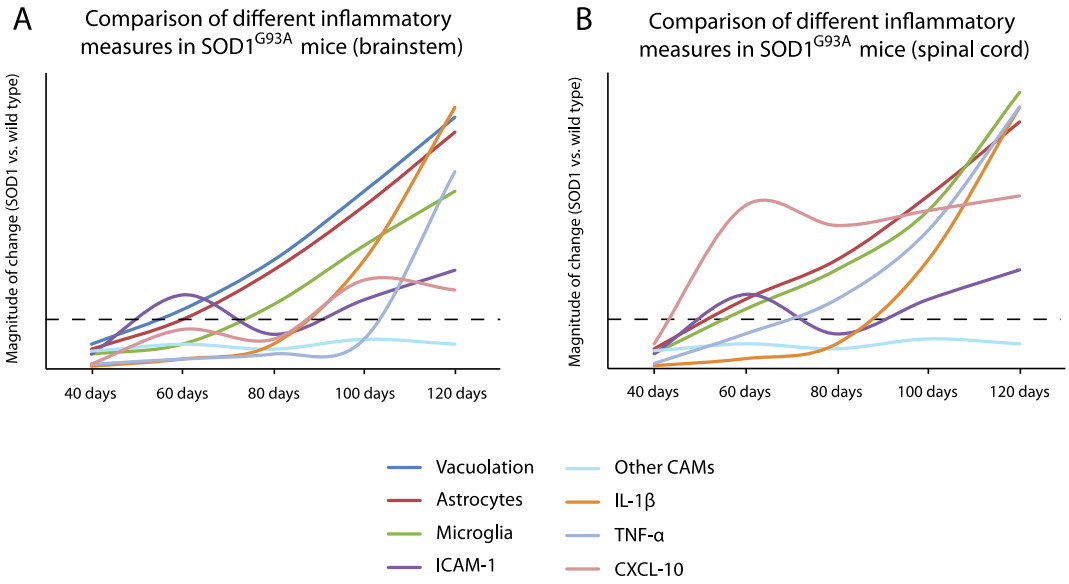


Figure 6.2 – Schematic representation of different components of the inflammatory response in *SOD1*^{G93A} mice

This figure is a schematic representation of different components of the inflammatory response, in the brainstem region (A) and spinal cord region (B), in *SOD1*^{G93A} compared with wild type mice. This is based on the pattern of change rather than specific values, to better compare the pattern between different markers. The dotted line represents the threshold of statistically significant differences.

In the brainstem region, astrocyte activation and vacuolation increase in a similar temporal fashion (significant from 60 days), with a slightly delayed microglial response (significant from 80 days). ICAM-1 shows increased activation at 60 days, possibly decreasing at 80 days, and then becoming statistically significant again at 100 and 120 days. No change in any other CAMs was observed. IL-1β and TNF-α, both show high expression post-symptomatically, with a slightly earlier response for IL-1β. CXCL-10 was increased at 60 days (but this was not statistically significant), and was significantly increased in expression at 100 and 120 days.

The pattern in the spinal cord was somewhat different to the brainstem region. Astrocytes and microglia showed a similar response here, with activation from 60 days onwards. The pattern for all CAMs was similar to that of the brainstem region, as was the cytokine IL-1β. TNF-α, on the other hand, had increased expression much earlier than in the brainstem, with increased expression from 80 days (earlier than IL-1β), and CXCL-10 had much more prominent up-regulation, with increases from 60 days, throughout the disease.

The cervical spinal cord mostly followed the ‘spinal cord’ pattern, except for activated microglia, which followed the ‘brainstem’ pattern.

Another potential difficulty with both human and animal trials, is that of dosing and CNS penetrance. Different dosing regimes makes comparisons between studies difficult, as some drugs can even have bi-phasic effects at different concentrations (Enz, 1981, Eilam and Szechtman, 1989). CNS penetrance is also a very important issue. Many drugs that have failed to show a therapeutic effect in humans and animals when injected systemically may have an effect when delivered into the CNS, so there is a danger that we may have missed out promising targets because the compounds were not able to enter the areas of pathology in high enough concentrations. Moreover, there are important efflux transporters present on the BBB that are involved with transport of potential toxic chemicals out of the CNS, and which underlie the phenomenon of multi-drug resistance. Two of these drug transporters, p-glycoprotein and breast cancer resistance protein, are upregulated throughout the disease process in *SOD1* mice and ALS patients (Jablonski et al., 2012). The combination of poor penetrance of the BBB, and the presence of efflux transporters, make pharmacological treatment of neurological conditions a considerable challenge.

The results presented in Chapter 5 provide strong evidence that targeted anti-inflammatory treatment can be effective in *SOD1*^{G93A} mice. Consistent with previous attempts to treat human ALS with prednisolone (Werdelin et al., 1990), treatment with free methylprednisolone provided no observable therapeutic effect, either in terms of motor behaviour, motor neuron counts, or glial activation compared with saline treated animals. However, liposomally-packaged methylprednisolone that was targeted to the CNS (2B3-201) rescued pathology with greater numbers of healthy neurons, and reduced vacuolation in the trigeminal, facial and hypoglossal nuclei. However, this effect was midbrain/brainstem-specific, as no therapeutic effect was found in the ventral horn of the spinal cord, which may explain why no differences in motor behaviour could be found between treatment groups.

The mechanism of 2B3-201 has not been identified, but there is evidence to suggest that it may be mediated through altering astrocytic phenotype. GFAP immunoreactivity mirrors the effect found for neuronal numbers and vacuolation, with GFAP activation significantly reduced in the three cranial motor nuclei, but not in the ventral horn of the spinal cord. Excitotoxicity is a common theme in ALS pathogenesis; increased glutamate levels have been noted in ALS patients (Spreux-Varoquaux et al., 2002), and there are altered glutamate transporter (GLT-1) levels in both ALS patients and animals models (Rothstein et al., 1995, Bruijn et al., 1997b, Howland et al., 2002). GLT-1 is essential for glutamate clearance from the synaptic cleft, so any reduction in GLT-1 levels, or disruption to normal glutamate-glutamine metabolism can leave neurons vulnerable to excitotoxic damage, as increased glutamate causes an influx of calcium ions, which damages many cellular components, including DNA and the cytoskeleton. If it could be shown that activated astrocytes, as defined by upregulation of the intermediate filament GFAP, cause an increase in glutamate and associated damage, targeting this process would be an attractive idea therapeutically.

Overall, the data from Chapter 5 provides evidence that CNS-targeted therapies are promising for the treatment of degenerative disease. These findings suggest that previously non-targeted treatments that were unsuccessful in either clinical or preclinical trials should perhaps be re-evaluated with regards to penetrance to the CNS, as the negative findings could equally be due to poor BBB permeability or expression of efflux transporters, as to poor therapeutic efficacy.

6.7 Future directions

The two main issues that are unresolved from the work presented in this thesis are: i) the source of the discrepancy between the lack of BBB permeability changes reported here, and the positive findings previously reported by other groups (discussed in Section 6.3); and ii) the lack of adhesion molecule expression on the vascular endothelium, despite an increase in pro-inflammatory cytokine production (discussed in Section 6.4).

With regards to BBB permeability, I would investigate whether the BBB changes shown in previous models are in fact due to pathogen exposure and the interaction between peripheral and central inflammatory pathways. I would take *SOD1*^{G93A} mice and wild type controls, and expose them at various time points (pre-symptomatic, peri-symptomatic, post-symptomatic) either to LPS systemically, or, more physiologically to a live virus, and scan them every day for 5 days following administration using Gd-DTPA and T_1 MRI to see a) whether this causes a breakdown at the BBB, and b) what is the time course of the disruption. As more animal houses are moving to cleaner and cleaner environments, this finding could have important consequences for how mice are housed; the human environment is far from pathogen free, so if systemic inflammation can significantly alter central pathology, we should be cautious about keeping mice in an overly clean environment, to increase the external validity of the model and increase translatability to humans.

Concerning the activation of the endothelium, I would investigate the hypothesis that overexpression of SOD1 protein (whether mutated or unmutated) interferes in the normal pathway between cytokine signalling and adhesion molecule expression, and that this underlies the dampened adhesion molecule expression in *SOD1*^{G93A} mice. As an initial experiment I would take wild type, transgenic *SOD1*^{G93A} mice carrying a disease mutation (*SOD1*^{G93A}) and transgenic *SOD1* mice overexpressing the wild type protein to the same degree (*SOD1*^{hWT}) at 40 days, where there is little in the way of inflammation, giving mice intracerebral injections of IL-1β or saline. If this hypothesis is true, then I would predict a marked inflammatory response in wild type mice after IL-1β treatment, including expression of VCAM-1, ICAM-1 and E-selectin, and an attenuated response in both the *SOD1*^{G93A} and *SOD1*^{hWT} mice, as both lines have an overexpression of functional SOD1 protein. If, on the other hand, the lack of adhesion expression is due to some interacting feature of the disease that is specific to the gene mutation, then there would be marked inflammation in wild type and *SOD1*^{hWT} mice, and attenuation of the inflammatory response in *SOD1*^{G93A} only.

6.8 Conclusion

This thesis has explored neuroinflammatory and vascular changes in *SOD1*^{G93A} mice. Despite extensive neuroinflammation with regards to glial activation and cytokine release, there are surprisingly few vascular changes in this model, suggesting that this is not necessary for disease progression in *SOD1* ALS. These inflammatory pathways seem to contribute strongly to the progression of the disease, and targeted delivery of anti-inflammatory therapies into the areas of pathology appears to be a promising avenue to pursue in delaying disease progression in the clinic. Our understanding of BBB changes is still in its infancy, and research into this in the future may provide insight into the underlying biology of the disease, particularly in investigating how the interaction between central and peripheral inflammatory mechanisms alters the characteristics of the BBB.

References

Abbott NJ, Ronnback L, Hansson E (2006) Astrocyte-endothelial interactions at the blood-brain barrier. Nat Rev Neurosci 7:41-53.

Abramzon Y, Johnson JO, Scholz SW, Taylor JP, Brunetti M, Calvo A, Mandrioli J, Benatar M, Mora G, Restagno G, Chio A, Traynor BJ (2012) Valosin-containing protein (VCP) mutations in sporadic amyotrophic lateral sclerosis. Neurobiol Aging 33:2231 e2231-2236.

Afifi AK, Aleu FP, Goodgold J, MacKay B (1966) Ultrastructure of atrophic muscle in amyotrophic lateral sclerosis. Neurology 16:475-481.

Alexander MD, Traynor BJ, Miller N, Corr B, Frost E, McQuaid S, Brett FM, Green A, Hardiman O (2002) "True" sporadic ALS associated with a novel SOD-1 mutation. Ann Neurol 52:680-683.

Alexianu ME, Kozovska M, Appel SH (2001) Immune reactivity in a mouse model of familial ALS correlates with disease progression. Neurology 57:1282-1289.

Allen TH, Orahovats PD (1948) Spectrophotometric measurement of traces of the dye T-1824 by extraction with cellophane from both blood serum and urine of normal dogs. Am J Physiol 154:27-37.

Allingham RR, Liu Y, Rhee DJ (2009) The genetics of primary open-angle glaucoma: a review. Exp Eye Res 88:837-844.

Amodio R, Esposito E, De Ruvo C, Bellavia V, Amodio E, Carruba G (2006) Red wine extract prevents neuronal apoptosis in vitro and reduces mortality of transgenic mice. Ann N Y Acad Sci 1089:88-97.

Andersen PM, Forsgren L, Binzer M, Nilsson P, Ala-Hurula V, Keranen ML, Bergmark L, Saarinen A, Haltia T, Tarvainen I, Kinnunen E, Udd B, Marklund SL (1996) Autosomal recessive adult-onset amyotrophic lateral sclerosis associated with homozygosity for Asp90Ala CuZn-superoxide dismutase mutation. A clinical and genealogical study of 36 patients. Brain 119 (Pt 4):1153-1172.

Andersen PM, Nilsson P, Keranen ML, Forsgren L, Hagglund J, Karlsborg M, Ronnevi LO, Gredal O, Marklund SL (1997) Phenotypic heterogeneity in motor neuron disease patients with CuZn-superoxide dismutase mutations in Scandinavia. Brain 120 (Pt 10):1723-1737.

Andersen PM, Sims KB, Xin WW, Kiely R, O'Neill G, Ravits J, Pioro E, Harati Y, Brower RD, Levine JS, Heinicke HU, Seltzer W, Boss M, Brown RH, Jr. (2003) Sixteen novel mutations in the Cu/Zn superoxide dismutase gene in amyotrophic lateral sclerosis: a decade of discoveries, defects and disputes. Amyotroph Lateral Scler Other Motor Neuron Disord 4:62-73.

Andersson MK, Stahlberg A, Arvidsson Y, Olofsson A, Semb H, Stenman G, Nilsson O, Aman P (2008) The multifunctional FUS, EWS and TAF15 proto-oncoproteins show cell type-specific expression patterns and involvement in cell spreading and stress response. BMC Cell Biol 9:37.

Andjus PR, Bataveljic D, Vanhoutte G, Mitrecic D, Pizzolante F, Djogo N, Nicaise C, Gankam Kengne F, Gangitano C, Michetti F, van der Linden A, Pochet R, Bacic G (2009) In vivo morphological changes in animal models of amyotrophic lateral sclerosis and Alzheimer's-like disease: MRI approach. Anat Rec (Hoboken) 292:1882-1892.

Andreassen OA, Jenkins BG, Dedeoglu A, Ferrante KL, Bogdanov MB, Kaddurah-Daouk R, Beal MF (2001) Increases in cortical glutamate concentrations in transgenic amyotrophic lateral sclerosis mice are attenuated by creatine supplementation. J Neurochem 77:383-390.

Andrews JM, Gardner MB, Wolfgram FJ, Ellison GW, Porter DD, Brandkamp WW (1974) Studies on a murine form of spontaneous lower motor neuron degeneration--the wobbler (wa) mouse. Am J Pathol 76:63-78.

Angenstein F, Niessen HG, Goldschmidt J, Vielhaber S, Ludolph AC, Scheich H (2004) Age-dependent changes in MRI of motor brain stem nuclei in a mouse model of ALS. Neuroreport 15:2271-2274.

Annunziata P, Volpi N (1985) High levels of C3c in the cerebrospinal fluid from amyotrophic lateral sclerosis patients. Acta Neurol Scand 72:61-64.

Anthony DC, Couch Y, Losey P, Evans MC (2012) The systemic response to brain injury and disease. Brain Behav Immun 26:534-540.

Appel SH, Beers DR, Henkel JS (2010) T cell-microglial dialogue in Parkinson's disease and amyotrophic lateral sclerosis: are we listening? Trends Immunol 31:7-17.

Aquilano K, Vigilanza P, Rotilio G, Ciriolo MR (2006) Mitochondrial damage due to SOD1 deficiency in SH-SY5Y neuroblastoma cells: a rationale for the redundancy of SOD1. FASEB J 20:1683-1685.

Arvilommi AM, Salmi M, Kalimo K, Jalkanen S (1996) Lymphocyte binding to vascular endothelium in inflamed skin revisited: a central role for vascular adhesion protein-1 (VAP-1). Eur J Immunol 26:825-833.

Aschner M, Sonnewald U, Tan KH (2002) Astrocyte modulation of neurotoxic injury. Brain Pathol 12:475-481.

Ash PE, Zhang YJ, Roberts CM, Saldi T, Hutter H, Buratti E, Petrucelli L, Link CD (2010) Neurotoxic effects of TDP-43 overexpression in C. elegans. Hum Mol Genet 19:3206-3218.

Ayala YM, Misteli T, Baralle FE (2008) TDP-43 regulates retinoblastoma protein phosphorylation through the repression of cyclin-dependent kinase 6 expression. Proc Natl Acad Sci U S A 105:3785-3789.

Babu GN, Kumar A, Chandra R, Puri SK, Kalita J, Misra UK (2008) Elevated inflammatory markers in a group of amyotrophic lateral sclerosis patients from northern India. Neurochem Res 33:1145-1149.

Banerjee R, Mosley RL, Reynolds AD, Dhar A, Jackson-Lewis V, Gordon PH, Przedborski S, Gendelman HE (2008) Adaptive immune neuroprotection in G93A-SOD1 amyotrophic lateral sclerosis mice. PLoS One 3:e2740.

Barten DM, Ruddle NH (1994) Vascular cell adhesion molecule-1 modulation by tumor necrosis factor in experimental allergic encephalomyelitis. J Neuroimmunol 51:123-133.

Basser PJ, Mattiello J, LeBihan D (1994) MR diffusion tensor spectroscopy and imaging. Biophys J 66:259-267.

Basser PJ, Pierpaoli C (1996) Microstructural and physiological features of tissues elucidated by quantitative-diffusion-tensor MRI. J Magn Reson B 111:209-219.

Bataveljic D, Djogo N, Zupunski L, Bajic A, Nicaise C, Pochet R, Bacic G, Andjus PR (2009) Live monitoring of brain damage in the rat model of amyotrophic lateral sclerosis. Gen Physiol Biophys 28 Spec No:212-218.

Bataveljic D, Stamenkovic S, Bacic G, Andjus PR (2011) Imaging cellular markers of neuroinflammation in the brain of the rat model of amyotrophic lateral sclerosis. Acta Physiol Hung 98:27-31.

Bay-Richter C, Janelidze S, Hallberg L, Brundin L (2011) Changes in behaviour and cytokine expression upon a peripheral immune challenge. Behav Brain Res 222:193-199.

Bazzoni G, Dejana E (2004) Endothelial cell-to-cell junctions: molecular organization and role in vascular homeostasis. Physiol Rev 84:869-901.

Beal MF (1996) Mitochondria, free radicals, and neurodegeneration. Curr Opin Neurobiol 6:661-666.

Beal MF, Ferrante RJ, Browne SE, Matthews RT, Kowall NW, Brown RH, Jr. (1997) Increased 3-nitrotyrosine in both sporadic and familial amyotrophic lateral sclerosis. Ann Neurol 42:644-654.

Beall DP, Martin D, Chin BB (1998) Decreased bilateral frontal lobe perfusion in dementia of amyotrophic lateral sclerosis. Clin Nucl Med 23:855-856.

Beato M (1989) Gene regulation by steroid hormones. Cell 56:335-344.

Bechmann I, Galea I, Perry VH (2007) What is the blood-brain barrier (not)? Trends Immunol 28:5-11.

Beckman JS, Carson M, Smith CD, Koppenol WH (1993) ALS, SOD and peroxynitrite. Nature 364:584.

Beers DR, Henkel JS, Xiao Q, Zhao W, Wang J, Yen AA, Siklos L, McKercher SR, Appel SH (2006) Wild-type microglia extend survival in PU.1 knockout mice with familial amyotrophic lateral sclerosis. Proc Natl Acad Sci U S A 103:16021-16026.

Beers DR, Henkel JS, Zhao W, Wang J, Appel SH (2008) CD4+ T cells support glial neuroprotection, slow disease progression, and modify glial morphology in an animal model of inherited ALS. Proc Natl Acad Sci U S A 105:15558-15563.

Beers DR, Zhao W, Liao B, Kano O, Wang J, Huang A, Appel SH, Henkel JS (2011) Neuroinflammation modulates distinct regional and temporal clinical responses in ALS mice. Brain Behav Immun 25:1025-1035.

Bendotti C, Carri MT (2004) Lessons from models of SOD1-linked familial ALS. Trends Mol Med 10:393-400.

Benveniste H, Einstein G, Kim KR, Hulette C, Johnson GA (1999) Detection of neuritic plaques in Alzheimer's disease by magnetic resonance microscopy. Proc Natl Acad Sci U S A 96:14079-14084.

Berger JV, Deumens R, Goursaud S, Schafer S, Lavand'homme P, Joosten EA, Hermans E (2011) Enhanced neuroinflammation and pain hypersensitivity after peripheral nerve injury in rats expressing mutated superoxide dismutase 1. J Neuroinflammation 8:33.

Bezzi P, Volterra A (2001) A neuron-glia signalling network in the active brain. Curr Opin Neurobiol 11:387-394.

Birken DL, Oldendorf WH (1989) N-acetyl-L-aspartic acid: a literature review of a compound prominent in 1H-NMR spectroscopic studies of brain. Neurosci Biobehav Rev 13:23-31.

Blair IP, Williams KL, Warraich ST, Durnall JC, Thoeng AD, Manavis J, Blumbergs PC, Vucic S, Kiernan MC, Nicholson GA (2010) FUS mutations in amyotrophic lateral sclerosis: clinical, pathological, neurophysiological and genetic analysis. J Neurol Neurosurg Psychiatry 81:639-645.

Block ML, Hong JS (2007) Chronic microglial activation and progressive dopaminergic neurotoxicity. Biochem Soc Trans 35:1127-1132.

Bochner BS, Luscinskas FW, Gimbrone MA, Jr., Newman W, Sterbinsky SA, Derse-Anthony CP, Klunk D, Schleimer RP (1991) Adhesion of human basophils, eosinophils, and neutrophils to interleukin 1-activated human vascular endothelial cells: contributions of endothelial cell adhesion molecules. J Exp Med 173:1553-1557.

Boillee S, Yamanaka K, Lobsiger CS, Copeland NG, Jenkins NA, Kassiotis G, Kollias G, Cleveland DW (2006) Onset and progression in inherited ALS determined by motor neurons and microglia. Science 312:1389-1392.

Bordet T, Buisson B, Michaud M, Drouot C, Galea P, Delaage P, Akentieva NP, Evers AS, Covey DF, Ostuni MA, Lacapere JJ, Massaad C, Schumacher M, Steidl EM, Maux D, Delaage M, Henderson CE, Pruss RM (2007) Identification and characterization of cholest-4-en-3-one, oxime (TRO19622), a novel drug candidate for amyotrophic lateral sclerosis. J Pharmacol Exp Ther 322:709-720.

Bosco DA, Lemay N, Ko HK, Zhou H, Burke C, Kwiatkowski TJ, Jr., Sapp P, McKenna-Yasek D, Brown RH, Jr., Hayward LJ (2010) Mutant FUS proteins that cause amyotrophic lateral sclerosis incorporate into stress granules. Hum Mol Genet 19:4160-4175.

Boston-Howes W, Williams EO, Bogush A, Scolere M, Pasinelli P, Trotti D (2008) Nordihydroguaiaretic acid increases glutamate uptake in vitro and in vivo: therapeutic implications for amyotrophic lateral sclerosis. Exp Neurol 213:229-237.

Bottomley PA, Lee Y, Weiss RG (1997) Total creatine in muscle: imaging and quantification with proton MR spectroscopy. Radiology 204:403-410.

Brambilla R, Bracchi-Ricard V, Hu WH, Frydel B, Bramwell A, Karmally S, Green EJ, Bethea JR (2005) Inhibition of astroglial nuclear factor kappaB reduces inflammation and improves functional recovery after spinal cord injury. The Journal of experimental medicine 202:145-156.

Brand A, Richter-Landsberg C, Leibfritz D (1993) Multinuclear NMR studies on the energy metabolism of glial and neuronal cells. Dev Neurosci 15:289-298.

Brant-Zawadzki M, Bartkowski HM, Ortendahl DA, Pitts LH, Hylton NM, Nishimura MC, Crooks LE (1984) NMR in experimental cerebral edema: value of T1 and T2 calculations. AJNR Am J Neuroradiol 5:125-129.

Brooks BR (1994) El Escorial World Federation of Neurology criteria for the diagnosis of amyotrophic lateral sclerosis. Subcommittee on Motor Neuron Diseases/Amyotrophic Lateral Sclerosis of the World Federation of Neurology Research Group on Neuromuscular Diseases and the El Escorial "Clinical limits of amyotrophic lateral sclerosis" workshop contributors. J Neurol Sci 124 Suppl:96-107.

Brooks KJ, Hill MD, Hockings PD, Reid DG (2004) MRI detects early hindlimb muscle atrophy in Gly93Ala superoxide dismutase-1 (G93A SOD1) transgenic mice, an animal model of familial amyotrophic lateral sclerosis. NMR Biomed 17:28-32.

Broom KA, Anthony DC, Lowe JP, Griffin JL, Scott H, Blamire AM, Styles P, Perry VH, Sibson NR (2007) MRI and MRS alterations in the preclinical phase of murine prion disease: association with neuropathological and behavioural changes. Neurobiol Dis 26:707-717.

Brown RH, Jr. (1995) Superoxide dismutase in familial amyotrophic lateral sclerosis: models for gain of function. Curr Opin Neurobiol 5:841-846.

Bruijn LI, Beal MF, Becher MW, Schulz JB, Wong PC, Price DL, Cleveland DW (1997a) Elevated free nitrotyrosine levels, but not protein-bound nitrotyrosine or hydroxyl radicals, throughout amyotrophic lateral sclerosis (ALS)-like disease implicate tyrosine nitration as an aberrant in vivo property of one familial ALS-linked superoxide dismutase 1 mutant. Proc Natl Acad Sci U S A 94:7606-7611.

Bruijn LI, Becher MW, Lee MK, Anderson KL, Jenkins NA, Copeland NG, Sisodia SS, Rothstein JD, Borchelt DR, Price DL, Cleveland DW (1997b) ALS-linked SOD1 mutant G85R mediates damage to astrocytes and promotes rapidly progressive disease with SOD1-containing inclusions. Neuron 18:327-338.

Bruijn LI, Houseweart MK, Kato S, Anderson KL, Anderson SD, Ohama E, Reaume AG, Scott RW, Cleveland DW (1998) Aggregation and motor neuron toxicity of an ALS-linked SOD1 mutant independent from wild-type SOD1. Science 281:1851-1854.

Bruijn LI, Miller TM, Cleveland DW (2004) Unraveling the mechanisms involved in motor neuron degeneration in ALS. Annu Rev Neurosci 27:723-749.

Bucher S, Braunstein KE, Niessen HG, Kaulisch T, Neumaier M, Boeckers TM, Stiller D, Ludolph AC (2007) Vacuolization correlates with spin-spin relaxation time in motor brainstem nuclei and behavioural tests in the transgenic G93A-SOD1 mouse model of ALS. Eur J Neurosci 26:1895-1901.

Buchthal F, Olsen PZ (1970) Electromyography and muscle biopsy in infantile spinal muscular atrophy. Brain 93:15-30.

Buratti E, Baralle FE (2008) Multiple roles of TDP-43 in gene expression, splicing regulation, and human disease. Front Biosci 13:867-878.

Buratti E, Dork T, Zuccato E, Pagani F, Romano M, Baralle FE (2001) Nuclear factor TDP-43 and SR proteins promote in vitro and in vivo CFTR exon 9 skipping. EMBO J 20:1774-1784.

Campbell SJ, Anthony DC, Oakley F, Carlsen H, Elsharkawy AM, Blomhoff R, Mann DA (2008) Hepatic nuclear factor kappa B regulates neutrophil recruitment to the injured brain. J Neuropathol Exp Neurol 67:223-230.

Cardona AE, Pioro EP, Sasse ME, Kostenko V, Cardona SM, Dijkstra IM, Huang D, Kidd G, Dombrowski S, Dutta R, Lee JC, Cook DN, Jung S, Lira SA, Littman DR, Ransohoff RM (2006) Control of microglial neurotoxicity by the fractalkine receptor. Nat Neurosci 9:917-924.

Carlos TM, Clark RS, Franicola-Higgins D, Schiding JK, Kochanek PM (1997) Expression of endothelial adhesion molecules and recruitment of neutrophils after traumatic brain injury in rats. J Leukoc Biol 61:279-285.

Carlos TM, Harlan JM (1994) Leukocyte-endothelial adhesion molecules. Blood 84:2068-2101.

Carpenter S (1968) Proximal axonal enlargement in motor neuron disease. Neurology 18:841-851.

Cereda C, Baiocchi C, Bongioanni P, Cova E, Guareschi S, Metelli MR, Rossi B, Sbalsi I, Cuccia MC, Ceroni M (2008) TNF and sTNFR1/2 plasma levels in ALS patients. J Neuroimmunol 194:123-131.

Chad DA, Hammer K, Sargent J (1986) Slow resolution of multifocal weakness and fasciculation: a reversible motor neuron syndrome. Neurology 36:1260-1263.

Chang JL, Lomen-Hoerth C, Murphy J, Henry RG, Kramer JH, Miller BL, Gorno-Tempini ML (2005) A voxel-based morphometry study of patterns of brain atrophy in ALS and ALS/FTLD. Neurology 65:75-80.

Chao CC, Hu S, Close K, Choi CS, Molitor TW, Novick WJ, Peterson PK (1992) Cytokine release from microglia: differential inhibition by pentoxifylline and dexamethasone. J Infect Dis 166:847-853.

Charles T, Swash M (2001) Amyotrophic lateral sclerosis: current understanding. J Neurosci Nurs 33:245-253.

Chaulet C, Croix C, Alagille D, Normand S, Delwail A, Favot L, Lecron JC, Viaud-Massuard MC (2011) Design, synthesis and biological evaluation of new thalidomide analogues as TNF-alpha and IL-6 production inhibitors. Bioorg Med Chem Lett 21:1019-1022.

Chen YZ, Bennett CL, Huynh HM, Blair IP, Puls I, Irobi J, Dierick I, Abel A, Kennerson ML, Rabin BA, Nicholson GA, Auer-Grumbach M, Wagner K, De Jonghe P, Griffin JW, Fischbeck KH, Timmerman V, Cornblath DR, Chance PF (2004) DNA/RNA helicase gene mutations in a form of juvenile amyotrophic lateral sclerosis (ALS4). Am J Hum Genet 74:1128-1135.

Chen YZ, Hashemi SH, Anderson SK, Huang Y, Moreira MC, Lynch DR, Glass IA, Chance PF, Bennett CL (2006) Senataxin, the yeast Sen1p orthologue: characterization of a unique protein in which recessive mutations cause ataxia and dominant mutations cause motor neuron disease. Neurobiol Dis 23:97-108.

Chen Z, Ma L (2010) Grey matter volume changes over the whole brain in amyotrophic lateral sclerosis: A voxel-wise meta-analysis of voxel based morphometry studies. Amyotroph Lateral Scler 11:549-554.

Chiba T, Yamada M, Sasabe J, Terashita K, Aiso S, Matsuoka M, Nishimoto I (2006) Colivelin prolongs survival of an ALS model mouse. Biochem Biophys Res Commun 343:793-798.

Chio A, Traynor BJ, Lombardo F, Fimognari M, Calvo A, Ghiglione P, Mutani R, Restagno G (2008) Prevalence of SOD1 mutations in the Italian ALS population. Neurology 70:533-537.

Chiu IM, Chen A, Zheng Y, Kosaras B, Tsiftsoglou SA, Vartanian TK, Brown RH, Jr., Carroll MC (2008) T lymphocytes potentiate endogenous neuroprotective inflammation in a mouse model of ALS. Proc Natl Acad Sci U S A 105:17913-17918.

Choi CI, Lee YD, Gwag BJ, Cho SI, Kim SS, Suh-Kim H (2008) Effects of estrogen on lifespan and motor functions in female hSOD1 G93A transgenic mice. J Neurol Sci 268:40-47.

Clasen RA, Pandolfi S, Hass GM (1970) Vital staining, serum albumin and the blood-brain barrier. J Neuropathol Exp Neurol 29:266-284.

Clement AM, Nguyen MD, Roberts EA, Garcia ML, Boillee S, Rule M, McMahon AP, Doucette W, Siwek D, Ferrante RJ, Brown RH, Jr., Julien JP, Goldstein LS, Cleveland DW (2003) Wild-type nonneuronal cells extend survival of SOD1 mutant motor neurons in ALS mice. Science 302:113-117.

Cleveland DW, Rothstein JD (2001) From Charcot to Lou Gehrig: deciphering selective motor neuron death in ALS. Nat Rev Neurosci 2:806-819.

Corral LG, Haslett PA, Muller GW, Chen R, Wong LM, Ocampo CJ, Patterson RT, Stirling DI, Kaplan G (1999) Differential cytokine modulation and T cell activation by two distinct classes of thalidomide analogues that are potent inhibitors of TNF-alpha. J Immunol 163:380-386.

Cudkowicz ME, McKenna-Yasek D, Chen C, Hedley-Whyte ET, Brown RH, Jr. (1998) Limited corticospinal tract involvement in amyotrophic lateral sclerosis subjects with the A4V mutation in the copper/zinc superoxide dismutase gene. Ann Neurol 43:703-710.

Cunningham C, Wilcockson DC, Campion S, Lunnon K, Perry VH (2005) Central and systemic endotoxin challenges exacerbate the local inflammatory response and increase neuronal death during chronic neurodegeneration. J Neurosci 25:9275-9284.

Dal Canto MC, Gurney ME (1994) Development of central nervous system pathology in a murine transgenic model of human amyotrophic lateral sclerosis. Am J Pathol 145:1271-1279.

David S, Kroner A (2011) Repertoire of microglial and macrophage responses after spinal cord injury. Nature reviews Neuroscience 12:388-399.

Davies CA, Loddick SA, Toulmond S, Stroemer RP, Hunt J, Rothwell NJ (1999) The progression and topographic distribution of interleukin-1beta expression after

permanent middle cerebral artery occlusion in the rat. J Cereb Blood Flow Metab 19:87-98.

Davies TH, Ning YM, Sanchez ER (2002) A new first step in activation of steroid receptors: hormone-induced switching of FKBP51 and FKBP52 immunophilins. J Biol Chem 277:4597-4600.

Dedeoglu A, Choi JK, Cormier K, Kowall NW, Jenkins BG (2004) Magnetic resonance spectroscopic analysis of Alzheimer's disease mouse brain that express mutant human APP shows altered neurochemical profile. Brain Res 1012:60-65.

DeJesus-Hernandez M, Mackenzie IR, Boeve BF, Boxer AL, Baker M, Rutherford NJ, Nicholson AM, Finch NA, Flynn H, Adamson J, Kouri N, Wojtas A, Sengdy P, Hsiung GY, Karydas A, Seeley WW, Josephs KA, Coppola G, Geschwind DH, Wszolek ZK, Feldman H, Knopman DS, Petersen RC, Miller BL, Dickson DW, Boylan KB, Graff-Radford NR, Rademakers R (2011) Expanded GGGGCC hexanucleotide repeat in noncoding region of C9ORF72 causes chromosome 9p-linked FTD and ALS. Neuron 72:245-256.

Delisle MB, Carpenter S (1984) Neurofibrillary axonal swellings and amyotrophic lateral sclerosis. J Neurol Sci 63:241-250.

Deng HX, Shi Y, Furukawa Y, Zhai H, Fu R, Liu E, Gorrie GH, Khan MS, Hung WY, Bigio EH, Lukas T, Dal Canto MC, O'Halloran TV, Siddique T (2006) Conversion to the amyotrophic lateral sclerosis phenotype is associated with intermolecular linked insoluble aggregates of SOD1 in mitochondria. Proc Natl Acad Sci U S A 103:7142-7147.

Deniselle MC, Lavista-Llanos S, Ferrini MG, Lima AE, Roldan AG, De Nicola AF (1999) In vitro differences between astrocytes of control and wobbler mice spinal cord. Neurochem Res 24:1535-1541.

DePaul R, Abbs JH, Caligiuri M, Gracco VL, Brooks BR (1988) Hypoglossal, trigeminal, and facial motoneuron involvement in amyotrophic lateral sclerosis. Neurology 38:281-283.

Di Giorgio FP, Boulting GL, Bobrowicz S, Eggan KC (2008) Human embryonic stem cell-derived motor neurons are sensitive to the toxic effect of glial cells carrying an ALS-causing mutation. Cell Stem Cell 3:637-648.

Di Giorgio FP, Carrasco MA, Siao MC, Maniatis T, Eggan K (2007) Non-cell autonomous effect of glia on motor neurons in an embryonic stem cell-based ALS model. Nat Neurosci 10:608-614.

Diaz-Amarilla P, Olivera-Bravo S, Trias E, Cragnolini A, Martinez-Palma L, Cassina P, Beckman J, Barbeito L (2011) Phenotypically aberrant astrocytes that promote motoneuron damage in a model of inherited amyotrophic lateral sclerosis. Proc Natl Acad Sci U S A 108:18126-18131.

Dickerman Z, Grant DR, Faiman C, Winter JS (1984) Intraadrenal steroid concentrations in man: zonal differences and developmental changes. J Clin Endocrinol Metab 59:1031-1036.

Dickerson SS, Kemeny ME (2004) Acute stressors and cortisol responses: a theoretical integration and synthesis of laboratory research. Psychol Bull 130:355-391.

Diener PS, Bregman BS (1994) Neurotrophic factors prevent the death of CNS neurons after spinal cord lesions in newborn rats. Neuroreport 5:1913-1917.

Dinarello CA (2009) Immunological and inflammatory functions of the interleukin-1 family. Annu Rev Immunol 27:519-550.

Dobrowolny G, Giacinti C, Pelosi L, Nicoletti C, Winn N, Barberi L, Molinaro M, Rosenthal N, Musaro A (2005) Muscle expression of a local Igf-1 isoform protects motor neurons in an ALS mouse model. J Cell Biol 168:193-199.

Domeniconi M, Hempstead BL, Chao MV (2007) Pro-NGF secreted by astrocytes promotes motor neuron cell death. Mol Cell Neurosci 34:271-279.

Dong A, Shen J, Zeng M, Campochiaro PA (2011) Vascular cell-adhesion molecule-1 plays a central role in the proangiogenic effects of oxidative stress. Proc Natl Acad Sci U S A 108:14614-14619.

Donnenfeld H, Kascsak RJ, Bartfeld H (1984) Deposits of IgG and C3 in the spinal cord and motor cortex of ALS patients. J Neuroimmunol 6:51-57.

Dore-Duffy P, LaManna JC (2007) Physiologic angiodynamics in the brain. Antioxid Redox Signal 9:1363-1371.

Dousset V, Brochet B, Deloire MS, Lagoarde L, Barroso B, Caille JM, Petry KG (2006) MR imaging of relapsing multiple sclerosis patients using ultra-small-particle iron oxide and compared with gadolinium. AJNR Am J Neuroradiol 27:1000-1005.

Dousset V, Grossman RI, Ramer KN, Schnall MD, Young LH, Gonzalez-Scarano F, Lavi E, Cohen JA (1992) Experimental allergic encephalomyelitis and multiple sclerosis: lesion characterization with magnetization transfer imaging. Radiology 182:483-491.

Drachman DB, Frank K, Dykes-Hoberg M, Teismann P, Almer G, Przedborski S, Rothstein JD (2002) Cyclooxygenase 2 inhibition protects motor neurons and prolongs survival in a transgenic mouse model of ALS. Ann Neurol 52:771-778.

Duchen LW (1978) Motor neuron diseases in man and animals. Invest Cell Pathol 1:249-262.

Eilam D, Szechtman H (1989) Biphasic effect of D-2 agonist quinpirole on locomotion and movements. Eur J Pharmacol 161:151-157.

Ekestern E (2004) Neurotrophic factors and amyotrophic lateral sclerosis. Neurodegener Dis 1:88-100.

Elliott JL (2001) Cytokine upregulation in a murine model of familial amyotrophic lateral sclerosis. Brain Res Mol Brain Res 95:172-178.

Ellis CM, Simmons A, Dawson JM, Williams SC, Leigh PN (1999) Distinct hyperintense MRI signal changes in the corticospinal tracts of a patient with motor neuron disease. Amyotroph Lateral Scler Other Motor Neuron Disord 1:41-44.

Elmore S (2007) Apoptosis: a review of programmed cell death. Toxicol Pathol 35:495-516.

Emery AE, Hausmanowa-Petrusewicz I, Davie AM, Holloway S, Skinner R, Borkowska J (1976) International collaborative study of the spinal muscular atrophies. Part 1. Analysis of clinical and laboratory data. J Neurol Sci 29:83-94.

Engelhardt JI, Appel SH (1990) IgG reactivity in the spinal cord and motor cortex in amyotrophic lateral sclerosis. Arch Neurol 47:1210-1216.

Engelhardt JI, Tajti J, Appel SH (1993) Lymphocytic infiltrates in the spinal cord in amyotrophic lateral sclerosis. Arch Neurol 50:30-36.

Enz A (1981) Biphasic influence of a 8 alpha-amino ergoline, CU 32-085, on striatal dopamine synthesis and turnover in vivo in the rat. Life Sci 29:2227-2234.

Evans MC, Modo M, Talbot K, Sibson N, Turner MR (2012) Magnetic resonance imaging of pathological processes in rodent models of amyotrophic lateral sclerosis. Amyotroph Lateral Scler 13:288-301.

Facchinetti F, Sasaki M, Cutting FB, Zhai P, MacDonald JE, Reif D, Beal MF, Huang PL, Dawson TM, Gurney ME, Dawson VL (1999) Lack of involvement of neuronal nitric oxide synthase in the pathogenesis of a transgenic mouse model of familial amyotrophic lateral sclerosis. Neuroscience 90:1483-1492.

Falangola MF, Lee SP, Nixon RA, Duff K, Helpern JA (2005) Histological co-localization of iron in Abeta plaques of PS/APP transgenic mice. Neurochem Res 30:201-205.

Fang L, Teuchert M, Huber-Abel F, Schattauer D, Hendrich C, Dorst J, Zettlmeissel H, Wlaschek M, Scharffetter-Kochanek K, Kapfer T, Tumani H, Ludolph AC, Brettschneider J (2010) MMP-2 and MMP-9 are elevated in spinal cord and skin in a mouse model of ALS. J Neurol Sci 294:51-56.

Feeney SJ, McKelvie PA, Austin L, Jean-Francois MJ, Kapsa R, Tombs SM, Byrne E (2001) Presymptomatic motor neuron loss and reactive astrocytosis in the SOD1 mouse model of amyotrophic lateral sclerosis. Muscle Nerve 24:1510-1519.

Feldman EL, Bromberg MB, Albers JW, Pestronk A (1991) Immunosuppressive treatment in multifocal motor neuropathy. Ann Neurol 30:397-401.

Feng D, Nagy JA, Pyne K, Dvorak HF, Dvorak AM (1998) Neutrophils emigrate from venules by a transendothelial cell pathway in response to FMLP. J Exp Med 187:903-915.

Ferri A, Cozzolino M, Crosio C, Nencini M, Casciati A, Gralla EB, Rotilio G, Valentine JS, Carri MT (2006) Familial ALS-superoxide dismutases associate with mitochondria and shift their redox potentials. Proc Natl Acad Sci U S A 103:13860-13865.

Ferri A, Nencini M, Casciati A, Cozzolino M, Angelini DF, Longone P, Spalloni A, Rotilio G, Carri MT (2004) Cell death in amyotrophic lateral sclerosis: interplay between neuronal and glial cells. FASEB J 18:1261-1263.

Fidler JA, Treleaven CM, Frakes A, Tamsett TJ, McCrate M, Cheng SH, Shihabuddin LS, Kaspar BK, Dodge JC (2011) Disease progression in a mouse model of amyotrophic lateral sclerosis: the influence of chronic stress and corticosterone. FASEB J 25:4369-4377.

Filippi M, Campi A, Dousset V, Baratti C, Martinelli V, Canal N, Scotti G, Comi G (1995) A magnetization transfer imaging study of normal-appearing white matter in multiple sclerosis. Neurology 45:478-482.

Filippini N, Douaud G, Mackay CE, Knight S, Talbot K, Turner MR (2010) Corpus callosum involvement is a consistent feature of amyotrophic lateral sclerosis. Neurology 75:1645-1652.

Fischer LR, Culver DG, Tennant P, Davis AA, Wang M, Castellano-Sanchez A, Khan J, Polak MA, Glass JD (2004) Amyotrophic lateral sclerosis is a distal axonopathy: evidence in mice and man. Exp Neurol 185:232-240.

Fischer LR, Igoudjil A, Magrane J, Li Y, Hansen JM, Manfredi G, Glass JD (2011) SOD1 targeted to the mitochondrial intermembrane space prevents motor neuropathy in the Sod1 knockout mouse. Brain 134:196-209.

Flood DG, Reaume AG, Gruner JA, Hoffman EK, Hirsch JD, Lin YG, Dorfman KS, Scott RW (1999) Hindlimb motor neurons require Cu/Zn superoxide dismutase for maintenance of neuromuscular junctions. Am J Pathol 155:663-672.

Fortunato SJ, Menon R (2003) IL-1 beta is a better inducer of apoptosis in human fetal membranes than IL-6. Placenta 24:922-928.

Friedlander RM, Brown RH, Gagliardini V, Wang J, Yuan J (1997) Inhibition of ICE slows ALS in mice. Nature 388:31.

Frucht DM, Fukao T, Bogdan C, Schindler H, O'Shea JJ, Koyasu S (2001) IFN-gamma production by antigen-presenting cells: mechanisms emerge. Trends Immunol 22:556-560.

Funk CD (2001) Prostaglandins and leukotrienes: advances in eicosanoid biology. Science 294:1871-1875.

Furukawa Y, Fu R, Deng HX, Siddique T, O'Halloran TV (2006) Disulfide cross-linked protein represents a significant fraction of ALS-associated Cu, Zn-superoxide dismutase aggregates in spinal cords of model mice. Proc Natl Acad Sci U S A 103:7148-7153.

Gaillard PJ, Appeldoorn CC, Rip J, Dorland R, van der Pol SM, Kooij G, de Vries HE, Reijerkerk A (2012) Enhanced brain delivery of liposomal methylprednisolone improved therapeutic efficacy in a model of neuroinflammation. J Control Release.

Galbiati M, Onesto E, Zito A, Crippa V, Rusmini P, Mariotti R, Bentivoglio M, Bendotti C, Poletti A (2012) The anabolic/androgenic steroid nandrolone exacerbates gene expression modifications induced by mutant SOD1 in muscles of mice models of amyotrophic lateral sclerosis. Pharmacol Res 65:221-230.

Gamez J, Cervera C, Codina A (1999) Flail arm syndrome of Vulpian-Bernhart's form of amyotrophic lateral sclerosis. J Neurol Neurosurg Psychiatry 67:258.

Ganel R, Ho T, Maragakis NJ, Jackson M, Steiner JP, Rothstein JD (2006) Selective up-regulation of the glial Na+-dependent glutamate transporter GLT1 by a neuroimmunophilin ligand results in neuroprotection. Neurobiol Dis 21:556-567.

Garbuzova-Davis S, Haller E, Saporta S, Kolomey I, Nicosia SV, Sanberg PR (2007a) Ultrastructure of blood-brain barrier and blood-spinal cord barrier in SOD1 mice modeling ALS. Brain Res 1157:126-137.

Garbuzova-Davis S, Saporta S, Haller E, Kolomey I, Bennett SP, Potter H, Sanberg PR (2007b) Evidence of compromised blood-spinal cord barrier in early and late symptomatic SOD1 mice modeling ALS. PLoS One 2:e1205.

Garbuzova-Davis S, Saporta S, Sanberg PR (2008) Implications of blood-brain barrier disruption in ALS. Amyotroph Lateral Scler 9:375-376.

Gargiulo Monachelli G, Meyer M, Rodriguez GE, Garay LI, Sica RE, De Nicola AF, Gonzalez Deniselle MC (2011) Endogenous progesterone is associated to amyotrophic lateral sclerosis prognostic factors. Acta Neurol Scand 123:60-67.

Gass A, Barker GJ, Kidd D, Thorpe JW, MacManus D, Brennan A, Tofts PS, Thompson AJ, McDonald WI, Miller DH (1994) Correlation of magnetization transfer ratio with clinical disability in multiple sclerosis. Ann Neurol 36:62-67.

Gery I, Gershon RK, Waksman BH (1972) Potentiation of the T-lymphocyte response to mitogens. I. The responding cell. J Exp Med 136:128-142.

Gery I, Waksman BH (1972) Potentiation of the T-lymphocyte response to mitogens. II. The cellular source of potentiating mediator(s). J Exp Med 136:143-155.

Ghadge GD, Slusher BS, Bodner A, Canto MD, Wozniak K, Thomas AG, Rojas C, Tsukamoto T, Majer P, Miller RJ, Monti AL, Roos RP (2003) Glutamate carboxypeptidase II inhibition protects motor neurons from death in familial amyotrophic lateral sclerosis models. Proc Natl Acad Sci U S A 100:9554-9559.

Gifondorwa DJ, Robinson MB, Hayes CD, Taylor AR, Prevette DM, Oppenheim RW, Caress J, Milligan CE (2007) Exogenous delivery of heat shock protein 70 increases lifespan in a mouse model of amyotrophic lateral sclerosis. J Neurosci 27:13173-13180.

Gonatas NK, Stieber A, Mourelatos Z, Chen Y, Gonatas JO, Appel SH, Hays AP, Hickey WF, Hauw JJ (1992) Fragmentation of the Golgi apparatus of motor neurons in amyotrophic lateral sclerosis. Am J Pathol 140:731-737.

Gonzalez Deniselle MC, Gonzalez SL, De Nicola AF (2001) Cellular basis of steroid neuroprotection in the wobbler mouse, a genetic model of motoneuron disease. Cell Mol Neurobiol 21:237-254.

Gonzalez Deniselle MC, Gonzalez SL, Lima AE, Wilkin G, De Nicola AF (1999a) The 21-aminosteroid U-74389F attenuates hyperexpression of GAP-43 and NADPH-diaphorase in the spinal cord of wobbler mouse, a model for amyotrophic lateral sclerosis. Neurochem Res 24:1-8.

Gonzalez Deniselle MC, Gonzalez SL, Piroli GG, Lima AE, De Nicola AF (1996) The 21-aminosteroid U-74389F increases the number of glial fibrillary acidic protein-expressing astrocytes in the spinal cord of control and Wobbler mice. Cell Mol Neurobiol 16:61-72.

Gonzalez Deniselle MC, Grillo CA, Gonzalez S, Roig P, De Nicola AF (1999b) Evidence for down-regulation of GAP-43 mRNA in Wobbler mouse spinal motoneurons by corticosterone and a 21-aminosteroid. Brain Res 841:78-84.

Gordon S (2003) Alternative activation of macrophages. Nat Rev Immunol 3:23-35.

Gowing G, Lalancette-Hebert M, Audet JN, Dequen F, Julien JP (2009) Macrophage colony stimulating factor (M-CSF) exacerbates ALS disease in a mouse model through altered responses of microglia expressing mutant superoxide dismutase. Exp Neurol 220:267-275.

Graesser D, Mahooti S, Madri JA (2000) Distinct roles for matrix metalloproteinase-2 and alpha4 integrin in autoimmune T cell extravasation and residency in brain parenchyma during experimental autoimmune encephalomyelitis. J Neuroimmunol 109:121-131.

Groeneveld GJ, Van Muiswinkel FL, Sturkenboom JM, Wokke JH, Bar PR, Van den Berg LH (2004) Ovariectomy and 17beta-estradiol modulate disease progression of a mouse model of ALS. Brain Res 1021:128-131.

Gurney ME (1994) Transgenic-mouse model of amyotrophic lateral sclerosis. N Engl J Med 331:1721-1722.

Gurney ME, Cutting FB, Zhai P, Doble A, Taylor CP, Andrus PK, Hall ED (1996) Benefit of vitamin E, riluzole, and gabapentin in a transgenic model of familial amyotrophic lateral sclerosis. Ann Neurol 39:147-157.

Gurney ME, Pu H, Chiu AY, Dal Canto MC, Polchow CY, Alexander DD, Caliendo J, Hentati A, Kwon YW, Deng HX, et al. (1994) Motor neuron degeneration in mice that express a human Cu,Zn superoxide dismutase mutation. Science 264:1772-1775.

Gygi SP, Rochon Y, Franza BR, Aebersold R (1999) Correlation between protein and mRNA abundance in yeast. Mol Cell Biol 19:1720-1730.

Haeggstrom JZ, Wetterholm A (2002) Enzymes and receptors in the leukotriene cascade. Cell Mol Life Sci 59:742-753.

Hafezparast M, Klocke R, Ruhrberg C, Marquardt A, Ahmad-Annuar A, Bowen S, Lalli G, Witherden AS, Hummerich H, Nicholson S, Morgan PJ, Oozageer R, Priestley JV, Averill S, King VR, Ball S, Peters J, Toda T, Yamamoto A, Hiraoka Y, Augustin M, Korthaus D, Wattler S, Wabnitz P, Dickneite C, Lampel S, Boehme F, Peraus G, Popp A, Rudelius M, Schlegel J, Fuchs H, Hrabe de Angelis M, Schiavo G, Shima DT, Russ AP, Stumm G, Martin JE, Fisher EM (2003) Mutations in dynein link motor neuron degeneration to defects in retrograde transport. Science 300:808-812.

Hall ED, Oostveen JA, Gurney ME (1998) Relationship of microglial and astrocytic activation to disease onset and progression in a transgenic model of familial ALS. Glia 23:249-256.

Haraldsen G, Kvale D, Lien B, Farstad IN, Brandtzaeg P (1996) Cytokine-regulated expression of E-selectin, intercellular adhesion molecule-1 (ICAM-1), and vascular cell adhesion molecule-1 (VCAM-1) in human microvascular endothelial cells. J Immunol 156:2558-2565.

Hardin-Pouzet H, Krakowski M, Bourbonniere L, Didier-Bazes M, Tran E, Owens T (1997) Glutamate metabolism is down-regulated in astrocytes during experimental allergic encephalomyelitis. Glia 20:79-85.

Harris ED (1998) Amyotrophic lateral sclerosis: a lesson in deficiency diseases. Nutr Rev 56:81-84.

Harris JM, Chess RB (2003) Effect of pegylation on pharmaceuticals. Nat Rev Drug Discov 2:214-221.

Hayes-Punzo A, Mulcrone P, Meyer M, McHugh J, Svendsen CN, Suzuki M (2012) Gonadectomy and dehydroepiandrosterone (DHEA) do not modulate disease progression in the G93A mutant SOD1 rat model of amyotrophic lateral sclerosis. Amyotroph Lateral Scler 13:311-314.

Hayward C, Swingler RJ, Simpson SA, Brock DJ (1996) A specific superoxide dismutase mutation is on the same genetic background in sporadic and familial cases of amyotrophic lateral sclerosis. Am J Hum Genet 59:1165-1167.

Helpern JA, Lee SP, Falangola MF, Dyakin VV, Bogart A, Ardekani B, Duff K, Branch C, Wisniewski T, de Leon MJ, Wolf O, O'Shea J, Nixon RA (2004) MRI assessment of neuropathology in a transgenic mouse model of Alzheimer's disease. Magn Reson Med 51:794-798.

Henkel JS, Beers DR, Siklos L, Appel SH (2006) The chemokine MCP-1 and the dendritic and myeloid cells it attracts are increased in the mSOD1 mouse model of ALS. Mol Cell Neurosci 31:427-437.

Henkel JS, Beers DR, Zhao W, Appel SH (2009) Microglia in ALS: the good, the bad, and the resting. J Neuroimmune Pharmacol 4:389-398.

Henkel JS, Engelhardt JI, Siklos L, Simpson EP, Kim SH, Pan T, Goodman JC, Siddique T, Beers DR, Appel SH (2004) Presence of dendritic cells, MCP-1, and activated microglia/macrophages in amyotrophic lateral sclerosis spinal cord tissue. Ann Neurol 55:221-235.

Hensley K, Fedynyshyn J, Ferrell S, Floyd RA, Gordon B, Grammas P, Hamdheydari L, Mhatre M, Mou S, Pye QN, Stewart C, West M, West S, Williamson KS (2003) Message and protein-level elevation of tumor necrosis factor alpha (TNF alpha) and TNF alpha-modulating cytokines in spinal cords of the G93A-SOD1 mouse model for amyotrophic lateral sclerosis. Neurobiol Dis 14:74-80.

Hensley K, Floyd RA, Gordon B, Mou S, Pye QN, Stewart C, West M, Williamson K (2002) Temporal patterns of cytokine and apoptosis-related gene expression in spinal cords of the G93A-SOD1 mouse model of amyotrophic lateral sclerosis. J Neurochem 82:365-374.

Hewitt C, Kirby J, Highley JR, Hartley JA, Hibberd R, Hollinger HC, Williams TL, Ince PG, McDermott CJ, Shaw PJ (2010) Novel FUS/TLS mutations and pathology in familial and sporadic amyotrophic lateral sclerosis. Arch Neurol 67:455-461.

Hicks GG, Singh N, Nashabi A, Mai S, Bozek G, Klewes L, Arapovic D, White EK, Koury MJ, Oltz EM, Van Kaer L, Ruley HE (2000) Fus deficiency in mice results in defective B-lymphocyte development and activation, high levels of chromosomal instability and perinatal death. Nat Genet 24:175-179.

Higgins CMJ, Jung CW, Xu ZS (2003) ALS-associated mutant SOD1G93A causes mitochondrial vacuolation by expansion of the intermembrane space and by involvement of SOD1 aggregation and peroxisomes. Bmc Neuroscience 4:-.

Hirano A (1996) Neuropathology of ALS: an overview. Neurology 47:S63-66.

Hirano A, Nakano I, Kurland LT, Mulder DW, Holley PW, Saccomanno G (1984) Fine structural study of neurofibrillary changes in a family with amyotrophic lateral sclerosis. J Neuropathol Exp Neurol 43:471-480.

Hiroi M, Ohmori Y (2003) Constitutive nuclear factor kappaB activity is required to elicit interferon-gamma-induced expression of chemokine CXC ligand 9 (CXCL9) and CXCL10 in human tumour cell lines. Biochem J 376:393-402.

Hirtz D, Thurman DJ, Gwinn-Hardy K, Mohamed M, Chaudhuri AR, Zalutsky R (2007) How common are the "common" neurologic disorders? Neurology 68:326-337.

Ho YS, Gargano M, Cao J, Bronson RT, Heimler I, Hutz RJ (1998) Reduced fertility in female mice lacking copper-zinc superoxide dismutase. J Biol Chem 273:7765-7769.

Hoek RM, Ruuls SR, Murphy CA, Wright GJ, Goddard R, Zurawski SM, Blom B, Homola ME, Streit WJ, Brown MH, Barclay AN, Sedgwick JD (2000) Down-regulation of the macrophage lineage through interaction with OX2 (CD200). Science 290:1768-1771.

Holmoy T, Roos PM, Kvale EO (2006) ALS: cytokine profile in cerebrospinal fluid T-cell clones. Amyotroph Lateral Scler 7:183-186.

Hortobagyi T, Troakes C, Nishimura AL, Vance C, van Swieten JC, Seelaar H, King A, Al-Sarraj S, Rogelj B, Shaw CE (2011) Optineurin inclusions occur in a minority of TDP-43 positive ALS and FTLD-TDP cases and are rarely observed in other neurodegenerative disorders. Acta Neuropathol 121:519-527.

Howland DS, Liu J, She Y, Goad B, Maragakis NJ, Kim B, Erickson J, Kulik J, DeVito L, Psaltis G, DeGennaro LJ, Cleveland DW, Rothstein JD (2002) Focal loss of the glutamate transporter EAAT2 in a transgenic rat model of SOD1 mutant-mediated amyotrophic lateral sclerosis (ALS). Proc Natl Acad Sci U S A 99:1604-1609.

Hoyte LC, Brooks KJ, Nagel S, Akhtar A, Chen R, Mardiguian S, McAteer MA, Anthony DC, Choudhury RP, Buchan AM, Sibson NR (2010) Molecular magnetic resonance imaging of acute vascular cell adhesion molecule-1 expression in a mouse model of cerebral ischemia. J Cereb Blood Flow Metab 30:1178-1187.

Hrabe de Angelis MH, Flaswinkel H, Fuchs H, Rathkolb B, Soewarto D, Marschall S, Heffner S, Pargent W, Wuensch K, Jung M, Reis A, Richter T, Alessandrini F, Jakob T, Fuchs E, Kolb H, Kremmer E, Schaeble K, Rollinski B, Roscher A, Peters C, Meitinger T, Strom T, Steckler T, Holsboer F, Klopstock T, Gekeler F, Schindewolf C, Jung T, Avraham K, Behrendt H, Ring J, Zimmer A, Schughart K, Pfeffer K, Wolf E, Balling R (2000) Genome-wide, large-scale production of mutant mice by ENU mutagenesis. Nat Genet 25:444-447.

Hu MT, Ellis CM, Al-Chalabi A, Leigh PN, Shaw CE (1998) Flail arm syndrome: a distinctive variant of amyotrophic lateral sclerosis. J Neurol Neurosurg Psychiatry 65:950-951.

Huang C, Zhou H, Tong J, Chen H, Liu YJ, Wang D, Wei X, Xia XG (2011) FUS transgenic rats develop the phenotypes of amyotrophic lateral sclerosis and frontotemporal lobar degeneration. PLoS Genet 7:e1002011.

Huang EJ, Zhang J, Geser F, Trojanowski JQ, Strober JB, Dickson DW, Brown RH, Jr., Shapiro BE, Lomen-Hoerth C (2010) Extensive FUS-immunoreactive pathology

in juvenile amyotrophic lateral sclerosis with basophilic inclusions. Brain Pathol 20:1069-1076.

Huisman TA (2003) Diffusion-weighted imaging: basic concepts and application in cerebral stroke and head trauma. Eur Radiol 13:2283-2297.

Igarashi Y, Utsumi H, Chiba H, Yamada-Sasamori Y, Tobioka H, Kamimura Y, Furuuchi K, Kokai Y, Nakagawa T, Mori M, Sawada N (1999) Glial cell line-derived neurotrophic factor induces barrier function of endothelial cells forming the blood-brain barrier. Biochem Biophys Res Commun 261:108-112.

Iida A, Hosono N, Sano M, Kamei T, Oshima S, Tokuda T, Kubo M, Nakamura Y, Ikegawa S (2012) Optineurin mutations in Japanese amyotrophic lateral sclerosis. J Neurol Neurosurg Psychiatry 83:233-235.

Ikeda J, Kohriyama T, Nakamura S (2000) Elevation of serum soluble E-selectin and antisulfoglucuronyl paragloboside antibodies in amyotrophic lateral sclerosis. Eur J Neurol 7:541-547.

Isgaard J, Aberg D, Nilsson M (2007) Protective and regenerative effects of the GH/IGF-I axis on the brain. Minerva endocrinologica 32:103-113.

Israelsson C, Bengtsson H, Lobell A, Nilsson LN, Kylberg A, Isaksson M, Wootz H, Lannfelt L, Kullander K, Hillered L, Ebendal T (2010) Appearance of Cxcl10-expressing cell clusters is common for traumatic brain injury and neurodegenerative disorders. Eur J Neurosci 31:852-863.

Jaarsma D, Haasdijk ED, Grashorn JA, Hawkins R, van Duijn W, Verspaget HW, London J, Holstege JC (2000) Human Cu/Zn superoxide dismutase (SOD1) overexpression in mice causes mitochondrial vacuolization, axonal degeneration, and premature motoneuron death and accelerates motoneuron disease in mice expressing a familial amyotrophic lateral sclerosis mutant SOD1. Neurobiol Dis 7:623-643.

Jaarsma D, Teuling E, Haasdijk ED, De Zeeuw CI, Hoogenraad CC (2008) Neuron-specific expression of mutant superoxide dismutase is sufficient to induce amyotrophic lateral sclerosis in transgenic mice. J Neurosci 28:2075-2088.

Jablonski MR, Jacob DA, Campos C, Miller DS, Maragakis NJ, Pasinelli P, Trotti D (2012) Selective increase of two ABC drug efflux transporters at the blood-spinal cord barrier suggests induced pharmacoresistance in ALS. Neurobiol Dis 47:194-200.

Janaky R, Varga V, Saransaari P, Oja SS (1993) Glutathione modulates the N-methyl-D-aspartate receptor-activated calcium influx into cultured rat cerebellar granule cells. Neurosci Lett 156:153-157.

Janknecht R (2005) EWS-ETS oncoproteins: the linchpins of Ewing tumors. Gene 363:1-14.

Janoff A, Zeligs JD (1968) Vascular injury and lysis of basement membrane in vitro by neutral protease of human leukocytes. Science 161:702-704.

Jenkins BG, Klivenyi P, Kustermann E, Andreassen OA, Ferrante RJ, Rosen BR, Beal MF (2000) Nonlinear decrease over time in N-acetyl aspartate levels in the absence of neuronal loss and increases in glutamine and glucose in transgenic Huntington's disease mice. J Neurochem 74:2108-2119.

Jenkins BG, Koroshetz WJ, Beal MF, Rosen BR (1993) Evidence for impairment of energy metabolism in vivo in Huntington's disease using localized 1H NMR spectroscopy. Neurology 43:2689-2695.

Jenkins BG, Rosas HD, Chen YC, Makabe T, Myers R, MacDonald M, Rosen BR, Beal MF, Koroshetz WJ (1998) 1H NMR spectroscopy studies of Huntington's disease: correlations with CAG repeat numbers. Neurology 50:1357-1365.

Jiang F, DeSilva S, Turnbull J (2000) Beneficial effect of ginseng root in SOD-1 (G93A) transgenic mice. J Neurol Sci 180:52-54.

Jiang F, Li WP, Kwiecien J, Turnbull J (2006) A study of the purine derivative AIT-082 in G93A SOD1 transgenic mice. Int J Immunopathol Pharmacol 19:489-498.

Johanson CE, Stopa EG, McMillan PN (2011) The blood-cerebrospinal fluid barrier: structure and functional significance. Methods Mol Biol 686:101-131.

Johnson JO, Mandrioli J, Benatar M, Abramzon Y, Van Deerlin VM, Trojanowski JQ, Gibbs JR, Brunetti M, Gronka S, Wuu J, Ding J, McCluskey L, Martinez-Lage M, Falcone D, Hernandez DG, Arepalli S, Chong S, Schymick JC, Rothstein J, Landi F, Wang YD, Calvo A, Mora G, Sabatelli M, Monsurro MR, Battistini S, Salvi F, Spataro R, Sola P, Borghero G, Galassi G, Scholz SW, Taylor JP, Restagno G, Chio A, Traynor BJ (2010) Exome sequencing reveals VCP mutations as a cause of familial ALS. Neuron 68:857-864.

Johnston JA, Dalton MJ, Gurney ME, Kopito RR (2000) Formation of high molecular weight complexes of mutant Cu, Zn-superoxide dismutase in a mouse model for familial amyotrophic lateral sclerosis. Proc Natl Acad Sci U S A 97:12571-12576.

Jung C, Rong Y, Doctrow S, Baudry M, Malfroy B, Xu Z (2001) Synthetic superoxide dismutase/catalase mimetics reduce oxidative stress and prolong survival in a mouse amyotrophic lateral sclerosis model. Neurosci Lett 304:157-160.

Juniper EF, Kline PA, Vanzieleghem MA, Ramsdale EH, O'Byrne PM, Hargreave FE (1990) Long-term effects of budesonide on airway responsiveness and clinical asthma severity in inhaled steroid-dependent asthmatics. Eur Respir J 3:1122-1127.

Kalmar B, Novoselov S, Gray A, Cheetham ME, Margulis B, Greensmith L (2008) Late stage treatment with arimoclomol delays disease progression and prevents protein aggregation in the SOD1 mouse model of ALS. J Neurochem 107:339-350.

Kalueff AV, Wheaton M, Murphy DL (2007) What's wrong with my mouse model? Advances and strategies in animal modeling of anxiety and depression. Behav Brain Res 179:1-18.

Kang SJ, Sanchez I, Jing N, Yuan J (2003) Dissociation between neurodegeneration and caspase-11-mediated activation of caspase-1 and caspase-3 in a mouse model of amyotrophic lateral sclerosis. J Neurosci 23:5455-5460.

Kantarci K, Reynolds G, Petersen RC, Boeve BF, Knopman DS, Edland SD, Smith GE, Ivnik RJ, Tangalos EG, Jack CR, Jr. (2003) Proton MR spectroscopy in mild cognitive impairment and Alzheimer disease: comparison of 1.5 and 3 T. AJNR Am J Neuroradiol 24:843-849.

Karlsson J, Fong KS, Hansson MJ, Elmer E, Csiszar K, Keep MF (2004) Life span extension and reduced neuronal death after weekly intraventricular cyclosporin injections in the G93A transgenic mouse model of amyotrophic lateral sclerosis. J Neurosurg 101:128-137.

Kaspar BK, Llado J, Sherkat N, Rothstein JD, Gage FH (2003) Retrograde viral delivery of IGF-1 prolongs survival in a mouse ALS model. Science 301:839-842.

Kassa RM, Mariotti R, Bonaconsa M, Bertini G, Bentivoglio M (2009) Gene, cell, and axon changes in the familial amyotrophic lateral sclerosis mouse sensorimotor cortex. J Neuropathol Exp Neurol 68:59-72.

Kassubek J, Unrath A, Huppertz HJ, Lule D, Ethofer T, Sperfeld AD, Ludolph AC (2005) Global brain atrophy and corticospinal tract alterations in ALS, as investigated by voxel-based morphometry of 3-D MRI. Amyotroph Lateral Scler Other Motor Neuron Disord 6:213-220.

Kawai M, Nishikomori R, Jung EY, Tai G, Yamanaka C, Mayumi M, Heike T (1995) Pyrrolidine dithiocarbamate inhibits intercellular adhesion molecule-1 biosynthesis induced by cytokines in human fibroblasts. J Immunol 154:2333-2341.

Keller AF, Gravel M, Kriz J (2009) Live imaging of amyotrophic lateral sclerosis pathogenesis: disease onset is characterized by marked induction of GFAP in Schwann cells. Glia 57:1130-1142.

Keller JN, Mark RJ, Bruce AJ, Blanc E, Rothstein JD, Uchida K, Waeg G, Mattson MP (1997) 4-Hydroxynonenal, an aldehydic product of membrane lipid peroxidation, impairs glutamate transport and mitochondrial function in synaptosomes. Neuroscience 80:685-696.

Kiaei M, Kipiani K, Petri S, Chen J, Calingasan NY, Beal MF (2005) Celastrol blocks neuronal cell death and extends life in transgenic mouse model of amyotrophic lateral sclerosis. Neurodegener Dis 2:246-254.

Kiaei M, Petri S, Kipiani K, Gardian G, Choi DK, Chen J, Calingasan NY, Schafer P, Muller GW, Stewart C, Hensley K, Beal MF (2006) Thalidomide and lenalidomide extend survival in a transgenic mouse model of amyotrophic lateral sclerosis. J Neurosci 26:2467-2473.

Kieran D, Hafezparast M, Bohnert S, Dick JR, Martin J, Schiavo G, Fisher EM, Greensmith L (2005) A mutation in dynein rescues axonal transport defects and extends the life span of ALS mice. J Cell Biol 169:561-567.

Kieran D, Kalmar B, Dick JR, Riddoch-Contreras J, Burnstock G, Greensmith L (2004) Treatment with arimoclomol, a coinducer of heat shock proteins, delays disease progression in ALS mice. Nat Med 10:402-405.

Kim JH, Wu TH, Budde MD, Lee JM, Song SK (2010) Noninvasive detection of brainstem and spinal cord axonal degeneration in an amyotrophic lateral sclerosis mouse model. NMR Biomed.

Klein RS (2004) Regulation of neuroinflammation: the role of CXCL10 in lymphocyte infiltration during autoimmune encephalomyelitis. J Cell Biochem 92:213-222.

Klivenyi P, Ferrante RJ, Matthews RT, Bogdanov MB, Klein AM, Andreassen OA, Mueller G, Wermer M, Kaddurah-Daouk R, Beal MF (1999) Neuroprotective

effects of creatine in a transgenic animal model of amyotrophic lateral sclerosis. Nat Med 5:347-350.

Klivenyi P, Kiaei M, Gardian G, Calingasan NY, Beal MF (2004) Additive neuroprotective effects of creatine and cyclooxygenase 2 inhibitors in a transgenic mouse model of amyotrophic lateral sclerosis. J Neurochem 88:576-582.

Koh SH, Kim Y, Kim HY, Hwang S, Lee CH, Kim SH (2007) Inhibition of glycogen synthase kinase-3 suppresses the onset of symptoms and disease progression of G93A-SOD1 mouse model of ALS. Exp Neurol 205:336-346.

Koh SH, Lee SM, Kim HY, Lee KY, Lee YJ, Kim HT, Kim J, Kim MH, Hwang MS, Song C, Yang KW, Lee KW, Kim SH, Kim OH (2006) The effect of epigallocatechin gallate on suppressing disease progression of ALS model mice. Neurosci Lett 395:103-107.

Kong JM, Xu ZS (1998) Massive mitochondrial degeneration in motor neurons triggers the onset of amyotrophic lateral sclerosis in mice expressing a mutant SOD1. Journal of Neuroscience 18:3241-3250.

Korting HC, Schafer-Korting M, Klovekorn W, Klovekorn G, Martin C, Laux P (1995) Comparative efficacy of hamamelis distillate and hydrocortisone cream in atopic eczema. Eur J Clin Pharmacol 48:461-465.

Kruman, II, Pedersen WA, Springer JE, Mattson MP (1999) ALS-linked Cu/Zn-SOD mutation increases vulnerability of motor neurons to excitotoxicity by a mechanism involving increased oxidative stress and perturbed calcium homeostasis. Exp Neurol 160:28-39.

Kuhle J, Lindberg RL, Regeniter A, Mehling M, Steck AJ, Kappos L, Czaplinski A (2009) Increased levels of inflammatory chemokines in amyotrophic lateral sclerosis. Eur J Neurol 16:771-774.

Kumar M, Abdel-Dayem HM (1999) Three generations of amyotrophic lateral sclerosis in a family: SPECT brain perfusion findings. Clin Nucl Med 24:539-540.

Kuroda M, Sok J, Webb L, Baechtold H, Urano F, Yin Y, Chung P, de Rooij DG, Akhmedov A, Ashley T, Ron D (2000) Male sterility and enhanced radiation sensitivity in TLS(-/-) mice. EMBO J 19:453-462.

Kushner PD, Stephenson DT, Wright S (1991) Reactive astrogliosis is widespread in the subcortical white matter of amyotrophic lateral sclerosis brain. J Neuropathol Exp Neurol 50:263-277.

Kwiatkowski TJ, Jr., Bosco DA, Leclerc AL, Tamrazian E, Vanderburg CR, Russ C, Davis A, Gilchrist J, Kasarskis EJ, Munsat T, Valdmanis P, Rouleau GA, Hosler BA, Cortelli P, de Jong PJ, Yoshinaga Y, Haines JL, Pericak-Vance MA, Yan J, Ticozzi N, Siddique T, McKenna-Yasek D, Sapp PC, Horvitz HR, Landers JE, Brown RH, Jr. (2009) Mutations in the FUS/TLS gene on chromosome 16 cause familial amyotrophic lateral sclerosis. Science 323:1205-1208.

Laaksovirta H, Peuralinna T, Schymick JC, Scholz SW, Lai SL, Myllykangas L, Sulkava R, Jansson L, Hernandez DG, Gibbs JR, Nalls MA, Heckerman D, Tienari PJ, Traynor BJ (2010) Chromosome 9p21 in amyotrophic lateral sclerosis in Finland: a genome-wide association study. Lancet Neurol 9:978-985.

Lagier-Tourenne C, Cleveland DW (2009) Rethinking ALS: the FUS about TDP-43. Cell 136:1001-1004.

Laird AS, Van Hoecke A, De Muynck L, Timmers M, Van den Bosch L, Van Damme P, Robberecht W (2010) Progranulin is neurotrophic in vivo and protects against a mutant TDP-43 induced axonopathy. PLoS One 5:e13368.

Lalancette-Hebert M, Gowing G, Simard A, Weng YC, Kriz J (2007) Selective ablation of proliferating microglial cells exacerbates ischemic injury in the brain. J Neurosci 27:2596-2605.

Lambrechts D, Storkebaum E, Morimoto M, Del-Favero J, Desmet F, Marklund SL, Wyns S, Thijs V, Andersson J, van Marion I, Al-Chalabi A, Bornes S, Musson R, Hansen V, Beckman L, Adolfsson R, Pall HS, Prats H, Vermeire S, Rutgeerts P, Katayama S, Awata T, Leigh N, Lang-Lazdunski L, Dewerchin M, Shaw C, Moons L, Vlietinck R, Morrison KE, Robberecht W, Van Broeckhoven C, Collen D, Andersen PM, Carmeliet P (2003) VEGF is a modifier of amyotrophic lateral sclerosis in mice and humans and protects motoneurons against ischemic death. Nat Genet 34:383-394.

Langkammer C, Enzinger C, Quasthoff S, Grafenauer P, Soellinger M, Fazekas F, Ropele S (2010) Mapping of iron deposition in conjunction with assessment of nerve fiber tract integrity in amyotrophic lateral sclerosis. J Magn Reson Imaging 31:1339-1345.

Lanson NA, Jr., Maltare A, King H, Smith R, Kim JH, Taylor JP, Lloyd TE, Pandey UB (2011) A Drosophila model of FUS-related neurodegeneration reveals genetic interaction between FUS and TDP-43. Hum Mol Genet 20:2510-2523.

Lanzrein AS, Johnston CM, Perry VH, Jobst KA, King EM, Smith AD (1998) Longitudinal study of inflammatory factors in serum, cerebrospinal fluid, and brain tissue in Alzheimer disease: interleukin-1beta, interleukin-6, interleukin-1 receptor antagonist, tumor necrosis factor-alpha, the soluble tumor necrosis factor receptors I and II, and alpha1-antichymotrypsin. Alzheimer Dis Assoc Disord 12:215-227.

Lasiglie D, Traggiai E, Federici S, Alessio M, Buoncompagni A, Accogli A, Chiesa S, Penco F, Martini A, Gattorno M (2011) Role of IL-1 beta in the development of human T(H)17 cells: lesson from NLPR3 mutated patients. PLoS One 6:e20014.

Lee P, Peng H, Gelbart T, Wang L, Beutler E (2005) Regulation of hepcidin transcription by interleukin-1 and interleukin-6. Proc Natl Acad Sci U S A 102:1906-1910.

Lee SC, Liu W, Dickson DW, Brosnan CF, Berman JW (1993) Cytokine production by human fetal microglia and astrocytes. Differential induction by lipopolysaccharide and IL-1 beta. J Immunol 150:2659-2667.

Lee SW, Kim WJ, Choi YK, Song HS, Son MJ, Gelman IH, Kim YJ, Kim KW (2003) SSeCKS regulates angiogenesis and tight junction formation in blood-brain barrier. Nat Med 9:900-906.

Lefebvre S, Burglen L, Reboullet S, Clermont O, Burlet P, Viollet L, Benichou B, Cruaud C, Millasseau P, Zeviani M, et al. (1995) Identification and characterization of a spinal muscular atrophy-determining gene. Cell 80:155-165.

Leichsenring A, Linnartz B, Zhu XR, Lubbert H, Stichel CC (2006) Ascending neuropathology in the CNS of a mutant SOD1 mouse model of amyotrophic lateral sclerosis. Brain Res 1096:180-195.

Leigh PN, Swash M (1991) Cytoskeletal pathology in motor neuron diseases. Adv Neurol 56:115-124.

Leonardi A, Abbruzzese G, Arata L, Cocito L, Vische M (1984) Cerebrospinal fluid (CSF) findings in amyotrophic lateral sclerosis. J Neurol 231:75-78.

Lever TE, Gorsek A, Cox KT, O'Brien KF, Capra NF, Hough MS, Murashov AK (2009) An animal model of oral dysphagia in amyotrophic lateral sclerosis. Dysphagia 24:180-195.

Levine TP, Daniels RD, Gatta AT, Wong LH, Hayes MJ (2013) The product of C9orf72, a gene strongly implicated in neurodegeneration, is structurally related to DENN Rab-GEFs. Bioinformatics 29:499-503.

Li L, Lu J, Tay SS, Moochhala SM, He BP (2007) The function of microglia, either neuroprotection or neurotoxicity, is determined by the equilibrium among factors released from activated microglia in vitro. Brain Res 1159:8-17.

Li M, Ona VO, Guegan C, Chen M, Jackson-Lewis V, Andrews LJ, Olszewski AJ, Stieg PE, Lee JP, Przedborski S, Friedlander RM (2000) Functional role of caspase-1 and caspase-3 in an ALS transgenic mouse model. Science 288:335-339.

Li Q, Li H, Roughton K, Wang X, Kroemer G, Blomgren K, Zhu C (2010) Lithium reduces apoptosis and autophagy after neonatal hypoxia-ischemia. Cell Death Dis 1:e56.

Liachko NF, Guthrie CR, Kraemer BC (2010) Phosphorylation promotes neurotoxicity in a Caenorhabditis elegans model of TDP-43 proteinopathy. J Neurosci 30:16208-16219.

Lincecum JM, Vieira FG, Wang MZ, Thompson K, De Zutter GS, Kidd J, Moreno A, Sanchez R, Carrion IJ, Levine BA, Al-Nakhala BM, Sullivan SM, Gill A, Perrin S (2010) From transcriptome analysis to therapeutic anti-CD40L treatment in the SOD1 model of amyotrophic lateral sclerosis. Nat Genet 42:392-399.

Liu D, Wen J, Liu J, Li L (1999) The roles of free radicals in amyotrophic lateral sclerosis: reactive oxygen species and elevated oxidation of protein, DNA, and membrane phospholipids. FASEB J 13:2318-2328.

Liu G, Fiala M, Mizwicki MT, Sayre J, Magpantay L, Siani A, Mahanian M, Chattopadhyay M, La Cava A, Wiedau-Pazos M (2012) Neuronal phagocytosis by inflammatory macrophages in ALS spinal cord: inhibition of inflammation by resolvin D1. Am J Neurodegener Dis 1:60-74.

Liu J, Lillo C, Jonsson PA, Vande Velde C, Ward CM, Miller TM, Subramaniam JR, Rothstein JD, Marklund S, Andersen PM, Brannstrom T, Gredal O, Wong PC, Williams DS, Cleveland DW (2004) Toxicity of familial ALS-linked SOD1 mutants from selective recruitment to spinal mitochondria. Neuron 43:5-17.

Lomen-Hoerth C, Anderson T, Miller B (2002) The overlap of amyotrophic lateral sclerosis and frontotemporal dementia. Neurology 59:1077-1079.

Lorenzl S, Narr S, Angele B, Krell HW, Gregorio J, Kiaei M, Pfister HW, Beal MF (2006) The matrix metalloproteinases inhibitor Ro 28-2653 [correction of Ro 26-2853] extends survival in transgenic ALS mice. Exp Neurol 200:166-171.

Loscher W, Potschka H (2005) Drug resistance in brain diseases and the role of drug efflux transporters. Nat Rev Neurosci 6:591-602.

Lu Y, Ferris J, Gao FB (2009) Frontotemporal dementia and amyotrophic lateral sclerosis-associated disease protein TDP-43 promotes dendritic branching. Mol Brain 2:30.

Lubos E, Kelly NJ, Oldebeken SR, Leopold JA, Zhang YY, Loscalzo J, Handy DE (2011) Glutathione peroxidase-1 deficiency augments proinflammatory cytokine-induced redox signaling and human endothelial cell activation. J Biol Chem 286:35407-35417.

Lucas SM, Rothwell NJ, Gibson RM (2006) The role of inflammation in CNS injury and disease. Br J Pharmacol 147 Suppl 1:S232-240.

Ludolph AC, Bendotti C, Blaugrund E, Chio A, Greensmith L, Loeffler JP, Mead R, Niessen HG, Petri S, Pradat PF, Robberecht W, Ruegg M, Schwalenstocker B, Stiller D, van den Berg L, Vieira F, von Horsten S (2010) Guidelines for preclinical animal research in ALS/MND: A consensus meeting. Amyotroph Lateral Scler 11:38-45.

Mackenzie IR, Bigio EH, Ince PG, Geser F, Neumann M, Cairns NJ, Kwong LK, Forman MS, Ravits J, Stewart H, Eisen A, McClusky L, Kretzschmar HA, Monoranu CM, Highley JR, Kirby J, Siddique T, Shaw PJ, Lee VM, Trojanowski JQ (2007) Pathological TDP-43 distinguishes sporadic amyotrophic lateral sclerosis from amyotrophic lateral sclerosis with SOD1 mutations. Ann Neurol 61:427-434.

Mackenzie IR, Foti D, Woulfe J, Hurwitz TA (2008) Atypical frontotemporal lobar degeneration with ubiquitin-positive, TDP-43-negative neuronal inclusions. Brain 131:1282-1293.

Mackenzie IR, Rademakers R, Neumann M (2010) TDP-43 and FUS in amyotrophic lateral sclerosis and frontotemporal dementia. Lancet Neurol 9:995-1007.

Magistretti PJ, Pellerin L, Rothman DL, Shulman RG (1999) Energy on demand. Science 283:496-497.

Mantovani S, Garbelli S, Pasini A, Alimonti D, Perotti C, Melazzini M, Bendotti C, Mora G (2009) Immune system alterations in sporadic amyotrophic lateral sclerosis patients suggest an ongoing neuroinflammatory process. J Neuroimmunol 210:73-79.

Marchesi VT (1961) The site of leucocyte emigration during inflammation. Q J Exp Physiol Cogn Med Sci 46:115-118.

Marchetto MC, Muotri AR, Mu Y, Smith AM, Cezar GG, Gage FH (2008) Non-cell-autonomous effect of human SOD1 G37R astrocytes on motor neurons derived from human embryonic stem cells. Cell Stem Cell 3:649-657.

Martin-Fontecha A, Thomsen LL, Brett S, Gerard C, Lipp M, Lanzavecchia A, Sallusto F (2004) Induced recruitment of NK cells to lymph nodes provides IFN-gamma for T(H)1 priming. Nat Immunol 5:1260-1265.

Martinez FO, Gordon S, Locati M, Mantovani A (2006) Transcriptional profiling of the human monocyte-to-macrophage differentiation and polarization: new molecules and patterns of gene expression. J Immunol 177:7303-7311.

Maruyama H, Morino H, Ito H, Izumi Y, Kato H, Watanabe Y, Kinoshita Y, Kamada M, Nodera H, Suzuki H, Komure O, Matsuura S, Kobatake K, Morimoto N, Abe K, Suzuki N, Aoki M, Kawata A, Hirai T, Kato T, Ogasawara K, Hirano A, Takumi T, Kusaka H, Hagiwara K, Kaji R, Kawakami H (2010) Mutations of optineurin in amyotrophic lateral sclerosis. Nature 465:223-226.

Mattiazzi M, D'Aurelio M, Gajewski CD, Martushova K, Kiaei M, Beal MF, Manfredi G (2002) Mutated human SOD1 causes dysfunction of oxidative phosphorylation in mitochondria of transgenic mice. Journal of Biological Chemistry 277:29626-29633.

Mattson MP, Camandola S (2001) NF-kappaB in neuronal plasticity and neurodegenerative disorders. J Clin Invest 107:247-254.

McAteer MA, Sibson NR, von Zur Muhlen C, Schneider JE, Lowe AS, Warrick N, Channon KM, Anthony DC, Choudhury RP (2007) In vivo magnetic resonance imaging of acute brain inflammation using microparticles of iron oxide. Nat Med 13:1253-1258.

McColl BW, Rothwell NJ, Allan SM (2007) Systemic inflammatory stimulus potentiates the acute phase and CXC chemokine responses to experimental stroke and exacerbates brain damage via interleukin-1- and neutrophil-dependent mechanisms. J Neurosci 27:4403-4412.

McGeer PL, McGeer EG (2002) Inflammatory processes in amyotrophic lateral sclerosis. Muscle Nerve 26:459-470.

McNab G, Reeves JL, Salmi M, Hubscher S, Jalkanen S, Adams DH (1996) Vascular adhesion protein 1 mediates binding of T cells to human hepatic endothelium. Gastroenterology 110:522-528.

Meininger V, Lacomblez L, Salachas F (2000) What has changed with riluzole? J Neurol 247:19-22.

Meissner F, Molawi K, Zychlinsky A (2010) Mutant superoxide dismutase 1-induced IL-1beta accelerates ALS pathogenesis. Proc Natl Acad Sci U S A 107:13046-13050.

Meister A, Anderson ME (1983) Glutathione. Annu Rev Biochem 52:711-760.

Miana-Mena FJ, Munoz MJ, Yague G, Mendez M, Moreno M, Ciriza J, Zaragoza P, Osta R (2005) Optimal methods to characterize the G93A mouse model of ALS. Amyotroph Lateral Scler Other Motor Neuron Disord 6:55-62.

Michalec L, Choudhury BK, Postlethwait E, Wild JS, Alam R, Lett-Brown M, Sur S (2002) CCL7 and CXCL10 orchestrate oxidative stress-induced neutrophilic lung inflammation. J Immunol 168:846-852.

Militello A, Vitello G, Lunetta C, Toscano A, Maiorana G, Piccoli T, La Bella V (2002) The serum level of free testosterone is reduced in amyotrophic lateral sclerosis. J Neurol Sci 195:67-70.

Millan J, Hewlett L, Glyn M, Toomre D, Clark P, Ridley AJ (2006) Lymphocyte transcellular migration occurs through recruitment of endothelial ICAM-1 to caveola- and F-actin-rich domains. Nat Cell Biol 8:113-123.

Miller R (2003) Riluzole for ALS: what is the evidence? Amyotroph Lateral Scler Other Motor Neuron Disord 4:135.

Miller RG, Mitchell JD, Lyon M, Moore DH (2003) Riluzole for amyotrophic lateral sclerosis (ALS)/motor neuron disease (MND). Amyotroph Lateral Scler Other Motor Neuron Disord 4:191-206.

Milligan NM, Newcombe R, Compston DA (1987) A double-blind controlled trial of high dose methylprednisolone in patients with multiple sclerosis: 1. Clinical effects. J Neurol Neurosurg Psychiatry 50:511-516.

Minciacchi D, Kassa RM, Del Tongo C, Mariotti R, Bentivoglio M (2009) Voronoi-based spatial analysis reveals selective interneuron changes in the cortex of FALS mice. Exp Neurol 215:77-86.

Miyazaki K, Ohta Y, Nagai M, Morimoto N, Kurata T, Takehisa Y, Ikeda Y, Matsuura T, Abe K (2011) Disruption of neurovascular unit prior to motor neuron degeneration in amyotrophic lateral sclerosis. J Neurosci Res 89:718-728.

Mogi M, Harada M, Kondo T, Riederer P, Inagaki H, Minami M, Nagatsu T (1994) Interleukin-1 beta, interleukin-6, epidermal growth factor and transforming growth factor-alpha are elevated in the brain from parkinsonian patients. Neurosci Lett 180:147-150.

Moisse K, Strong MJ (2006) Innate immunity in amyotrophic lateral sclerosis. Biochim Biophys Acta 1762:1083-1093.

Molla M, Gironella M, Salas A, Closa D, Biete A, Gimeno M, Coronel P, Pique JM, Panes J (2005) Protective effect of superoxide dismutase in radiation-induced intestinal inflammation. Int J Radiat Oncol Biol Phys 61:1159-1166.

Moller DR, Wysocka M, Greenlee BM, Ma X, Wahl L, Flockhart DA, Trinchieri G, Karp CL (1997) Inhibition of IL-12 production by thalidomide. J Immunol 159:5157-5161.

Moreau C, Devos D, Brunaud-Danel V, Defebvre L, Perez T, Destee A, Tonnel AB, Lassalle P, Just N (2005) Elevated IL-6 and TNF-alpha levels in patients with ALS: inflammation or hypoxia? Neurology 65:1958-1960.

Moreira AL, Sampaio EP, Zmuidzinas A, Frindt P, Smith KA, Kaplan G (1993) Thalidomide exerts its inhibitory action on tumor necrosis factor alpha by enhancing mRNA degradation. J Exp Med 177:1675-1680.

Mori S, Zhang J (2006) Principles of diffusion tensor imaging and its applications to basic neuroscience research. Neuron 51:527-539.

Morimoto RI (2011) The heat shock response: systems biology of proteotoxic stress in aging and disease. Cold Spring Harb Symp Quant Biol 76:91-99.

Morita M, Al-Chalabi A, Andersen PM, Hosler B, Sapp P, Englund E, Mitchell JE, Habgood JJ, de Belleroche J, Xi J, Jongjaroenprasert W, Horvitz HR, Gunnarsson LG, Brown RH, Jr. (2006) A locus on chromosome 9p confers susceptibility to ALS and frontotemporal dementia. Neurology 66:839-844.

Mosser DM, Edwards JP (2008) Exploring the full spectrum of macrophage activation. Nat Rev Immunol 8:958-969.

Mourelatos Z, Gonatas NK, Stieber A, Gurney ME, Dal Canto MC (1996) The Golgi apparatus of spinal cord motor neurons in transgenic mice expressing mutant Cu,Zn superoxide dismutase becomes fragmented in early, preclinical stages of the disease. Proc Natl Acad Sci U S A 93:5472-5477.

Mulder DW, Kurland LT, Offord KP, Beard CM (1986) Familial adult motor neuron disease: amyotrophic lateral sclerosis. Neurology 36:511-517.

Muller WA (1995) Migration of leukocytes across the vascular intima molecules and mechanisms. Trends Cardiovasc Med 5:15-20.

Muller WA (2003) Leukocyte-endothelial-cell interactions in leukocyte transmigration and the inflammatory response. Trends Immunol 24:327-334.

Murakami R (1987) A histological study of the development of the penis of wild-type and androgen-insensitive mice. J Anat 153:223-231.

Murakami T, Yang SP, Xie L, Kawano T, Fu D, Mukai A, Bohm C, Chen F, Robertson J, Suzuki H, Tartaglia GG, Vendruscolo M, Kaminski Schierle GS, Chan FT, Moloney A, Crowther D, Kaminski CF, Zhen M, St George-Hyslop P (2012) ALS mutations in FUS cause neuronal dysfunction and death in Caenorhabditis elegans by a dominant gain-of-function mechanism. Hum Mol Genet 21:1-9.

Murphy J, Henry R, Lomen-Hoerth C (2007a) Establishing subtypes of the continuum of frontal lobe impairment in amyotrophic lateral sclerosis. Arch Neurol 64:330-334.

Murphy JM, Henry RG, Langmore S, Kramer JH, Miller BL, Lomen-Hoerth C (2007b) Continuum of frontal lobe impairment in amyotrophic lateral sclerosis. Arch Neurol 64:530-534.

Murray CL, Skelly DT, Cunningham C (2011a) Exacerbation of CNS inflammation and neurodegeneration by systemic LPS treatment is independent of circulating IL-1beta and IL-6. J Neuroinflammation 8:50.

Murray ME, DeJesus-Hernandez M, Rutherford NJ, Baker M, Duara R, Graff-Radford NR, Wszolek ZK, Ferman TJ, Josephs KA, Boylan KB, Rademakers R, Dickson DW (2011b) Clinical and neuropathologic heterogeneity of c9FTD/ALS associated with hexanucleotide repeat expansion in C9ORF72. Acta Neuropathol 122:673-690.

Myers MJ, Pullen JK, Ghildyal N, Eustis-Turf E, Schook LB (1989) Regulation of IL-1 and TNF-alpha expression during the differentiation of bone marrow derived macrophage. J Immunol 142:153-160.

Nagai M, Aoki M, Miyoshi I, Kato M, Pasinelli P, Kasai N, Brown RH, Jr., Itoyama Y (2001) Rats expressing human cytosolic copper-zinc superoxide dismutase transgenes with amyotrophic lateral sclerosis: associated mutations develop motor neuron disease. J Neurosci 21:9246-9254.

Nagai M, Re DB, Nagata T, Chalazonitis A, Jessell TM, Wichterle H, Przedborski S (2007) Astrocytes expressing ALS-linked mutated SOD1 release factors selectively toxic to motor neurons. Nat Neurosci 10:615-622.

Nagano I, Ilieva H, Shiote M, Murakami T, Yokoyama M, Shoji M, Abe K (2005) Therapeutic benefit of intrathecal injection of insulin-like growth factor-1 in a mouse model of Amyotrophic Lateral Sclerosis. J Neurol Sci 235:61-68.

Nagata Y, Fujita K, Yamauchi M, Kato T, Ando M, Honda M (1998) Neurochemical changes in the spinal cord in degenerative motor neuron diseases. Mol Chem Neuropathol 33:237-247.

Naor S, Keren Z, Bronshtein T, Goren E, Machluf M, Melamed D (2009) Development of ALS-like disease in SOD-1 mice deficient of B lymphocytes. J Neurol 256:1228-1235.

Nesic O, Xu GY, McAdoo D, High KW, Hulsebosch C, Perez-Pol R (2001) IL-1 receptor antagonist prevents apoptosis and caspase-3 activation after spinal cord injury. J Neurotrauma 18:947-956.

Neumann M, Sampathu DM, Kwong LK, Truax AC, Micsenyi MC, Chou TT, Bruce J, Schuck T, Grossman M, Clark CM, McCluskey LF, Miller BL, Masliah E, Mackenzie IR, Feldman H, Feiden W, Kretzschmar HA, Trojanowski JQ, Lee VM (2006) Ubiquitinated TDP-43 in frontotemporal lobar degeneration and amyotrophic lateral sclerosis. Science 314:130-133.

Neymotin A, Petri S, Calingasan NY, Wille E, Schafer P, Stewart C, Hensley K, Beal MF, Kiaei M (2009) Lenalidomide (Revlimid) administration at symptom onset is neuroprotective in a mouse model of amyotrophic lateral sclerosis. Exp Neurol 220:191-197.

Nguyen MD, D'Aigle T, Gowing G, Julien JP, Rivest S (2004) Exacerbation of motor neuron disease by chronic stimulation of innate immunity in a mouse model of amyotrophic lateral sclerosis. J Neurosci 24:1340-1349.

Nguyen MD, Julien JP, Rivest S (2001) Induction of proinflammatory molecules in mice with amyotrophic lateral sclerosis: no requirement for proapoptotic interleukin-1beta in neurodegeneration. Ann Neurol 50:630-639.

Nicaise C, Mitrecic D, Demetter P, De Decker R, Authelet M, Boom A, Pochet R (2009a) Impaired blood-brain and blood-spinal cord barriers in mutant SOD1-linked ALS rat. Brain Res 1301:152-162.

Nicaise C, Soyfoo MS, Authelet M, De Decker R, Bataveljic D, Delporte C, Pochet R (2009b) Aquaporin-4 overexpression in rat ALS model. Anat Rec (Hoboken) 292:207-213.

Nicaise C, Soyfoo MS, Delporte C, Pochet R (2010) Aquaporin-4 as a potential marker of BBB disruption in ALS models. Amyotroph Lateral Scler 11:253-254.

Niebroj-Dobosz I, Rafalowska J, Fidzianska A, Gadamski R, Grieb P (2007) Myelin composition of spinal cord in a model of amyotrophic lateral sclerosis (ALS) in SOD1G93A transgenic rats. Folia Neuropathol 45:236-241.

Niessen HG, Angenstein F, Sander K, Kunz WS, Teuchert M, Ludolph AC, Heinze HJ, Scheich H, Vielhaber S (2006) In vivo quantification of spinal and bulbar motor neuron degeneration in the G93A-SOD1 transgenic mouse model of ALS by T2 relaxation time and apparent diffusion coefficient. Exp Neurol 201:293-300.

Niessen HG, Debska-Vielhaber G, Sander K, Angenstein F, Ludolph AC, Hilfert L, Willker W, Leibfritz D, Heinze HJ, Kunz WS, Vielhaber S (2007) Metabolic

progression markers of neurodegeneration in the transgenic G93A-SOD1 mouse model of amyotrophic lateral sclerosis. Eur J Neurosci 25:1669-1677.

Nimchinsky EA, Young WG, Yeung G, Shah RA, Gordon JW, Bloom FE, Morrison JH, Hof PR (2000) Differential vulnerability of oculomotor, facial, and hypoglossal nuclei in G86R superoxide dismutase transgenic mice. J Comp Neurol 416:112-125.

Nobile-Orazio E (2001) Multifocal motor neuropathy. J Neuroimmunol 115:4-18.

O'Brien KM, Dirmeier R, Engle M, Poyton RO (2004) Mitochondrial protein oxidation in yeast mutants lacking manganese-(MnSOD) or copper- and zinc-containing superoxide dismutase (CuZnSOD): evidence that MnSOD and CuZnSOD have both unique and overlapping functions in protecting mitochondrial proteins from oxidative damage. J Biol Chem 279:51817-51827.

Ohmori Y, Hamilton TA (1993) Cooperative interaction between interferon (IFN) stimulus response element and kappa B sequence motifs controls IFN gamma- and lipopolysaccharide-stimulated transcription from the murine IP-10 promoter. J Biol Chem 268:6677-6688.

Oosthuyse B, Moons L, Storkebaum E, Beck H, Nuyens D, Brusselmans K, Van Dorpe J, Hellings P, Gorselink M, Heymans S, Theilmeier G, Dewerchin M, Laudenbach V, Vermylen P, Raat H, Acker T, Vleminckx V, Van Den Bosch L, Cashman N, Fujisawa H, Drost MR, Sciot R, Bruyninckx F, Hicklin DJ, Ince C, Gressens P, Lupu F, Plate KH, Robberecht W, Herbert JM, Collen D, Carmeliet P (2001) Deletion of the hypoxia-response element in the vascular endothelial growth factor promoter causes motor neuron degeneration. Nat Genet 28:131-138.

Osawa T, Mizuno Y, Fujita Y, Takatama M, Nakazato Y, Okamoto K (2011) Optineurin in neurodegenerative diseases. Neuropathology 31:569-574.

Palin K, Cunningham C, Forse P, Perry VH, Platt N (2008) Systemic inflammation switches the inflammatory cytokine profile in CNS Wallerian degeneration. Neurobiol Dis 30:19-29.

Pardridge WM (2003) Blood-brain barrier drug targeting: the future of brain drug development. Mol Interv 3:90-105, 151.

Pardridge WM, Mietus LJ (1979) Transport of steroid hormones through the rat blood-brain barrier. Primary role of albumin-bound hormone. J Clin Invest 64:145-154.

Pasco A, Ter Minassian A, Chapon C, Lemaire L, Franconi F, Darabi D, Caron C, Benoit JP, Le Jeune JJ (2006) Dynamics of cerebral edema and the apparent diffusion coefficient of water changes in patients with severe traumatic brain injury. A prospective MRI study. Eur Radiol 16:1501-1508.

Pasinelli P, Borchelt DR, Houseweart MK, Cleveland DW, Brown RH, Jr. (1998) Caspase-1 is activated in neural cells and tissue with amyotrophic lateral sclerosis-associated mutations in copper-zinc superoxide dismutase. Proc Natl Acad Sci U S A 95:15763-15768.

Pasinelli P, Brown RH (2006) Molecular biology of amyotrophic lateral sclerosis: insights from genetics. Nat Rev Neurosci 7:710-723.

Pearson JP, Williams NM, Majounie E, Waite A, Stott J, Newsway V, Murray A, Hernandez D, Guerreiro R, Singleton AB, Neal J, Morris HR (2011) Familial

frontotemporal dementia with amyotrophic lateral sclerosis and a shared haplotype on chromosome 9p. J Neurol 258:647-655.

Pehar M, Cassina P, Vargas MR, Castellanos R, Viera L, Beckman JS, Estevez AG, Barbeito L (2004) Astrocytic production of nerve growth factor in motor neuron apoptosis: implications for amyotrophic lateral sclerosis. J Neurochem 89:464-473.

Pekny M, Nilsson M (2005) Astrocyte activation and reactive gliosis. Glia 50:427-434.

Peretti-Viton P, Azulay JP, Trefouret S, Brunel H, Daniel C, Viton JM, Flori A, Salazard B, Pouget J, Serratrice G, Salamon G (1999) MRI of the intracranial corticospinal tracts in amyotrophic and primary lateral sclerosis. Neuroradiology 41:744-749.

Perry VH, Cunningham C, Holmes C (2007) Systemic infections and inflammation affect chronic neurodegeneration. Nat Rev Immunol 7:161-167.

Perry VH, Nicoll JA, Holmes C (2010) Microglia in neurodegenerative disease. Nat Rev Neurol 6:193-201.

Persson L, Hansson HA, Sourander P (1976) Extravasation, spread and cellular uptake of Evans blue-labelled albumin around a reproducible small stab-wound in the rat brain. Acta Neuropathol 34:125-136.

Pestka S, Langer JA, Zoon KC, Samuel CE (1987) Interferons and their actions. Annu Rev Biochem 56:727-777.

Pestronk A, Adams RN, Kuncl RW, Drachman DB, Clawson LL, Cornblath DR (1989) Differential effects of prednisone and cyclophosphamide on autoantibodies in human neuromuscular disorders. Neurology 39:628-633.

Petrik MS, Wilson JM, Grant SC, Blackband SJ, Tabata RC, Shan X, Krieger C, Shaw CA (2007) Magnetic resonance microscopy and immunohistochemistry of the CNS of the mutant SOD murine model of ALS reveals widespread neural deficits. Neuromolecular Med 9:216-229.

Pierpaoli C, Jezzard P, Basser PJ, Barnett A, Di Chiro G (1996) Diffusion tensor MR imaging of the human brain. Radiology 201:637-648.

Pioro EP, Wang Y, Moore JK, Ng TC, Trapp BD, Klinkosz B, Mitsumoto H (1998) Neuronal pathology in the wobbler mouse brain revealed by in vivo proton magnetic resonance spectroscopy and immunocytochemistry. Neuroreport 9:3041-3046.

Platanias LC (2005) Mechanisms of type-I- and type-II-interferon-mediated signalling. Nat Rev Immunol 5:375-386.

Polazzi E, Monti B (2010) Microglia and neuroprotection: from in vitro studies to therapeutic applications. Prog Neurobiol 92:293-315.

Poloni M, Facchetti D, Mai R, Micheli A, Agnoletti L, Francolini G, Mora G, Camana C, Mazzini L, Bachetti T (2000) Circulating levels of tumour necrosis factor-alpha and its soluble receptors are increased in the blood of patients with amyotrophic lateral sclerosis. Neurosci Lett 287:211-214.

Pramatarova A, Laganiere J, Roussel J, Brisebois K, Rouleau GA (2001) Neuron-specific expression of mutant superoxide dismutase 1 in transgenic mice does not lead to motor impairment. J Neurosci 21:3369-3374.

Pringle CE, Hudson AJ, Munoz DG, Kiernan JA, Brown WF, Ebers GC (1992) Primary lateral sclerosis. Clinical features, neuropathology and diagnostic criteria. Brain 115 (Pt 2):495-520.

Puls I, Jonnakuty C, LaMonte BH, Holzbaur EL, Tokito M, Mann E, Floeter MK, Bidus K, Drayna D, Oh SJ, Brown RH, Jr., Ludlow CL, Fischbeck KH (2003) Mutant dynactin in motor neuron disease. Nat Genet 33:455-456.

Rademakers R, Stewart H, Dejesus-Hernandez M, Krieger C, Graff-Radford N, Fabros M, Briemberg H, Cashman N, Eisen A, Mackenzie IR (2010) Fus gene mutations in familial and sporadic amyotrophic lateral sclerosis. Muscle Nerve 42:170-176.

Radi R, Beckman JS, Bush KM, Freeman BA (1991) Peroxynitrite-induced membrane lipid peroxidation: the cytotoxic potential of superoxide and nitric oxide. Arch Biochem Biophys 288:481-487.

Radunovic A, Delves HT, Robberecht W, Tilkin P, Enayat ZE, Shaw CE, Stevic Z, Apostolski S, Powell JF, Leigh PN (1997) Copper and zinc levels in familial amyotrophic lateral sclerosis patients with CuZnSOD gene mutations. Ann Neurol 42:130-131.

Ramesh T, Lyon AN, Pineda RH, Wang C, Janssen PM, Canan BD, Burghes AH, Beattie CE (2010) A genetic model of amyotrophic lateral sclerosis in zebrafish displays phenotypic hallmarks of motoneuron disease. Dis Model Mech 3:652-662.

Ray A, Prefontaine KE (1994) Physical association and functional antagonism between the p65 subunit of transcription factor NF-kappa B and the glucocorticoid receptor. Proc Natl Acad Sci U S A 91:752-756.

Reaume AG, Elliott JL, Hoffman EK, Kowall NW, Ferrante RJ, Siwek DF, Wilcox HM, Flood DG, Beal MF, Brown RH, Jr., Scott RW, Snider WD (1996) Motor neurons in Cu/Zn superoxide dismutase-deficient mice develop normally but exhibit enhanced cell death after axonal injury. Nat Genet 13:43-47.

Reinholz MM, Merkle CM, Poduslo JF (1999) Therapeutic benefits of putrescine-modified catalase in a transgenic mouse model of familial amyotrophic lateral sclerosis. Exp Neurol 159:204-216.

Renton AE, Majounie E, Waite A, Simon-Sanchez J, Rollinson S, Gibbs JR, Schymick JC, Laaksovirta H, van Swieten JC, Myllykangas L, Kalimo H, Paetau A, Abramzon Y, Remes AM, Kaganovich A, Scholz SW, Duckworth J, Ding J, Harmer DW, Hernandez DG, Johnson JO, Mok K, Ryten M, Trabzuni D, Guerreiro RJ, Orrell RW, Neal J, Murray A, Pearson J, Jansen IE, Sondervan D, Seelaar H, Blake D, Young K, Halliwell N, Callister JB, Toulson G, Richardson A, Gerhard A, Snowden J, Mann D, Neary D, Nalls MA, Peuralinna T, Jansson L, Isoviita VM, Kaivorinne AL, Holtta-Vuori M, Ikonen E, Sulkava R, Benatar M, Wuu J, Chio A, Restagno G, Borghero G, Sabatelli M, Heckerman D, Rogaeva E, Zinman L, Rothstein JD, Sendtner M, Drepper C, Eichler EE, Alkan C, Abdullaev Z, Pack SD, Dutra A, Pak E, Hardy J, Singleton A, Williams NM, Heutink P, Pickering-Brown S, Morris HR, Tienari PJ, Traynor BJ (2011) A hexanucleotide repeat expansion in C9ORF72 is the cause of chromosome 9p21-linked ALS-FTD. Neuron 72:257-268.

Rentzos M, Michalopoulou M, Nikolaou C, Cambouri C, Rombos A, Dimitrakopoulos A, Vassilopoulos D (2005) The role of soluble intercellular adhesion molecules in neurodegenerative disorders. J Neurol Sci 228:129-135.

Rezaie T, Child A, Hitchings R, Brice G, Miller L, Coca-Prados M, Heon E, Krupin T, Ritch R, Kreutzer D, Crick RP, Sarfarazi M (2002) Adult-onset primary open-angle glaucoma caused by mutations in optineurin. Science 295:1077-1079.

Riches DW, Chan ED, Winston BW (1996) TNF-alpha-induced regulation and signalling in macrophages. Immunobiology 195:477-490.

Ripps ME, Huntley GW, Hof PR, Morrison JH, Gordon JW (1995) Transgenic mice expressing an altered murine superoxide dismutase gene provide an animal model of amyotrophic lateral sclerosis. Proc Natl Acad Sci U S A 92:689-693.

Rival Y, Del Maschio A, Rabiet MJ, Dejana E, Duperray A (1996) Inhibition of platelet endothelial cell adhesion molecule-1 synthesis and leukocyte transmigration in endothelial cells by the combined action of TNF-alpha and IFN-gamma. J Immunol 157:1233-1241.

Roeber S, Mackenzie IR, Kretzschmar HA, Neumann M (2008) TDP-43-negative FTLD-U is a significant new clinico-pathological subtype of FTLD. Acta Neuropathol 116:147-157.

Rogers DC, Peters J, Martin JE, Ball S, Nicholson SJ, Witherden AS, Hafezparast M, Latcham J, Robinson TL, Quilter CA, Fisher EM (2001) SHIRPA, a protocol for behavioral assessment: validation for longitudinal study of neurological dysfunction in mice. Neurosci Lett 306:89-92.

Roozendaal B, Kim S, Wolf OT, Kim MS, Sung KK, Lee S (2012) The cortisol awakening response in amyotrophic lateral sclerosis is blunted and correlates with clinical status and depressive mood. Psychoneuroendocrinology 37:20-26.

Rosen DR (1993) Mutations in Cu/Zn superoxide dismutase gene are associated with familial amyotrophic lateral sclerosis. Nature 364:362.

Roth G, Rohr J, Magistris MR, Ochsner F (1986) Motor neuropathy with proximal multifocal persistent conduction block, fasciculations and myokymia. Evolution to tetraplegia. Eur Neurol 25:416-423.

Rothstein JD (2009) Current hypotheses for the underlying biology of amyotrophic lateral sclerosis. Ann Neurol 65 Suppl 1:S3-9.

Rothstein JD, Martin LJ, Kuncl RW (1992) Decreased glutamate transport by the brain and spinal cord in amyotrophic lateral sclerosis. N Engl J Med 326:1464-1468.

Rothstein JD, Patel S, Regan MR, Haenggeli C, Huang YH, Bergles DE, Jin L, Dykes Hoberg M, Vidensky S, Chung DS, Toan SV, Bruijn LI, Su ZZ, Gupta P, Fisher PB (2005) Beta-lactam antibiotics offer neuroprotection by increasing glutamate transporter expression. Nature 433:73-77.

Rothstein JD, Van Kammen M, Levey AI, Martin LJ, Kuncl RW (1995) Selective loss of glial glutamate transporter GLT-1 in amyotrophic lateral sclerosis. Ann Neurol 38:73-84.

Rowland LP, Shneider NA (2001) Amyotrophic lateral sclerosis. N Engl J Med 344:1688-1700.

Rule RR, Schuff N, Miller RG, Weiner MW (2010) Gray matter perfusion correlates with disease severity in ALS. Neurology 74:821-827.

Ryu H, Smith K, Camelo SI, Carreras I, Lee J, Iglesias AH, Dangond F, Cormier KA, Cudkowicz ME, Brown RH, Jr., Ferrante RJ (2005) Sodium phenylbutyrate prolongs survival and regulates expression of anti-apoptotic genes in transgenic amyotrophic lateral sclerosis mice. J Neurochem 93:1087-1098.

Sakai A, Kume N, Nishi E, Tanoue K, Miyasaka M, Kita T (1997) P-selectin and vascular cell adhesion molecule-1 are focally expressed in aortas of hypercholesterolemic rabbits before intimal accumulation of macrophages and T lymphocytes. Arterioscler Thromb Vasc Biol 17:310-316.

Salmi M, Jalkanen S (2001) VAP-1: an adhesin and an enzyme. Trends Immunol 22:211-216.

Salmi M, Rajala P, Jalkanen S (1997) Homing of mucosal leukocytes to joints. Distinct endothelial ligands in synovium mediate leukocyte-subtype specific adhesion. J Clin Invest 99:2165-2172.

Sargsyan SA, Blackburn DJ, Barber SC, Monk PN, Shaw PJ (2009) Mutant SOD1 G93A microglia have an inflammatory phenotype and elevated production of MCP-1. Neuroreport 20:1450-1455.

Saria A, Lundberg JM (1983) Evans blue fluorescence: quantitative and morphological evaluation of vascular permeability in animal tissues. J Neurosci Methods 8:41-49.

Sasaki S, Ohsawa Y, Yamane K, Sakuma H, Shibata N, Nakano R, Kikugawa K, Mizutani T, Tsuji S, Iwata M (1998) Familial amyotrophic lateral sclerosis with widespread vacuolation and hyaline inclusions. Neurology 51:871-873.

Sathasivam S, Ince PG, Shaw PJ (2001) Apoptosis in amyotrophic lateral sclerosis: a review of the evidence. Neuropathol Appl Neurobiol 27:257-274.

Sathasivam S, Shaw PJ (2005) Apoptosis in amyotrophic lateral sclerosis--what is the evidence? Lancet Neurol 4:500-509.

Schmitt-John T, Drepper C, Mussmann A, Hahn P, Kuhlmann M, Thiel C, Hafner M, Lengeling A, Heimann P, Jones JM, Meisler MH, Jockusch H (2005) Mutation of Vps54 causes motor neuron disease and defective spermiogenesis in the wobbler mouse. Nat Genet 37:1213-1215.

Schutz B, Reimann J, Dumitrescu-Ozimek L, Kappes-Horn K, Landreth GE, Schurmann B, Zimmer A, Heneka MT (2005) The oral antidiabetic pioglitazone protects from neurodegeneration and amyotrophic lateral sclerosis-like symptoms in superoxide dismutase-G93A transgenic mice. J Neurosci 25:7805-7812.

Schwartz AL (1990) Cell biology of intracellular protein trafficking. Annu Rev Immunol 8:195-229.

Serres S, Anthony DC, Jiang Y, Broom KA, Campbell SJ, Tyler DJ, van Kasteren SI, Davis BG, Sibson NR (2009a) Systemic inflammatory response reactivates immune-mediated lesions in rat brain. J Neurosci 29:4820-4828.

Serres S, Anthony DC, Jiang Y, Campbell SJ, Broom KA, Khrapitchev A, Sibson NR (2009b) Comparison of MRI signatures in pattern I and II multiple sclerosis models. NMR Biomed 22:1014-1024.

Serres S, Mardiguian S, Campbell SJ, McAteer MA, Akhtar A, Krapitchev A, Choudhury RP, Anthony DC, Sibson NR (2011) VCAM-1-targeted magnetic resonance imaging reveals subclinical disease in a mouse model of multiple sclerosis. FASEB J 25:4415-4422.

Serres S, Soto MS, Hamilton A, McAteer MA, Carbonell WS, Robson MD, Ansorge O, Khrapitchev A, Bristow C, Balathasan L, Weissensteiner T, Anthony DC, Choudhury RP, Muschel RJ, Sibson NR (2012) Molecular MRI enables early and sensitive detection of brain metastases. Proc Natl Acad Sci U S A 109:6674-6679.

Shan X, Chiang PM, Price DL, Wong PC (2010) Altered distributions of Gemini of coiled bodies and mitochondria in motor neurons of TDP-43 transgenic mice. Proc Natl Acad Sci U S A 107:16325-16330.

Shan X, Vocadlo D, Krieger C (2009) Mislocalization of TDP-43 in the G93A mutant SOD1 transgenic mouse model of ALS. Neurosci Lett 458:70-74.

Shaw CA, Pasqualotto BA, Curry K (1996) Glutathione-induced sodium currents in neocortex. Neuroreport 7:1149-1152.

Shaw PJ (1999) Motor neurone disease. BMJ 318:1118-1121.

Shefner JM, Reaume AG, Flood DG, Scott RW, Kowall NW, Ferrante RJ, Siwek DF, Upton-Rice M, Brown RH, Jr. (1999) Mice lacking cytosolic copper/zinc superoxide dismutase display a distinctive motor axonopathy. Neurology 53:1239-1246.

Shimizu Y, Newman W, Gopal TV, Horgan KJ, Graber N, Beall LD, van Seventer GA, Shaw S (1991) Four molecular pathways of T cell adhesion to endothelial cells: roles of LFA-1, VCAM-1, and ELAM-1 and changes in pathway hierarchy under different activation conditions. J Cell Biol 113:1203-1212.

Shin JH, Cho SI, Lim HR, Lee JK, Lee YA, Noh JS, Joo IS, Kim KW, Gwag BJ (2007) Concurrent administration of Neu2000 and lithium produces marked improvement of motor neuron survival, motor function, and mortality in a mouse model of amyotrophic lateral sclerosis. Mol Pharmacol 71:965-975.

Sibson NR, Blamire AM, Perry VH, Gauldie J, Styles P, Anthony DC (2002) TNF-alpha reduces cerebral blood volume and disrupts tissue homeostasis via an endothelin- and TNFR2-dependent pathway. Brain 125:2446-2459.

Silva MC, Fox S, Beam M, Thakkar H, Amaral MD, Morimoto RI (2011) A genetic screening strategy identifies novel regulators of the proteostasis network. PLoS Genet 7:e1002438.

Simard AR, Rivest S (2007) Neuroprotective effects of resident microglia following acute brain injury. J Comp Neurol 504:716-729.

Simpson IA, Carruthers A, Vannucci SJ (2007) Supply and demand in cerebral energy metabolism: the role of nutrient transporters. J Cereb Blood Flow Metab 27:1766-1791.

Smith JK, Castillo M, Kwock L (2003) MR spectroscopy of brain tumors. Magn Reson Imaging Clin N Am 11:415-429, v-vi.

Smith MA, Harris PLR, Sayre LM, Perry G (1997) Iron accumulation in Alzheimer disease is a source of redox-generated free radicals. Proceedings of the National Academy of Sciences 94:9866-9868.

Smith MC (1960) Nerve fibre degeneration in the brain in amyotrophic lateral sclerosis. JNeurolNeurosurgPsychiatry 23:269-282.

Snowden JS, Rollinson S, Thompson JC, Harris JM, Stopford CL, Richardson AM, Jones M, Gerhard A, Davidson YS, Robinson A, Gibbons L, Hu Q, DuPlessis D, Neary D, Mann DM, Pickering-Brown SM (2012) Distinct clinical and pathological characteristics of frontotemporal dementia associated with C9ORF72 mutations. Brain 135:693-708.

Song JH, Huang CS, Nagata K, Yeh JZ, Narahashi T (1997) Differential action of riluzole on tetrodotoxin-sensitive and tetrodotoxin-resistant sodium channels. J Pharmacol Exp Ther 282:707-714.

Song SK, Sun SW, Ju WK, Lin SJ, Cross AH, Neufeld AH (2003) Diffusion tensor imaging detects and differentiates axon and myelin degeneration in mouse optic nerve after retinal ischemia. Neuroimage 20:1714-1722.

Song SK, Sun SW, Ramsbottom MJ, Chang C, Russell J, Cross AH (2002) Dysmyelination revealed through MRI as increased radial (but unchanged axial) diffusion of water. Neuroimage 17:1429-1436.

Song SK, Yoshino J, Le TQ, Lin SJ, Sun SW, Cross AH, Armstrong RC (2005) Demyelination increases radial diffusivity in corpus callosum of mouse brain. Neuroimage 26:132-140.

Sperfeld AD, Karitzky J, Brummer D, Schreiber H, Haussler J, Ludolph AC, Hanemann CO (2002) X-linked bulbospinal neuronopathy: Kennedy disease. Arch Neurol 59:1921-1926.

Spreux-Varoquaux O, Bensimon G, Lacomblez L, Salachas F, Pradat PF, Le Forestier N, Marouan A, Dib M, Meininger V (2002) Glutamate levels in cerebrospinal fluid in amyotrophic lateral sclerosis: a reappraisal using a new HPLC method with coulometric detection in a large cohort of patients. J Neurol Sci 193:73-78.

Springer TA (1990) Adhesion receptors of the immune system. Nature 346:425-434.

Stallings NR, Puttaparthi K, Luther CM, Burns DK, Elliott JL (2010) Progressive motor weakness in transgenic mice expressing human TDP-43. Neurobiol Dis 40:404-414.

Steinwall O, Klatzo I (1966) Selective vulnerability of the blood-brain barrier in chemically induced lesions. J Neuropathol Exp Neurol 25:542-559.

Stommel EW, Cohen JA, Fadul CE, Cogbill CH, Graber DJ, Kingman L, Mackenzie T, Channon Smith JY, Harris BT (2009) Efficacy of thalidomide for the treatment of amyotrophic lateral sclerosis: a phase II open label clinical trial. Amyotroph Lateral Scler 10:393-404.

Streit WJ (2002) Microglia as neuroprotective, immunocompetent cells of the CNS. Glia 40:133-139.

Sugai F, Yamamoto Y, Miyaguchi K, Zhou Z, Sumi H, Hamasaki T, Goto M, Sakoda S (2004) Benefit of valproic acid in suppressing disease progression of ALS model mice. Eur J Neurosci 20:3179-3183.

Sugihara K, Maruyama H, Kamada M, Morino H, Kawakami H (2011) Screening for OPTN mutations in amyotrophic lateral sclerosis in a mainly Caucasian population. Neurobiol Aging 32:1923 e1929-1910.

Sui Y, Potula R, Dhillon N, Pinson D, Li S, Nath A, Anderson C, Turchan J, Kolson D, Narayan O, Buch S (2004) Neuronal apoptosis is mediated by CXCL10 overexpression in simian human immunodeficiency virus encephalitis. Am J Pathol 164:1557-1566.

Sui Y, Stehno-Bittel L, Li S, Loganathan R, Dhillon NK, Pinson D, Nath A, Kolson D, Narayan O, Buch S (2006) CXCL10-induced cell death in neurons: role of calcium dysregulation. Eur J Neurosci 23:957-964.

Sun SW, Song SK, Harms MP, Lin SJ, Holtzman DM, Merchant KM, Kotyk JJ (2005) Detection of age-dependent brain injury in a mouse model of brain amyloidosis associated with Alzheimer's disease using magnetic resonance diffusion tensor imaging. Exp Neurol 191:77-85.

Sunyach C, Michaud M, Arnoux T, Bernard-Marissal N, Aebischer J, Latyszenok V, Gouarne C, Raoul C, Pruss RM, Bordet T, Pettmann B (2012) Olesoxime delays muscle denervation, astrogliosis, microglial activation and motoneuron death in an ALS mouse model. Neuropharmacology 62:2346-2352.

Suzuki N, Aoki M, Warita H, Kato M, Mizuno H, Shimakura N, Akiyama T, Furuya H, Hokonohara T, Iwaki A, Togashi S, Konno H, Itoyama Y (2010) FALS with FUS mutation in Japan, with early onset, rapid progress and basophilic inclusion. J Hum Genet 55:252-254.

Swingle WW, Davanzo JP, Glenister D, Crossfield HC, Wagle G (1959) Role of gluco- and mineralocorticoids in salt and water metabolism of adrenalectomized dogs. Am J Physiol 196:283-286.

Szebeni J (1998) The interaction of liposomes with the complement system. Crit Rev Ther Drug Carrier Syst 15:57-88.

Tada S, Okuno T, Yasui T, Nakatsuji Y, Sugimoto T, Kikutani H, Sakoda S (2011) Deleterious effects of lymphocytes at the early stage of neurodegeneration in an animal model of amyotrophic lateral sclerosis. J Neuroinflammation 8:19.

Takenaka T, Kawakami T, Hikawa N, Gotoh H (1990) Axoplasmic transport of mitochondria in cultured dorsal root ganglion cells. Brain Res 528:285-290.

Talbot K (2002) Motor neurone disease. Postgrad Med J 78:513-519.

Tanaka M, Mokhtari GK, Terry RD, Balsam LB, Lee KH, Kofidis T, Tsao PS, Robbins RC (2004) Overexpression of human copper/zinc superoxide dismutase (SOD1) suppresses ischemia-reperfusion injury and subsequent development of graft coronary artery disease in murine cardiac grafts. Circulation 110:II200-206.

Taoufiq Z, Pino P, Dugas N, Conti M, Tefit M, Mazier D, Vouldoukis I (2006) Transient supplementation of superoxide dismutase protects endothelial cells against Plasmodium falciparum-induced oxidative stress. Mol Biochem Parasitol 150:166-173.

Tateishi T, Hokonohara T, Yamasaki R, Miura S, Kikuchi H, Iwaki A, Tashiro H, Furuya H, Nagara Y, Ohyagi Y, Nukina N, Iwaki T, Fukumaki Y, Kira J (2010a) Multiple system degeneration with basophilic inclusions in Japanese ALS patients with FUS mutation. Acta Neuropathol 119:355-364.

Tateishi T, Yamasaki R, Tanaka M, Matsushita T, Kikuchi H, Isobe N, Ohyagi Y, Kira J (2010b) CSF chemokine alterations related to the clinical course of amyotrophic lateral sclerosis. J Neuroimmunol 222:76-81.

Teuchert M, Fischer D, Schwalenstoecker B, Habisch HJ, Bockers TM, Ludolph AC (2006) A dynein mutation attenuates motor neuron degeneration in SOD1(G93A) mice. Exp Neurol 198:271-274.

Thornberry NA, Bull HG, Calaycay JR, Chapman KT, Howard AD, Kostura MJ, Miller DK, Molineaux SM, Weidner JR, Aunins J, et al. (1992) A novel heterodimeric cysteine protease is required for interleukin-1 beta processing in monocytes. Nature 356:768-774.

Thornhill MH, Haskard DO (1990) IL-4 regulates endothelial cell activation by IL-1, tumor necrosis factor, or IFN-gamma. J Immunol 145:865-872.

Thurston JH, Sherman WR, Hauhart RE, Kloepper RF (1989) myo-inositol: a newly identified nonnitrogenous osmoregulatory molecule in mammalian brain. Pediatr Res 26:482-485.

Tiemessen MM, Jagger AL, Evans HG, van Herwijnen MJ, John S, Taams LS (2007) CD4+CD25+Foxp3+ regulatory T cells induce alternative activation of human monocytes/macrophages. Proc Natl Acad Sci U S A 104:19446-19451.

Titos E, Rius B, Gonzalez-Periz A, Lopez-Vicario C, Moran-Salvador E, Martinez-Clemente M, Arroyo V, Claria J (2011) Resolvin D1 and its precursor docosahexaenoic acid promote resolution of adipose tissue inflammation by eliciting macrophage polarization toward an M2-like phenotype. J Immunol 187:5408-5418.

Trieu VN, Liu R, Liu XP, Uckun FM (2000) A specific inhibitor of janus kinase-3 increases survival in a transgenic mouse model of amyotrophic lateral sclerosis. Biochem Biophys Res Commun 267:22-25.

Tsai KJ, Yang CH, Fang YH, Cho KH, Chien WL, Wang WT, Wu TW, Lin CP, Fu WM, Shen CK (2010) Elevated expression of TDP-43 in the forebrain of mice is sufficient to cause neurological and pathological phenotypes mimicking FTLD-U. J Exp Med 207:1661-1673.

Tudor EL, Galtrey CM, Perkinton MS, Lau KF, De Vos KJ, Mitchell JC, Ackerley S, Hortobagyi T, Vamos E, Leigh PN, Klasen C, McLoughlin DM, Shaw CE, Miller CC (2010) Amyotrophic lateral sclerosis mutant vesicle-associated membrane protein-associated protein-B transgenic mice develop TAR-DNA-binding protein-43 pathology. Neuroscience 167:774-785.

Turner BJ, Murray SS, Piccenna LG, Lopes EC, Kilpatrick TJ, Cheema SS (2004a) Effect of p75 neurotrophin receptor antagonist on disease progression in transgenic amyotrophic lateral sclerosis mice. J Neurosci Res 78:193-199.

Turner BJ, Talbot K (2008) Transgenics, toxicity and therapeutics in rodent models of mutant SOD1-mediated familial ALS. Prog Neurobiol 85:94-134.

Turner MR (2011) MRI as a frontrunner in the search for amyotrophic lateral sclerosis biomarkers? Biomark Med 5:79-81.

Turner MR, Bakker M, Sham P, Shaw CE, Leigh PN, AL-Chalabi A (2002) Prognostic modeling of therapeutic interventions in amyotrophic

lateral sclerosis. Amyotrophic Lateral Sclerosis and Other Motor Neuron Disorders 3:15-21.

Turner MR, Cagnin A, Turkheimer FE, Miller CC, Shaw CE, Brooks DJ, Leigh PN, Banati RB (2004b) Evidence of widespread cerebral microglial activation in amyotrophic lateral sclerosis: an [11C](R)-PK11195 positron emission tomography study. Neurobiol Dis 15:601-609.

Turner MR, Grosskreutz J, Kassubek J, Abrahams S, Agosta F, Benatar M, Filippi M, Goldstein LH, van den Heuvel M, Kalra S, Lulé D, Mohammadi B (2011 epub) Towards a neuroimaging biomarker for amyotrophic lateral sclerosis. The Lancet Neurology 10:400-403.

Turner MR, Kiernan MC, Leigh PN, Talbot K (2009) Biomarkers in amyotrophic lateral sclerosis. Lancet Neurol 8:94-109.

Turner MR, Parton MJ, Shaw CE, Leigh PN, Al-Chalabi A (2003) Prolonged survival in motor neuron disease: a descriptive study of the King's database 1990-2002. J Neurol Neurosurg Psychiatry 74:995-997.

Uitto VJ, Schwartz D, Veis A (1980) Degradation of basement-membrane collagen by neutral proteases from human leukocytes. Eur J Biochem 105:409-417.

Underwood CK, Kurniawan ND, Butler TJ, Cowin GJ, Wallace RH (2011) Non-invasive diffusion tensor imaging detects white matter degeneration in the spinal cord of a mouse model of amyotrophic lateral sclerosis. Neuroimage 55:455-461.

Upton-Rice MN, Cudkowicz ME, Warren L, Mathew RK, Ren JM, Finklestein SP, Brown RH, Jr. (1999) Basic fibroblast growth factor does not prolong survival in a transgenic model of familial amyotrophic lateral sclerosis. Ann Neurol 46:934.

Van Damme P, Leyssen M, Callewaert G, Robberecht W, Van Den Bosch L (2003) The AMPA receptor antagonist NBQX prolongs survival in a transgenic mouse model of amyotrophic lateral sclerosis. Neurosci Lett 343:81-84.

Van Den Bosch L, Robberecht W (2008) Crosstalk between astrocytes and motor neurons: what is the message? Exp Neurol 211:1-6.

Van Den Bosch L, Storkebaum E, Vleminckx V, Moons L, Vanopdenbosch L, Scheveneels W, Carmeliet P, Robberecht W (2004) Effects of vascular endothelial growth factor (VEGF) on motor neuron degeneration. Neurobiol Dis 17:21-28.

Van Den Bosch L, Van Damme P, Bogaert E, Robberecht W (2006) The role of excitotoxicity in the pathogenesis of amyotrophic lateral sclerosis. Biochim Biophys Acta 1762:1068-1082.

Vance C, Al-Chalabi A, Ruddy D, Smith BN, Hu X, Sreedharan J, Siddique T, Schelhaas HJ, Kusters B, Troost D, Baas F, de Jong V, Shaw CE (2006) Familial amyotrophic lateral sclerosis with frontotemporal dementia is linked to a locus on chromosome 9p13.2-21.3. Brain 129:868-876.

Vance C, Rogelj B, Hortobagyi T, De Vos KJ, Nishimura AL, Sreedharan J, Hu X, Smith B, Ruddy D, Wright P, Ganesalingam J, Williams KL, Tripathi V, Al-Saraj S, Al-Chalabi A, Leigh PN, Blair IP, Nicholson G, de Belleroche J, Gallo JM, Miller CC, Shaw CE (2009) Mutations in FUS, an RNA processing protein, cause familial amyotrophic lateral sclerosis type 6. Science 323:1208-1211.

Verbeek MM, Westphal JR, Ruiter DJ, de Waal RM (1995) T lymphocyte adhesion to human brain pericytes is mediated via very late antigen-4/vascular cell adhesion molecule-1 interactions. J Immunol 154:5876-5884.

Verstraete E, Biessels GJ, van Den Heuvel MP, Visser F, Luijten PR, van Den Berg LH (2010) No evidence of microbleeds in ALS patients at 7 Tesla MRI. Amyotroph Lateral Scler 11:555-557.

Vijayvergiya C, Beal MF, Buck J, Manfredi G (2005) Mutant superoxide dismutase 1 forms aggregates in the brain mitochondrial matrix of amyotrophic lateral sclerosis mice. J Neurosci 25:2463-2470.

Viner RI, Huhmer AF, Bigelow DJ, Schoneich C (1996) The oxidative inactivation of sarcoplasmic reticulum Ca(2+)-ATPase by peroxynitrite. Free Radic Res 24:243-259.

Vivekananda U, Manjalay ZR, Ganesalingam J, Simms J, Shaw CE, Leigh PN, Turner MR, Al-Chalabi A (2011) Low index-to-ring finger length ratio in sporadic ALS supports prenatally defined motor neuronal vulnerability. J Neurol Neurosurg Psychiatry 82:635-637.

von Kienlin M, Kunnecke B, Metzger F, Steiner G, Richards JG, Ozmen L, Jacobsen H, Loetscher H (2005) Altered metabolic profile in the frontal cortex of PS2APP transgenic mice, monitored throughout their life span. Neurobiol Dis 18:32-39.

von Tell D, Armulik A, Betsholtz C (2006) Pericytes and vascular stability. Exp Cell Res 312:623-629.

Waibel S, Reuter A, Malessa S, Blaugrund E, Ludolph AC (2004) Rasagiline alone and in combination with riluzole prolongs survival in an ALS mouse model. J Neurol 251:1080-1084.

Wallays G, Ceuppens JL (1993) Human T lymphocyte activation by pokeweed mitogen induces production of TNF-alpha and GM-CSF and helper signaling by IL-1 and IL-6 results in IL-2-dependent T cell growth. Eur Cytokine Netw 4:269-277.

Wang CC, Lin WN, Lee CW, Lin CC, Luo SF, Wang JS, Yang CM (2005a) Involvement of p42/p44 MAPK, p38 MAPK, JNK, and NF-kappaB in IL-1beta-induced VCAM-1 expression in human tracheal smooth muscle cells. Am J Physiol Lung Cell Mol Physiol 288:L227-237.

Wang HY, Wang IF, Bose J, Shen CK (2004) Structural diversity and functional implications of the eukaryotic TDP gene family. Genomics 83:130-139.

Wang J, Farr GW, Hall DH, Li F, Furtak K, Dreier L, Horwich AL (2009) An ALS-linked mutant SOD1 produces a locomotor defect associated with aggregation and synaptic dysfunction when expressed in neurons of Caenorhabditis elegans. PLoS Genet 5:e1000350.

Wang J, Xu G, Li H, Gonzales V, Fromholt D, Karch C, Copeland NG, Jenkins NA, Borchelt DR (2005b) Somatodendritic accumulation of misfolded SOD1-L126Z in

motor neurons mediates degeneration: alphaB-crystallin modulates aggregation. Hum Mol Genet 14:2335-2347.

Waragai M (1997) MRI and clinical features in amyotrophic lateral sclerosis. Neuroradiology 39:847-851.

Watson MR, Lagow RD, Xu K, Zhang B, Bonini NM (2008) A drosophila model for amyotrophic lateral sclerosis reveals motor neuron damage by human SOD1. J Biol Chem 283:24972-24981.

Wegorzewska I, Bell S, Cairns NJ, Miller TM, Baloh RH (2009) TDP-43 mutant transgenic mice develop features of ALS and frontotemporal lobar degeneration. Proc Natl Acad Sci U S A 106:18809-18814.

Weihl CC, Pestronk A, Kimonis VE (2009) Valosin-containing protein disease: inclusion body myopathy with Paget's disease of the bone and fronto-temporal dementia. Neuromuscul Disord 19:308-315.

Weinstein DA, Roy CN, Fleming MD, Loda MF, Wolfsdorf JI, Andrews NC (2002) Inappropriate expression of hepcidin is associated with iron refractory anemia: implications for the anemia of chronic disease. Blood 100:3776-3781.

Werdelin L, Boysen G, Jensen TS, Mogensen P (1990) Immunosuppressive treatment of patients with amyotrophic lateral sclerosis. Acta Neurol Scand 82:132-134.

West M, Mhatre M, Ceballos A, Floyd RA, Grammas P, Gabbita SP, Hamdheydari L, Mai T, Mou S, Pye QN, Stewart C, West S, Williamson KS, Zemlan F, Hensley K (2004) The arachidonic acid 5-lipoxygenase inhibitor nordihydroguaiaretic acid inhibits tumor necrosis factor alpha activation of microglia and extends survival of G93A-SOD1 transgenic mice. J Neurochem 91:133-143.

Weydt P, Hong SY, Kliot M, Moller T (2003) Assessing disease onset and progression in the SOD1 mouse model of ALS. Neuroreport 14:1051-1054.

Wiedau-Pazos M, Goto JJ, Rabizadeh S, Gralla EB, Roe JA, Lee MK, Valentine JS, Bredesen DE (1996) Altered reactivity of superoxide dismutase in familial amyotrophic lateral sclerosis. Science 271:515-518.

Williams R, Dhillon NK, Hegde ST, Yao H, Peng F, Callen S, Chebloune Y, Davis RL, Buch SJ (2009) Proinflammatory cytokines and HIV-1 synergistically enhance CXCL10 expression in human astrocytes. Glia 57:734-743.

Wils H, Kleinberger G, Janssens J, Pereson S, Joris G, Cuijt I, Smits V, Ceuterick-de Groote C, Van Broeckhoven C, Kumar-Singh S (2010) TDP-43 transgenic mice develop spastic paralysis and neuronal inclusions characteristic of ALS and frontotemporal lobar degeneration. Proc Natl Acad Sci U S A 107:3858-3863.

Wilson JM, Petrik MS, Grant SC, Blackband SJ, Lai J, Shaw CA (2004) Quantitative measurement of neurodegeneration in an ALS-PDC model using MR microscopy. Neuroimage 23:336-343.

Wong D, Prameya R, Dorovini-Zis K (1999) In vitro adhesion and migration of T lymphocytes across monolayers of human brain microvessel endothelial cells: regulation by ICAM-1, VCAM-1, E-selectin and PECAM-1. J Neuropathol Exp Neurol 58:138-152.

Wong PC, Pardo CA, Borchelt DR, Lee MK, Copeland NG, Jenkins NA, Sisodia SS, Cleveland DW, Price DL (1995) An adverse property of a familial ALS-linked SOD1 mutation causes motor neuron disease characterized by vacuolar degeneration of mitochondria. Neuron 14:1105-1116.

Wyble CW, Desai TR, Clark ET, Hynes KL, Gewertz BL (1996) Physiologic concentrations of TNFalpha and IL-1beta released from reperfused human intestine upregulate E-selectin and ICAM-1. J Surg Res 63:333-338.

Xia HZ, Kannapell CC, Fu SM, Sung SS (1993) Differential regulation of human B-lymphocyte tumor necrosis factor-alpha (TNF-alpha) and lymphotoxin (TNF-beta) production by protein phosphatase 1 and 2A inhibitor. Blood 82:2806-2812.

Xing Z, Jordana M, Kirpalani H, Driscoll KE, Schall TJ, Gauldie J (1994) Cytokine expression by neutrophils and macrophages in vivo: endotoxin induces tumor necrosis factor-alpha, macrophage inflammatory protein-2, interleukin-1 beta, and interleukin-6 but not RANTES or transforming growth factor-beta 1 mRNA expression in acute lung inflammation. Am J Respir Cell Mol Biol 10:148-153.

Xu YF, Gendron TF, Zhang YJ, Lin WL, D'Alton S, Sheng H, Casey MC, Tong J, Knight J, Yu X, Rademakers R, Boylan K, Hutton M, McGowan E, Dickson DW, Lewis J, Petrucelli L (2010) Wild-type human TDP-43 expression causes TDP-43 phosphorylation, mitochondrial aggregation, motor deficits, and early mortality in transgenic mice. J Neurosci 30:10851-10859.

Yamanaka K, Chun SJ, Boillee S, Fujimori-Tonou N, Yamashita H, Gutmann DH, Takahashi R, Misawa H, Cleveland DW (2008) Astrocytes as determinants of disease progression in inherited amyotrophic lateral sclerosis. Nat Neurosci 11:251-253.

Yamanaka K, Cleveland DW (2005) Determinants of rapid disease progression in ALS. Neurology 65:1859-1860.

Yang Y, Hentati A, Deng HX, Dabbagh O, Sasaki T, Hirano M, Hung WY, Ouahchi K, Yan J, Azim AC, Cole N, Gascon G, Yagmour A, Ben-Hamida M, Pericak-Vance M, Hentati F, Siddique T (2001) The gene encoding alsin, a protein with three guanine-nucleotide exchange factor domains, is mutated in a form of recessive amyotrophic lateral sclerosis. Nat Genet 29:160-165.

Yednock TA, Cannon C, Fritz LC, Sanchez-Madrid F, Steinman L, Karin N (1992) Prevention of experimental autoimmune encephalomyelitis by antibodies against alpha 4 beta 1 integrin. Nature 356:63-66.

Yeruva S, Ramadori G, Raddatz D (2008) NF-kappaB-dependent synergistic regulation of CXCL10 gene expression by IL-1beta and IFN-gamma in human intestinal epithelial cell lines. Int J Colorectal Dis 23:305-317.

Yoong KF, McNab G, Hubscher SG, Adams DH (1998) Vascular adhesion protein-1 and ICAM-1 support the adhesion of tumor-infiltrating lymphocytes to tumor endothelium in human hepatocellular carcinoma. J Immunol 160:3978-3988.

Yoshihara T, Ishigaki S, Yamamoto M, Liang Y, Niwa J, Takeuchi H, Doyu M, Sobue G (2002) Differential expression of inflammation- and apoptosis-related genes in spinal cords of a mutant SOD1 transgenic mouse model of familial amyotrophic lateral sclerosis. J Neurochem 80:158-167.

Yoshimoto T, Takeda K, Tanaka T, Ohkusu K, Kashiwamura S, Okamura H, Akira S, Nakanishi K (1998) IL-12 up-regulates IL-18 receptor expression on T cells, Th1 cells, and B cells: synergism with IL-18 for IFN-gamma production. J Immunol 161:3400-3407.

Zang DW, Cheema SS (2002) Degeneration of corticospinal and bulbospinal systems in the superoxide dismutase 1(G93A G1H) transgenic mouse model of familial amyotrophic lateral sclerosis. Neurosci Lett 332:99-102.

Zang DW, Yang Q, Wang HX, Egan G, Lopes EC, Cheema SS (2004) Magnetic resonance imaging reveals neuronal degeneration in the brainstem of the superoxide dismutase 1 transgenic mouse model of amyotrophic lateral sclerosis. Eur J Neurosci 20:1745-1751.

Zhang D, Iyer LM, He F, Aravind L (2012) Discovery of Novel DENN Proteins: Implications for the Evolution of Eukaryotic Intracellular Membrane Structures and Human Disease. Front Genet 3:283.

Zhang R, Gascon R, Miller RG, Gelinas DF, Mass J, Hadlock K, Jin X, Reis J, Narvaez A, McGrath MS (2005) Evidence for systemic immune system alterations in sporadic amyotrophic lateral sclerosis (sALS). J Neuroimmunol 159:215-224.

Zhang YJ, Xu YF, Cook C, Gendron TF, Roettges P, Link CD, Lin WL, Tong J, Castanedes-Casey M, Ash P, Gass J, Rangachari V, Buratti E, Baralle F, Golde TE, Dickson DW, Petrucelli L (2009) Aberrant cleavage of TDP-43 enhances aggregation and cellular toxicity. Proc Natl Acad Sci U S A 106:7607-7612.

Zhao W, Beers DR, Henkel JS, Zhang W, Urushitani M, Julien JP, Appel SH (2010) Extracellular mutant SOD1 induces microglial-mediated motoneuron injury. Glia 58:231-243.

Zhao W, Xie W, Xiao Q, Beers DR, Appel SH (2006) Protective effects of an anti-inflammatory cytokine, interleukin-4, on motoneuron toxicity induced by activated microglia. J Neurochem 99:1176-1187.

Zheng C, Skold MK, Li J, Nennesmo I, Fadeel B, Henter JI (2007) VEGF reduces astrogliosis and preserves neuromuscular junctions in ALS transgenic mice. Biochem Biophys Res Commun 363:989-993.

Zhong Z, Deane R, Ali Z, Parisi M, Shapovalov Y, O'Banion MK, Stojanovic K, Sagare A, Boillee S, Cleveland DW, Zlokovic BV (2008) ALS-causing SOD1 mutants generate vascular changes prior to motor neuron degeneration. Nat Neurosci 11:420-422.

Zhou Z, Liu Y, Miao AD, Wang SQ (2005) Protocatechuic aldehyde suppresses TNF-alpha-induced ICAM-1 and VCAM-1 expression in human umbilical vein endothelial cells. Eur J Pharmacol 513:1-8.

Zinszner H, Sok J, Immanuel D, Yin Y, Ron D (1997) TLS (FUS) binds RNA in vivo and engages in nucleo-cytoplasmic shuttling. J Cell Sci 110 (Pt 15):1741-1750.

Zlokovic BV (2008) The blood-brain barrier in health and chronic neurodegenerative disorders. Neuron 57:178-201.

Appendix

Principles of MRI

Nuclear spin

As discussed above, ^{1}H is the obvious choice for probing biological samples; biological tissues contain a high proportion of water and hydrocarbons, and protium is the most abundant isotope of hydrogen.

A nucleus contains a spin, whereby the nucleus rotates about an axis. This can be thought of like a vector, with a direction and magnitude. Because of the composition of the atomic nucleus, this spin results in a magnetic moment that is parallel to the axis of rotation (see **Figure 1**A). At rest, protons are orientated randomly in space with respect to one another, which will give a zero sum of spin vectors - in other words there will be no net magnetization. However, when an external magnetic field is applied (B_0), the protons will begin to rotate, or precess about the external field (**Figure 1**B). The movement of a spin can be seen in a 3-dimensional Cartesian co-ordinate system, with *z* direction being parallel with B_0, and *x* and *y* being perpendicular to B_0; *x* and *y* vary with time, but *z* is constant with time. The precession of the nucleus around the magnetic field can be calculated empirically using the Larmor equation:

Equation 1 $$\omega_0 = \gamma B_0/2\pi$$

Where ω_0 is the Larmor or resonant frequency (MHz) and γ is the gyromagnetic ratio, which is a constant value specific to the nucleus in question. Larmor

frequency is also known as the *resonance* frequency, hence the title magnetic resonance imaging. If we now perform a sum of the vectors, we no longer get a result of zero; in the direction perpendicular to B_0 (*x* and *y*), spins are still distributed randomly, so there is no net magnetization (sum = 0), but in the direction parallel to B_0 (*z*) there is a non-zero sum of vectors due to a coupling between B_0 and the spinning protons. These spins are either aligned parallel to B_0 (spin up), or anti-parallel (spin down), resulting in an energy difference proportional to B_0, as the spin up orientation has a lower energy than spin down. In a population of protons, there will be more orientated in the lower energy, spin down orientation, than spin up, so the protons within the tissue become polarized: there is a net magnetization (M_0) proportional to B_0, which is parallel to B_0. This is the basis to all MR applications – this configuration of longitudinal magnetization (parallel to B_0), with no transverse (perpendicular) component is the equilibrium of the system, and the state that protons will return to following any disruption to the system.

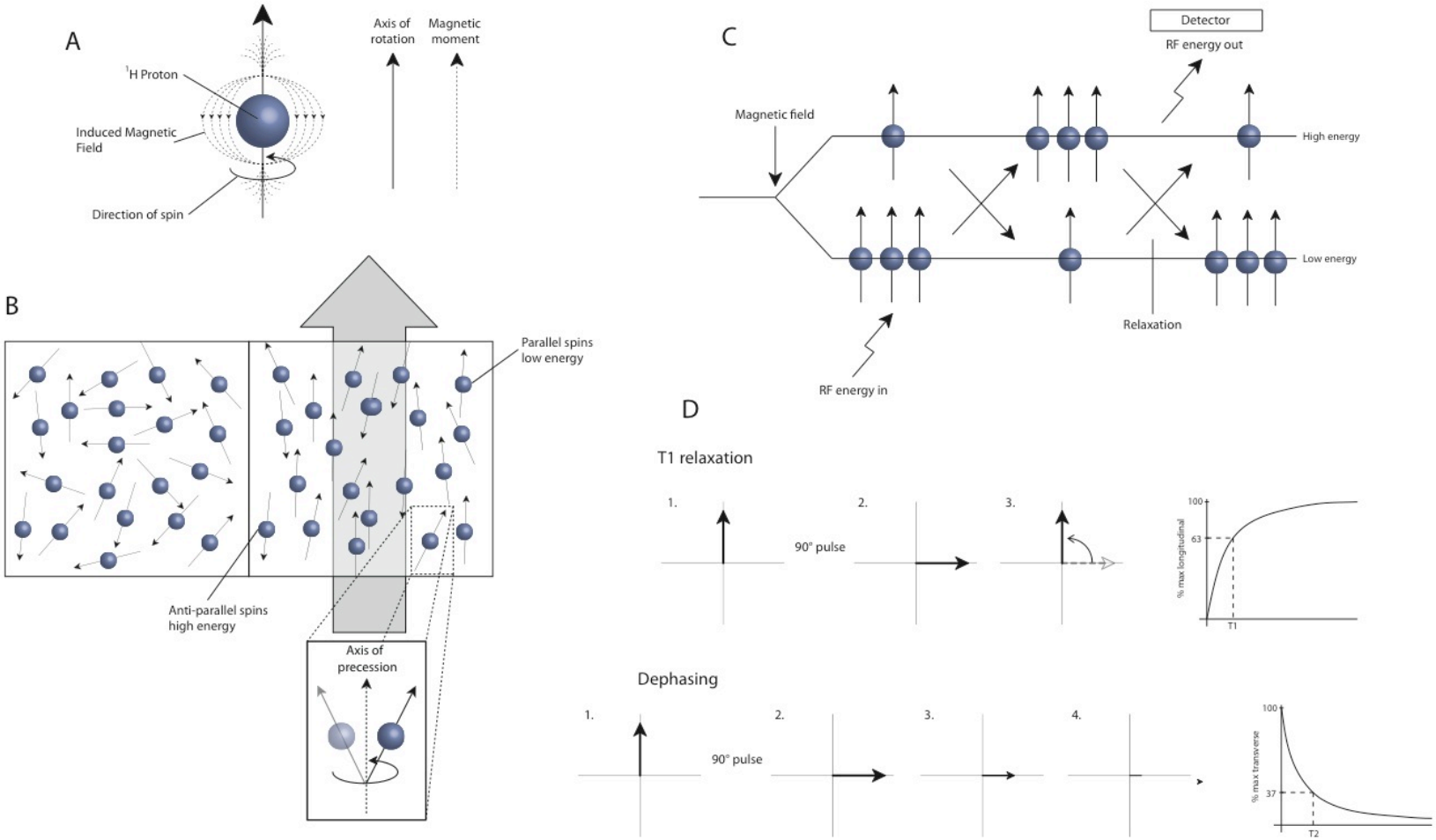


Figure 1 – Principles of nuclear magnetic resonance spin and signal detection (see next page for figure legend)

Figure 1 (previous page) – principles of NMR spin and signal detection

The basic magnetic properties of a proton are illustrated in Figure A. A proton spins around an axis, and in doing so creates a small magnetic field, with the magnetic moment parallel to the axis of rotation. Outside of a magnetic field, the protons are orientated randomly with respect to one another (B, left panel), but in a magnetic field of a given direction (B, right panel), the protons tend to align either parallel with the magnetic field (low energy), or anti-parallel wit the magnetic field (high energy), and precess about the axis of the magnetic field. The split of high energy and low energy protons is unequal, with a slightly larger population of low-energy compared to high-energy spins. The splitting of energy levels is shown in Figure C, and on application of a radiofrequency (rf) pulse of the appropriate wavelength, energy is put into the system, flipping energy levels so that low energy become high energy spins. After removing the (rf) pulse, the spins "relax" to their original conformation, and the net movement of high energy spins back to low energy spins releases the energy in a pulse of the same frequency, which can be measured by a detector. In T_1 relaxation (Figure D, top row), the vector sum of all the spins is initially orientated parallel to the magnetic field (longitudinal axis - 1.). A radiofrequency pulse deflects the population to, for example, 90° (transverse axis - 2.), which gradually relaxes back to the longitudinal axis (3.). This can be illustrated graphically (Figure D, top right graph), and T_1 is defined as the time taken to regain 63% of the longitudinal magnetization. T_2 on the other hand is defined as loss of transverse magnetization (Figure D, bottom row). This is explained by two mechanisms. The first is the relaxation of the population back to the longitudinal orientation, as for T_1 above. However, in addition to this, after application of the RF pulse, spins begin to dephase (i.e. spin at different speeds), and this loss of coherence results in a diminution of the vector (2. – 4.). T_2 is defined as the time taken for transverse magnetization to be reduced to 37% of its original value (Figure D, bottom right graph).

Radiofrequency pulses

All MRI sequences rely on manipulations of net magnetization by radiofrequency (rf) pulses (**Figure 1**C). A pulse of rf energy is applied to a population of protons. Spin up nuclei (low energy) will absorb this energy, moving to a higher energy state, and spin down nuclei (high energy) will emit energy at the same frequency as they move to a lower energy state. Because there is a larger population of spin up nuclei as described above, the net change is absorption at ω_0. Absorption of rf energy causes M_0 to rotate in a direction perpendicular to both B_0, which if applied for long enough results in full rotation into the transverse plane (90° pulse).

When the rf energy is removed, the protons will move back towards the equilibrium position, regaining longitudinal magnetization and losing transverse magnetization, emitting energy. This is what generates the signal in all MRI

experiments – the energy change that occurs when protons move from an excited state back to equilibrium.

T_1 relaxation time

T_1 relaxation time is the time required for the *z* (longitudinal) component of the net magnetization to return to 63% of its original value (**Figure 1**D, top row). For a 90° rf pulse, after excitation the net magnetization will rotate fully into the transverse plane, so the longitudinal magnetization will be 0%. The protons will then release energy to their surroundings over time and return to equilibrium, so T_1 will increase exponentially over time until it reaches 100%. It is this feature that determines the contrast seen in tissue. The molecular structure of proteins in the tissue, and the presence of metal ions will affect the frequency of molecular motion in surrounding molecules.

On T1-weighted scans, the intensity for tissue types from most bright to most dark is white matter – grey matter – CSF.

T_2 and T_2* relaxation time

T_2 relaxation time is the time required for the transverse magnetization component (magnetization in the *x,y* plane) to decay to 37% of its original value. After a 90° rf pulse, the excited protons are rotated fully into the transverse plane with all protons rotating with the same resonant frequency, thereby having 100% phase coherence. Nearby protons will have a very similar magnetic environment, so will initially have almost the same resonant frequency, so will easily absorb energy from their neighbours, leading to a de-phasing and loss of transverse magnetization. Given this explanation, it can be deduced that T_2 relaxation time is therefore always less than or equal to T_1 relaxation.

True T_2 relaxation only comes from the irreversible loss of coherence due to interactions with adjacent spins. However, in reality, spins rarely encounter a 100% homogeneous magnetic field, and fluctuations in magnetic field as the proton precesses result in changes to the resonant frequency and therefore more de-phasing. One source of such non-uniformity is the magnetic susceptibility artefact. Different tissues have different degree of polarization of spins, and therefore the local magnetic field becomes distorted at the junction between different tissue types. The typical example of this in MRI of the head is the air pockets of the sinus, which causes profound magnetic susceptibility artefacts. T_2* relaxation is defined as the total loss of transverse magnetization, due to both T_2 relaxation, and the addition de-phasing due to magnetic inhomogeneities. T_2* imaging is particularly useful in certain pathologies where ferric iron deposition is present, as this also has large magnetic susceptibility effects. For example, using this technique, iron-containing amyloid-β plaques can be imaged using MRI (Benveniste et al., 1999).

On T_2-weighted scans, the intensity for tissue types from most bright to most dark is CSF – grey matter – white matter.

Diffusion-weighted imaging

Diffusion weighted imaging (DWI) allows the exploration of tissue microstructure by sensitising the MRI acquisition parameters to tissue water diffusion (Basser and Pierpaoli, 1996, Pierpaoli et al., 1996). At any temperature about 0 K, water molecules vibrate, which underpins the phenomenon of Brownian motion. When there are no barriers to diffusion, water will move in all directions equally (isotropic diffusion), but if there are barriers (such as highly organised neuronal tracts), the molecules are able to move in some directions more freely than others (anisotropic diffusion). By sensitizing MR images to this feature, we can infer structure in biological samples.

MRI scans can be ‘diffusion-weighted’ (DW) using pairs of opposite gradients (Mori and Zhang, 2006) in a spin echo paradigm. In a typical diffusion-weighted sequence, a 90° rf pulse is used to flip the spins to the transverse plane, then allowed to return slightly to equilibrium. In this period, a gradient is applied in a specific direction, which will lead to a de-phasing of spins along the axis of the gradient due to differences in magnetic field (see **Equation 1** above). This is then removed, and a 180° rf pulse is applied, inverting the spins. Finally, an equal gradient is applied as the one between the 90° and 180° pulses, and once the same amount of time has elapsed as between the 90°and 180° pulse there will be an echo. For molecules that have not moved during the sequence, there will be large echo, as the two gradients are equal but in opposite directions (because the 180° pulse has inverted the spins), so the initial de-phasing will be cancelled out by the second re-phasing. However, when diffusion has occurred, the molecule will experience a different magnetic field for the re-phasing than it experience in the de-phasing, and therefore there will be decreased synchrony, and therefore a loss of signal.

Each voxel is measured from a number of different directions (generally 6 or more), this information can be integrated to calculate the apparent diffusion coefficient (ADC). From these values, an apparent diffusion coefficient (ADC) map can be constructed, by taking an average of the three directions at each voxel (see **Equation 2**). ADC is susceptible to changes in tissue structure as well as metabolic effects.

Equation 2 $ADC_i = (ADC_x + ADC_y + ADC_z)/3$

Diffusion tensor imaging (DTI) reconstructs diffusion directions in 3-dimensional space from a number of DW scans (minimum 3) using the diffusion tensor (Basser et al., 1994), which unlike the ADC map is able to provide directional information. The diffusion tensor can be seen as a 3-dimensional ellipsoid, with three main directions (eigenvectors): λ_1, which corresponds to the long axis of the ellipsoid (length), also known as axial diffusivity ($\lambda_{\parallel}$); and λ_2 and λ_3, which correspond to the two shorter axes (width and depth), which are generally averaged to give a value of radial diffusivity ($\lambda_{\perp}$). In brain white matter, which typically has more of an ellipsoid shape compared with grey matter, radial diffusivity is often seen as a measure of tract integrity, as this is the main obstacle to diffusion. Increased radial diffusivity is therefore suggestive of demyelination, with axial diffusivity more indicative of axonal damage (Song et al., 2002, Song et al., 2003, Song et al., 2005).

Fractional anisotropy (FA) is a widely used surrogate index of tract integrity. This is also based on the diffusion tensor, and is a direct measure of the shape of the ellipsoid, with 0 being completely spherical, and 1 being completely ellipsoid.

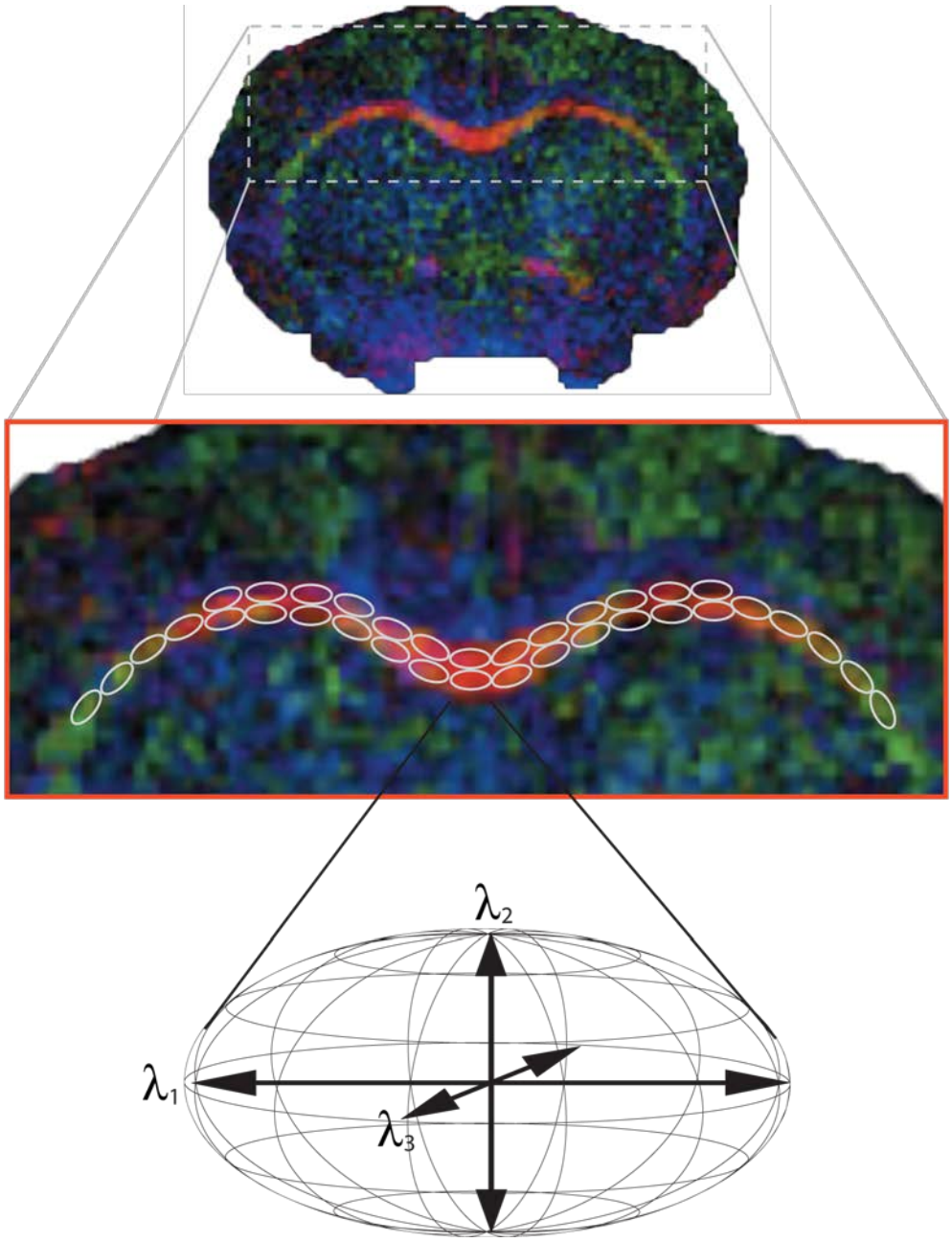


Figure 3 - Deriving the diffusion tensor.

Diffusion in white matter tracts where most fibres travel in the same direction (such as the corpus callosum) can be seen as a series of 3D ellipsoids (centre rectangle). Each ellipsoid is defined by three eigenvectors, λ_1 (primary), λ_2 and λ_3, with λ_1 representing diffusion parallel with fibre tracts (axial diffusivity, $\lambda_{\parallel}$), and the average of λ_2 and λ_3 representing diffusion orthogonal to fibre tracts (radial diffusivity, $\lambda_{\perp}$). Averaging all three eigenvalues provides an estimate of mean diffusion, and integrating them can provide the commonly-used measure, fractional anisotropy (FA).

(Figure modified from Guilfoyle *et al.* (2003) with permission)

Magnetization transfer imaging

Within a water solution or tissue, there are two types of water molecule – free water, and water bound to macromolecules (hydration). Free water has a high resonant frequency and narrow resonant peak, as it is not slowed by interaction with other molecules, and much longer T_2, because less dephasing occurs from less extra-molecular interactions. By contrast bound water has a much lower resonant frequency and a very broad resonant peak, as well as short T_2 relaxation time, because interactions with macromolecules causes quick de-phasing and slows down spins. As a result of T_2 relaxation being less than 200ms in bound protons, this population contributes very little to the MRI signal in traditional sequences. In magnetization transfer imaging, an off-resonant pulse is used to saturate the spins from bound water molecules, which removes longitudinal magnetization, and the transverse magnetization is quickly lost after switching off the pulse. Because of spin-spin interactions, this loss of longitudinal magnetization can be transferred from the bound pool of protons to the free pool of protons, which increases T_1 in the free proton pool, and reduces signal in tissues where magnetization transfer happens more readily.

This adds additional contrast to tissues with lots of magnetization transfer (water-containing tissues) compared to tissues with less magnetization transfer (fat-containing tissues). By subtracting a pre-saturation image from a saturation image, a magnetization transfer ratio (MTR) can be calculated:

Equation 3 $$MTR = (MT_{pre\text{-}sat} - MT_{sat}) / MT_{sat}$$

Where MT_{sat} is the T_1 or proton density image with magnetization transfer saturation and $MT_{pre\text{-}sat}$ is A T_1 or proton density scan with the same parameters

as the saturation, but without the off-resonance saturation pulse. Studies have used MTR as a marker of tissue integrity, as changes such as demyelination or cellular damage will cause changes in the bound / free proton ratio, and therefore will lead to differences on MTR images.

Magnetic resonance spectroscopy

Magnetic resonance spectroscopy (MRS) relies on much the same underlying principals as MRI, and fundamentally relies on a concept known as the chemical shift. In **Equation 1**, I showed that the resonant frequency (ω_0) of a proton is determined by the magnetic field it is exposed to. This comes from two main sources: i) the applied magnetic field B_0; and ii) alterations to the field due to the molecular environment. In MRS, unlike MRI, the magnetic field is kept constant as there are no applied gradients, meaning that the magnetic field a proton experiences, and therefore ω_0 is determined solely by the molecular environment.

A good comparison to explain this phenomenon is a proton in water compared to a proton in fat. In water (H_2O) two protons are bound to a single Oxygen atom, whereas in a simple hydrocarbon, an alkane (C_nH_{2n+2}) protons are bound to carbon atoms in a long continuous chain. This different molecular environment produces different effective magnetic fields, meaning that the protons in each case process with a different ω_0. The difference in magnetic field is called **chemical shielding** and the shift in resonant frequency is called a **chemical shift**. This principal is the same for all hydrogen-containing molecules, so the relative amounts of any hydrogen-containing molecule can be investigated in this way.